Riga Technical University

Faculty of Electronics and Telecommunications

Institute of Radioelectronics

Nikolajs Ponomarenko

Doctoral student of "Electronics" study program

Study of Frequency and Microstructure Dependencies of Magnetic Losses of Ferrite Materials and Components

Doctoral Thesis

Scientific supervisor

Dr. habil. sc. ing., prof.

J. Jankovskis

Rīga 2014

ABSTRACT

In this thesis it is shown, that complex permeability (CP) in the form of complex initial permeability (CIP) as intrinsic property (InP) of polycrystalline ferrites (PF) is possible to model basing on effects following from polycrystal grain size distribution. In order to prove this there were experimentally studied a large amount of magnetic spectra of different ferrite sample groups. The studied groups of samples were selected both from available industrially made ones and from specially made samples (so to get similar microstructure within the group of samples). In its turn the study of CIP as extrinsic property (ExP) is performed experimentally. In particular it shows, that dimensional resonance depends on cross section L, number of turns N of its winding and nonmagnetic gap δ width. The obtained CIP as InP is viewed as the reference dependence allowing for better insight in ExP phenomena. Also, there was developed, and implemented in MATLAB®, an accurate and effective method for verification of quality of incomplete, noisy or rather doubtful (low quality) spectra by means of Kramers-Kronig relations.

Keywords: polycrystalline ferrites, complex initial permeability, intrinsic property, polycrystal grain size distribution, extrinsic property, dimensional resonance, Kramers-Kronig relations.

ANOTĀCIJA

Šajā darbā ir parādīts, ka komplekso magnētisko caurlaidību (KC) kompleksās sākuma caurlaidības (KSC) veidā kā pašpiemītošo īpašību (intrinsic property, InP) polikristaliskos ferītos (PF) ir iespējams modelēt, izejot no efektiem, kas izriet no polikristalisko graudu izmēra sadalījumiem. Nolūkā to pierādīt tika eksperimentāli izpētīti un analizēti dažādu ferītu paraugu grupu magnētiskie spektri. Pētāmo paraugu grupas tika izvēlētas kā no rūpnieciski ražotiem, tā arī no speciāli izgatavotiem paraugiem (lai iegūt vienādu mikrostruktūru visiem paraugiem grupā). Savukārt KC izpēte kā nepašpiemītošs raksturojums (extrinsic property, ExP) tika veikta eksperimentāli. Tā parāda, ka dimensionālā rezonanse ir atkarīga no šķērsgriezuma lielākā izmēra L, mērtinuma vijumu skaita N un no nemagnētiskās spraugas δ lieluma. Iegūtie KSC spektri kā InP attiecībā pret ExP tiek uzskatīti par references atkarībām, ļaujot dziļāk izprast ExP parādības. Šajā darbā ir izveidota un realizēta MATLAB® vidē programma efektīvai nepilnīgo, trokšņaino vai dažkārt apšaubāmas (ar slikto kvalitāti) kvalitātes spektru novērtēšanai ar Kramersa-Kroniga sakarību palīdzību.

Atslēgvārdi: polikristāliskie ferīti, kompleksa sākuma caurlaidība, pašpiemītošās īpašības, polikristālisko graudu izmēru sadalījums, nepašpiemītošas īpašības, dimensionāla rezonanse, Kramersa-Kroniga sakarības.

ACKNOWLEDGEMENT

The research presented in this thesis was developed in the Riga Technical University, under the supervision of Dr. habil. sc. ing., prof. Jānis Jankovskis. I am grateful to him for guidance, advices, availability, patience and enthusiasm within the work progress. Additional thanks to the academic staff of Riga Technical University for the given knowledge and experience during the study process, Nina Mironova-Ulmane for the advices about the research details within the thesis and J. Barloti for the great help in preparing of the test samples. Special thanks to my wife and parents for patience and guidance.

This work also has been supported by a funding of the ESF project.

TABLE OF CONTENTS

List of main abbreviations

1D	one dimensional
2D	two dimensional
3D	three dimensional
AC	alternating current
ACp	absorption component
CCM	continuous current mode
CIP	complex initial permeability
CP	complex permeability
DC	direct current
DCp	dispersion component
DIF	diffusion after effect
DR	dimensional resonance
DW	domain wall
EMC	electromagnetic compatibility
EMI	electromagnetic interference
EMIC	electromagnetic inductive coupling
ESL	equivalent series inductance
ESR	equivalent series resistance
ExP	extrinsic property
FFDM	flux-field directional materials
FM	frequency modulation
GSE	generalized Steinmetz equation
HF	high frequency
iGSE	improved GSE
InP	intrinsic property
IQG	intrinsic quality group
KKR	Kramers-Kronig relations
LPS	linear power supplies
MS	magnetic spectra
MSE	modified Steinmetz equation
MSG	modulating signal generator
MST	microstructure
NGG	normal grains growth
NSR	natural spin resonance
PCB	printed circuit board
PF	polycrystalline ferrites
PFC	power factor correctors
r.m.s	root mean square
RFI	radio frequency interference
SCL	shortened coaxial line
SE	Steinmetz equation
SEM	scanning electronic microscope
SMPS	switched mode power supplies
SST	spread spectrum technology
TQG	technical quality group
VCO	voltage-controlled oscillator
VNA	vector network analyzer
WPC	wireless power charging

List of used physical values

f_{SW}	switching frequency
f	frequency
$\mu(0)$, μ_{stat}	static permeability
$\dot{\mu}(f)$	complex permeability
B_m	maximum flux density
B_S	saturation flux density
M_S	saturation magnetization
$\mu'(f)$	complex permeability dispersion (real) component
$\mu''(f)$	complex permeability absorption (imaginary) component
$tan\delta(f)$	magnetic loss tangent
P_i	specific loss
P_h	hysteresis loss
P_e	eddy-current loss
P_a	anomalous loss
k_h	hysteresis coefficient
π	constant $\pi = 3.1415$ ...
d	the dimension of the core (for laminations – d is the thickness, for cylindrical and spherical shapes – d stands for diameter)
ρ	resistivity
W_i	specific loss energy
W_h	hysteresis loss energy
W_e	eddy-current loss energy
W_a	anomalous loss energy
W_{tot}	experimentally observed (total) loss energy
B_r	remnant flux density
H_c	coercive field strength
H_m	field strength maximum
μ_a	amplitude permeability
μ_0	magnetic constant
B	flux density
H	field strength
R_h	series hysteresis loss resistance
I	the r.m.s. current
A	the effective cross-sectional area
ω	angular frequency
L	the inductance
β	the core cross-section shape constant

$R_{in}\|R_{out}$	the inner or the outer diameter of toroidal core
l_e	the magnetic path length
R_e	the eddy current series loss resistance
$tan\delta_h$	hysteresis loss tangent
$tan\delta_e$	eddy-current loss tangent
$tan\delta_a$	the anomalous loss tangent
P_{core}	the magnetic core average loss power dissipation per unit volume
k, α, β	empirical coefficients
f_r	the pulse repetition frequency
T	the period
f_{eq}	the equivalent frequency
P	power loss
t	time
δ	phase angle
$\dot{Z}$	complex impedance
L_s	series inductance
R_s	series resistance
L_0	geometric inductance
$\dot{Y}$	complex admittance
R_p	parallel resistance
L_p	parallel inductance
$\mu_s^{'}$	real series component of CIP
$\mu_s^{''}$	imaginary series component of CIP
$\mu_p^{'}$	real parallel component of CIP
$\mu_p^{''}$	imaginary parallel component of CIP
X_s^*	complex susceptibility
$X_s^{'}$	the real part of the complex susceptibility
$X_s^{''}$	the imaginary part of the complex susceptibility
τ	the relaxation time
$\mu_{DIF}^{'}(f)$	relaxation type diffusion after effect dispersion component
$\mu_{DW}^{'}(f)$	large amplitude dispersion attributed to DW processes
$\mu_{DW}^{''}$	DW component absorption curve
$\mu_{NSR}^{'}(f)$	the small amplitude dispersion related to the natural spin resonance
f_0	the resonance frequency
ξ	the normalized damping constant
$\mu_{max}^{''}$	ACp maximum
f_u	ACp maximum frequency
D	grain size
$f(D), f_{ln}(D)$	the probability density functions
D_{med}	the median
σ_{ln}, σ_D	the standard deviations
D_a	average (mean) grain size
f_{rot}	the rotation process resonance frequency
γ	the gyromagnetic ratio
D_{a0}	the average diameter of monodomain grains
D_{th}	the grain size threshold
D_{eff}	the effective grain size
f_{osc}	resonating frequency of polycrystal grain
C_1, $C_1^{'}$ and $C_2^{'}$	constants
$\mu_{exp}^{''}(f)$	the experimental ACp
f_a, f_b	the model specific frequency working points
σ_a, σ_b	the model specific dispersion working points
N_P	primary winding
N_S	secondary winding
N_D	demagnetizing winding
U_{in}	input voltage
U_{out}	output voltage
$f_{sw}(t)$	instantaneous switching frequency
Δf_{sw}	the switching frequency deviation
$m(t)$	modulating signal
f_{sw0}	the nominal switching frequency
r_C	capacitor equivalent series resistance
L_C	capacitor equivalent series inductance
R_L	inductor equivalent series resistance
C_0	inductor parallel self capacitance
P_w	winding losses
P_{mc}	magnetic core lossees
I_L	the r.m.s. current of a inductor
I_{Lac}	AC component of the inductor current

I_{out}	DC component of the inductor current
D_C	duty cycle
L	inductance
N	number of turns
S	magnetic core cross section area
$P_{lossmod}$	the average power loss of the inductor in the case of frequency modulation
$p_{im}(t)$	instantaneous losses in the power inductor
T_m	modulation period
K	an integer number, $K=T_m/T_{sw}$
P_{ind}	inductor average power loss
x	coordinate on x axis
y	coordinate on y axis
m_i, c_i	linear function coefficients
Δ	measuring step
N_i	grain number in *i*-th group in 1 mm^3 of material
D_i	grain number in *i*-th group
$\sum V$	cumulative volume of grains in 1 mm^3 of material
$\sum S$	specific surface area
m	the number of intersections per unit length of the secant
g_{av}	average number of grain boundaries that are found on the one secant
l_{av}	average number of the secants in micrograph
n	the grain number in one micrograph
$\overline{D}$	average diameter of grain for MST analysis
φ	phase shift between these two voltages
R	resistance
R_m	magnetic resistance
d_1, d_2	inner and outer diameters of toroid
$\dot{\varepsilon}$	complex permittivity
ε'	real part of the complex permittivity
ε''	imaginary part of the complex permittivity
C	capacitance
C_0	the geometric capacitance
ε_0	vacuum permittivity
λ	wave length
ε_r	relative permittivity
μ_r	relative permeability
c_0	velocity of electromagnetic waves in vacuum
μ_0	vacuum permeability
δ	nonmagnetic gap size in sample

"…the situation in ferrites seemed at first time to be more complicated than in metals and gave rise to the legend that ferrite is a non reproducible material"
A. Globus [45]

1 INTRODUCTION

Nowadays technology and science is focusing on three global problems [110]: **energy, environment and health**. Magnetic materials can contribute in each of them: in energy mainly by the increase of efficiency of energy conversion; in environment by decrease of electromagnetic pollution and generation of excess heat; in health by use of magnetic technologies (e. g. drug delivery). In all of these cases the role of magnetic materials is undeniable. The soft magnetic materials (such as ferrites – which are the objects of this investigation), usually as polycrystals, but sometimes as amorphous and nanocrystalline materials as well), represent the *magnetics* "pillar" of power electronics (i. e., being one of the three traditional pillars of power electronics: power semiconductors; control; and magnetics [105]). Magnetics contributions in these problems include: improved performance of magnetic components; reduced electromagnetic interference (EMI) and better electromagnetic compatibility (EMC); lower cost alternatives to existing solutions; development of tools based on magnetic characterization; and advanced measuring probes. Thus, the role of soft magnetic materials is significant in developing an up to date power electronics.

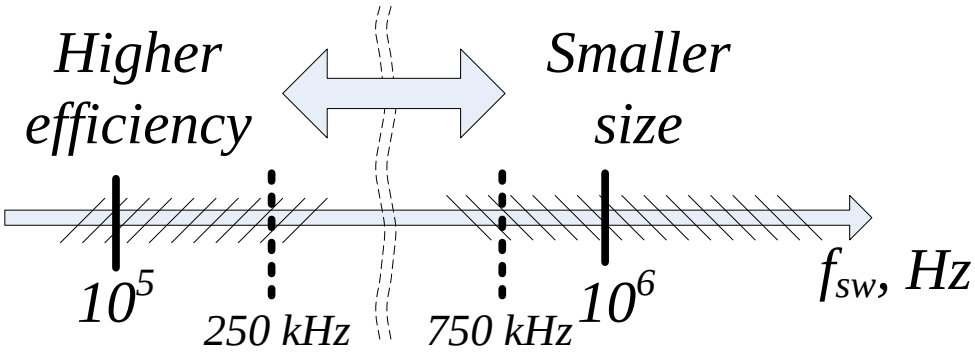

Figure 1.1 Power Integrations 500W Hyper LCS family resonant converter efficiency and size dependence from frequency (data from [125])

The electronics units (especially – hand-held devices) tend to become lighter and smaller, even so maintaining high efficiency. While the signal processing parts of electronics (e. g., microprocessors) are following the Moore's Law, power supply electronics based on

the highest efficiency converters – switched mode power supplies (SMPS), is developing much more slowly: its power density is doubling only in every ten years [35] (since 1970). Even this is obtained mainly through the use of higher switching frequencies, f_{SW}, which in their turn are growing by a factor approaching ten in recent decades [35]. The use of high f_{SW} affects nearly every performance characteristic of SMPS [115, 118] and requires new attention to be placed even on the parasitic impedances, effects from printed circuit board

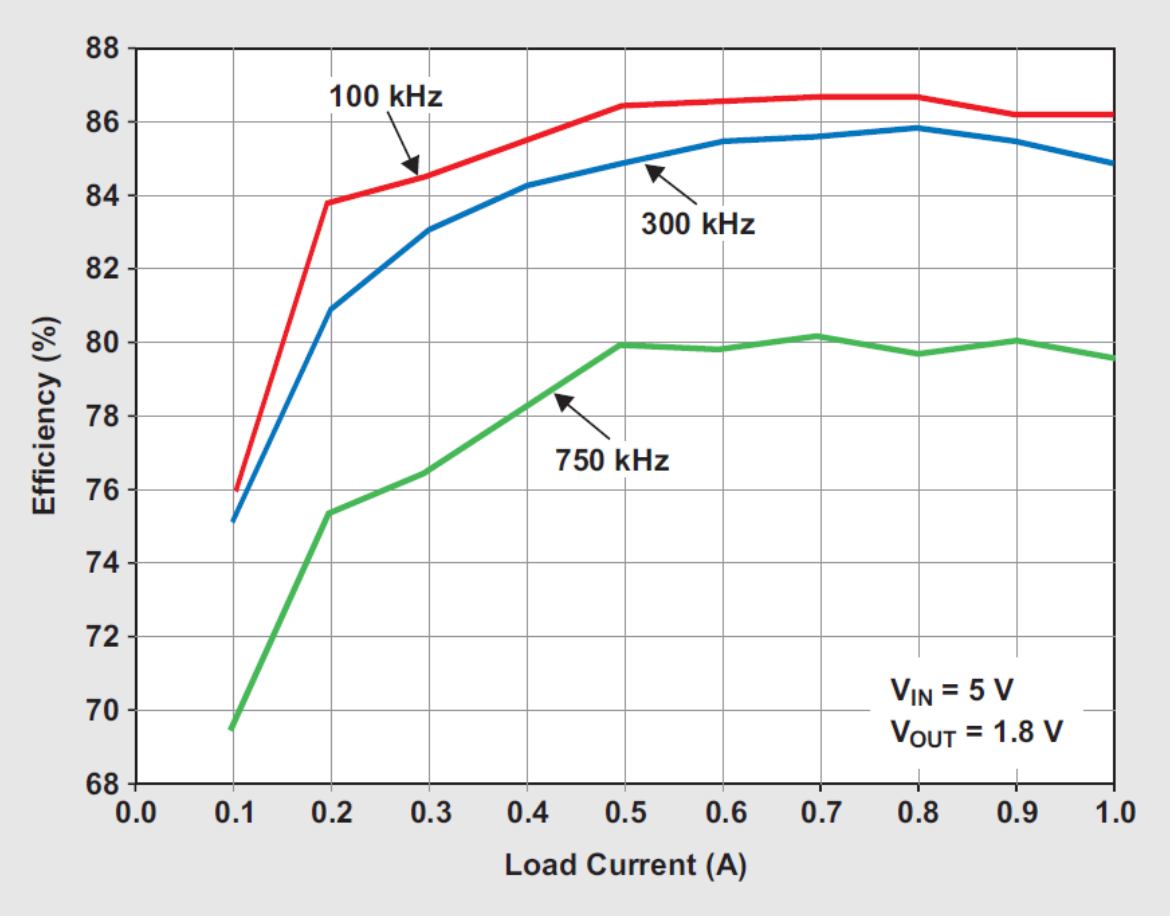

Figure 1.2 Efficiency of TPS54160 at three example frequencies [115].

(PCB) layout, potential sources of large output ripple switching spikes, and EMI – both conducted and radiated [90]. Therefore unjustifiably high f_{SW} often results in lower efficiency (as it is shown in Fig. 1.1 for Power Integrations 500 W Hyper LCS family resonant converter [125]: it can be seen that there exists a gap between two possible choices – smaller size as operating at 750 kHz and maximum efficiency (up to 97 %) at 250 kHz). Other research [106] on the high frequency DC/DC converter TPS54160 gave similar results. From Fig. 1.2 it is clearly seen that efficiency decreases with increased switching frequency. Moreover, according to [115], calculated device area savings between 100 kHz and 750 kHz realizations

are almost 250 mm^2, but the inductor in fact occupies the same area both for 300 kHz and 750 kHz applications, since there is a limit to the availability of appropriately sized inductors, if mass produced ones are used [115].

The solution provided in this connection is a design trade-off [82] between smaller size (but with a decrease of efficiency), or the highest efficiency (possible with larger size). Nevertheless, higher f_{SW} provides the possibility of using smaller magnetic components in SMPS due to the reduction in size of magnetic components. But drastically reducing the size of inductive components affects the preservation of high efficiency. Besides design of inductive components with small dimensions is seriously hampered if along with high efficiency the wide working frequency range is needed.

Nowadays, the PF remains the typical core materials used for the production of high efficiency components. For many high frequency (HF) applications of PF – for signal and switch mode power supply electronics as inductive components, for electromagnetic compatibility and wireless power supply as elements, components, and HF absorbing materials. The improvements of magnetics for SMPS mainly are related with that of polycrystalline ferrites (PF). They (especially MnZn and NiZn ferrites) are the common choice for inductive component cores applications within frequency range of several kilohertz to several megahertz. Besides, there are increasingly stringent requirements to dimensions, reliability, stability of inductive components in wide frequency range. This makes it to be more attentive to the choice of conventional ferrites (basing on deeper understanding of their nature) and dictates the trends for development of new ones. Often, the PF primary task is to concentrate and guide the magnetic flux. Potentially this and other functions are fulfilled, to a greater or lesser extent, by PF being found either as *intrinsic* or *extrinsic* reality. The term *intrinsic* in the context of this work is used for distinction between the characteristics of PF samples that directly depend on composition and structure of materials, as opposed to those as *extrinsic* ones affected by quantity and shape factors. It is quite clear that the definite characteristic of PF in accordance with the conditions may be as intrinsic property (InP) or extrinsic property (ExP). Still it remains to be mentioned that there is possible to distinguish two "degrees" of InP of PF samples in relation to their processing technology and resulting MST: *"true intrinsic"* in the case of microstructure without intragrain defects and *simply "intrinsic"* in the opposite case.

As a such PF are formed by compaction from powders-pronouncedly porous collection of small particles to dense and strong product on heating them to appropriate temperature (through, e. g., calcination and sintering process). Throughout this the high porosity of

starting power material (which practically is only an intergranular one) decreases during the sintering process as a consequence of grain growth progression [45]. So the total porosity measured on PF, as a rule is the intergranular one, which plays only a minor role in the magnetization processes realized by domain walls (DW) (in contrast – the intragranular porosity is able to pin DW). Intragranular porosity actually exists in PF of conventional technology (at least in coarse grains) and thus substantially may influence DW processes. So the study of *true InP* (determined by chemical composition and typical microstructure (MST) *per se*) of PF is possible only on PF of special technology [45, 46, 47] which enables MST with perfect (or practically perfect) grains and allows to obtain the fundamental relationships for PF. Another degree of InP – *simple intrinsic* is possible to use for the group of PF representing huge amount of samples of conventional (industrial, laboratory) ceramic technology. They are differing from true InP group only by quality of MST: the grains (especially coarse ones) are with intragrain porosity. Such an occurance is typical and rather universal for great amount of PF samples; their characteristics, at least in principle, is possible to deduce from those of true InP group by some modifications.

In contrast to this in many engineering applications of PF we are dealing with their ExP (in this study: the dimensional resonance, influence of width of nonmagnetic gap). Platform for study of ExP comes from that of intrinsic ones.

Turning back to the flux concentration, of most concern are the primary magnetic characteristics of the material: relative permeability (both static permeability, $\mu(0)$, and complex permeability (CP), $\dot{\mu}(f)$, specified within the frequency, f, range of interest) and the saturation parameters (the saturation flux density, B_S, or the magnetization, M_S). The saturation parameters are universally available specifications not depending on the form of characterization of PF – as InP or ExP ones. Contrary to this CP $\dot{\mu}(f) = \mu'(f) - j\mu''(f)$ with $\mu'(f)$ as dispersion part, (component, DCp), and $\mu''(f)$ as the absorption part, (component, ACp), are more intricate characteristics which manufactures are specifying as a rule as InP for relatively small toroidal cores [140] and yet not always. And this in spite of reality that CP as InP and ExP typically differ widely, so their ability to concentrate the flux (typically under conditions of small magnetic losses) at the definite *f*. In the regards to losses CP is the key characteristic since HF losses of magnetic materials are directly related to CP, defining the value of magnetic loss tangent as: $tan\delta(f) = \mu''(f)/\mu'(f)$ and by Eq. 2.17 specific loss as well. In addition, for obtaining high efficiency at higher power levels the magnetic cores should be designed with significantly larger dimensions than low-power cores (the available

data, in general, represents the low power core specifications). But with larger dimensions of the core the new problem may arise that cannot be accounted using only specifications for low power ring cores. Such a problem is called the dimensional resonance (DR) in the core, which as well is investigated in this study.

The purpose of this work lies in:

- investigate the problems of presentation of complex initial permeability including the frequencies of large amplitude broadband dispersion (domain wall one);
- study of PF microstructure with the aim to form the basis for more deep understanding and modeling capabilities of complex permeability;
- study of the complex initial permeability in accordance with the microstructure (which is characterized by the mean grain size and size dispersion).

Investigators throughout the world over a period of six decades (i. e., active investigations of PF) have measured a great number of CIP spectra (data of several ones are included in our analysis) but often without details of MS (essential for the problems examined here) and from time to time with insufficient quality (that is verified by the correspondence of ACp and DCp of CIP to Kramers-Kronig relations (KKR) [145] by the use of proper numerical procedure). All this adds up to the necessity for further experiments especially in the field of MnZn ferrites due to their possibility of showing up DR.

The analytical presentation of CIP based on *grain size distribution effects model* [64] is described and experimentally substantiated. The experimental measurement frequency range was chosen so as to obtain most of the large amplitude broadband absorption region of CIP. The above stated practical applications determines the importance of this work.

The main subjects of research in this work are manganese zinc (MnZn) and nickel zinc (NiZn) ferrites (Table 1.1), as these materials are most common for application in SMPS. Both ferrite types can be made for use in particular applications by varying the Zn to Mn and Zn to Ni ratio. With the aim of nonlinearity effects neglection, the samples in this study are investigated under the action of weak fields, i. e., in fact CP $\dot{\mu}(f)$ is viewed as a complex initial permeability (CIP). Potentially the results gained for weak fields can be taken as the platform for understanding higher fields and non-sinusoidal excitations [159, 160].

Table 1.1 Magnetic and geometrical parameters of studied ferrite samples

Group	№	Dimensions, mm	$\mu(0)$	*The making of samples*
NiZn, 4S60	A1	R12 × 8 × 6	2000	*Cut from ferrite tile*
	A2	R20 × 10 × 6	2000	
	A3	R31.5 × 20.5 × 6	2000	
	A4	R40 × 23.5 × 6	2000	
MnZn, 6000HM1	B1	R10 × 4.3 × 10	6000	*Cut from ferrite tile*
	B2	R20 × 9.1 × 10	6000	
	B3	R25 × 12 × 10	6000	
	B4	R30 × 14.3 × 10	6000	
	B5	R33 × 10 × 10	6000	
MnZn, TDK T37	C1	R12.5 × 7.5 × 5	6500	*Commercial products*
	C2	R20 × 10 × 7	6500	
	C3	R40 × 24 × 16	6000	

In this work there are offered and proved the following theses:

- that losses, which are connected with main absorption region of magnetic permeability as frequency characteristic of ferrite material, can be presented analytically by the modeling based on polycrystal grain size distribution effects;
- that CIP as intrinsic characteristic of polycrystallyne NiZn and MnZn (small sample) ferrites is possible to present by modeling based on microstructure effects;
- that CIP as extrinsic characteristic of sufficiently large MnZn ferrite samples exhibit dimensional resonance which (along with already known factors) depends on number of turns of measuring winding, but variations of characteristics of spectra are not following Snoek's Law type relations;
- that Kramers-Kronig relations are powerful tool both for their use for verification of quality of magnetic spectra, and for decomposition, extrapolation and physically reasonable interpretation of compound magnetic spectra as a whole.

The main results of the work were presented on following conferences:

- The 8th international scientific and practical conference, Rezekne, Latvia, June 20–22, 2011;

- The 7th International conference on functional materials and nanotechnologies (FM&NT), Riga, Latvia, April 17–20, 2012;
- The 2nd international conference on materials and applications for sensors and transducers (ICMAST), Budapest, Hungary May 24–28, 2012;
- The 17th International conference "Electronics' 13", Kaunas, Lithuania, June 17–19, 2013;
- The 8th International conference on functional materials and nanotechnologies (FM&NT), Tartu, Estonia, April 21–24, 2013;
- The 21st International conference on soft magnetic materials (SMM-21), Budapest, Hungary, 1–4 September, 2013.

And there are published six publications:

1. J. Jankovskis, N. Ponomarenko, P. Narica. An Investigation on High Frequency Permeability of Polycrystalline Ferrites. *Proceedings of the 8th International Scientific and Practical Conference, Latvia, Rezekne, 20–22 June, 2011.– pp. 194–201.*
2. J. Jankovskis, N. Ponomarenko, N. Mironova-Ulmane, D. Jakovlevs. Dimensional effects of sample geometry and microstructure of MnZn and NiZn ferrites. *2012 IOP Conf. Ser.: Mater. Sci. Eng.* **38** 012018 *– pp. 1–4.*
3. J. Jankovskis, N. Ponomarenko, D. Stepins. Frequency Dependence of Complex Permeability of Polycrystalline Ferrites Based on the Realities of Microstructure. *Key Engineering Materials, 543, 2013,– pp. 507–510.*
4. J.Jankovskis, D. Stepins, N. Ponomarenko. Effects of Spread Spectrum on Output Filter of Buck Converter. *Electronics and Electrical Engineering, 2013, Vol. 19, No. 5, pp. 45–48. e-ISSN 2029-5731. ISSN 1392-1215.*
5. J. Jankovskis, N. Ponomarenko, N. Mironova-Ulmane, D. Jakovlevs. The study of correlation between microstructure of ferrites and their complex permeability spectra. *2013 IOP Conf. Ser.: Mater. Sci. Eng.* **49** 012045 *– pp 1–4.*
6. J. Jankovskis, N. Ponomarenko. Complex permeabliity of ferrites as intrinsic and extrinsic properties. J. Chem. Chem. Eng. 8 (2014) pp. 85–91

The first publication is indexed in Rezekne Higher Educational Institution database (http://zdb.ru.lv) . The publications 2, 3, 4 and 5 are indexed in SCOPUS and IOP databases. The 6th publication is indexed in databases of Cambridge Science Abstracts (CSA); Ulrich's Periodicals Directory, Database of EBSCO, USA; Chinese Scientific Journals Database, VIP Corporation, Chongqing, China; Chinese Database of CEPS, American Federal Computer

Library center (OCLC), USA; Chemical Abstracts Service (CAS); Google Scholar; Proquest, USA; CCRIS; ChemID Subset; DIRLINE; Gene-Tox, HSDB; TOXLINE/Subset; Publicon Science.

1.1 Synopsis of the thesis

The subjects of the study are polycrystalline ferrites (e. g. MnZn and NiZn materials) and their field of application as cores in SMPS power and filter inductive elements is presented. The first chapter of the thesis provides an overview of the problems associated with high frequency applications of ferrites in SMPS and losses. The study of complex magnetic permeability is directly related to the high frequency losses in ferrites.

The brief review of the ferrite losses in relation to frequency (static hysteresis loss, classical eddy-current loss and anomalous loss) is drawn in second chapter. The Steinmetz empirical approach in describing the magnetization process in PF and a more physical way of describing the magnetization processes (a complex permeability approach) are described. The different modeling approaches of CIP are presented, e. g. complex permeability modeling taking account of PF microstructure. An overview of power supply, and the problems of its magnetic components in relation to frequency, is presented at the end of the chapter.

The analysis of experimental magnetic spectra quality by the means of Kramers-Kronig relations is provided in chapter 3. Also, with help of KKR there is shown magnetic spectra decomposition possibility.

The fourth chapter provides actual examples of the study of ferrite microstructure, and related problems, in a review of the literature. An overview of the methods, that help to obtain microstructure parameters of ferrites, and the ferrite groups studied, are presented. Experimental results, are presented for each ferrite group studied.

The fifth chapter represents different CIP measurement techniques. Each method's field of application, together with advantages and disadvantages, is collated in a table. The experimental results are presented at the end of the chapter.

Chapter 6 uses background provided by the previous chapters to give the evaluation of spectra by means of the analytical model. The microstructure analysis and measured CIP data is used to experimentally test the model concept based on grain distribution. The analysis of samples exhibiting the dimensional resonance is presented in this chapter too.

Conclusions and possible future investigations are drawn in Chapter 7.

2 FERRITE CHARACTERISTICS AND APPLICATIONS

2.1 Generalities of ferrite characteristics in relation to frequency

2.1.1 Typical components of magnetic loss

The frequency dependence of the characteristics of magnetic components must be taken into account in the design of SMPS (as it affects the performance of the whole device) and in designing the filter components (as it affects the effectiveness of dealing with unwanted signals). There are two sources of the losses in magnetic components: losses in windings and in the core material [37]. The winding losses are fairly well described [81, 153], but the study of core losses (CL) still remains current. Therefore, in modeling of SMPS it is essential to correctly account for CL in order to raise efficiency of the SMPS [36]. The total core power loss (per unit volume) is usually separated [18, 108, 146] into components(typically for metallic materials, but even sometimes for PF as well):

- quasi-static hysteresis loss: $P_h = k_h f B_m^n$ (Steinmetz form); (2.1)
- classical eddy-current loss $P_e = \frac{\pi^2}{6}\frac{d^2}{\rho} f^2 B_m^2$; (2.2)
- anomalous (often termed as residual for ferrites and excess for metallic materials) loss $P_a = const(fB_m)^{3/2}$ for iron-based materials [16] and no known analytic representation for ferrites.

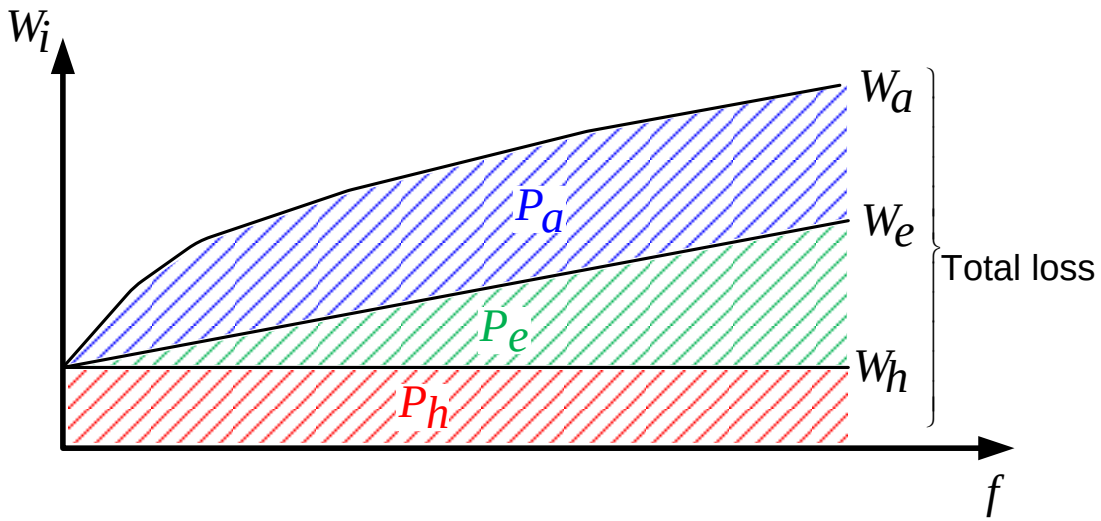

Figure 2.1. PF loss separation, adapted from [18].

Graphical display of components of total loss (Fig. 2.1) usually [18, 108] is more appropriate to analyse with help of loss energy $W_i = P_i/f$, where P_i stands for specific loss. Dealing with the loss energies (W_i) instead of power losses removes one power of frequency dependence of material power loss and thus the separation of losses becomes more descriptive

(constant W_h, linearly growing W_e and the rest as W_a). Generally adding up of W_h and W_e gives the value that is less than experimentally observed (total) value $W_{tot}(f) \equiv W_{exp}(f)$. To eliminate this discrepancy there is introduced anomalous loss $W_a = W_{exp}(f) - [W_h + W_e(f)]$.

2.1.2 Hysteresis loss

The **hysteresis loss** of energy usually is treated as due to magnetic domain processes in PF. The PF consists of a great number of differently oriented magnetic domains (Fig. 2.2). Boundaries of two adjacent domains form the domain wall (DW), where the magnetic moment direction changes (Fig. 2.2, *a*). If the external field *H* is applied to PF, the domains whose magnetization direction more closely corresponds to the applied field direction, will increase domain volume at the expense of oppositely oriented domains, and the domain wall will be displaced (Fig. 2.2, *b*). DW displacements vary under different field strengths for differently oriented domains. This process is also influenced by microstructure defects [183], which can prevent the DW displacement. Therefore, the hysteresis curve (Fig. 2.3) has a complicated form, that is centered around initial magnetization curve.

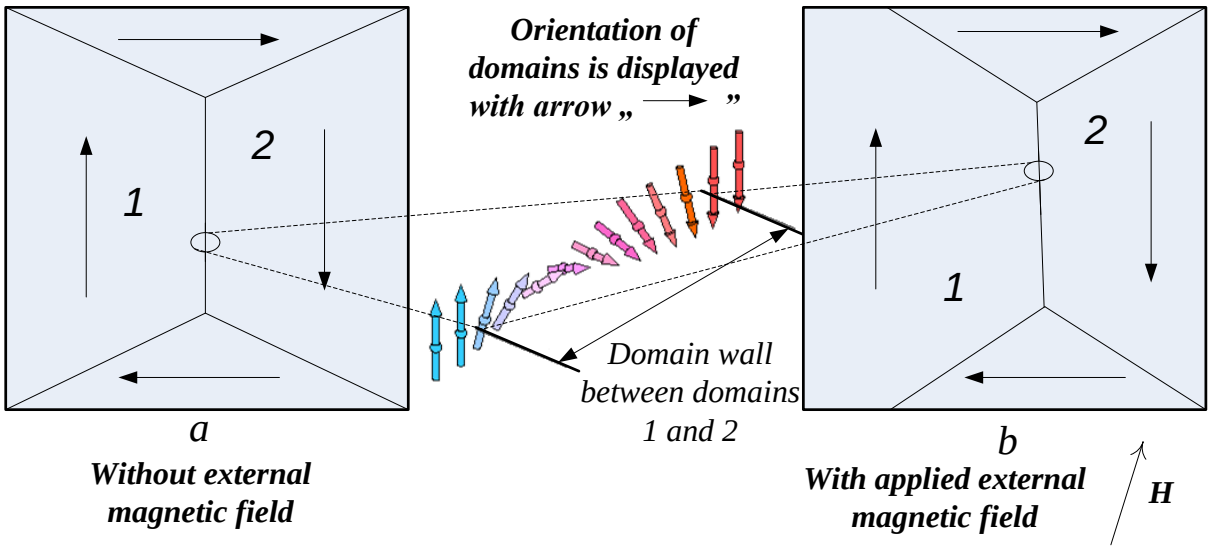

Figure 2.2. PF domain structure (a - without applied field, b - with applied field H) [183].

The initial magnetization curve can be divided into three regions (Fig. 2.3): 1) first region occurs due to reversible moving of domain walls, 2) second region – due to rotation of domain magnetization vectors in the direction of the applied field, 3) the third region describes the final magnetization process when all of the ferromagnetic magnetic moments tend to be oriented in the direction of the applied field: at the end of this region the domain

walls are fading and the magnetic moment becomes oriented in the direction of the applied field.

When the external field is removed the flux density does not return by the original path and at $H = 0$ there appears a remnant flux density B_r. To change dipole magnetization direction an opposing magnetic field is required, and at coercive field strength H_c the flux density becomes zero. The maximum flux density, where two branches of the limiting hysteresis curve coincide, gained with sufficiently higher field strength H_m, is called the saturation flux density B_s.

The area of the hysteresis loop characterizes the energy dissipation due to magnetization of material in alternating field. To reduce the hysteresis loss one must use materials with a smaller hysteresis loop. Also, to decrease the hysteresis loss (caused by irreversible DW displacements) suggested solutions are to use PF with smaller grains [23] or to eliminate DW processes by their pinning by anisotropic ions (such as Co^{2+}).

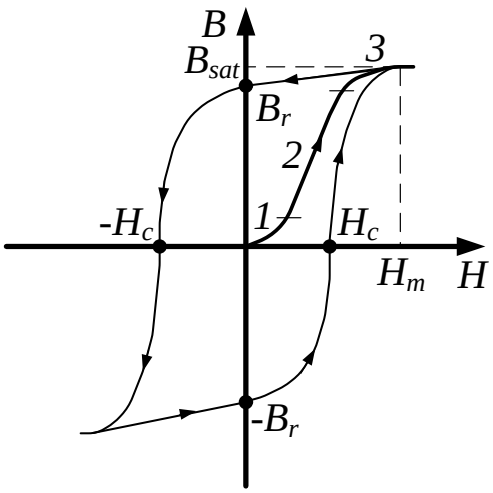

Figure 2.3. Hysteresis loop.

In [146] by means of using the Rayleigh hysteresis loop (i. e., in the low-field region, where $\mu(H) = \mu(0) + k_h H$) the expression for the hysteresis power loss density is presented as follows:

$$P_h = \oint BdH = \frac{4\mu_0 k_h H^3}{3} = \frac{4k_h B^3}{3\mu_0^2 \mu_a^2} \quad (2.3)$$

where k_h – is the hysteresis coefficient, μ_a– the amplitude permeability, μ_0– the magnetic constant, B– the flux density and H– is the field strength.

Then, the power dissipated in a ferrite core due to hysteresis loss is [146]:

$$P_h Al = P_h Alf = I^2 R_h \quad (2.4)$$

where R_h– is the series hysteresis loss resistance, I – is the r. m. s. current, and Al – is the core volume. Then expressing R_h will give:

$$R_h = \frac{4k_h B}{3\pi\mu_0\mu_a^2}\omega L \tag{2.5}$$

where ω – the angular frequency, and L – is the inductance.

Correspondingly, the hysteresis loss tangent is:

$$tan\delta_h = \frac{R_h}{\omega L} = \frac{4k_h B}{3\pi\mu_0\mu_a^2} = \frac{4k_h H}{3\pi\mu_a}, \tag{2.6}$$

and reveals proportionality to the field strength and inverse dependence on the amplitude permeability μ_a.

2.1.3 Classical eddy-current loss

The next loss component to consider is **eddy current loss**. Alternating magnetic flux in conductive medium induces eddy currents that result in energy losses called eddy current loss. The classical eddy-current loss for a sine wave is given as [140, 146]:

$$P_e = \frac{(\pi B_m f d)^2}{\rho\beta}, \tag{2.7}$$

where ρ – is the resistivity, B_m – the maximum flux density, f– the frequency, d – the dimension of the core (for laminations – d is the thickness, for cylindrical and spherical shapes – d stands for diameter), β is the core cross-section shape constant, with standard values [140, 146]:

$\beta = 6$ for laminations;

$\beta = 16$ for a cylinder;

$\beta = 20$ for a sphere;

The eddy-current loss, as it is shown in Fig. 2.1, becomes significant in total loss calculation, only at higher frequencies. Sometimes, instead of d, the effective cross-sectional area, A, of the core is used [136]. With core cross-section area for a toroidal shaped core ($A_{tor} = \frac{d^2 l_e \log(\frac{R_{out}}{R_{in}})}{3(R_{out}-R_{in})}$, where, $R_{in}|R_{out}$ – is the inner or the outer diameter of toroidal core respectively, l_e – the magnetic path length, d – the thickness of toroidal core [36]); with cross-section area of a cylinder ($A_c = \frac{\pi d^2}{4}$), the Eq. (2.7) can be written as [36, 140, 146, 160]:

$$P_e = \frac{\pi A}{4\rho} B_m^2 f^2 \tag{2.8}$$

In [160] it was also showed, that eddy-current loss depends on the actual waveform of excitation signal. For example, for a square-wave Eq. 2.8 can be written as:

$$P_e = \frac{2A}{\pi\rho} B_m^2 f^2 \quad (2.9)$$

This results in $\pi^2/8$ times difference between the loss for sine and square waves.

From the equations it can be seen, that eddy current losses are dependent on cross-section area of the core ($P_e \sim A$) and are proportional to the square of frequency ($P_e \sim f^2$), i. e., the losses will steeply increase at higher frequencies. Moreover, there is high dependence on actual signal waveform [160].

The eddy current loss tangent is [146]:

$$tan\delta_e = \frac{R_e}{\omega L} = \frac{\pi\mu_0\mu d^2 f}{\rho\beta}, \quad (2.10)$$

where R_e is the eddy current series loss resistance. The loss tangent dependency on the square of core dimension ($tan\delta_e \sim d^2$) means, that losses can be decreased by dividing the material into electrically isolated layers (or grains in PF).

The relations of classical eddy currents in fact are derived for metallic materials. The resistivity of PF is much higher and so there would be negligible eddy currents in NiZn-ferrites and only very small in MnZn ones. Nevertheless, formally for PF such term "eddy currents" is used as well since in the total losses there is possible to assume the existence of component proportional to $(fB_m)^2$. For one of the main magnetic materials for SMPS – MnZn ferrite the common view is that up to 200 kHz dominates hysteresis loss, but at higher frequencies – the eddy current loss [85].

2.1.4 Anomalous and total loss

The anomalous loss is still not adequately defined both physically and mathematically. In [36] are listed several possible reasons for this phenomenon in metallic ferromagnets: occurrence of domain walls; non-sinusoidal, non-uniform and non-repetitive domain wall motion; lack of flux penetration; non-sinusoidal flux density and localized variation of flux density; interaction between grains, grain size, grain orientation, and specimen thickness.

Most of these reasons are obviously related to the high level of exitation fields (in metallic materials). Nevertheless, PF in SMPS at frequencies above 500 kHz are normally used (because of rapid growth of loss with frequency) at low level fields (near 50 mT, [20]), i. e., at fields much lower than the saturation field (typically 400…500 mT). In [41] it was stated that several additional (to well known W_h and W_e) losses, e. g., connected with dielectric, DW relaxation, and DW/rotational resonances *"are all conventionally lumped into residual loss W_r, which is a way to summarize our inability to quantitatively predict the $W(f)$ behavior"*. To this must be added the opinion [167] that P_e and P_a are difficult to obtain

separately. In this situation it is possible to assume that a considerable contribution to excess loss comes from the dynamics of DW in grains of PF which can be represented by the frequency dependence of complex permeability (in [91] this contribution is termed as relaxation/resonance loss). Thus the study of complex permeability may provide more clearer understanding of excess loss as well.

It is seen from Fig. 2.1 that total loss is formed from three components: hysteresis loss; eddy loss; and anomalous (excess, residual) loss. From Eqs. (2.1) and (2.2) it follows that as $B_m \to 0$ the remaining part of the loss is the residual loss. This means that at low flux densities the ferrite with lower residual loss will give lower core loss. The anomalous (residual) loss tangent is defined as $tan\delta_a$ [146] (without a known analytical representation).

The total loss factor [146] now formally can be written as:

$$tan\delta_m/\mu = {}^{1}/_{\mu}\,(tan\delta_h + tan\delta_e + tan\delta_a) \tag{2.11}$$

or using loss tangent specific expressions:

$$\frac{tan\delta_m}{\mu} = \frac{4k_hB}{3\pi\mu_0\mu^2} + \frac{\pi\mu_0\mu d^2 f}{\rho\beta} + \frac{tan\delta_r}{\mu} \tag{2.12}$$

Thus the magnetic loss components are with different dependence on f and B_m, the knowledge of which are essential for designers of power supplies to predict the losses when implementing a new power ferrites. There are two general approaches for predicting the core loss of PS: first is predicting core loss based on CIP, the other is by using the Steinmetz equation and its modifications. Let us start with the latter.

2.1.5 Account of losses based on Steinmetz equation

In view of the fact that the components of magnetic loss of materials are not well separated and both hysteresis and eddy current loss are frequency and flux density dependent, the total loss is often in practice (not only that of magnetic core manufacturers', but scientific investigators' as well) still represented formally by the empirical Steinmetz equation (SE) (also known as the Power Law equation [36]):

$$P_{core} = kf^{\alpha}B_m^{\beta} \tag{2.13}$$

where P_{core} is the magnetic core average loss power dissipation per unit volume; k, α, β are the material dependent empirical coefficients determined by best fitting of the measured data (for ferrites α is between *1.1...1.9*, β is in range *1.6...3* [24]); f is the sinusoidal operation frequency; B_m is the peak value of magnetic flux density. In its original form (2.13) is usable only for sinusoidal signals. In addition, it can work only in a limited range of frequencies and flux density excitations [159]. To expand the limits of SE several modifications are done:

- Albach, Durban and Brockmeyer [6] in 1996 and [131] in 2001 modifies SE in relation to domain wall motion loss dependence on $\frac{dB}{dt}$ (so called Modified Steinmetz Equation, MSE):

$$P_{MSE} = k f_{eq}^{\alpha-1} B_m^{\beta} f_r \tag{2.14}$$

where $f_r = \frac{1}{T}$ is the pulse repetition frequency, T – the period of the flux waveform, and $f_{eq} = \frac{2}{\Delta B^2 \pi^2} \int_0^T \left(\frac{dB}{dt}\right)^2 dt$ – the equivalent frequency, dependent on a weighted average of $\frac{dB}{dt}$, and ΔB – peak-to-peak flux amplitude. From this it follows that the accuracy of this SE modification is limited by the type of averaging for f_{eq}.

- another modification of SE was proposed in 2001 by C. R. Sullivan, T. Abdallah, et al. [95]. Their modification was based on the assumption that instantaneous power loss depends only on instantaneous B, $\frac{dB}{dt}$, and the SE equation is then (called the Generalized Steinmetz Equation, GSE):

$$P(t) = k_i \left|\frac{dB}{dt}\right|^{\alpha} |B(t)|^{\beta}. \tag{2.15}$$

But the accuracy of this equation was not high, so in 2002 the same researchers proposed [155] a new, improved formula (improved Generalized Steinmetz Equation, iGSE (also known as Natural Steinmetz Extension [22])):

$$\overline{P(t)} = k_i (\Delta B)^{\beta-\alpha} \overline{\left|\frac{dB}{dt}\right|^{\alpha}} \tag{2.16}$$

where $k_i = \frac{0.5^{\beta} k f^{\alpha}}{(\Delta B)^{-\alpha} |\omega \cos(\omega t)|^{\alpha}}$. This approach provides an opportunity to use the original SE parameters, and gives good correlation with experimental data for square-wave and sine-wave data, but without accounting for the DC bias influence.

The iGSE method, based on more than 4 empirical parameters, proves to be an appropriate instrument for predicting the core loss only near the specific working point given by *B* and *f*. In principle, the most serious drawback of this is the lack of physical meaning of the parameters, and the impossibility of generalization and prediction.

More clear physical content of Steinmetz type relations may come from the ones derived more directly. Thus, if series equivalent circuit (Fig. 2.4, a) is assumed for real magnetic core with an ideal winding, then it is possible to derive:

$$P = (tan\delta/\mu_0\mu_r)\pi f B_m^2 \tag{2.17}$$

Considering the relation in more general case when the parameters incorporated may have dependence on f and B_m, i. e., $tan\delta \equiv tan\delta(f, B_m)$; $\mu_r \equiv \mu_r(f, B_m)$, and knowing their implicit functions the closed-form of Steinmetz relation can be derived (it is particularly

remarkable that relation similar with Eq. (2.17) was derived by Landau-Lifschitz [182] as well using electromagnetic field approach). Later (in subsection 4.3) Eq. (2.17) is used for analysis of MST influence on loss of magnetic core.

2.1.6 Complex permeability

The magnetic permeability and magnetic losses are significant factors in designing of magnetic components [23]. The total loss (schematically presented in Fig. 2.1) consists of the eddy-current, hysteresis and anomalous losses. The eddy current losses becomes higher with increased frequency and hysteresis loss increases with increasing amplitude of the AC field [23]. As described in Ch. 2.1.3, the anomalous loss is not mathematically defined and still cannot be fully described with empirical equations. According to observations (and curves shown on Fig. 2.1 as well) the anomalous loss is frequency dependent, thus it can be described (at least partly) with the frequency dependent characteristic of material, e. g., complex magnetic permeability $\dot{\mu}(f)$. In [73] – it was shown, that in specific case – under the action of low frequency and small fields the anomalous loss can be described with the complex initial permeability.

In general, if the alternating magnetic field $H = H_m e^{j\omega t}$ is applied to ferrite material, then the associated flux density B is usually delayed by the phase angle δ due to losses ($B = B_m e^{j\omega t - j\delta}$). Magnetic permeability then is a complex characteristic:

$$\dot{\mu} = \frac{\dot{B}}{\dot{H}} = \frac{B_m e^{j\omega t - j\delta}}{H_m e^{j\omega t}} = \frac{B_m}{H_m} e^{-j\delta} = \frac{B_m}{H_m} cos\delta - j\frac{B_m}{H_m} sin\delta = \mu' - j\mu'' \quad (2.18)$$

In equation (2.18) μ' is the real part: it characterizes the B component that is in phase with H. Imaginary part μ'' characterizes the B component that is delayed by $\pi/2$ phase-angle from H. Then from the (2.18) the loss factor tangent can be characterized as: $tan\delta = \mu''/\mu'$. Components $\mu'(f)$ and $\mu''(f)$ of $\dot{\mu}(f)$, considered as functions of frequency f, are forming CP spectrum (magnetic spectrum) (Fig. 2.5).

The (2.18) form of magnetic permeability is complex and it represents the material storage capacity of magnetic field and losses. So the real part of CIP, μ', can be related with inductance (i. e. energy storage), and imaginary part – with resistance (i. e. losses, power dissipation). In principle, we can use both the complex impedance or admittance for experimentally measured data. The two simplest forms of circuits used for separation of measured components on fixed frequency [146] are presented on Fig. 2.4. The relation of the complex impedance can be represented by the use of series components of complex permeability: $\dot{Z} = j\omega L_s + R_s = j\omega L_0(\mu_s' - j\mu_s'')$, where R_s and L_s are series resistance and

inductance, and $\mu_s^{'}$ and $\mu_s^{''}$ are real and imaginary series components of CIP (Fig. 2.4, a; Fig. 2.5, a). Then the magnetic losses can be described in terms of series components $\mu_s^{'}$ and $\mu_s^{''}$ as $tan\delta = \mu_s^{''}/\mu_s^{'}$.

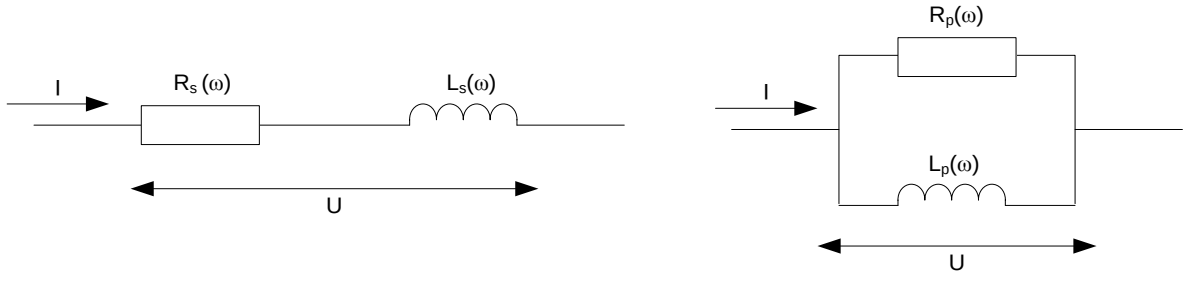

a *b*

Figure 2.4. Equivalent circuits for series (a) and parallel (b) representation of CIP [146,163] in the measurement process

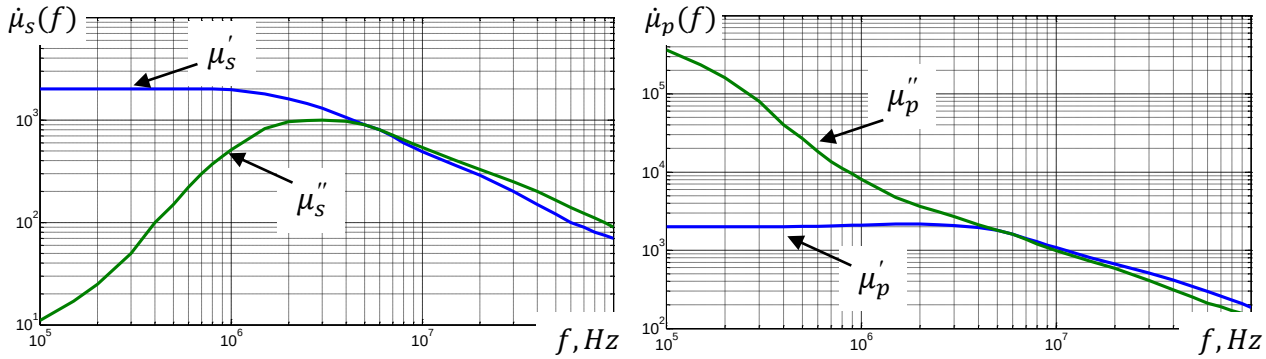

a *b*

Figure 2.5. Example of typical frequency dependence of complex magnetic permeability of the definite same sample ([146], Fig. 3.11.1). *a* - using the series components; *b* - using the parallel components.

By analogy with the impedance relation the relation for the complex admittance can be expressed, but in terms of parallel components:

$$\dot{Y} = \frac{1}{j\omega L_p} + \frac{1}{R_p} = \frac{1}{j\omega L_0}\left(\frac{1}{\mu_p^{'}} - \frac{1}{j\mu_p^{''}}\right) \quad (2.19)$$

where R_p and L_p are parallel resistance and inductance, and $\mu_p^{'}$ and $\mu_p^{''}$ are real and imaginary parallel components of CIP (Fig. 2.4, b; Fig. 2.5, b). Using the parallel components, the magnetic loss tangent is $tan\delta = \mu_p^{'}/\mu_p^{''}$.

The conversion from series to parallel components is as follows:

$$R_s = R_p/(1 + 1/tan^2\delta) \quad (2.20)$$

$$L_s = L_p/(1 + tan^2\delta) \quad (2.21)$$

$$\mu_p^{'} = \mu_s^{'}(1 + tan^2\delta) \quad (2.22)$$

$$\mu_p^{''} = \mu_s^{''}(1 + 1/tan^2\delta) \quad (2.23)$$

Nevertheless, the series representation of complex permeability is more compatible with Steinmetz equations and more closely correlated to the inner magnetization processes of PF [64–73]. During the process of research of PF the different approaches and models for ferrite cores are described, e. g., in [60, 163, 164], but none is suitable for practice (with frequency independent parameters).

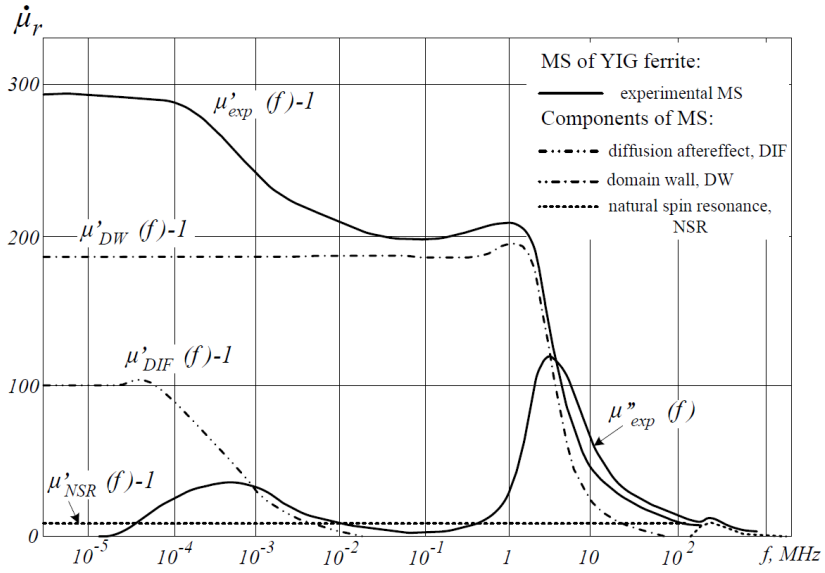

Figure 2.6 CP spectra decomposition [73]: the experimental ACp $\mu''(f)$ firstly is broken into three absorption components, from which were calculated corresponding DCp components: $\mu'_{DW}(f)$, $\mu'_{DIF}(f)$, $\mu'_{NSR}(f)$ by KKR.

In relation to interpretation of CIP spectra, even their physical nature, there is no consensus. Previously in the seventies and eighties (mainly by investigations inspired by the basic works of A. Globus and his collaborators, e. g., [45]) it was stated that CIP definitely depended on microstructure characteristics (more markedly on average grain size D_a) and that the dominating magnetization mechanism is DW displacement (nevertheless, at times however there appear groundless claims that the dominating magnetization process is the spin rotation [157]).

In fact, if magnetic spectra (MS) data are taken over a really broad frequency range there can be found in the most general case, three principal dispersion regions [53] (see Fig. 2.6, experimental data are taken from [53]):

a) in *kHz* range – relaxation type diffusion after effect (DIF, $\mu'_{DIF}(f)$), not always presented;

b) in the decades near 1 MHz – the large amplitude dispersion attributed to DW processes ($\mu'_{DW}(f)$);

c) at microwaves (near several 100 MHz) – the small amplitude dispersion ($\mu'_{NSR}(f)$) related to the natural spin resonance (NSR).

From the three observable dispersion regions of CIP (Fig. 2.6) of PF, most often investigations are concentrated within the large amplitude broadband region. This dispersion region (as a rule assumed to be connected directly with DW processes) is peculiar: in parallel with the really broad dispersion region it may show clear attributes of resonances, and, in addition, sensitivity to the microstructure of PF (typical for DW processes). All this presents severe problems for CIP interpretation, connection to MST, and modeling of its frequency dependence.

The DW displacement results in a larger DCp and ACp components than NSR, and therefore accounts for the high permeability of ferrites [23]. The NSR becomes of significance for higher frequencies (> 100 MHz), where it is dominant [23]. For generality let us deal with three dispersion spectrum of PF [53]. The contribution of each process into the whole CIP spectra becomes clearer, e. g, after decomposition of ACp $\mu''_{exp}(f)$ into the three mentioned components [73] (Fig. 2.6) and calculation of DCp $\mu'(f)$ by the use of Kramers-Kronig relations (3.1; 3.2).

For aforementioned it is more likely, that within the radiofrequency range (at room temperatures) for spinel and garnet type PF (most often used in practice) typically are dominating DW processes. Similarly as in Fig. 2.6 the contribution from NSR process in the total permeability $\dot{\mu}(f)$ of a sample is often small and frequency independent up to very high frequencies; this is why the modeling of CIP is restricted over the region of large amplitude dispersion and as DW processes. The modeling of complex permeability spectra under the action of low fields in fact deals with the anomalous loss [73].

2.1.7 Problems of presentations of complex permeability

The modeling of typical complex permeability spectra presents difficulties in the correct representation of components (Fig. 2.7): DCp often exhibit resonance attributes (positive ups and negative downs, Fig. 2.7), ACp is asymmetrical (along log *f* scale axis) and broadband (often extending over 2...3 decades of *f*). Researchers for a long time now have measured a great quantity of different complex permeability spectra; clearly, there are several approaches to their approximations.

The simplest one is simple relaxation (with only one relaxation time τ). In [55] e. g., it was suggested that complex susceptibility spectra X_s^* can be modeled by the use of a such simple relaxation as:

$$X_s' = \frac{X_i}{1+(\omega\tau)^2};\ X_s'' = \frac{\omega\tau X_i}{1+(\omega\tau)^2}, \tag{2.24}$$

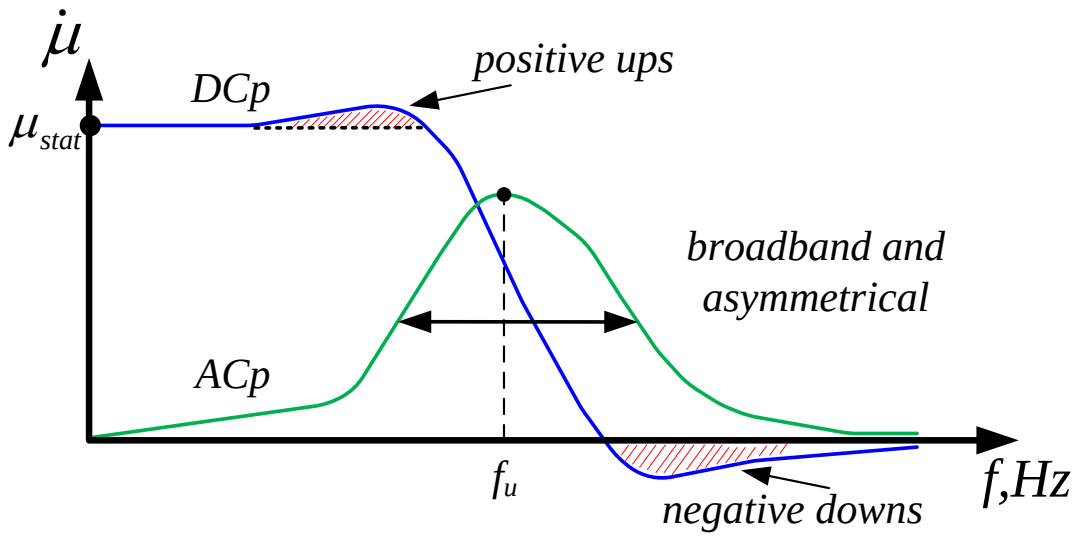

Figure 2.7 Typical complex permeability spectra

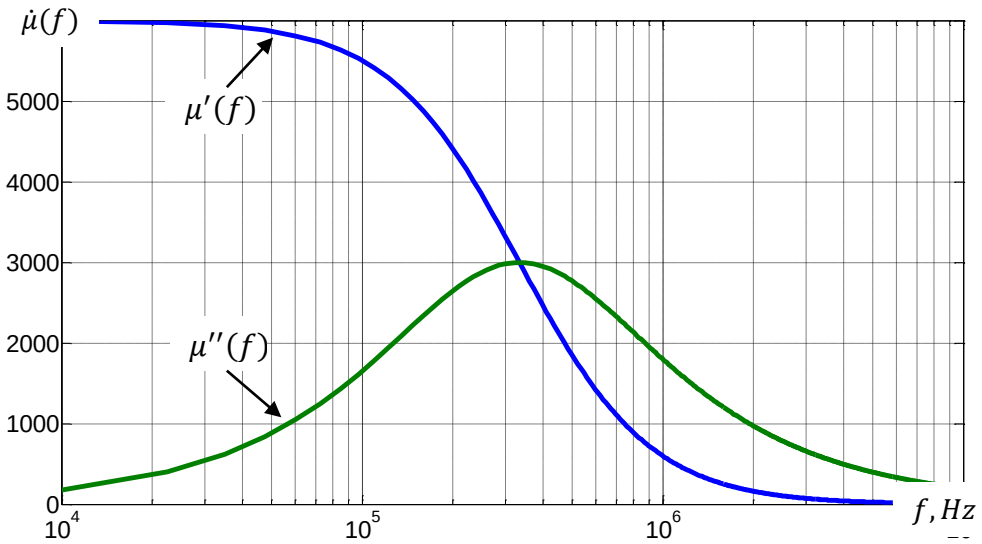

Figure 2.8 CIP made by use of Eq. (2.25) with $\mu_{stat} = 6000$ and $\tau = 3\ \mu s$

where X_s' and X_s'' represent the real and imaginary parts of the complex susceptibility, ω is the angular frequency, and τ – is the relaxation time, or in form of complex magnetic permeability [73]:

$$\mu'(f) = \frac{\mu_{stat}}{1+(\tau f)^2};\ \mu'' = \frac{\mu_{stat}\tau f}{1+(\tau f)^2}, \tag{2.25}$$

where μ_{stat} is static value of CIP. The CIP approximation presented in Fig. 2.8 represents the use of Eq. 2.25 with $\mu_{stat} = 6000$, $\tau = 3\ \mu s$ and f ranging from 10 kHz to 10 MHz. Even with the fact that this approximation of MS is pronouncedly broad, a closer look at typical

DCp (Fig. 2.7) reveals that in fact there may be clear evidence of resonance attributes as well, which it is not possible to represent by relaxation relations.

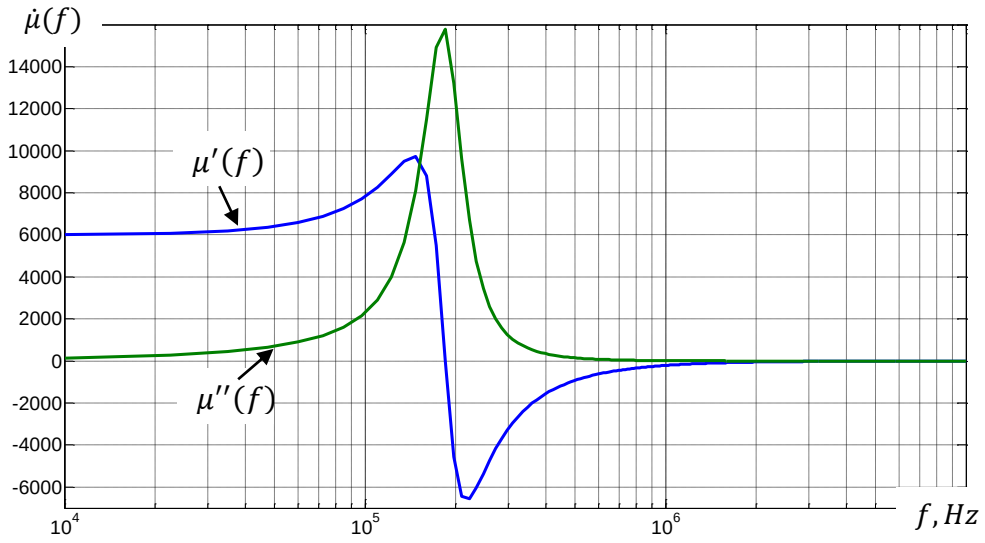

Figure 2.9 CIP made by use of Eq. (2.26) with $\mu_{stat} = 6000$ and $\xi = 0.2$

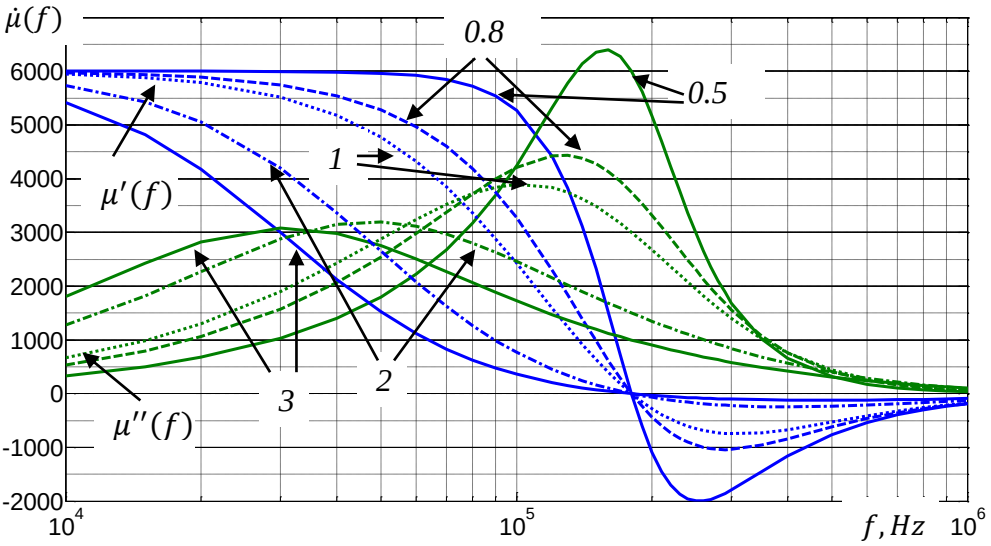

Figure 2.10 CIP made by use of Eq. (2.26) with $\mu_{stat} = 6000$ and $\xi = 0.5, 0.8, 1, 2, 3$

If MS is approximated by the use of simple harmonic oscillator relations:

$$\mu'(f) = \frac{\mu_{stat} f_0^2 (f_0^2 - f^2)}{(f_0^2 - f^2)^2 + 4\xi^2 f_0^2 f^2};\ \mu'' = \frac{2\mu_{stat} \xi f f_0^3}{(f_0^2 - f^2)^2 + 4\xi^2 f_0^2 f^2} \qquad (2.26)$$

with f_0 as the resonance frequency and ξ as the normalized damping *constant*, then in the case of $\xi < 0.5$ the resonance features can be reproduced [73] (Fig. 2.9; Fig. 2.10, with $\mu_{stat} = 6000$, $f_0 = 180000\ Hz$, f changing from 10 kHz to 1 MHz and ξ = 0.5, 0.8, 1, 2 and 3 respectively), but in the substantially tighter frequency limits corresponding to much narrower

width of ACp (usually measured on half-level between the ascending and descending parts of absorption).

Inadequate representation of MS by the relaxation and the resonance dependences separately (but at the same time with several features of reality) naturally suggests their superposition, i. e., joint use of Eqs. (2.25) and (2.26) (in fact proposed by Y. Naito [111]). In this case it is assumed that for frequency $f \to 0$ static permeability μ_{stat} is the sum:

$$\mu_{stat} = \mu_{stat/relax} + \mu_{stat/reson} \tag{2.27}$$

i. e., is divided into relaxation, $\mu_{stat/relax}$, and resonance, $\mu_{stat/reson}$, components. For complex permeability similar components are used with their frequency dependences according to Eq. 2.25 and Eq. 2.26 correspondingly.

Even though there is no physical background for such decomposition of $\dot{\mu}(f)$ (as well as of parameters τ, ξ, f_0 estimation) other than the best fit to experimental data, such a formal approach nevertheless is used in a series of publications, obviously because of the freedom in choosing the parameters for the presentation of MS. The main limitations of this approach are its formality and clear ignorance of the effects of microstructure of PF on its CIP [53].

2.1.8 Role of microstructure

Undoubtedly, several of important characteristics of PF are its microstructure (MST)

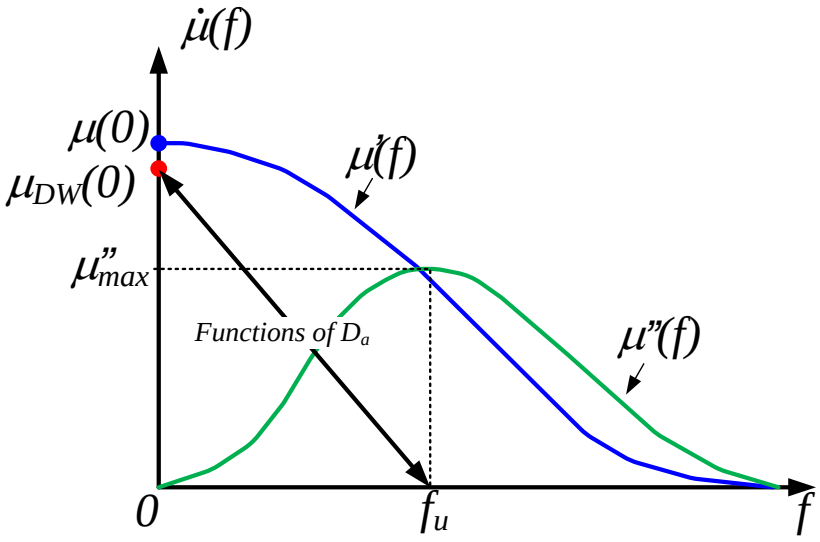

Figure 2.12. Complex permeability and its characteristic parameters

sensitive (e. g., complex initial permeability $\dot{\mu}(f)$ with its attributes: static initial permeability $\mu(0)$; typical representatives of ACp: maximum μ''_{max} and maximum frequency f_u

(Fig. 2.12)). To study the influence of MST on such characteristics (e.g., CIP) there is need for proper MST characterization to perform the quantitative account of it.

2.1.8.1 Characteristics of microstructure

First of all MST of PF (Fig. 2.13) is characterized by the law of its grain size *D* distribution. According to [89] MST obtained in the process of normal grains growth (NGG) almost without exceptions can be represented by log-normal distribution (independently of the material of sample, specific details of preparation conditions, average grain sizes and density):

$$f_{ln}(D) = \left(\frac{1}{D\sigma_{ln}\sqrt{2\pi}}\right)e^{\frac{-(lnD-lnD_{med})^2}{2\sigma_{ln}^2}}; \qquad f(D) = \left(\frac{loge}{D\sigma_D\sqrt{2\pi}}\right)e^{\frac{-(logD-logD_{med})^2}{2\sigma_D^2}} \tag{2.28}$$

where $f_{ln}(D)$ and $f(D)$ are the probability density functions, D_{med} is the median of lnD or $logD$ distribution, but the standard deviations σ_{ln} and σ_D correspondingly are interrelated:

$$\sigma_{ln} = ln10\sigma_D = 2.3\sigma_D. \tag{2.29}$$

According to [89] MST obtain in the process of NGG for ferrites gives $\sigma_{ln} = 0.45 \dots 0.55$ (or $\sigma_D = 0.2 \dots 0.24$).

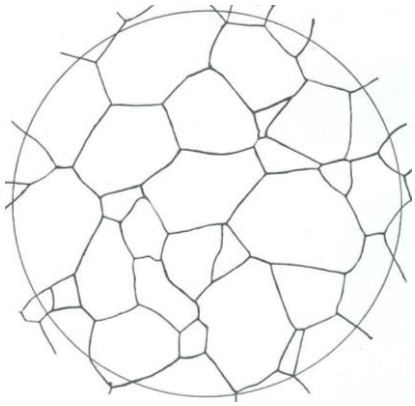

Figure 2.13. Example of micrograph of normal grain structure [12]

The next important characteristic of MST is its average (mean) grain size

$$D_a = D_{med}e^{0.5\sigma_D^2 ln^2 10}. \tag{2.30}$$

Contrary to the law of distribution, D_a is preparation conditions (mostly of sintering temperature and time) dependent. During NGG [50] *"the average (logarithmic) grain size lnD_a is shifted to larger values, but the height of the maximum and the standard deviation remain unchanged (Fig. 2.14, a). Such behaviour of the distribution is also referred to as self-similarity, i. e., if the distribution is plotted versus the normalized logarithmic grain size $ln(D/D_a)$, the distribution does not change during NGG."*

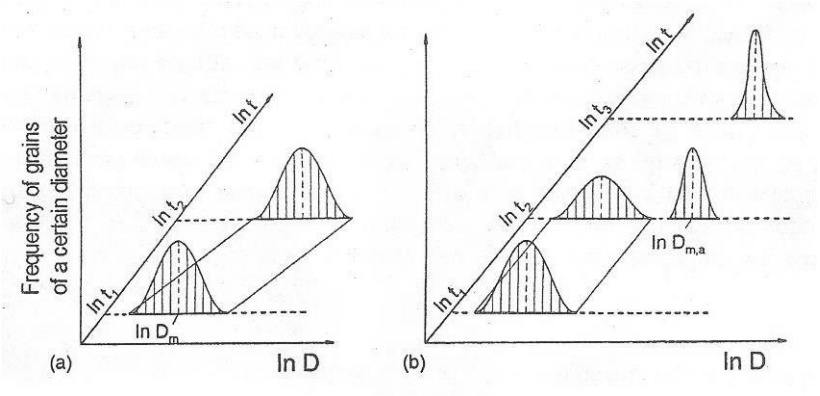

Figure 2.14. Schematic time dependence of grain size distribution for normal (a) and abnormal (b) grain growth [50].

So, within the normal grain growth the average grain size increases continuously with the increase of sintering time. Contrary to this abnormal grain growth leads to rapid growth of a few grains, while the other grains grow slowly or not at all [50], and the bimodal distribution appears (Fig. 2.14, b; the one distribution represents the slowly-growing small-grained matrix, the other – rapidly growing grains). The distribution of slowly-growing grains

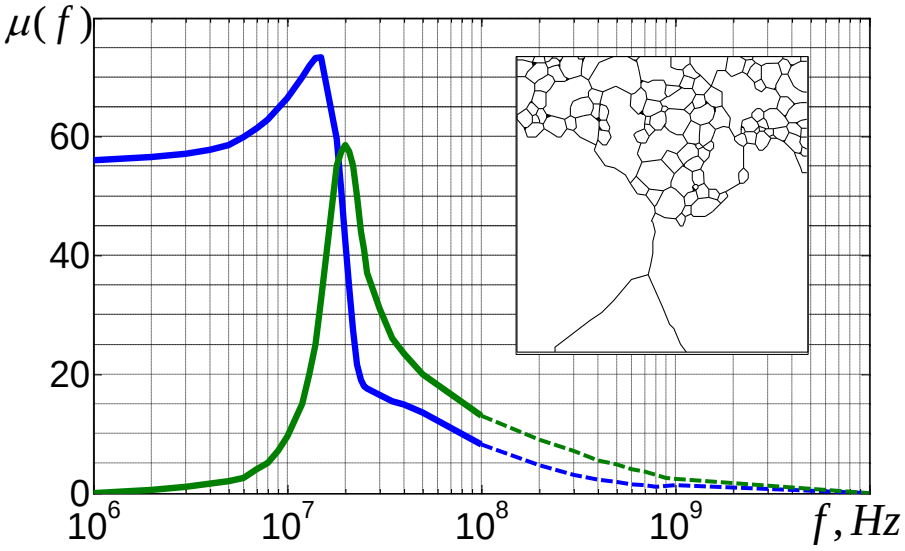

Figure 2.15. CMP of ferrite with unhomogenous MST: solid line – experimental data [43], dotted line – prolongation based on KKR [72].

becomes smaller and finally disappear (without changes of average grain size), oppositely – the distribution of abnormal grains (involving considerable amount of intragrain porosity) – changes within annealing time until abnormal grain growth ends (Fig. 2.14, b) [50]. This abnormality of grain growth forms unhomogeneous MST (small-grained matrix and large grains, Fig. 2.15) that correspondingly changes the typical form of CIP spectrum (Fig. 2.15).

The fundamental importance of D_a became widely evident from original investigations within the last decades of twenty century of A. Globus, M. Guyot and their collaborators on PF of special technology (from many publications highlighting only two the most comprehensive: [45], [53]). This technology includes: the composition of PF from oxides of high purity; the use of uncontaminating milling of oxides; the sintering at relatively low temperatures; a. o. [45]. All this results in PF samples of top quality: with homogeneous (i. e., log-normal) MST, porosity practically only as intergranular (intergrain) one, and grains without intragranular (intragrain) porosity. Such a porosity plays a minor role on the magnetization process attributes of whole PF sample if it results from magnetization processes of independent grains – several total characteristics of PF sample becomes MST dependent. Only the investigations on PF of this special technology, i. e., samples of top quality allow to reveal the true intrinsic nature of PF (in several previous publications these samples are referred to as: RSG – reference sample group, IQG – intrinsic quality group, or simply group one, PF1).

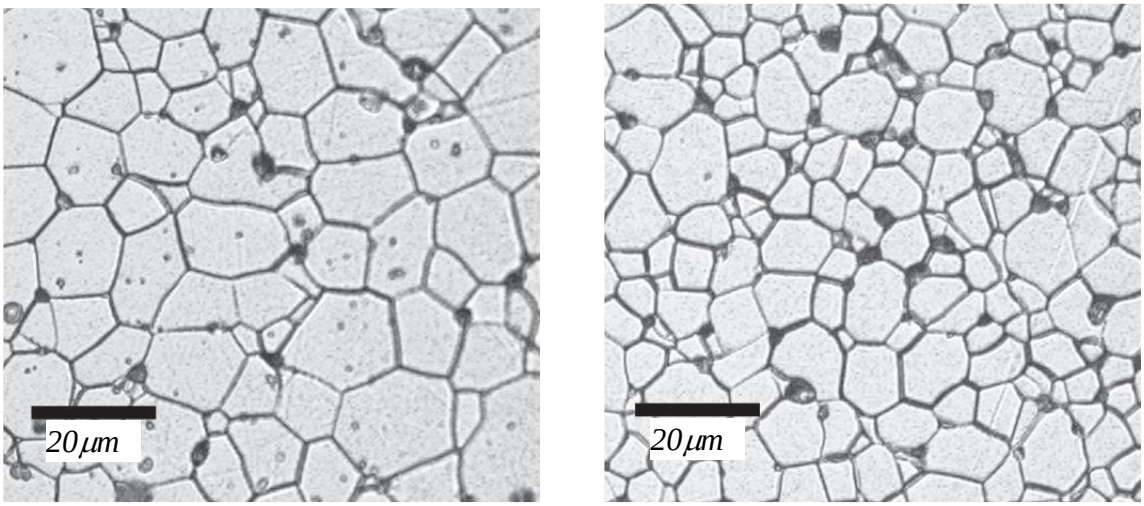

a) b)

Fig.2.16. Microstructures of (a)MB3 and (b)MBF4 ferrite materials [49] with the average grain sizes of 9 μm and 6 μm, respectively.

It should be mentioned, that real quality of MST (e. g., perfection of grains) to a large measure depends on the current value of D in the sample since it is resulting from actual processing technology of PF and laws of MST formation (e. g., in [34] it is stated that the pore-to-pore distance of intrapped pores does not change significantly when the MST changes from inter- to intragranular porosity). Consequently, the microstructure presented on Fig. 2.16 shows that there are defects mainly within coarser grain on PF (with $D \approx 9\ \mu m$, Fig. 2.16, a), but intragrain defects almost disappear within finer grained sample (with $D \approx 6\ \mu m$ Fig. 2.16,

b). Principles of inverse segregation and carried out direct experiments allows to conclude more generally that smaller grains within PF samples ($D < 3…5\ \mu m$ [109]) are rather perfect – with the negligible amount of enclosed defects (e. g., porosity). For the coarser grains the picture decisively depends on technology.

2.1.8.2 Microstructure-sensitive characteristics of PF

Importance of studying MST in relation to CIP of PF for trustworthy experimental results interpretation is widely discussed [5, 33, 64–70, 79, 84, 175, 177, a. o.]. The quality of microstructure substantially affects the magnetic and electric characteristics of ferrites. Among such magnetic characteristics are: the static initial permeability $\mu(0)$, the type of spectrum of CIP $\dot{\mu}(f)$, the coercitivity H_c, the hysteresis law [45], a. o. The influence of MST acts both through distribution of grain sizes and defects. The cause of defects in MST can be inappropriate chemical composition, granularity of initial oxides, sintering time and temperature, which lead to porosity in MST and unwanted impurities. To increase the magnetical and electrical capabilities of ferrites the improvements in methods of ferrite production are developed [79]. Effects of sintering conditions on magnetic properties of NiZn ferrites are studied at all times (more recently in [5]). The dependence of initial permeability of NiZn PF of normal grain growth is studied in [117] in relation to sintering temperature. According to [173], the new Sol-Gel method in ferrite preparation (at least for NiZn ferrites) can be used in preparation of optimum ferrite (with defects-free MST). NiZnCu ferrite preparation at relatively low temperature (250 °C) by using Sol-gel method is discussed in [79]. An investigation on CuZn ferrites was made in [5], providing information on chemical composition, grain size and sintering temperature to achieve best results in multilayer chip inductor production. Ferrite absorber improvement based on study of microstructure statistical parameters is proposed in [98].

All of the authors inclined to believe that microstructure has great influence to magnetical and electrical capability of ferrites and improvements can be made only if the MST is appropriate. The development of new MnZn ferrite compounds under thoughtful control of the ferrite preparation can decrease the core power loss by 40 % for high frequency region – up to 500 kHz in comparison with standard materials [176]. Therefore to achieve trustworthy results in the study of ferrites, the analysis of microstructure and its influence is necessary.

2.1.8.3 Role of microstructure on frequency dependent characteristics of PF

Practice shows that several characteristics of CIP (more notably, $\mu(0) \equiv \mu_s$ and f_u, Fig. 2.12) are interrelated. The knowledge of specific relationships of these interrelations are

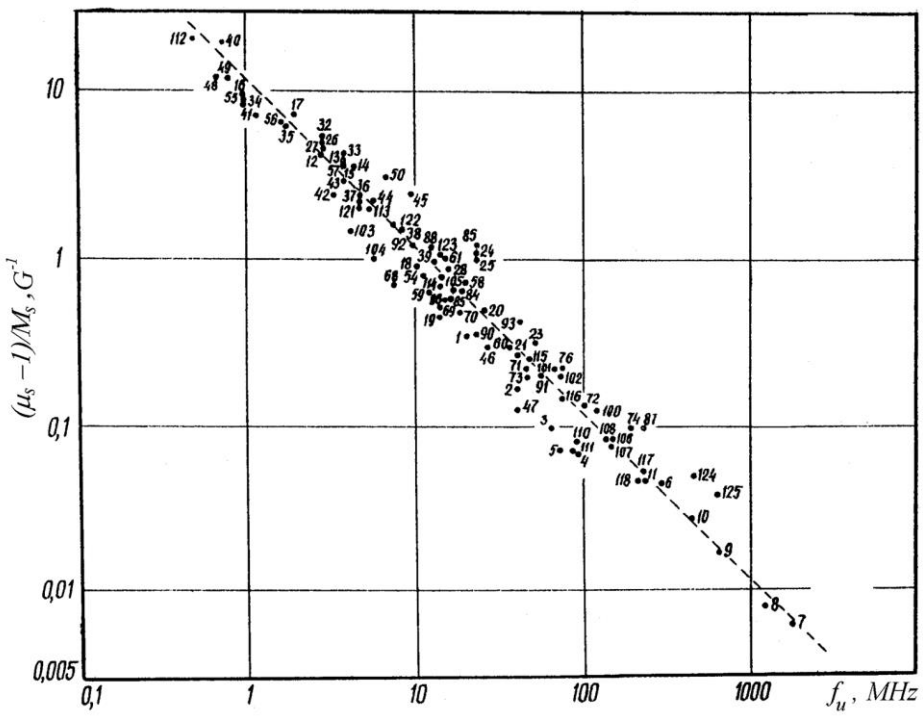

Figure 2.17 The data of PF used to proof Snoek's type relation [65, Fig. 2]

important for modeling of CIP. The process of setting up the relationships is not straightforward: it is not possible to base on definite theory (since there is no appropriate one) and so there is need to examine the empirical statistics of characteristics from great number of experimental CIP from publications all over the world.

Thus, there were analyzed, in [65], large amount of published data (Fig. 2.17, PF samples over 100, produced by different technologies but often without explicit data about MST).

As a guide for analysis of these data is taken the well known Snoek's Law [147]:

$$(\mu_s - 1) f_{rot} = \frac{4}{3} \gamma M_s \qquad (2.31)$$

where f_{rot} – is the rotation process resonance frequency, MHz; γ – the gyromagnetic ratio, 2.8 MHz/Oe; and M_s – the saturation magnetization, G. In [65] it was shown (Fig. 2.17), that as a first approximation of analyzed data (when MST characteristics are ignored or are not known) can be assumed Snoek's Law type expression:

$$(\mu_s - 1) f_u = 4\pi M_s \qquad (2.32)$$

This relation (dashed line in Fig. 2.17) shows that there is no fundamental difference between high and low permeability PF within a broad frequency range (and correspondingly in a broad range of resistivity: from a few $\Omega \cdot m$ up to 10^5 $\Omega \cdot m$)

Building a similar statistical data set for μ'' component (for the large amplitude absorption region where there is good reason to believe that frequency of DW absorption maximum and that of NSR do not coincide, so make the most in excluding the effects of other possible types of magnetization process except DW ones), in [65] it was found, that these data (Fig. 2.18) can be approximated as:

$$\mu''_{max} f_u = 2\pi M_s \quad (2.33)$$

where μ''_{max} – is maximum value of ACp. The last rough approximations 2.32 and 2.33 allows for ratio:

$$\mu''_{max}/(\mu_s - 1) = 0.5\,, \quad (2.34)$$

which shows that statistically the data of variety of PF samples tend to the simple relaxation process (which is to say that only as a rough approximation of CIP is possible to use the relaxation dependence with one relaxation time τ). Since the samples used in this variety are not of special technology and high dimensions, so it is possible to assume that Eqs. 2.32 and 2.33 reflect the averaged intrinsic features of PF.

For better presentation of intrinsic data of PF one more parameter is needed to be included in the analysis – the grain size D_a, as the representative of microstructure. Taking in account the different values of grain size, D_a(for fixed composition and technology samples), the new data subsets were created (Fig. 2.18), where the data from previous collection of data are used as well for reference (represented in Fig. 2.17) and several new ones with known D_a are added. For this new dataset (Fig. 2.18 – solid lines) coming from the data of high quality (special technology) garnet (No. 1...7 in Fig. 2.18 [65]) and spinel (No. 8...17 in Fig. 2.18 [65]) PF samples is possible to form two sub-lines crossing the main reference line in the vicinity of $D_a = 3 \ldots 4\ \mu m$. The sub-lines is possible to approximate by (in the coordinate system $\mu''_{max} D_a / M_s$ and f_u):

$$\mu''_{max} f_u D_a = (6 \ldots 8)\pi M_s. \quad (2.35)$$

Similar analysis for DCp gives [65]:

$$(\mu_s - 1) f_u D_a = 12\pi M_s. \quad (2.36)$$

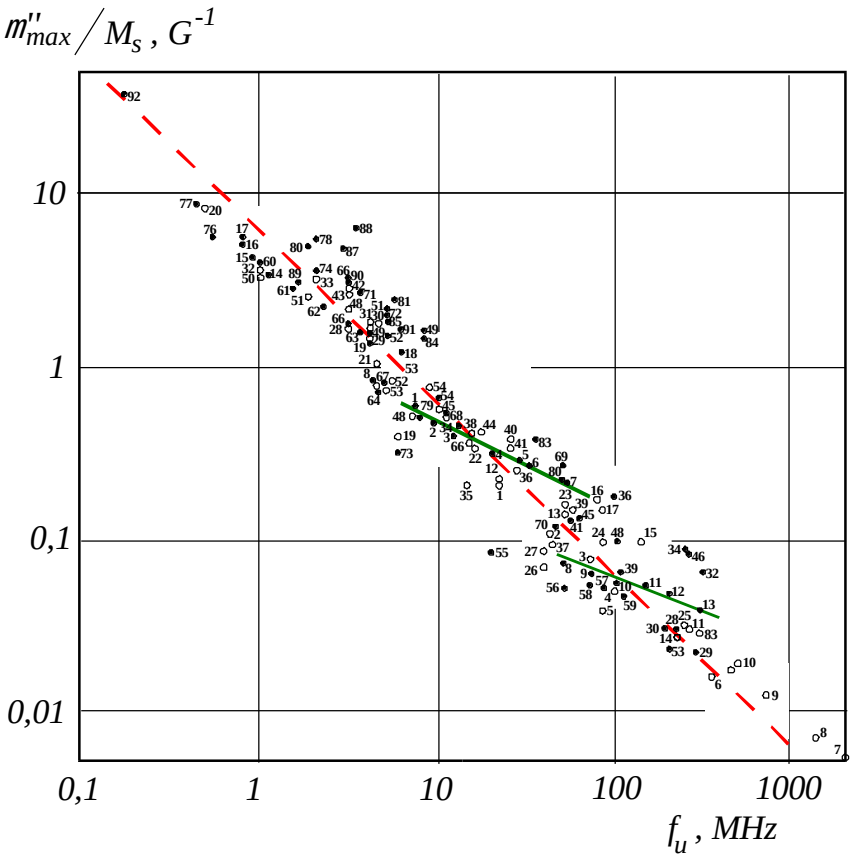

Figure 2.18 The data of PF used to establish the typical relations [65, Fig. 5]

Since these last relations are deduced from the data of special technology samples it is possible to assume that Eqs. 2.35 and 2.36 reflect the true intrinsic features of PF.

Consequently, the performed analysis of data uncover some regular trends which are possible to present by two pairs of empirical relations, individually revealing the true intrinsic and intrinsic properties of PF correspondingly:

$$\left.\begin{array}{l}(\mu_s - 1) f_u D_a = 12\pi M_s \\ \mu''_{max} f_u D_a = (6 \dots 8)\pi M_s\end{array}\right\} \qquad \left.\begin{array}{l}(\mu_s - 1) f_u = 4\pi M_s \\ \mu''_{max} f_u = 2\pi M_s\end{array}\right\} \tag{2.37}$$

It can be seen that the first pair translates to second one at $D_a = (3 \dots 4)\,\mu m$. To interpret these results it is appropriate to introduce the effective grain size D_{eff} [65] reflecting the pinning situation of DWs in the grains of PF samples.

In the case of DW pinned only at grain boundaries (as in Globus' model [45]; Fig. 2.20: a, b) that is expected in the true intrinsic samples, $D_{eff} \approx D_a$ and as a such is shown as linear relationship for all D_a (Fig. 2.19, line No. 1), meeting D_a axis in the range of very small, monodomain grains, D_{a0}. In this case all magnetization processes connected with DWs depend on D_a: influence of microstructure as *per se* appears in full measure.

Contrary to this in the case of (simply) intrinsic samples (of conventional ceramic technology) there are appearing the intragrain defects in the grains, pinning DWs (Fig. 2.20, c). However, from a number of experimental data it is possible to state, that small grains (less than $3\ldots5\ \mu m$ [109]) are without intragranular defects, so there is appearing some threshold size of grains, D_{th}.

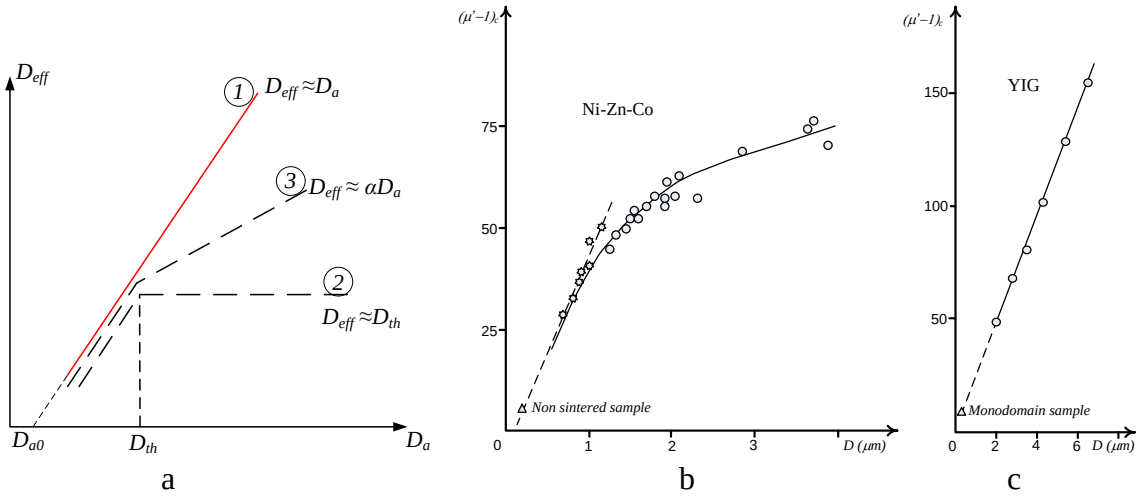

Figure 2.19 Conception of effective grain size D_{eff} and its experimental prototypes: a) possible relationships between D_{eff} and D based on domain-wall processes in grains [65, Fig.6]; b) Initial susceptibility $(\mu' - 1)$ versus mean grain size D for Ni-Zn-Co ferrite samples [43, c]; c) Initial susceptibility $(\mu' - 1)$ versus mean grain size D for YIG ferrite samples [43, c].

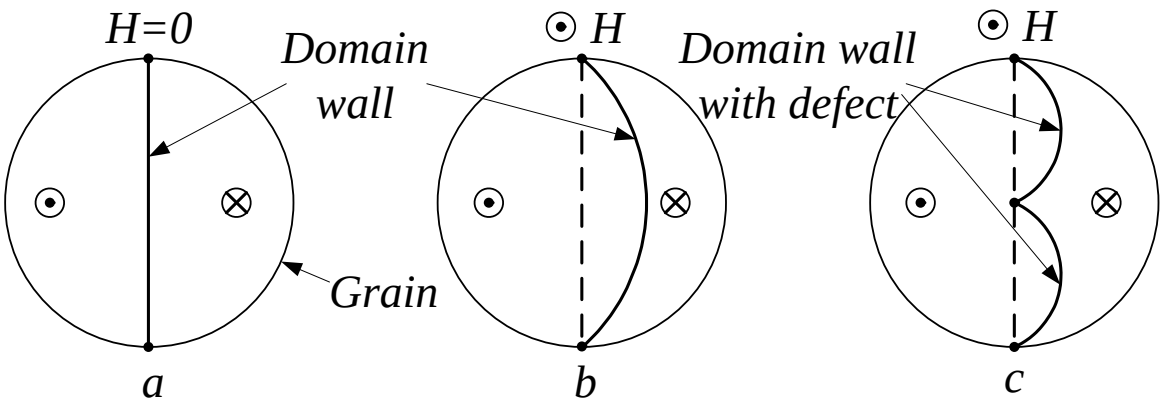

Figure 2.20 Schematic presentation of DW within a grain: a, b – Globus' model in a spherical grain without and with applied field; c – with applied field and pinning defect in the center of grain.

Above provided analysis of the data for usual technology, non-specialized PF obviously gives (Eqs. 2.37) $D_{th} = (3\ldots4)\ \mu m$, but in the case of specialized ones the results may be different (as in the example of power MnZn-ferrites optimized for higher frequencies $D_{th} <$

6 μm, Fig. 2.16 [49]; but for higher initial permeability $D_{th} < 15\ \mu m$ [34]). Since the pore-to-pore distance may be practically independent of D [34], then D_{eff} for $D > D_{th}$ may become $D_{eff} \approx D_{th} = const$ and take a general view of dependence of No. 2 (Fig. 2.19); obviously , a compromise between No. 1 and No. 2 (dependence No. 3, Fig. 2.19) may take a place as well. Clearly, in the last two cases the influence of MST on parameters of PF is obscured, the correct results can be obtained only on intrinsic group samples. In this case it is possible to relate the magnetization process directly to material MST and to apply quantitatively to the general concept that experimentally observed characteristics of the sample in fact are integral ones appearing as such in the process of natural averaging their inner parameters over the ranges set up, e.g., by the grain size distribution.

A particular example is the static initial permeability $\mu(0)$, the value of which may come from distributions of parameters within two (at least) domains:

- the value coming from *grain size D domain*: as to now mainly known as empirical data from experimental investigation of impact of MST; now is required the calculations based on grain size distribution, average grain size D_a, etc.;
- the value resulting from *operational frequency f domain*: substantiated by KKR, giving, e. g., $\mu(0) - 1 = {}^{2}/_{\pi} \int_0^{\infty} [\mu''(f)/f]\, df$ (schematically pictured in Fig. 2.12).

Currently, there are no quantitative analytic relations revealing the distribution effects in both of above mentioned domains, nor clearly seen interrelations between these domains. It is hoped that the model analyzed in the next subsections will correct this.

2.1.9 Modeling of complex permeability by accounting for the effects of microstructure

Typically, the overall appearance of most CIP spectra are similar: they look like the combination both of relaxation attributes (dispersion and absorption within a broad range of frequency) and resonance attributes (positive ups and negative downs on $\mu'(f)$ – the dispersion curves). It was shown in [47] that in such a case the most appropriate approximation comes from taking account of inhomogeneous broadening of absorption caused in fact by the distribution of grain sizes (Fig. 2.16).

This concept translated to spectrum of ferrites from IQG, assumes that every polycrystal grain of the sample can be considered as a low loss oscillator (more exactly: the DW in a current grain having $\mu_{stat} \propto D$ and resonating at $f_{osc} \propto 1/D^2$ with D standing for the current gain size). As a consequence the whole curve of ACp $\mu''(f)$ can be made up from

absorption curves of these tiny oscillators (having the absorption line $\mu''(f, f_{osc})$) with continuously distributed f_{osc} (for clarity in Fig. 2.15 the principle is shown as if ACp $\mu''(f)$ would be made up only by a group of a few oscillators). Further it is accepted that the grain size distribution probability density function is log-normal:

$$f(D) = (1/D\sigma_{lnD}\sqrt{2\pi})exp[-(lnD - lnD_{med})^2/2\sigma_{lnD}^2] , \quad (2.38)$$

where D_{med} is the median, and σ_{lnD} is the standard deviation of *lnD*. In principle, the log-normal distribution of grain sizes can be presented parallely either as variable *logD* or *lnD* (the former is used in this work since it more naturally agrees with typical offering of CIP

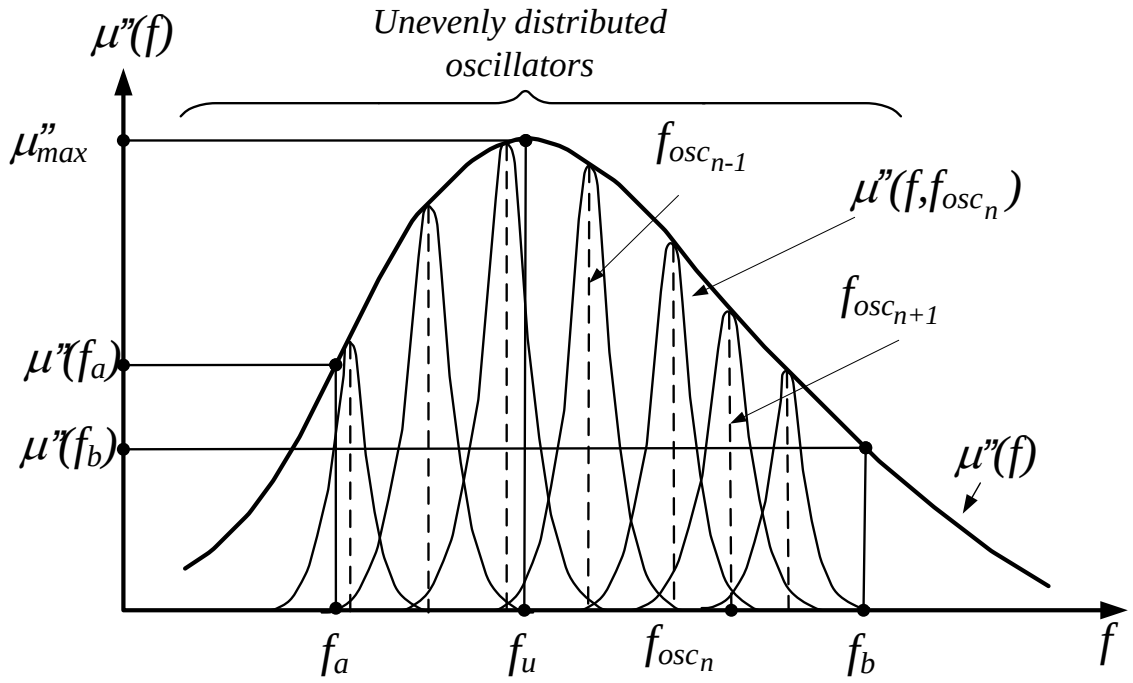

Figure 2.20 Inhomogeneous widening of ACp.

frequency curves in decades; the latter is one more often used for the study of MST). The value of σ_{lnD} for PF with MS formed in the process of normal grain growth (i.e., with normal MST) tends to values [89]:

$$\sigma_{lnD} \approx 0.5 \text{ or } \sigma_{log} \equiv \sigma_D = \sigma_{lnD}/ln10 \approx 0.22; \quad (2.39)$$

(the latter value emerges in the case when (2.38) is presented on a decimal logarithmic scale that is more appropriate for CIP analysis in the frequency *f*-domain).

Also it is assumed that the relationships for magnetization processes in the elementary volumes, i. e., in grains as a function of *D* are similar to those which can be deduced from the analysis of experimental data of a variety of PF samples in relation to their average grain size D_a. Thus, in relation to D_a IQG exhibit clear correlations: linearity and obeys the modified Snoek's law [68]:

$$\mu(0) - 1 = C_1 D_a; \tag{2.40}$$

$$\mu''_{max} f_u D_a / M_s = 2\pi/\sigma, \tag{2.41}$$

where C_1 – const.; hence ferrites from IQG are the most appropriate for theoretical analysis. In contradistinction, for ferrites from TQG such a clarity is lost – linearity (if at all) needs to be related to some effective grain D_{eff} and only the standard Snoek's law is fulfilled:

$$\mu(0) - 1 = C'_1 D_{eff}; \tag{2.42}$$

$$\mu''_{max} f_u / M_s = C'_2 \tag{2.43}$$

where C'_1 and C'_2 – const. In fact, just (2.40, 2.41) and (2.42, 2.43) as precedent patterns are used for true intrinsic and intrinsic samples respectively for dealing with their inner processes – ones in current grains *D* within PF samples.

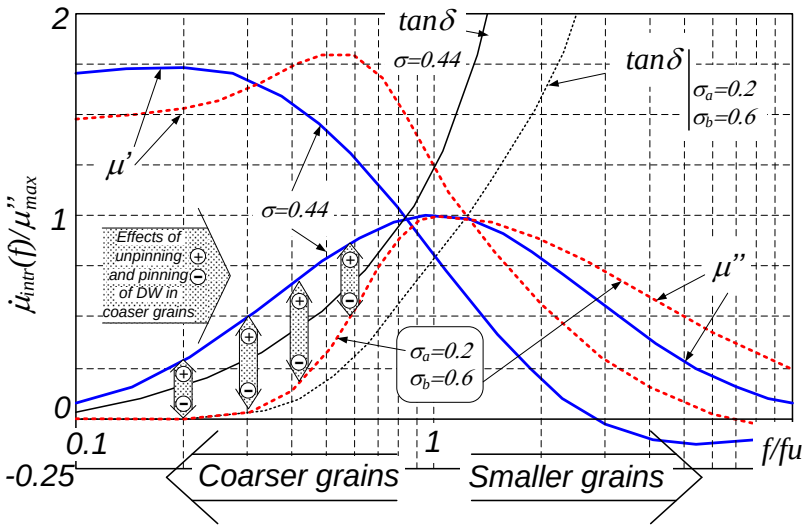

Fig.2.16 Potential possibilities of the model to transform from symmetrical to asymmetrical type of spectra [70]

From the previously mentioned interpretations and corresponding equations (2.40, 2.41) it emerges that for IQG ferrite samples there is a distribution not only of sizes *D*, but of related frequency response of elementary volumes too (Fig. 2.15). The response is expected to arise from DW resonating at frequency f_{osc}, $f_{osc} \propto 1/D^2$, setting up the static permeability of current grain $\mu_G(0) \propto D$, (that comes about from DW pinned only on the grain boundary – as in the model of Globus [45]).

The statistical averaging of ACp of permeability of grains (presented in more detail in [64] for IQG ferrites and for TQG ferrites in [66]) allows for ACp of CIP of true intrinsic sample to be obtained as:

$$\mu''(f) = \mu''_{max} exp[-(logf - logf_u)^2/2\sigma^2] \tag{2.44}$$

where μ''_{max} and f_u, Fig. 2.17, characterize the absorption maximum of $\mu''(f)$; but $\sigma = 2\sigma_D$ for IQG and $\sigma = \sigma_D$ for TQG. The relation for $\mu''(f)$ with three parameters of ACp: μ''_{max}, f_u, and σ represents the symmetrical MS (along *logf* axis from the $\mu''(f)$ standpoint, Fig.2.17).

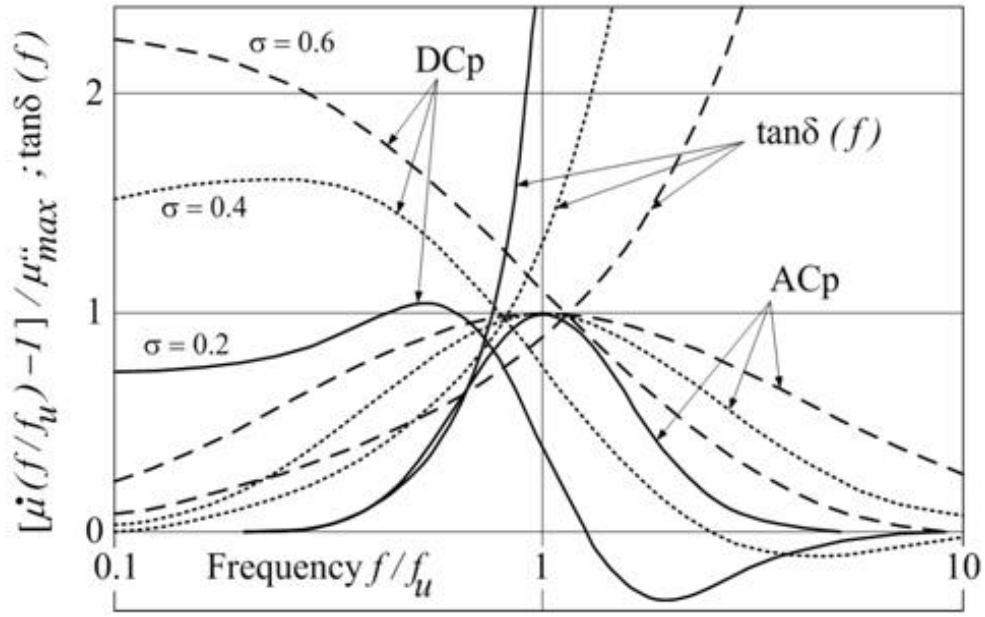

Figure. 2.17 Normalized symmetrical CIP spectra for three σ values, Eq. (2.44), DCp part is obtained by the use of KKR (3.1), [64].

The potential of Eq. 2.44 to represent MS (for different values of σ) as normalized curves is shown in Fig. 2.17: it can be seen that the change of σ (which in reality means the change of grain distribution) principally allows going from a mainly relaxation type of spectra (σ = *0.6*) to a clearly resonant one (σ = *0.2*), having the borderline (between resonance/relaxation) value near *0.5* (in the process the corresponding dispersion components DCp were calculated by the use of KKR). For any definite experimental spectrum $\mu''_{exp}(f)$, under the assumption that it and that of Eq. 2.44 should coincide at two frequencies: f_u and f_a, the specific value of σ for the presentation of the given MS by 2.44, can be evaluated from these chosen points on the curve $\mu''_{exp}(f)$ at frequency $f_a < f_u$(or $f_a > f_u$) and f_u:

$$\sigma = |log(f_u/f_a)|/\sqrt{2ln[\mu''_{max}/\mu''(f_a)]}\,. \qquad (2.45)$$

This result unquestionably is a step forward in physically substantiated presentation of CIP spectra. Even so, analysis of published experimental CIP spectra shows, that the majority of experimental MS show asymmetrical absorption curves $\mu''(f)$. In [67] it was shown that the reason for this comes from intragrain defects which in real PF appear in coarser grains and cause extra pinning of DW. So, instead of one low resonant frequency of DW (when it is

pinned only at grain boundaries) there are developing several higher frequencies from resonating fragments of pinned DW; accordingly, ACp of CIP at lower frequencies decreases because of this pinning (Fig. 2.16), and the spectrum goes asymmetric and more resonant as

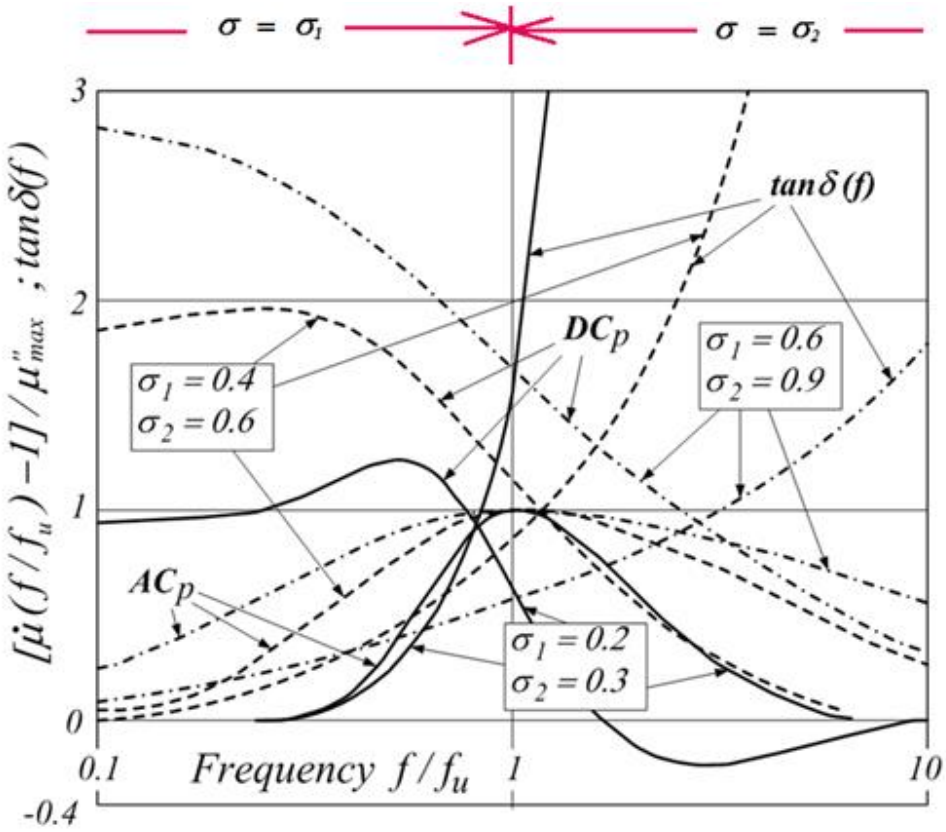

Figure 2.18 Normalized asymmetrical CIP spectra for different $\sigma_a = \sigma_1$ and $\sigma_b = \sigma_2$ values, Eq. (2.44), DCp part is obtained by the use of KKR (2.23), [64].

well. It is particularly notable that experimentally it is possible to observe the inverse process as well: by increasing the excitation field, DW becomes unpinned; the spectrum becomes more symmetrical and relaxant, practically with no changes in the HF part [Fig. 11 in 132] (schematically it can be seen in Fig. 2.16 too). It has been found that for the analytical presentation of asymmetrical MS it is possible to use Eq. 2.44 as well, but with two values of σ: one, σ_a for $f < f_u$ and another, σ_b for $f > f_u$. Corresponding frequency dependences of a such modified Eq. 2.44, in normalized form, for several combinations of $\sigma_a$and σ_b (naturally $\sigma_a < \sigma_b$) are shown in Fig. 2.18 – they realistically depict the most typical features of experimental MS. From Fig. 2.18 it is clearly seen, that for $\sigma_a < 0.5$ values the DCp resonance attributes are appearing at frequencies $f < f_u$; in its turn $\sigma_b$value, that typically is higher than 0.5 allows to make more relaxant DCp character at $f > f_u$. Thus, we can construct the spectra close to experimental spectra form both with relaxation and resonance

attributes (Fig. 2.18).

When Eq. (2.44) is used for the approximation of experimental CIP, then the corresponding values of σ can be found from the requirement of exact agreement between Eq. (2.44) and experimental CIP at three points: $\mu''_{max}@f_u$; $x\mu''_{max}@f_a < f_u$; $y\mu''_{max}@f_b > f_u$; ($x < 1$, $y < 1$); these characteristics allow to use (2.45) as well, which for the often used half-level absorption, when $x = y = 0.5$, transforms to:

$$\sigma_{a\ or\ b} = 0.85|\log(f_u/f_{a\ or\ b})|. \quad (2.46)$$

The physical background for this modification comes from the fact that the majority of real samples (of industry technology) belong to TQG of PF. This implies that in coarser grains (because of their larger size), there are intragrain defects pinning DW and thus fragmenting their displacement. This increases the shift in the frequency response (in relation to that of IQG), because instead of one low frequency $f_{osc}^{(LF)}$(corresponding to oscillating DW of full size within larger grains) there appear several higher frequencies $f_{osc}^{(HF)}$ corresponding to vibrations of the fragments of pinned DW; this lowers the value of σ_a and increases that of σ_b; the values thus gained only indirectly are related to actual grain size distribution. So, if in Eq. 2.45 the data from experimental ACp are inserted: $f_a \leq f_u$ (often such as $\mu''(f_a) \approx 0.5\mu''_{max}$); for σ_b, f_a is simply replaced by $f_b > f_u$. For symmetrical MS σ_a and σ_b obviously are equal.

As suggested above, the value of σ in the model characterizes the distribution of resonance frequencies f_{osc} of DW, and so σ is directly connected with the characteristic of distribution of grain sizes σ_D as well. The modeling of magnetic spectra by taking account of PF microstructure offers the physical background for unveiling the microstructure dependence of not only static magnetic permeability, but of complex magnetic permeability too. Included in the model assumption that DW are low loss resonators, offers universality: narrow distribution of grains ($\sigma < 0.5$) gives resonant type MS, but broad distribution ($\sigma > 0.5$) gives a relaxation type MS (contrary to this DW viewed as relaxators allows only for the relaxation type of MS). Graphical representation of CIP spectra by means of microstructure parameters allows the conclusions to be made that: symmetrical spectra represent PF with rather perfect grains; asymmetrical spectra point to the presence of a considerable amount of intragrain defects.

2.2 Magnetics for switch-mode power supply

An ideal power supply must provide a constant output DC voltage of desired value (or level), regardless of pollution of input voltage (ripples, level change, harmonics, etc.), nature of load (high/low impedance, inductive/capacitive character of load) and of the conditions in which it is used (high/low temperature, high humidity, etc.), at 100 % conversion efficiency. But in real power supplies there will always be losses, output ripples, noises.

There are two types of AC/DC power supplies: linear power supplies and switched mode power supplies.

Linear power supplies (LPS) are the most simple and cheap to construct, but they are bulky and have low efficiency. Due to low operating frequency (50–60 Hz) transformers used in LPS are massive and the weight of these power supplies becomes significant. The efficiency range of LPS is 35–65 % [104]; a large amount of energy is dissipated (mainly as a heat), which is undesirable because of drastic energy consumption all over the world.

Switched mode power supplies (SMPS) are more complex then LPS, but provide more efficient power conversion (the efficiency now reaches up to 97–98 % [125]). Due to the use of high switching frequency the construction of SMPS is more compact and lighter, but the SMPS output is noisier than LPS. The actual problems here are noise filtering, electromagnetic interference (EMI) and radio frequency interference (RFI) suppression, which adds complexity to the construction. To reduce typical nonlinear influences of loads on the power grid the power factor correctors (PFC) are added to construction, which adds more complexity and cost to the SMPS. But all these requirements are needed to minimize the world power consumption [104, 148]. Transformers, coils and filters should have high efficiency at high frequencies, though this is hard to achieve. To reduce energy losses and decrease the physical size ferrite cores are used. Often high impedance of coils with ferrite cores is a good way of suppressing the interference signals. Pulse transformers require ferrites of high permeability, low hysteresis factor and DC sensitivity; power transformers require low power losses and high saturation levels.

To solve these problems and develop the low loss high frequency magnetic materials – ferrites, different approaches are used for understanding power loss mechanisms, e. g. development of the loss measurement techniques [166, 169], and production and study of new low-loss ferrite compositions [113, 177]. Doping MnZn ferrites with SnO_2, TiO_2, Ta_2O_5 [177] or CaO_2, Co_2O_3, MoO_3 [112] dopants have a great influence on grain boundary resistivity and, therefore can improve micro-eddy current resistance within the core. Thus, the research into

MnZn ferrites [122], developed a new composition with high-electrical-resistive boundary layer, which reduces high frequency power loss (by lowering eddy-current and residual losses). In [106] there is developed a new ferrite material (H63A) which allows the construction of a multiple output 400 kHz power supply with reduced noise characteristics.

The current tendency is miniaturization of electronic devices and components [138]. Planar cores are a good choice for magnetic components in the case of further miniaturization; correct winding placement can enhance efficiency (due to minimization of winding losses). The problems associated with the use of planar cores are described in [86]. System on chip inductors are developed in [100]. Applying a ferrite polymer epoxy globe onto these inductors enhances the performance.

2.2.1 Ferrites for SMPS

There are several topologies available for SMPS. Each of topologies has its unique features, the selection of which is dependent on the working conditions. For the correct selection of the SMPS topology one should determine whether the output voltage should be lower or higher than the input voltage or should there be input to output dielectric isolation. Thus the SMPS can be divided to those with transformer in their topology (isolated) and without it (not isolated) [104].

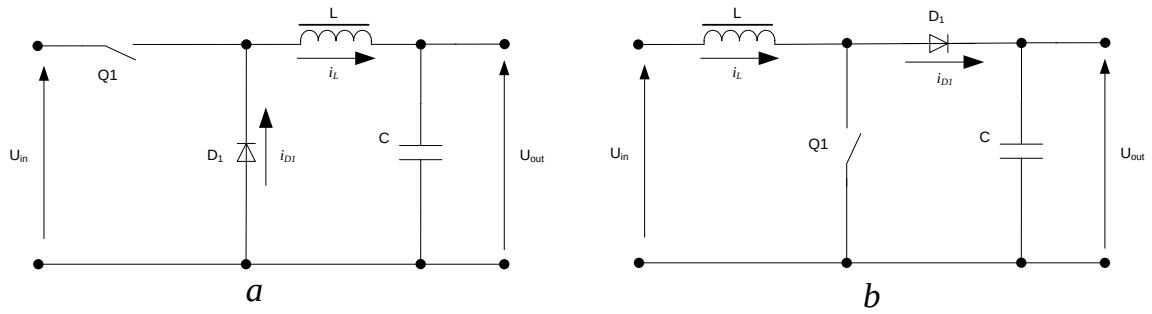

Figure 2.19. Simplified buck (a) and boost (b) converter topologies.

The majority of SMPS topologies are derived from the three non-isolated ones: buck (Fig. 2.19, a), boost (Fig. 2.19, b) and buck-boost. These topologies have the lowest component count (transistors, diodes, capacitors, inductors, etc.).

The buck converter is one of the cheapest and most common topologies used to step-down voltages, for applications where isolation is not required. The downside of this topology is discontinuous input current which results in higher EMI. In contrast – the continuous input current in boost (step up) converter topology makes it a good choice for power factor correction applications. In the buck-boost topology both input and output currents are

discontinuous, thus very large output capacitors are needed to achieve low ripple levels [104]. Nevertheless this converter type can both step up and step down voltage, which makes it useful for the applications where the input voltage varies over time.

To extend the limits of non-isolated topologies the transformers are used [104]. This provides input to output isolation; by varying the transformer turns ratio, the duty cycle of a transformer can be optimized and peak currents flowing minimized; the multiple outputs can be easily achieved with multiple secondary windings and the polarity of the output can be selected by the choice of polarity of secondary versus primary winding. The disadvantage can be additional transformer size, weight and power loss. The transformer operation (and so are converters) within the isolated topologies can be divided to symmetrical and asymmetrical [104].

In the asymmetrical converters the flux and magnetic field never changes sign, thus only half of the flux is used. This results in the need of demagnetizing of the core in each cycle. Such asymmetrical converter topologies are flyback and forward (Figs. 2.20; 2.21) [104]. On instance the symmetrical topologies, such as push-pull and bridge-type, utilizes all the available flux, so the usage of the core is more effective. This requires the even number of transistor switches. Therefore simmetrical converters can produce more power than asymmetrical ones.

The magnetic cores form an essential part of power supplies, and can be made from a great variety of materials and shapes, and can be classified into three main categories: tape wound cores, powder cores, and ferrites. Among them ferrites, having high resistivity, are

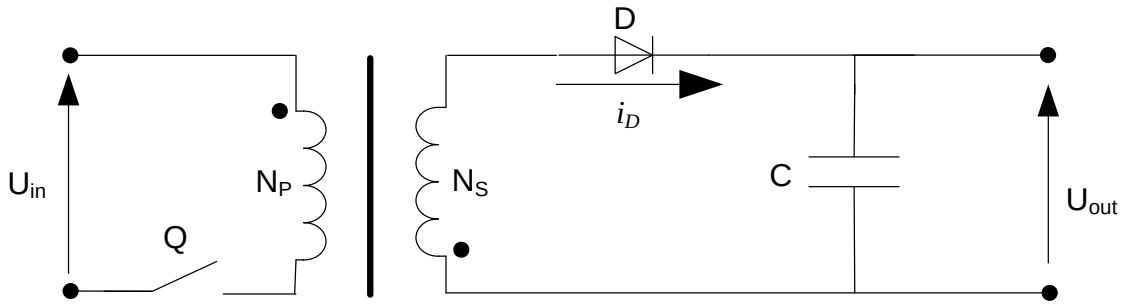

Figure 2.20 Flyback converter (N_P and N_S are coupled inductor primary and secondary windings, U_{in} and U_{out} - input and output voltages)

common core materials for high frequency applications.

In flyback converters (Fig. 2.20) the transformer accumulates energy during switch ON time (magnetization through primary winding) and transfers energy to the load during OFF time (demagnetization through secondary winding). Thus the flyback does not contain a real

transformer, but the coupled inductor instead. The fact that energy should be stored in the core results in greater expenses and larger size of the core in comparison to other topologies. Because of constant magnetization of the coupled inductor it should be made with a ferrite gapped core, or with magnetodielectric ring or split core. Ferrite cores with non-magnetic gap provide more stable inductance from the current change, thus avoiding core saturation. Magnetodielectrics provide a smooth change of inductance with current change, but without severe saturation. The energy transfer only during the transistor OFF time results with the need of the large output capacitor in order to achieve low output ripple. Nevertheless the flyback topology is the good choice for multiple output supplies, because each output requires only one diode and output capacitor [104].

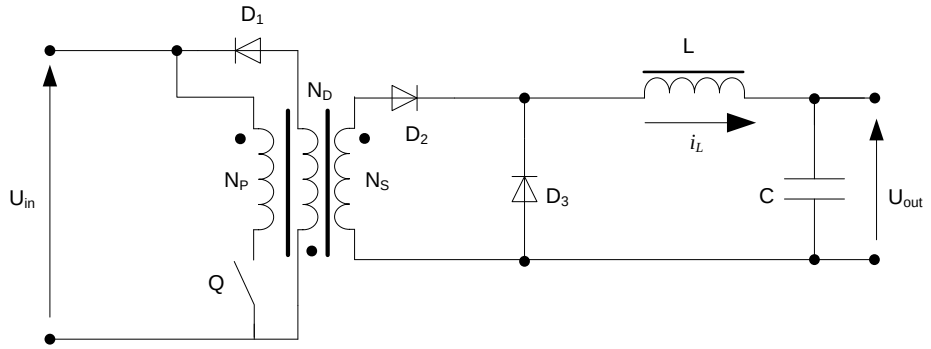

Figure 2.21 Forward converter (N_P and N_S stand for primary and secondary transformer windings, N_D – demagnetizing winding, U_{in} and U_{out} – input and output voltages)

The forward converter uses the real transformer, unlike the flyback (Fig. 2.21). The energy in forward converter is transferred to the output during transistor ON time without accumulation in the transformer. However, asymmetrical operation of the convertor requires for demagnetizing winding and a clamp diode to reset the core. The energy required to excite the core can be achieve by comparatively high primary inductance, thus there is no need for a gapped core. The standard ferrite cores with relatively high permeability (~ 3000 [104]) are the best choice for such application. The fact, that the energy is not stored in the transformer core allows for smaller transformer size and less core loss.

The push-pull converters, having two switches, utilizes the flux fully and can be made with middle tapped transformer (Fig. 2.22), with half bridge and full bridge schemes. The full utilization of flux means symmetrical operation mode, this results in smaller transformer size. Moreover, the bipolar switching results in doubled switching frequency of the output circuit, which allows for smaller sizes of output inductor and capacitor. In the half bridge scheme the primary transformer winding is connected through capacitors, therefore there is no DC current component. In contrast, the other two schemes can achieve a transformer core saturation if the

flux wing in each half cycle is not symmetrical. As the transformer core is working in HF fields (> = 500 kHz...1 MHz), the core should be chosen from MnZn ferrites. If the switching

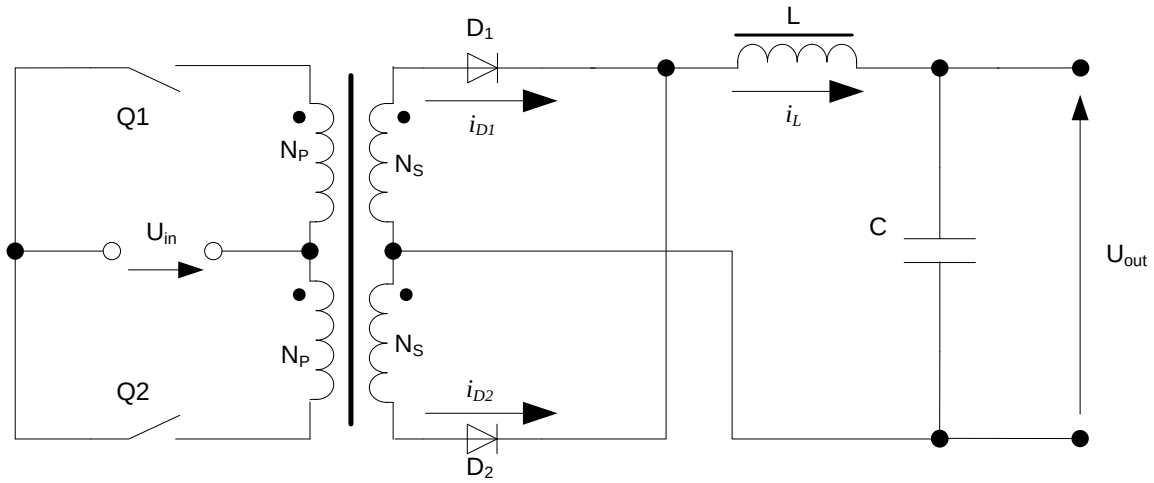

Figure 2.22 Push-pull converter (N_P and N_S stand for primary and secondary transformer windings, U_{in} and U_{out} - input and output voltages)

frequency is lower, then amorphous alloys can be chosen. The use of powder compounds is not a good choice, because they have low permeability values and are more expensive than ferrites.

The type of transformer core can be varied (Fig. 2.23). RM cores are easy to place on PCB due to their square shape, and also round winding bobbin is easy to wind. Nevertheless, it increases leakage inductance, which in turn increases complexity of winding, which results in decreased efficiency. The P cores are analogous to RM but have round shape and therefore it is more difficult to place them on PCB than RM cores. The rectangle shape of EP cores is easy to mount on PCB, and the core completely wraps the coil except for one side, which is placed on the PCB. The EFD cores are placed horizontally, therefore they have smaller height. The low profile LP cores are used when there is need for small dimensions of the device. Toroidal cores (for devices of small and medium power) are the cheapest type of core and have minimal leakage inductance in comparison to other core types. This results in reduced noise radiation and switch voltage overshoot. The disadvantages of toroidal cores are the complexity of winding, and the need of isolation of the core material (if the isolation is not included in the manufacture). Thus, the most universal remains the toroidal ring core. Therefore most of experimental measurements are performed on ring-shaped cores.

The core material can be varied too. Magnetodielectric material – mo-permalloy – has the best technical parameters, but is very expensive. Sendust and Cool Mu materials are cheaper, but to get same loss characteristics as mo-permalloy we need to increase core

dimensions due to the lower magnetic induction in the core. The ferrites has good technical parameters, relatively high permeability and can be made in any convenient core type.

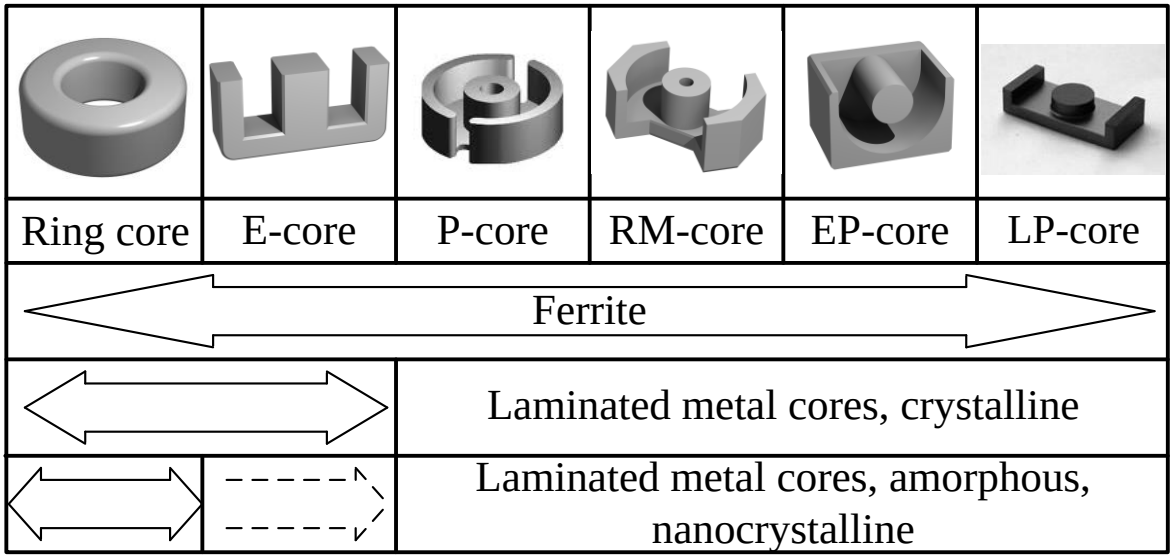

Figure 2.23 Core types of soft magnetic materials

Converter inductors have the same working principle, thus in the push-pull converter case – the mode of operation is easier than in forward or flyback converter working mode due to doubled switching frequency. The inductor works as an energy storage element (it accumulates energy and then transfer it to the load). The core of an inductor is working within fields, with a high DC current component. Therefore the core should be made either from ferrite with a non-magnetic air gap or magnetodielectric material.

However, if a non-standard operating mode of power supply occurs (low power mode or "Drop-Out" mode [32] (when input and output voltages are almost the same, and 100% duty cycle is achieved, minimum-on-time [31]), the power supply may enter the switching pulse skipping mode. In [32] the tests were performed on a Texas Instruments TPS43340-Q1 power supply, which results in 4 times switching frequency f_{SW} reduction under "Drop-Out" mode from 600 kHz to 150 kHz.

2.2.2 Research of effects of spread spectrum on output filter of buck converter

The miniaturization of power supplies, in general, is achieved by increased switching frequency, f_{SW} (which results in higher frequency noise applied to power supply components, for example – for a frequency of 200 kHz the harmonics of 600 kHz and 1 MHz appear [49]), and, thus it results in EMI problems. Decrease of EMI can be achieved both by traditional passive methods (filtering, shielding, grounding, proper PCB design, etc.) and by active

methods – spread spectrum technologies (SST) [154]. The latter method (also known as dithering) allows the suppression of f_{SW} harmonics at the point of their generation – switching transistors without intervention into the power parts of the converter. In concept SST is the use of frequency modulation (FM) of f_{SW} with a modulating signal of frequency f_m ($f_m \ll f_{SW}$). The modulation suppresses the amplitude of each harmonic of the naturally discrete harmonic spectrum of unmodulated f_{SW}, by converting them in corresponding noise bands but with significantly less noise intensity (Fig. 2.24). Thus the energy emitted by hard switching is not concentrated in high amplitude discrete harmonics but is spread out more evenly over a larger frequency range with the top levels of EMI considerably reduced. Hence the appropriate maximum f_{SW} can be determined by the use of EMC assurance methods.

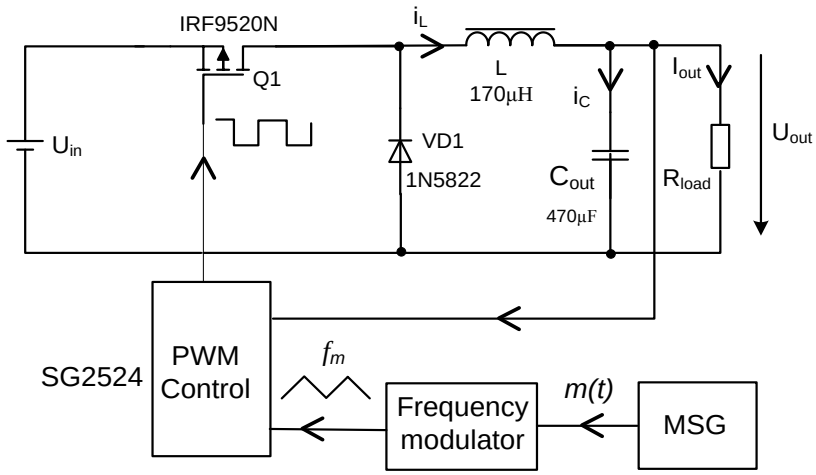

Fig. 2.23. Schematic of FM closed-loop buck converter used [76].

In the research of the effects of spread spectrum on the output filter of a closed-loop buck converter (Fig. 2.23), operating in continuous current mode (CCM) is used. The buck converter can operate both as an unmodulated converter and as a FM converter. In order to spread the spectrum and reduce peak EMI levels, the control circuit consists not only of PWM controller SG2524 but also consists of a frequency modulator and modulating signal generator (MSG). The triangular-like output signal f_m of the frequency modulator is fed into the PWM controller comparator input. If MSG is disconnected from the frequency modulator, then power MOSFET *Q1* f_{SW} is constant (unmodulated). If MSG is connected to the frequency modulator then f_{SW} is modulated by $m(t)$. The instantaneous switching frequency in this case is:

$$f_{sw}(t) = f_{sw0} + \Delta f_{sw} m(t), \tag{2.47}$$

where Δf_{sw} is the switching frequency deviation (in [76] 35 kHz); *m(t)* is triangular

modulating signal; f_{sw0} is the nominal switching frequency (in [76] 100 kHz).

In Fig. 2.24 input current spectra are shown for both unmodulated and FM buck converters. The effect of FM reducing EMI of the converter is clearly seen. After applying FM the noise energy formerly concentrated in discrete harmonics is spread over wider frequency range and peak EMI levels are noticeably reduced.

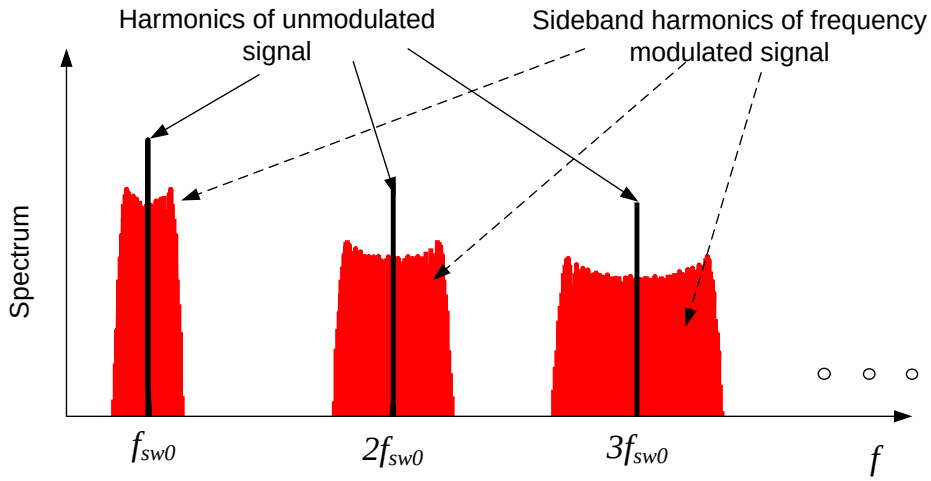

Fig. 2.24. Spectra of unmodulated and frequency modulated input current [76].

To account for losses produced by currents through L and C (respectively i_L and i_C), and for possible supplementary frequency effects at some particular high frequencies within the spread spectrum, there is need to consider the parasitics of the filter components. Specifically, for the usual three element equivalent circuit, there are two parasitics for each component: the equivalent series resistance (r_C, ESR) and inductance (L_C, ESL) for the capacitor and the equivalent series resistance (R_L) and parallel self-capacitance (C_0) for the inductor. In the following analysis it is assumed that losses generated in the components are equal to their resistance times the square of r.m.s. current through them. For the evaluation of the impact of SST on filter we are not interested in the absolute value of losses, but rather on their change relative to the unmodulated converter when there is only one value of $f_{SW} = f_{SWO}$. As in [76], this allows only for loss terms which are *constant* or non-linear functions of f_{SW}, and assumes that the linear terms compensate themselves in the case of symmetrical FM.

To evaluate effect the of FM on power inductor losses, first of all unmodulated buck converter power inductor loss will be analyzed, without considering the effects of core saturation. In general power inductor power loss can be divided into winding (P_w) and magnetic core (P_{mc}) losses. The winding losses for the unmodulated buck converter inductor are:

$$P_w = R_L I_L^2 , \tag{2.48}$$

where R_L is the power inductor resistance, I_L is the rms current of inductor. Considering that inductor current consists of both AC I_{Lac} and DC I_{out} components (Fig. 2.25), I_L is given by:

$$I_L = \sqrt{\frac{1}{T_{sw}} \int_0^{T_{sw}} (i_L(t))^2 dt} = \sqrt{I_{out}^2 + I_{Lac}^2} \tag{2.49}$$

where T_{sw} is the switching period, $I_{Lac} = \frac{(U_{in} - U_{out}) D_C T_{sw}}{2\sqrt{3} L}$ is the effective value of $i_{Lac}(t)$ (Fig. 2.25), D_C stands for duty cycle.

From (2.48)–(2.49) it can be derived that

$$P_w = R_L I_L^2 = R_L I_{Lout}^2 + \frac{R_L D_C{}^2 (U_{in} - U_{out})^2}{12 L^2 f_{sw}^2}. \tag{2.50}$$

In order to derive magnetic core losses P_{mc} the modified Steinmetz equation (2.14) for nonsinusoidal waveforms can be used. Assuming that inductor current changes linearly, as shown in Fig. 2.25, it can be derived for unmodulated buck converter from (2.14) thus

$$P_{mc} = C_m \left[\frac{2}{D_C (1 - D_C) \pi^2} \right]^{\alpha - 1} \left(\frac{(U_{in} - U_{out}) D_C}{2NS} \right)^{\beta} \frac{v_c}{f_{sw}^{\beta - \alpha}}, \tag{2.51}$$

where S is the magnetic core cross-section area; and N is the number of turns.

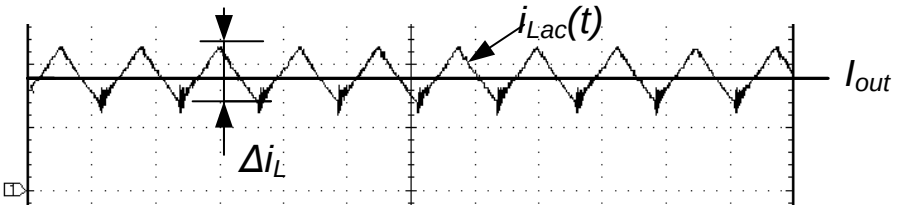

Fig.2.25. Unmodulated buck converter power inductor current. (Scale: 25 μs/div; 100 mA/div) [76].

As can be deduced from (2.50) and (2.51), inductor power loss for an unmodulated converter consists of two terms: loss that is independent of f_{sw} and loss which depends nonlinearly on it. It is obvious that nonlinearly dependent on f_{sw} losses can increase due to FM even if the coil is not saturated. In the case of an FM converter the average power losses of the inductor can be calculated as follows:

$$P_{loss\,\mathrm{mod}} = \frac{1}{T_m} \int_0^{T_m} p_{im}(t) dt \tag{2.52}$$

where $p_{im}(t)$ represents instantaneous losses in the power inductor. Taking into account that for FM T_{sw} is not constant, then the average power loss $P_{ind}(T_{sw,k})$ for each switching cycle $T_{sw,k}$ is a function of it. So (2.52) can be rewritten as follows:

$$P_{loss\,\mathrm{mod}} = \frac{1}{T_m}[\int_0^{t_1} p_{im}(t)dt + \int_{t_1}^{t_2} p_{im}(t)dt + ... + \int_{t_{k-1}}^{t_k} p_{im}(t)dt + \int_{t_{K-1}}^{t_K} p_{im}(t)dt] =$$
$$= \frac{1}{T_m}\sum_{k=1}^{K} P_{ind}(T_{sw,k})T_{sw,k} \tag{2.53}$$

where K is an integer number, $K = T_m/T_{sw}$. Considering that T_m (modulation period) is usually much higher that T_{sw} then instead of summation the integration can be used as follows

$$P_{loss\,\mathrm{mod}} = \frac{1}{T_m}\int_0^{T_m} P_{ind}(f_{sw}(t))dt \tag{2.54}$$

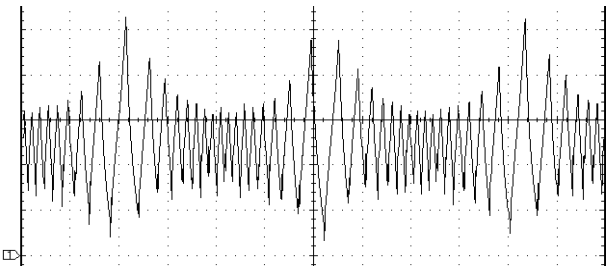

Fig. 2.26. FM buck converter power inductor current without core saturation effects. Parameters: f_{sw0} = 100 kHz; f_m = 5 kHz; Δf_{sw} = 35 kHz. (Scale: 50 μs/div; 100 mA/div) [76].

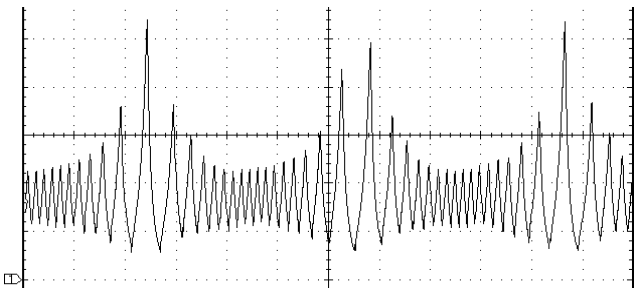

Fig. 2.27. FM buck converter power inductor current with core saturation effects. Parameters: f_{sw0} = 100 kHz; f_m = 5 kHz; Δf_{sw} = 35 kHz. (Scale: 50 μs/div; 400 mA/div) [76].

So the average power losses of the inductor can be calculated using (2.52), (2.50), (2.51) and (2.54). After using these equations it is concluded that FM can increase inductor loss, due to the terms in (2.51) and (2.50) that depend nonlinearly on f_{sw}.

In order to examine possible side effects of FM on the power inductor when the core is entering saturation, output current of the buck converter was increased to about three times nominal current (from 200 mA to 600 mA). Experimental inductor current is shown in Fig. 2.26 (when I_{out} = 200 mA) and Fig. 2.27 (when I_{out} = 600 mA). As can be seen in Fig. 2.26 there is no saturation of the magnetic core due to the use of FM. However, a sharp increase in the inductor current is observed when I_{out} = 600 mA as is seen in Fig. 2.27. This is

because the magnetic core material saturates when f_{sw} is in the vicinity of f_{swmin}. For the frequencies which are markedly higher than f_{swmin} there is no saturation.

Obviously, power inductor losses can drastically increase due to SST effects on power inductor resulting from saturation effects in the core. Therefore when designing an FM power converter it is important to choose f_{swmin} appropriately so as to avoid the magnetic core saturation. This reflects as a sharp increase in the power inductor current and consequently increase losses in the inductor. So when designing an FM converter, minimum switching frequency should be chosen appropriately to avoid core saturation.

2.2.3 Ferrites for EMC

The line filter deals with differential mode noise and common mode noise. The common mode noise is conducted on both signal and ground line in one direction; therefore, suppression filters must be installed on all lines where noise is conducted. Two windings are placed on the core, and are connected through the magnetic field of the core. This type of inductor is often called a common mode choke.

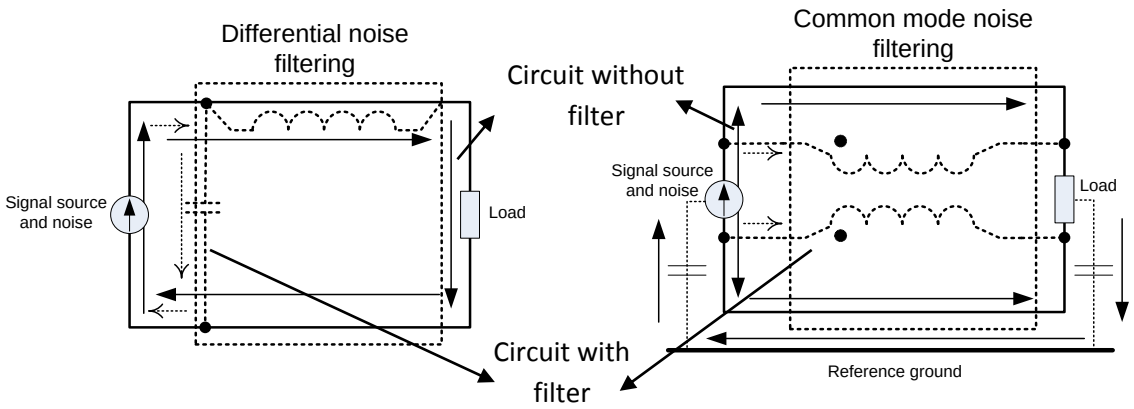

Figure 2.29 Common mode and differential mode filtering (solid arrows represent direction of the noise without filter, dotted arrows represent direction of noise with applied filter) adapted from [1, 2, 3]

Common mode choke coils are used for suppression of common mode noise signals. It acts as a simple wire for differential mode signals (differential signal flowing inside the choke produces equal and opposite magnetic fields which cancel each other), but produces high impedance for common mode signals (common mode signal flowing inside the choke produces equal and in phase magnetic fields which add together). The core material should be chosen from high permeability ferrite, because the core would work in low fields and the required inductance can be obtained with a minimal amount of turnings. The use of

magnetodielectrics is inexpedient due to their low magnetic permeability and the low cost of ferrites. Core type can be chosen between E, U and ring cores.

Differential noise is conducted on the signal line in one direction (with the signal). This noise is suppressed by one or two inductors installed on the signal line. Here, together with low amplitude noise, the high amplitude 50 Hz power supply current is present, which is equal to DC in these conditions. The core material can be chosen between ferrite cores with nonmagnetic gap or magnetodielectrc cores.

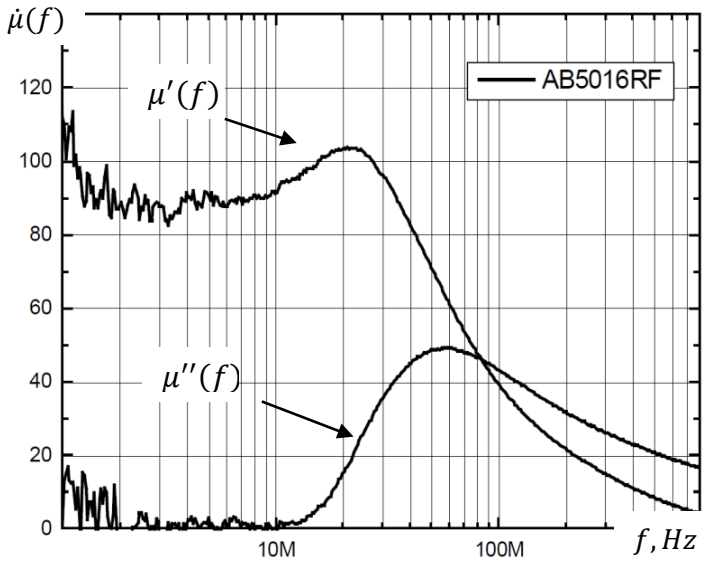

Figure 2.30. 3M AB5016RF FFDM material for wireless power application [102]

The modern and growing tendency for the recharging of hand-held electronics is wireless power charging (WPC) [102]. The electromagnetic inductive coupling (EMIC) approach in WPC standard tends to be the most cost-effective and easily implemented [102]. For dealing with interference with the function of other electronic components, or the heating of nearby components during operation, flux-field directional materials (FFDM) have been developed. FFDMs improve flux interaction with a coil, reduce eddy current losses, provide flux-field shielding, and minimize EMI to Wi-Fi or other antennae. Typical FFDM materials are sintered ferrites. The selection of sintered ferrites is based on working conditions (mainly NiZn and MnZn ferrites) [102], and losses, that typically are represented by CIP spectra.

The published data on CIP of 3M AB5016RF FFDM material (Fig. 2.30) is noisy at frequencies < 10 MHz and is not available at frequencies > 800 MHz, therefore the quality of this spectrum will be evaluated by the use of the model and KKR (see § 3).

2.3 Review of frequency dependent problems of ferrites.

The main problem in implementing a new design for magnetic related applications is to collect appropriate data on the materials that will be used [140–142,146].

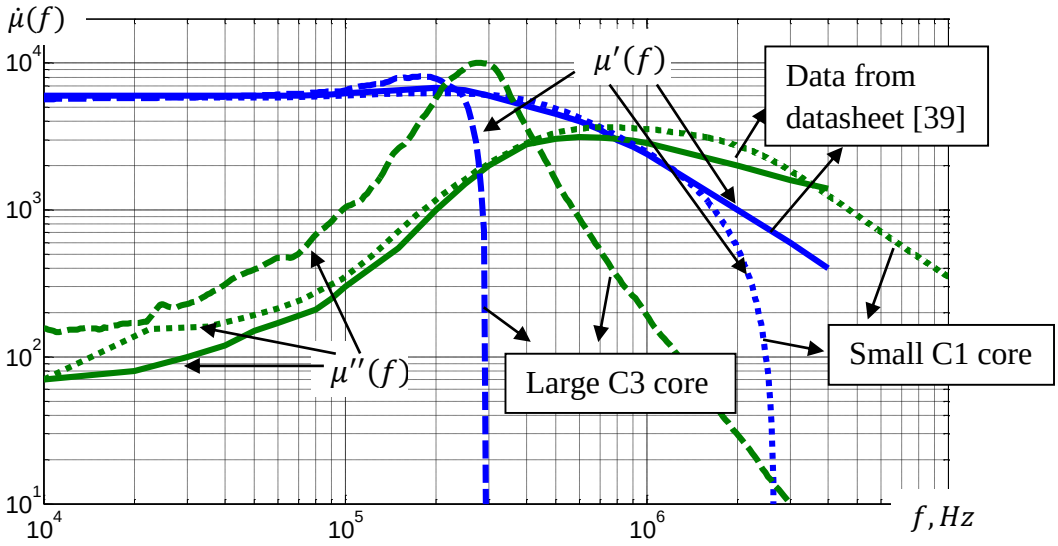

Figure 2.31 Measured and given [39] CMP for EPCOS T-35 material cores.

But, usually, provided information on ferrite core is based on low power measurements of small-sized toroidal cores, which is not always applicable. Larger cores of the same material can provide significant changes in material characteristics (see Figure 2.31). Therefore available information is incomplete for applications where such cores can be used. Furthermore, according to [140] the information provided in the design literature does not give solutions on how to deal with dimensional effects. The reality of this problem is easily noticeable in Figure 2.31 – with increased core size the absorption is greatly increased and dispersion has extremums over a greater extent; also the core working frequency range is lowered.

Newer-ending problems are related to the reduction of power losses of ferrites (especially MnZn ones) and increasing power supply efficiency [49]. Consequently, many new materials, that fulfill the demands of modern power supply designers, have been developed. In Fig. 2.32 there are presented trends of ferrite material development. The main directions represent different areas of ferrite production: power ferrites with increased magnetic flux density; ferrites for high frequency applications; low loss ferrites; and ferrites with improved temperature loss dependence. The MB3 material, being the general-purpose material [49] for power supply could not afford all the demands of nowadays electronics. So, the low loss MB4 material was developed and achieves the energy loss improvement for

about 20% versus MB3 material [49]. The MBT1 and MBT2 materials show low energy loss from room temperature to around 100 °C [49]. MB1H material offers high saturation magnetic flux density, which makes it possible to increase the design magnetic flux density of transformers (it is optimal for downsizing flyback SMPS [49]). MC2 material has low core loss at high frequencies (65 kW/m^3 @ 500 kHz, 50 mT, 100 °C [49]), thus this material is used within SMPS applications, where compact sizes and thin designs are required [49]. The more recent materials, in Fig. 2.32 (such as MS3, MBT3, a. o.) have even better characteristics than their previous representatives in each of application areas respectively.

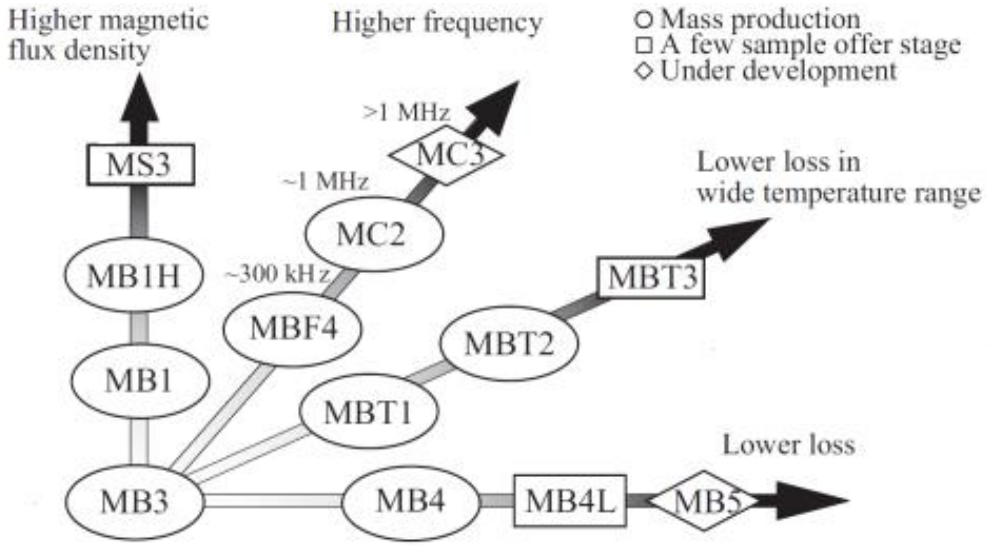

Figure 2.32. Schematic diagram of development of low loss MnZn ferrites for SMPS [49]

Simultaneous improvements of all ferrite characteristics cannot be achieved due to loss dependence on various factors (not only from the composition but on the microstructure too [49, 176], since low frequency hysteresis loss depends on microstructure defects, porosity; the high frequency eddy-current loss can be decreased by higher electrical resistance of the grain boundaries and smaller size of the grains [176] etc.). But the grain size cannot be decreased indefenetely; in [49] it is stated, that for forward mode SMPS, core loss at 100 kHz switching frequency, increases if grain diameter is decreased below 6 μm.

As a consequence, it is believed that the study of CIP frequency spectra in relation to their MST may contribute to a better understanding of the magnetization processes of PF, eventually resulting in a better representation of frequency dependencies and more effective application of PF.

3 APPLICATIONS OF KRAMERS-KRONIG RELATIONS (KKR) TO STUDIES OF CIP DATA

3.1 Practicalities of KKR

The Kramers-Kronig relations (KKR) relate the real and imaginary parts of a complex analytic function. As to physical systems KKR are often termed as dispersion relations and they are usable for linear casual cases. The relations are used to calculate the real part of a characteristic from the imaginary part,- and vice versa. Eq. (3.1) and (3.2) describe the interrelationship of the real and imaginary parts of CIP:

$$\mu'(f) - 1 = \frac{2}{\pi}\int_0^\infty \frac{x\mu''(x)}{x^2 - f^2}\,dx, \tag{3.1}$$

$$\mu''(f) = -\frac{2}{\pi} f \int_0^\infty \frac{\mu'(x)}{x^2 - f^2}\,dx. \tag{3.2}$$

We can see that the real and imaginary parts are dependent on each other, and the complex function can be reconstructed even if only one part is given over the full (non zero value) frequency range. The integration has an infinite upper limit, but for actual components of CIP we may operate within finite limits (e. g., from frequency $f_A = 0$ to f_B, beyond which ACp is zero, Fig. 3.1). For many investigation cases considerable utilities come from the relation following from Eq. (3.1):

$$\mu(0) - 1 = 2/\pi \int_0^\infty \mu''(f) d\ln f, \tag{3.3}$$

i.e. the value of static permeability (susceptibility $\chi(0) = \mu(0) - 1$) depends on the area under corresponding curve ($\mu''(f)$ or $\chi''(f)$) depicted in *logf* (or *lnf*) scale.

To transform the relation to the form, that can be applied to experimental results it is useful to replace the integration with a summation. Dividing the measured curve into short sub pieces we can assume that each small piece of curve is linear within its limits and then we can represent the $\mu'(x)$ or $\mu''(x)$ as the sum of linear function: $y_i = m_i x + c_i$. Now we can write the summation relations for the $\mu'(f)$ and $\mu''(f)$:

$$\mu'(f) - 1 = \frac{2}{\pi}\int_0^\infty \frac{x\mu''(x)}{x^2 - f^2}\,dx = \frac{2}{\pi}\sum_i \int_{a_i}^{b_i} \frac{x(m_i x + c_i)}{x^2 - f^2}\,dx \tag{3.4}$$

$$\mu''(f) = -\frac{2}{\pi} f \int_0^\infty \frac{\mu'(x)}{x^2 - f^2}\,dx = -\frac{2}{\pi} f \sum_i \int_{a_i}^{b_i} \frac{m_i x + c_i}{x^2 - f^2}\,dx \tag{3.5}$$

Writing the linear function for two points as $y(a_i)$ and $y(b_i)$, we eventually can obtain the coefficients *m* and *c*:

$$y(a_i) = m_i a_i + c_i;\ \ y(b_i) = m_i b_i + c_i \tag{3.6}$$

then from:

$y(b_i) - y(a_i) = m_i(b_i - a_i)$ we can find m_i:

$$m_i = \frac{y(b_i)-y(a_i)}{b_i-a_i}; \tag{3.7}$$

but from:

$y(b_i) + y(a_i) = m_i(b_i + a_i) + 2c_i$. Inserting m_i and solving for c_i we get:

$$c_i = \frac{y(a_i)b_i-y(b_i)a_i}{b_i+a_i} \tag{3.8}$$

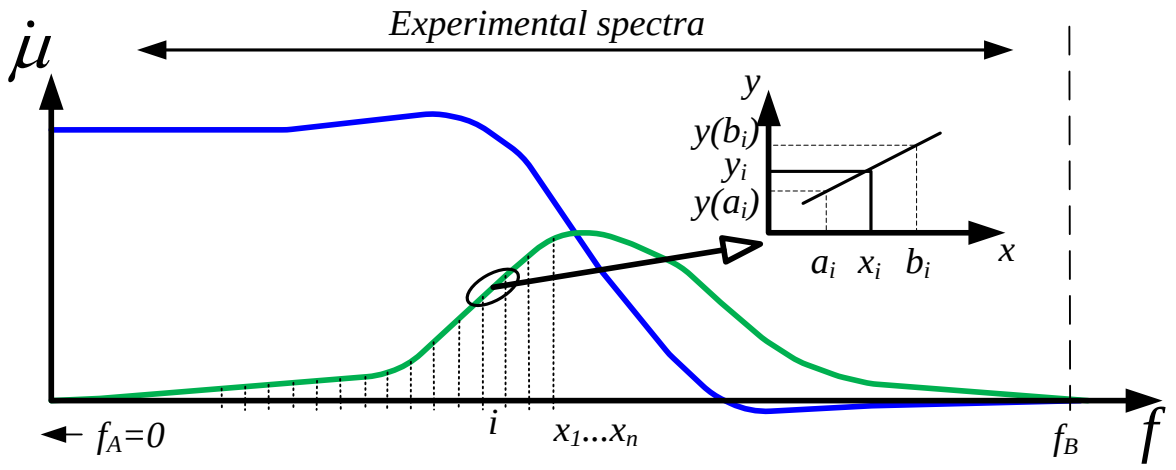

Figure 3.1. Concept of Kramers-Kronig application to measured CIP

Now, using integral solving relations [179] and substituting the integrals in Eqs. 3.4–3.5 with summation, we can write the final form of the K-K relations as:

$$\mu'(f) - 1 = \frac{2}{\pi}\sum_i \left(m_i(b_i - a_i) - \frac{m_i f}{2} ln \frac{|f-a_i|(b_i+f)}{(f+a_i)|b_i-f|} + \frac{c_i}{2} ln \frac{|b_i^2-f^2|}{|f^2-a_i^2|} \right) \tag{3.9}$$

$$\mu''(f) = \frac{2}{\pi}\sum_i \left(-\frac{m_i f}{2} ln \frac{|b_i^2-f^2|}{|f^2-a_i^2|} + \frac{c_i}{2} ln \frac{|f-a_i|(b_i+f)}{(f+a_i)|b_i-f|} \right) \tag{3.10}$$

The MATLAB® program code for Kramers-Kronig relations (based on Eq. (3.9) and (3.10)) is presented in Appendix 1.

3.2 Magnetic spectra quality – analysis from KKR viewpoint

At times, the experimental magnetic spectra are unclear, or of insufficient quality. In [193] it is suggested to use the Kramers-Kronig relations as a proper mathematical instrument for evaluating the doubtfull magnetic spectra. For example, the spectra presented by Dok Won Lee a. o. in [93, Fig. 1] clearly seems contradicting since three different values of $\mu(0)$ are connected with practically the same $\mu''(f)$ that is not possible (cf. Eq. 3.3), additionally they are noisy at lower frequencies (from 1 to ~ 50 MHz) (Fig. 3.2), so it is hard to find the correct value. The application of Kramers-Kronig relations (green dashed line) to above mentioned

permeability curves (blue solid line) reveals the true values for these inaccurate, noisy data, and also provided information that measured in [93, Fig. 1] permeability data is inaccurate (Fig. 3.3).

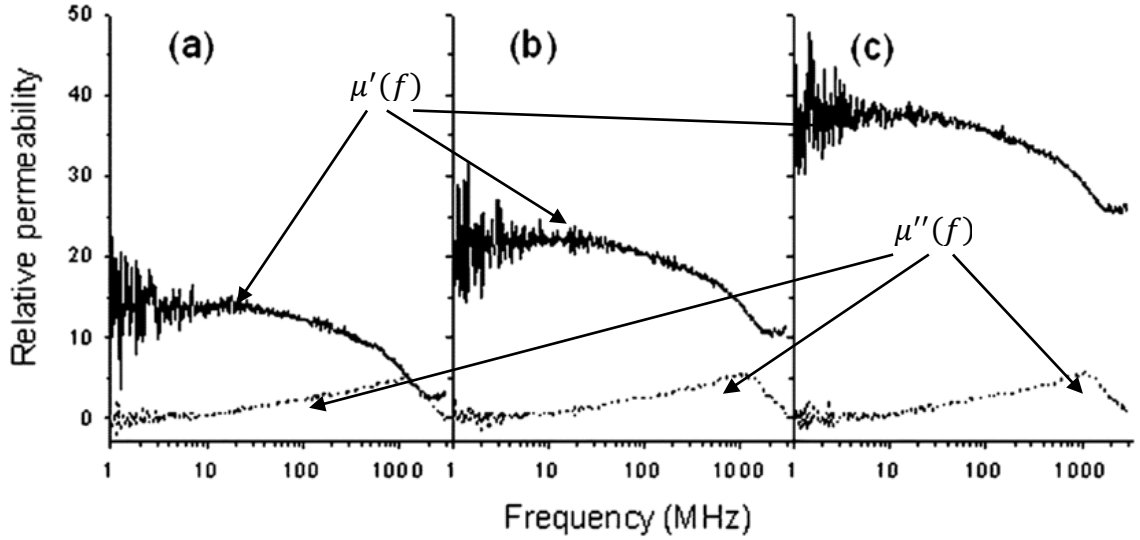

Figure 3.2 CIP spectrum of $Fe_{78}Si_{13}B_9$, measured with different sample thicknesses: (a) 27.5 μm, (b) 54,9 μm, (c) 110 μm [93].

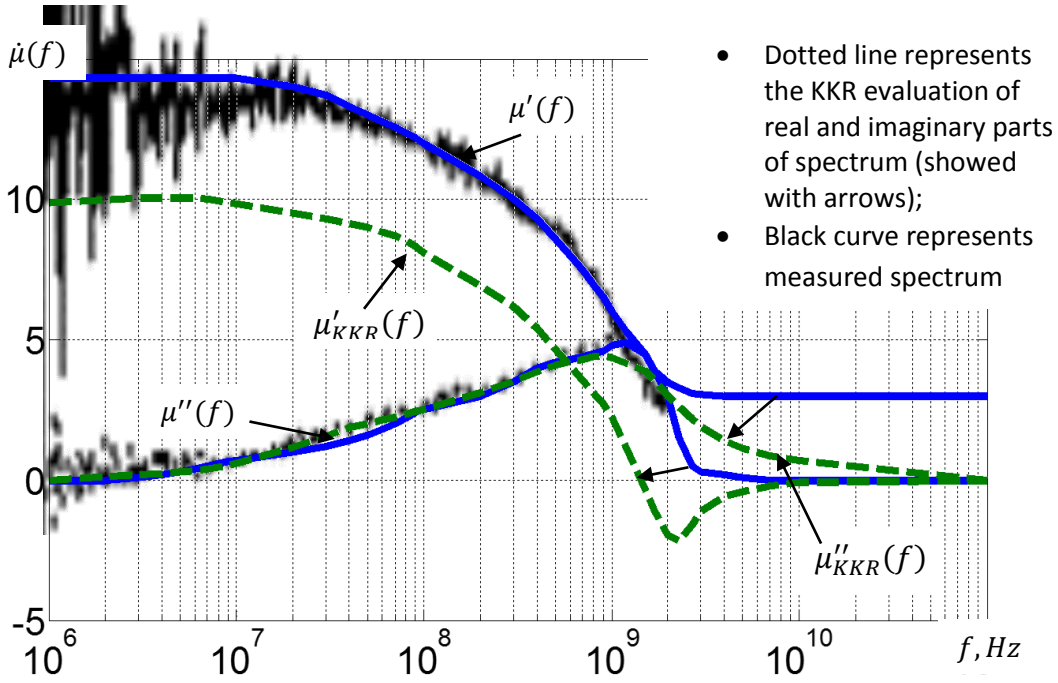

Figure 3.3 Checking of correctness of CIP spectrum of $Fe_{78}Si_{13}B_9$ [*"a"* from Fig. 3.2].

Unclear (noisy) experimental data is shown in Fig. 3.4., as CIP spectrum of $Ni_{0.2}Zn_{0.3}Fe_2O_4$ ferrite films [172]: it is rather noisy and it is experimentally defined at $2 \times 10^7 < f < 3 \times 10^9$ *Hz*. Thus, for correct evaluation of this spectrum, ACp was extrapolated on both sides to zero. The slope of right side was chosen so (with the help of the model

(subsection 2.1.9)) that after performing KKR evaluation, calculated DCp part slope ($3 \times 10^8 < f < 2 \times 10^9\ Hz$) will be same as experimental one. The analysis showed, that data provided up until *1…2 GHz* are more or less reliable; nevertheless originally they are not full and is noisy. But our approach is successful: the use of the model together with KKR for estimation of incomplete, noisy experimental CIP data allows for much more completeness.

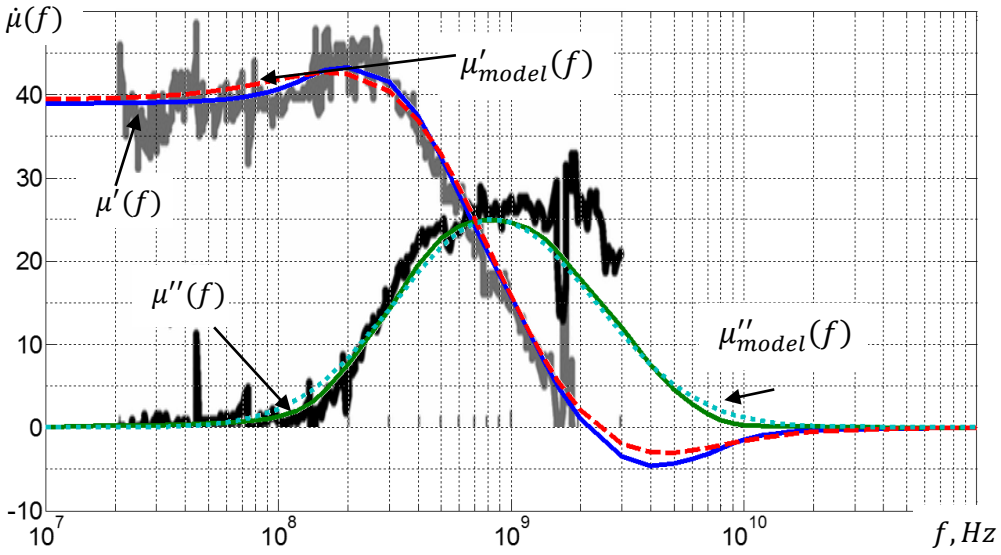

Figure 3.4 Spectrum of $Ni_{0.2}Zn_{0.3}Fe_2O_4$ ferrite [172] and its analyze by KKR.

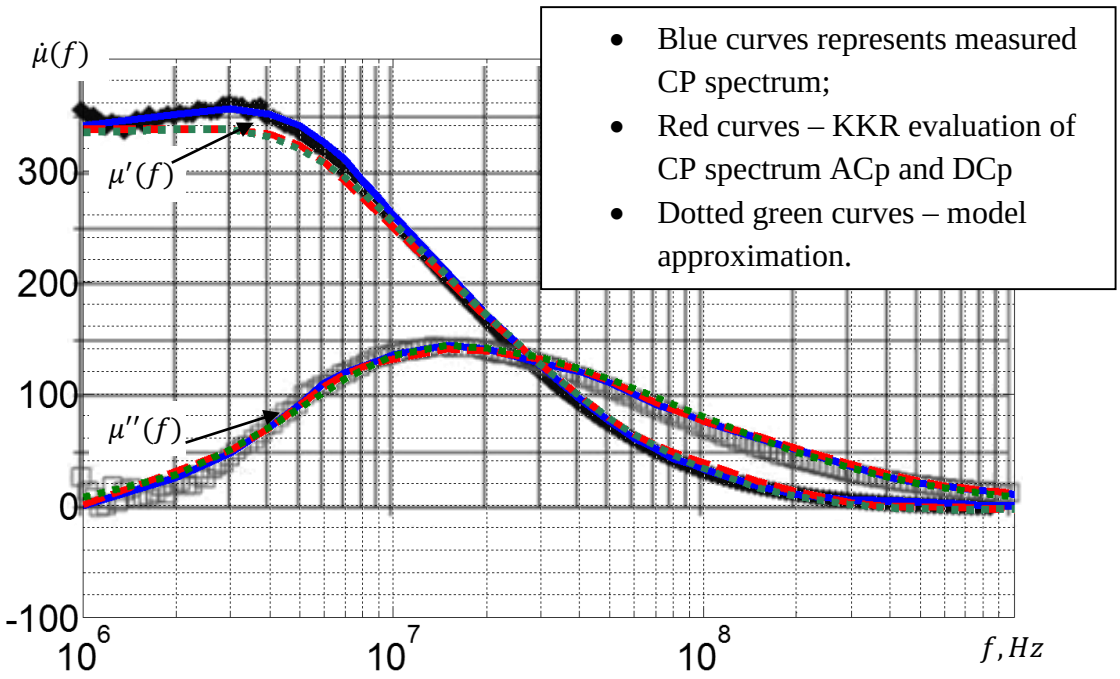

Figure 3.5 Analysis of 3M EM-600 [102] ferrite spectrum.

Company 3M flux-field directional material (FFDM) ferrites EM-600 and AB5016RF (Fig. 3.5 and Fig. 2.31, 3.6) were provided by the manufacturer with little noise at $f < 5$ MHz for EM-600 material and, also with noise at $f < 10$ MHz for AB5016RF; additionally, AB5016RF ferrite CIP data was not available above 800 MHz. Thus with help of applying the model and performing several KKR iterations, the curves were precized and prolonged. This revealed that presented data is reliable, even in case of AB5016RF ferrite spectrum (the model was applied with parameters of $\sigma_a = 0.48$ and $\sigma_b = 0.76$ for EM-600 ferrite and with $\sigma_a = 0.33$ and $\sigma_b = 0.68$ for AB5016RF).

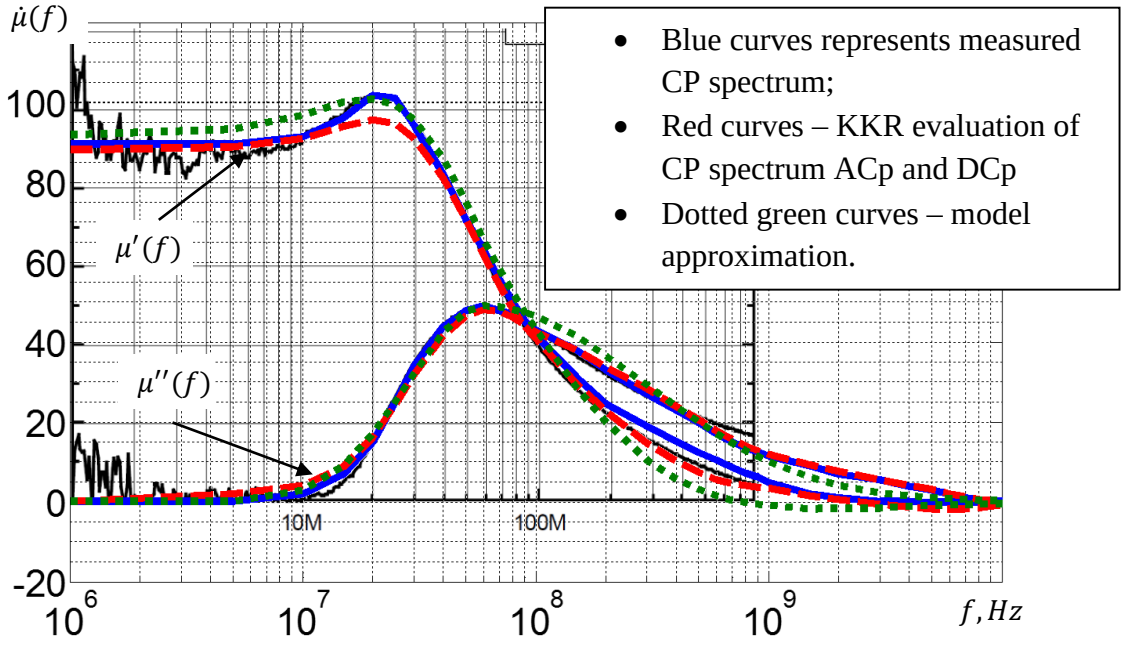

Figure 3.6 Analysis of 3M AB5016RF [102] ferrite spectrum.

The other publication, provided by Islam R. [63], presented the confusing data on $Ni_{0.55}Zn_{0.45}Fe_2O_4$ ferrite CIP spectra measured within different temperatures. According to (Fig. 4, Fig. 3 in [63]) – ACp has pronounced increase of amplitude at lower frequencies (red curve in Fig. 3.7), but the DCp does not represent any resonance attributes at these frequencies, instead – stays linear. The analysis of these curves with help of Kramers-Kronig relations proved the incorrectness of the experimental ACp low frequency data (Fig. 3.7). Though the measured frequency range in [63] was not enough to correctly apply the KKR (the end frequency is represented with 12 kHz). So for evaluation of imaginary part (dashed green line) – DCp (solid blue line) was prolonged till 5 MHz, the red line represents the measured ACp data. Additional figures from [63] can be found in Appendix 4, Fig. A4.1, Fig. A4.2.

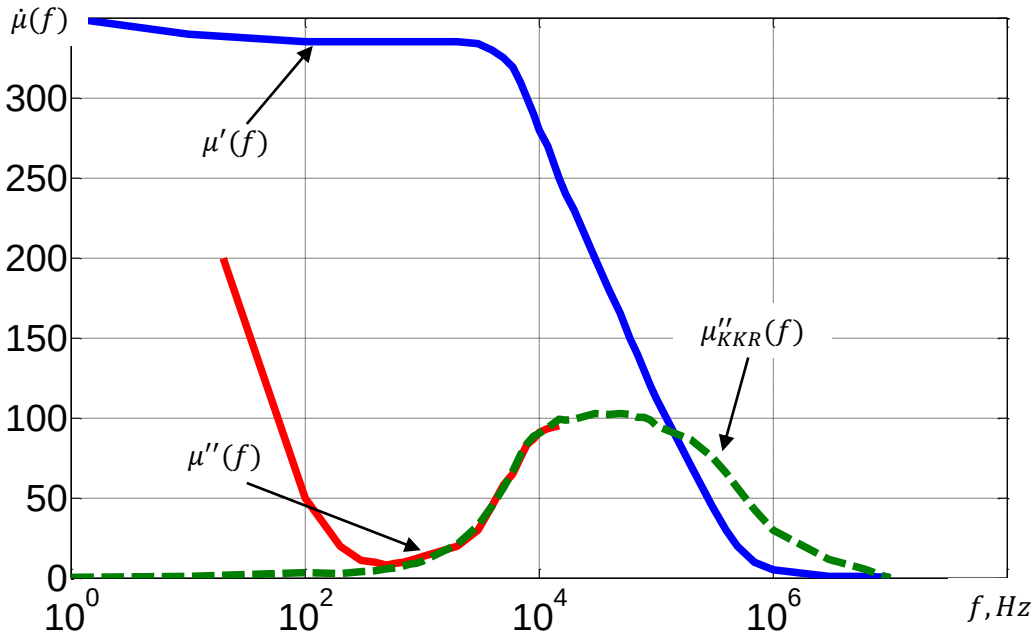

Figure 3.7 Permeability of spectra of $Ni_{0.55}Zn_{0.45}Fe_2O_4$ ferrite, adopted from [63, Fig. 3, Fig. 4, measured at T = 1250 °C]

All these examples prove that application of Kramers-Kronig relations on experimental data provides information on quality of measured data, points to confusing results and helps to estimate doubtful, noisy data. The combined use of the model and KKR, though, proved to be the good analytical, numerical instrument for evaluation of noisy CIP data. The method of the evaluation of noisy complex permeability data is reliable and indispensible in cases when studied data is not fully presented.

3.3 Decomposition of spectra

Within this research the decomposition of CIP spectra is intended for practical sake – to distinguish the role of DW and NSR components in total spectrum that is hard to measure directly. For this purpose as the tools there are used: principally KKR, but practically for DW component the model (subsection 2.1.9) accounting for grain size distribution effects in PF.

For example: the spectra measured by J. Slama, et. all. in [143], represents ACp with two resonances: domain wall resonance near $f = 90\ MHz$ and spin resonance near $f = 1.6\ GHz$, (Fig. 3.8). To obtain more detailed data on how both resonances contribute to whole CIP we can make the spectra decomposition.

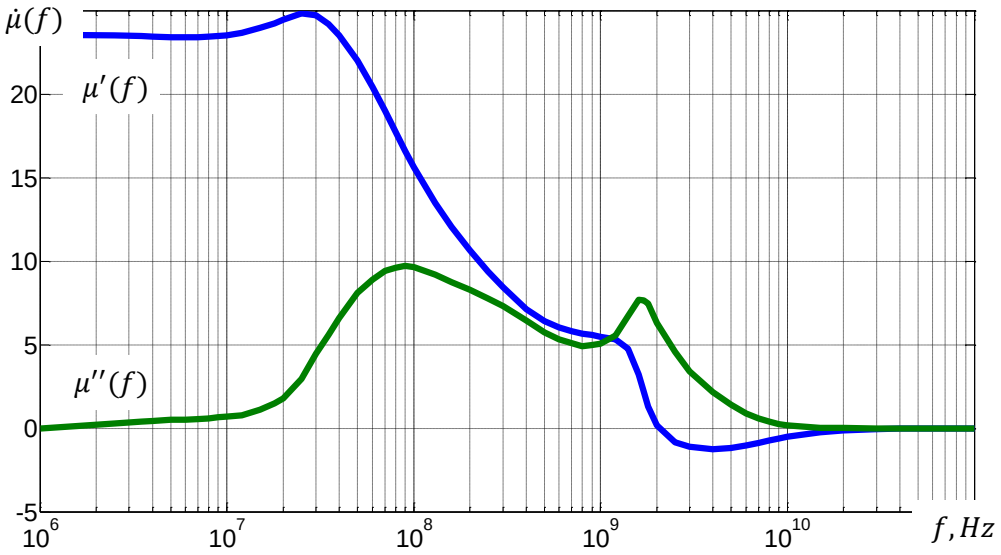

Figure 3.8. Broadband NiZn ferrite spectrum [143]

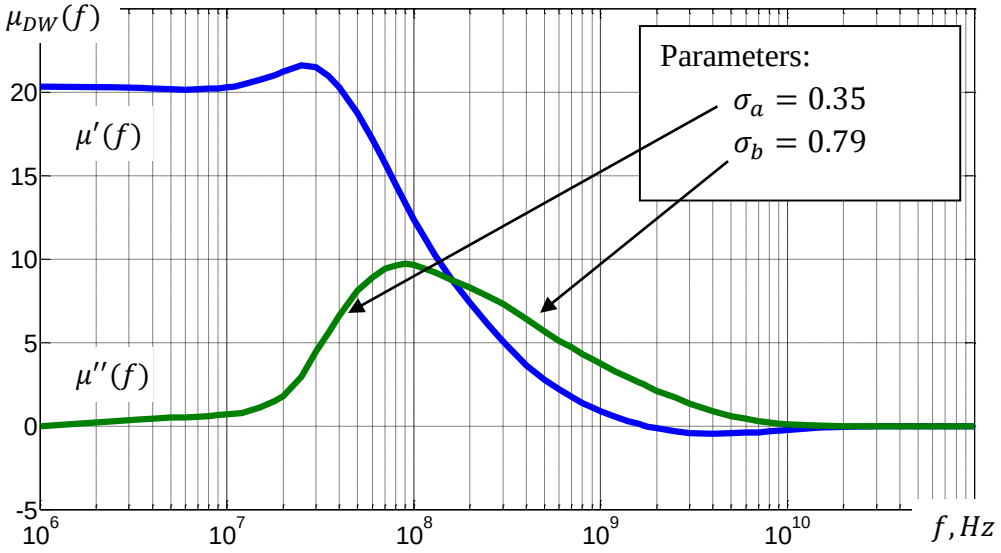

Figure 3.9 Contribution of DW component to the measured [143] CIP spectrum.

For correct decomposition of spectra we can use the help of a model (§ 2.1.8) based on account of microstructure. Applying it to DW resonance curve we obtain the spectra without spin resonance (Fig. 3.9), and then with help of Kramers-Kronig relations we construct the real part of it. Identically we can get the real part of spin resonance (Fig. 3.10).

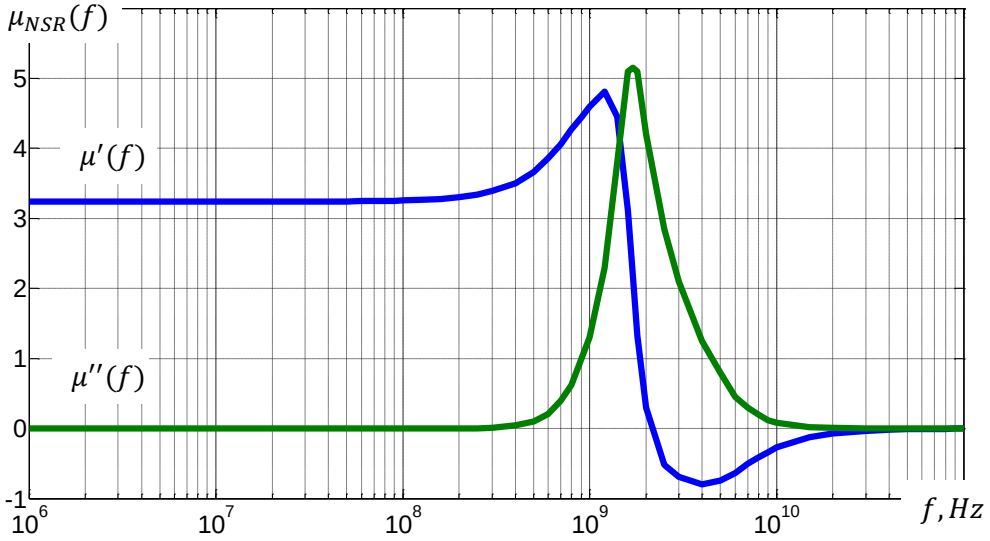

Figure 3.10. Contribution of spin component to the total spectrum in Fig. 3.14 [143]

Large set of data provided in [53] (Fig. 3.8) for YIG ferrite is a good field for the evaluation of PF magnetic spectra components contribution into complex permeability spectra.

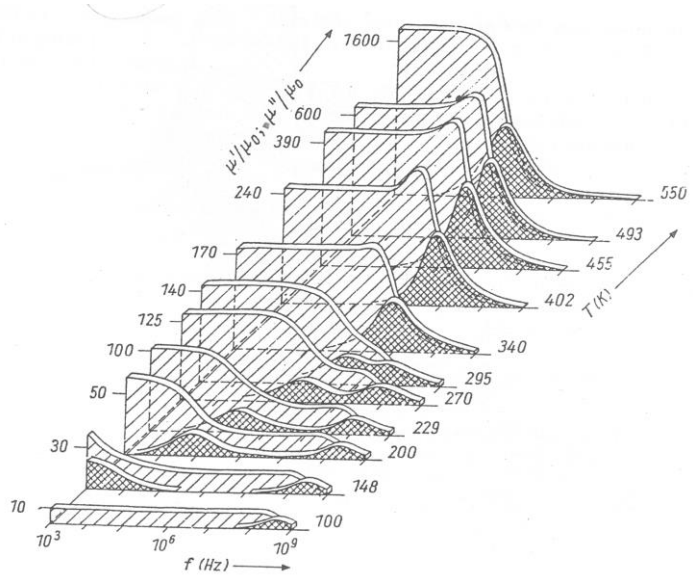

Figure 3.8. Wide range (temperature and frequency) spectra
for an iron-deficient YIG sample [53].

On the following figures using the original data (presented by blue solid line), model application (dashed green line) in coupe with KKR (red dotted curve – evaluation of spectra quality), we can evaluate the DW ACp component contribution.

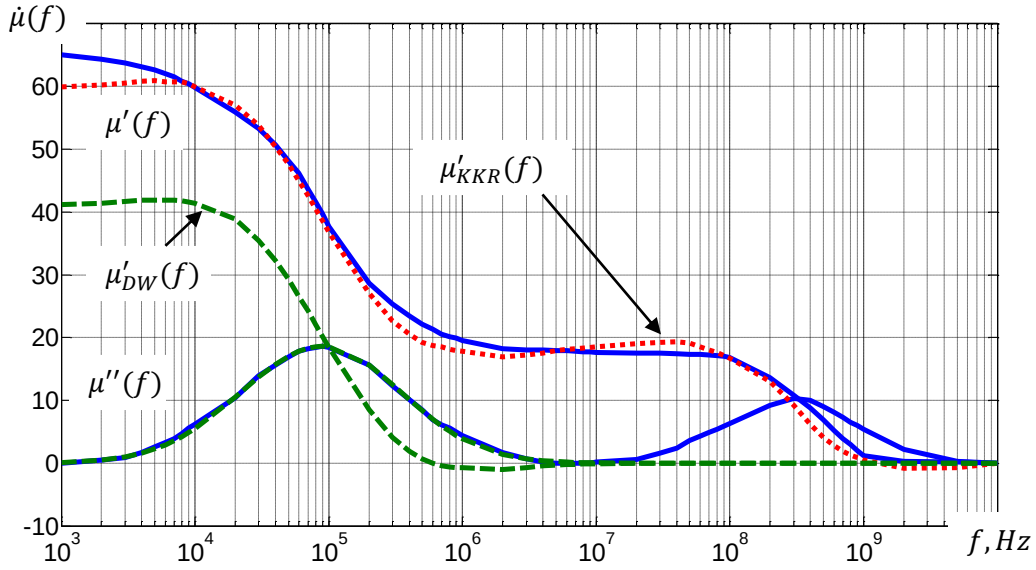

Figure 3.9. DW contribution to whole spectrum ofYIG sample [53] at T = 200 K, $\sigma_a = 0.6$, $\sigma_b = 0.6$ $\sigma_{av} = 0.6$, $\mu'_{exp} = 65$, $\mu'_{DW} = 41$ (63 %)

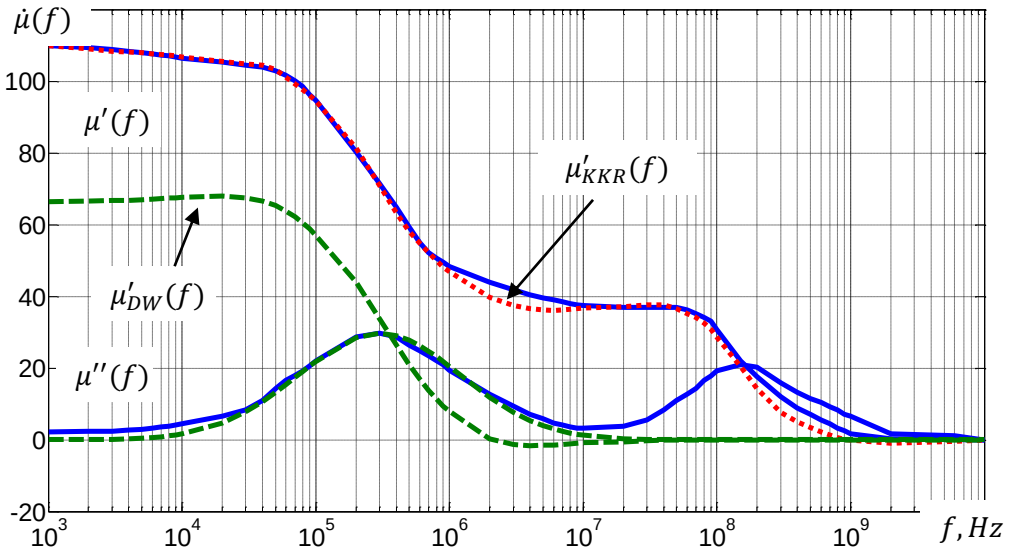

Figure 3.10. DW contribution to whole spectrum of YIG sample [53] at T = 229 K, $\sigma_a = 0.61$, $\sigma_b = 0.61$ $\sigma_{av} = 0.61$, $\mu'_{exp} = 110$, $\mu'_{DW} = 66.5$ (60.4 %)

Taking for analysis two CIP spectra with distinctly shown DW and NSR regions (Fig. 3.9, 3.10) we can see that the DW component contribution to whole CIP spectrum is about 60 %. Applying the model to the DW component gave almost the same value of $\sigma_{av} \approx 0.6$, which signals of rather symmetrical DCp and of good quality of microstructure.

The results of spectra decomposition showed, that:

- it is possible to distinguish for the contribution of DW and NSR components to whole spectrum;
- real values of ACp maximums and corresponding frequencies can be precised with decomposition (e. g. in case of close DW and NSR absorptions localization)

Thus, the decomposition of spectra into components allows to estimate the component contribution to CIP, which is hard to measure directly. Also, using inverse process (as it is showed in Fig. 6.4) we can estimate missed component contribution (in this case the NSR) on the whole spectrum and thus evaluate measured spectra quality. The study of low permeability spectrum (Fig. 3.8) proves, that contribution of NSR part to $\mu(0)$ is less than 20 % (in the case of high permeability CIP spectrum, the NSR contribution is even less, in some cases it can be ignored, e. g., fig. 2.6).

4 STUDY OF MICROSTRUCTURE OF SAMPLES USED; MST ASPECTS FOR PF OF SMPS

Mathematical statistical methods are used for describing of microstructure parameters of PF [89, 124]. Commonly for randomly taken data of some parameter, there can be defined mean arithmetical value, standard deviation, dispersion and others. Microstructure can be characterized by some parameter (e. g., grain diameter) or value (e. g., number of grains in volume). The most complete characterization can be achieved with probability density distribution function of these parameters or values. The diameters of globular grains have log-normal distribution function [187], and from this function we can easily determine the statistical parameters of MST.

The microstructure of ferrites is three dimensional, but it is hard to obtain 3D characteristics. Nevertheless, this 3D structure is possible to study by the use of either intersect planes or intersect lines, thus obtaining 2D or 1D characteristics respectively. Between all these different dimension approaches exists strong mathematical relations. The basis of stereometric method of describing the MST parameters lies within 7 strong mathematical relations, which describe phases, grain boundaries, number of grains, etc. in alloy [187]. Our interest lies in obtaining of statistical parameters of MST: D_a – average diameter of grain (in statistical analysis it will be marked as $\overline{D}$), $\sigma(D)$ – standard deviation of grain diameter and $\sigma(lnD)$ standard deviation of diameter logarithm.

There are developed many statistical methods for microstructure analysis: Jeffries' planimetric procedure, Heyn linear intercept procedure, E. Shail's arithmetic series method, A. G. Spector's chords method, S. A. Saltikov's enlarged index method, a. o. [12, 187].

Along with manual calculation there are developed automatic measurement methods with image analyzers. But automatic measurement greatly depends on micrograph quality, quality of polished surface, microstructure's complicity. Nevertheless, with developing of image processing there are developed new methods in quantitative analysis of the image [59, 165], which claim that statistical confidence degree can be achieved up to 95 % after image processing (Fig. 4.1). Adjusting the quality of the image of micrograph and adding corresponding image processing algorithm there can be achieved that most of grain boundaries are visible (Fig. 4.1) [165]. Use of these methods can, e. g., improve the correctness of processing of complicated, multi-phased, fine-grained microstructures [33].

a)

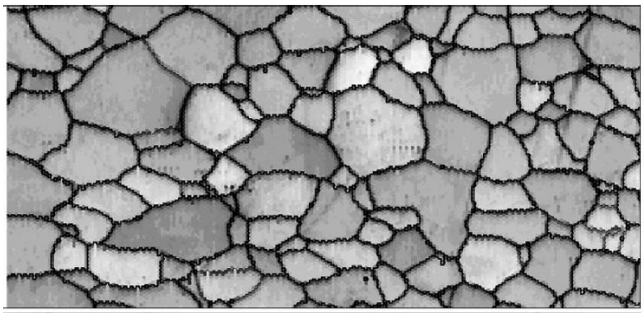

b)

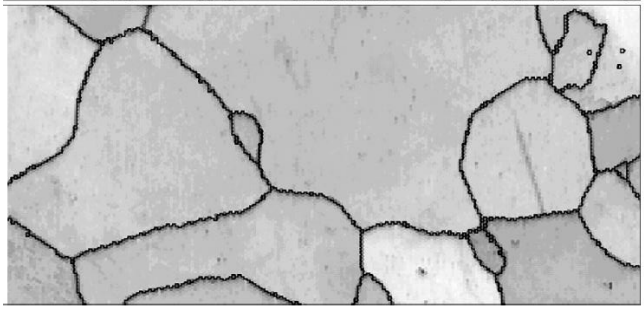

Figure 4.1. Grain boundaries selection example *a)* and closer view on grain boundary selection quality, *b)* [165].

The less time-consuming and sufficiently precise method assumed to be the Saltikov's enlarged indexes method [187, 193]. Therefore due to availability of this method, the analysis of MST of the samples studied in this work will be done basing on the use of it. This method is based on stereometric relations, which can describe grain distribution in three-dimensional space by using of micrographs. Thus we need to decrypt the micrograph, if it is not in excellent condition (therefore manual characterization methods have advantage instead of automatic image processing methods, because scratches that can be seen by an eye – can be recognized as grain boundaries with automatic methods). Using this method there is no need of differential estimation of measurement of diameters or chords of individual intersects as it is in other methods, and there is no need of separation of grains into groups by their sizes, which is most laborious process in quantitative microanalysis.

4.1 Statistical microstructural parameters of studied ferrites

In order to obtain micrographs of studied ferrite samples with seen grain boundaries, the surface of studied ferrite samples was polished with fine abrasives, and then etched. NiZn ferrites were etched in orthophosphoric acid, MnZn ferrites – in hydrofluoric acid. Temperature, etching time and acid concentration was selected individually for each ferrite group (average etching time for MnZn ferrite – 5 minutes in 60 °C acid, for NiZn ferrite – 10 minutes in 100 °C acid). The microstructure photos obtained with scanning electronic microscope (SEM) analysis were taken on the surface of split ferrite material.

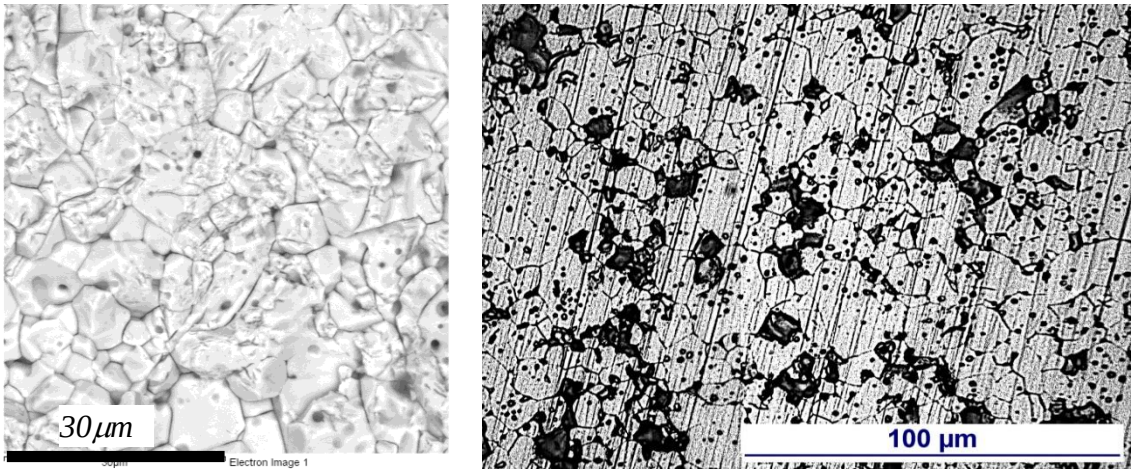

a) b)

Fig. 4.2. Micrographs for NiZn ferrite: a) – SEM image, b) – etched surface.

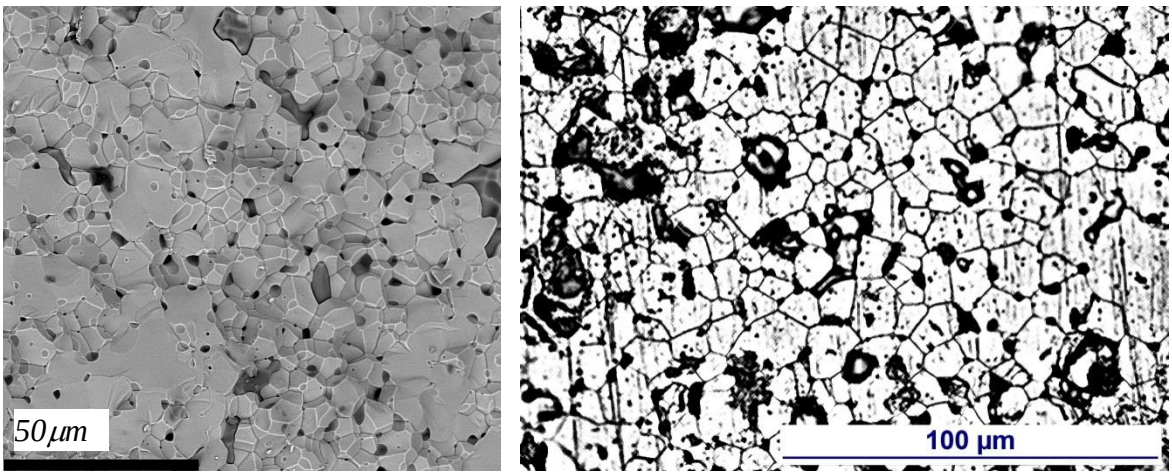

a) b)

Fig. 4.3. Micrographs for MnZn ferrite (T37): a) – SEM image, b) – etched surface.

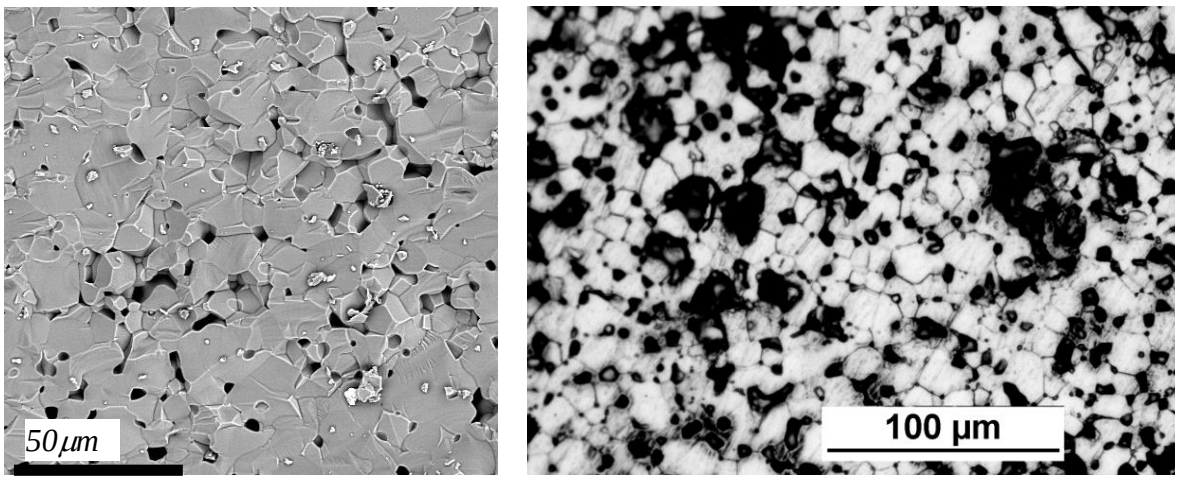

a) b)

Fig. 4.4. Micrographs for MnZn ferrite (6000HM-1): a) – SEM image, b) – etched surface.

As we can see from Figs. 4.2, 4.3, 4.4: it is hard to obtain excellent quality of polished surface due to crumbled grains and pores. The micrograph decryption is based on finding amount, dimensions of crumbled grains and pores. Then we can construct the lognormal distribution function [185]:

$$N_i = \frac{N\Delta}{\sqrt{2\pi}D_i\sigma_{\ln D}} e^{\left(-\frac{\left(\ln D_i - \overline{\ln D}\right)^2}{2\sigma^2_{\ln D}}\right)}, \quad (4.1)$$

where N_i is grain number in *i*-th group in 1 mm^3 of material; D_i – grain number in *i*-th group; Δ – measuring step, mm; $\overline{D} = n/N$ – average diameter of grain;

$$\overline{\ln D} = \ln \overline{D} - 0{,}5\sigma^2_{\ln D} \quad (4.2)$$

grain diameter average logarithm;

$$\sigma_{\ln D} = \sqrt{\sigma^2_{\ln D}} \quad (4.3)$$

standard deviation of grain diameter logarithm, where $\sigma^2_{\ln D} = \ln\left[1 + \frac{\sigma_D^2}{\left(\overline{D}\right)^2}\right]$;

$$\sigma_D = \sqrt{\frac{\sum S}{\pi N} - \left(\overline{D}\right)^2} \quad (4.4)$$

standard deviation of grain diameter;

$$N = 6\pi^2\left(\frac{n}{\sum S}\right)^3 \sum V \quad (4.5)$$

the number of grains in 1 mm^3 of material, where cumulative volume of grains in 1 mm^3 of material $\sum V = 1$ – because we have single phase structure [181].

The characteristics that are done directly from micrographs are:

specific surface area – $\sum S = 2m$, where $m = g_{av}/l_{av}$ – the number of intersections per unit length of the secant, g_{av} – average number of grain boundaries that are found on the one secant, l_{av} – average number of the secants in micrograph.

The grain number in one micrograph: $n = x + 0{,}5y + 0{,}25z$, where *x* stands for whole grains, *y* – grains that are found on the edges of the micrograph, *z* – grains that are found on the corners of the micrograph (Fig. 4.5).

To obtain reliable results for microstructural parameters the micrographs were taken from different parts of sample. Data obtained from all the micrographs was used for final calculations of statistical MST parameters ($\bar{D}, \sigma_D, \sigma_{lnD}$).

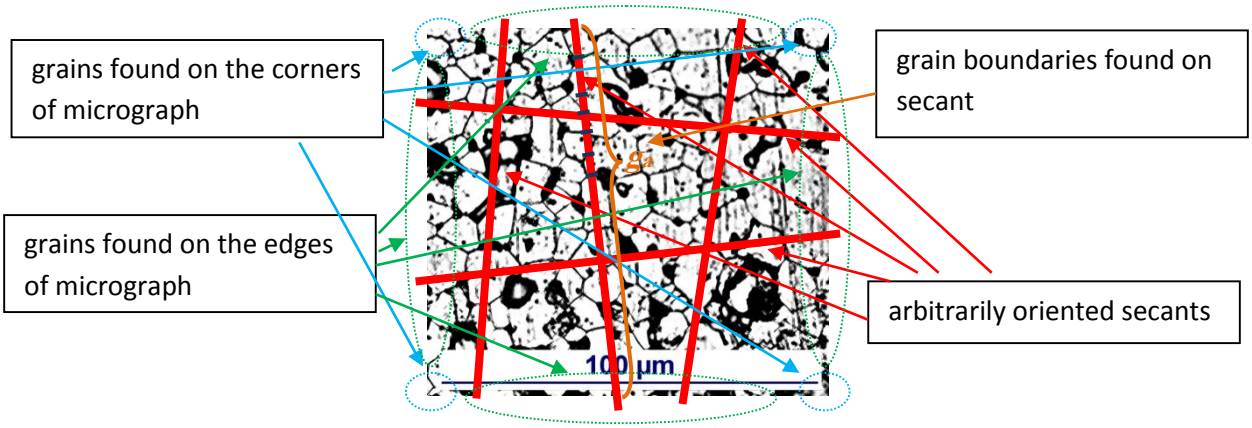

Fig. 4.5. Example of obtaining micrograph-obtained characteristics for MnZn ferrite (T37) using Saltikov's method.

The obtained data shows that microstructure – aggregation of polycrystal grains is that of normal grain growth for all of the ferrite samples (because σ_{lnD} tend to 0.5 as it is for MST with lognormal grain distribution [64, 89]). Nevertheless, there is clearly noticeable from micrographs, that all of ferrites have defects within numerous of grains.

Table 4.1. Statistical parameters of studied ferrite samples.

Group	№	D, μm	σ_{lnD}
NiZn, 4S60	A1	7.9	0.55
	A2	7.9	0.55
	A3	7.9	0.55
	A4	7.9	0.55
MnZn, 6000HM1	B1	12.9	0.53
	B2	12.9	0.53
	B3	12.9	0.53
	B4	12.9	0.53
	B5	12.9	0.53
MnZn, T37	C1	10.7	0.53
	C2	12.7	0.52
	C3	13.4	0.53

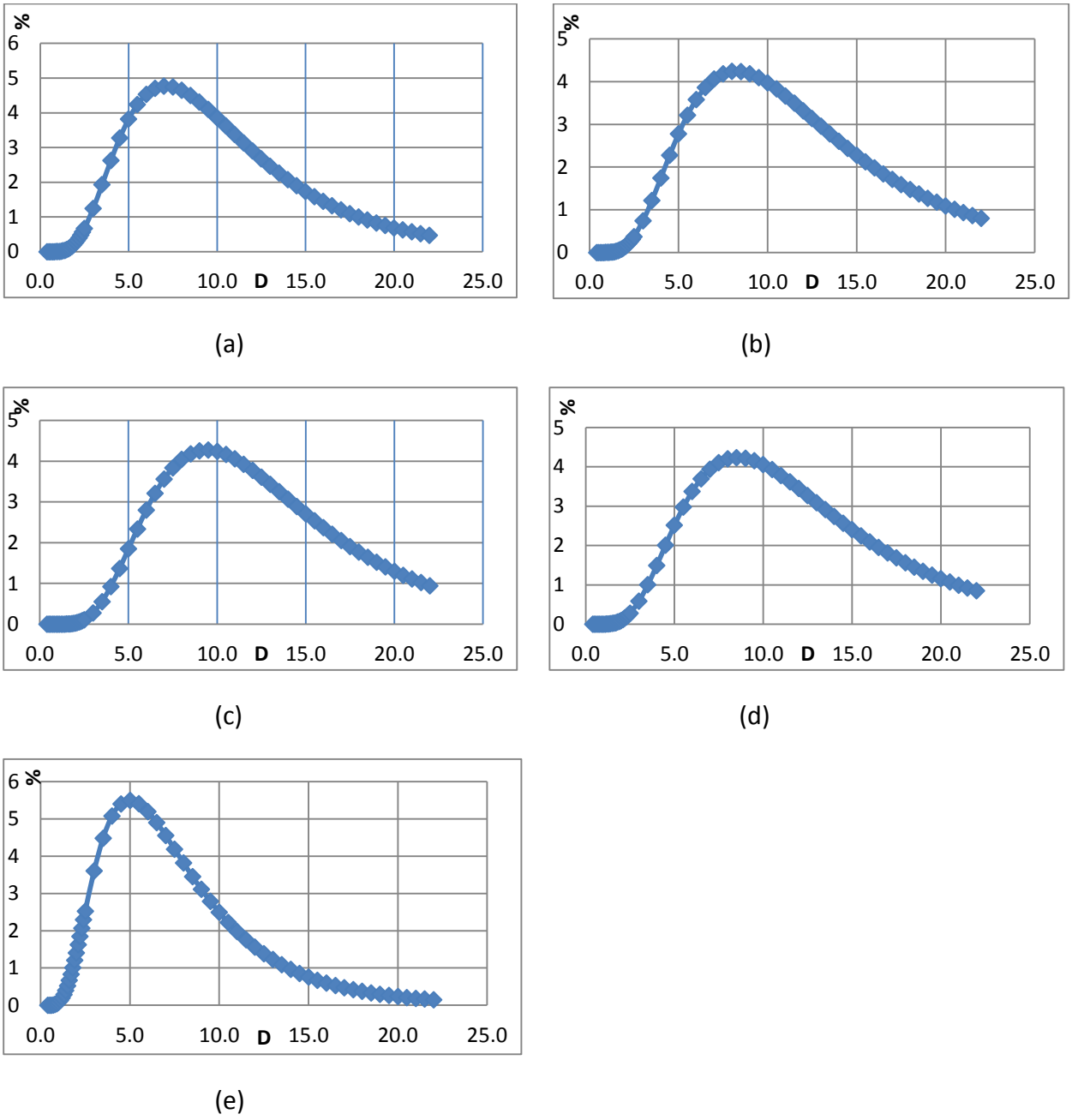

Fig.4.6. Grain distribution function for MnZn C1 (a), C2 (b), C3 (c) samples, MnZn B1...5 (d) samples, NiZn A1..4 (e) samples.

The grain size probability distribution functions for different types of ferrites – Fig. 4.6 provides us the information about grain size distribution in different ferrite samples. Curves *a...c* on Fig. 4.6 provides information on industrially made ferrite cores; it is clearly noticeable, that larger core dimensions results in larger average grain size D_a of the core. The Fig. 4.6, *d* and *e* curves, characterize grain distribution in cutted ferrite cores from ferrite tiles, therefore it is the same for all studied PF in these groups, but the character of distribution is different for NiZn and MnZn ferrite groups.

Thus, studied samples show normal, homogenous MST (Fig. 2.13) that obeys (2.28) and will be used for examine of CIP spectra. The absence of such inhomogenities in microstructure of studied samples as well as $\sigma(lnD)$ value close to 0.5 allows us to assume that the MST is that of normal grain growth.

4.2 Preparing of samples with similar microstructure

For the research of CIP of the samples we need to make series of experiments on each researched ferrite group. The quality of MST of samples points to quality of material.

In the following investigations of correlation of MST and CIP spectra it is proposed to resolve two problems:

1) dependence of CIP spectra on different geometric dimensions under fixed MST;
2) correlation of definite CIP spectrum with the MST of sample.

In the first case there is need for samples of similar composition and MST but of different geometries. To fulfill this ferrite cores should be cutted off from the same ferrite tile, that had same preparing and sintering conditions within whole tile area. Similarity of MST (as a grain aggregate characteristics of which are random variables) can be described by grain size distribution function, grain average diameter D_a, and standard deviation $\sigma(D)$.

Generally, ferrite cutting methods are: machine cutting (preferably with diamond disk, because the ferrite is brittle and can brake if the sharpness is not enough) aided with coolant, laser or plasma cutting (lasers and plasma cutting leaves a burnouts or melting of material at the cut edge, also performs with high temperature), and waterjet cutting.

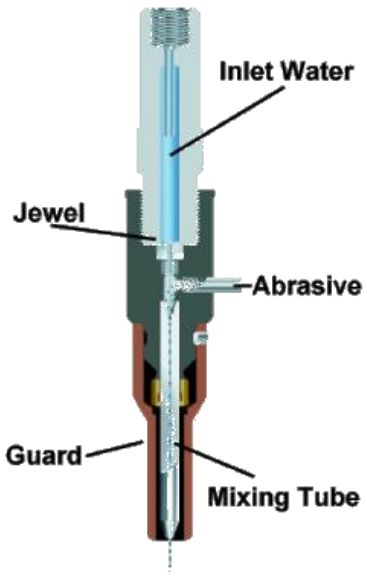

Figure 4.7. Water Jet cutter head [161]

Tested ferrite cores were cut off from single ferrite tile with waterjet technique. Waterjet cutting was selected due to it benefits in relation to other techniques (mechanical, laser or plasma cutting) [77, 158, 161]:

- cutting is performed without overheating;
- width of the cut (kerf) is relatively thin (for abrasive cutting – 0.508 mm to 1.27 mm, for non abrasive cutting – 0.076 mm to 0.178 mm) which minimizes the loss of material;
- does not add burnouts of the material and does not add material melting;

- does not add undesired impurity (water under high pressure (up to 4100 bar) is mixed with abrasives (in our case – garnet) and does not leave remnants on the surface);
- high cutting speed;
- can make every desired form of core.

The only problem of this method is to find the water jet pressure level high enough to cut through ferrite tile, but not to break the material.

Figure 4.8 Surface of the cutted ferrite sample

There were produced two groups of ferrite cores with different inner/outer diameter (ID/OD) and cross section area (A) for experiments. First group is cut off from Ferroxcube 4S60 ferrite tiles [40], second group is cut off from Nevaferrit – 6000HM-1 ferrite tiles [112]. The quality of cutted surface is shown on Fig. 4.8.

Table 4.2. Parameters of studied samples

Group	№	Dimensions, mm	A, mm^2	$\mu(0)$	$\mu(0)_{exp}$
	A1	R12x8x6	12	2000	2200
NiZn,	A2	R20x10x6	30	2000	2100
4S60 [36]	A3	R31.5x20.5x6	33	2000	2125
	A4	R40x23.5x6	51	2000	2140
	B1	R10x4.3x10	28.5	6000	6750
MnZn,	B2	R20x9.1x10	54.5	6000	6530
6000HM1	B3	R25x12x10	65	6000	6650
[105]	B4	R30x14.3x10	78.5	6000	6850
	B5	R33x10x10	115	6000	6523

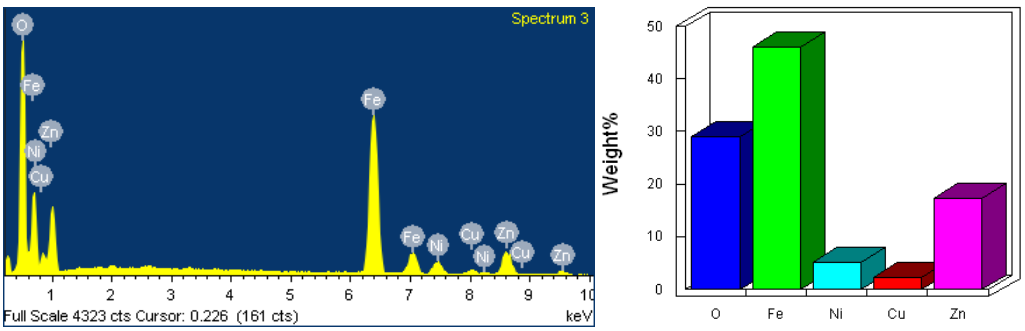

Figure 4.9. Elemental analysis of NiZn samples [71]

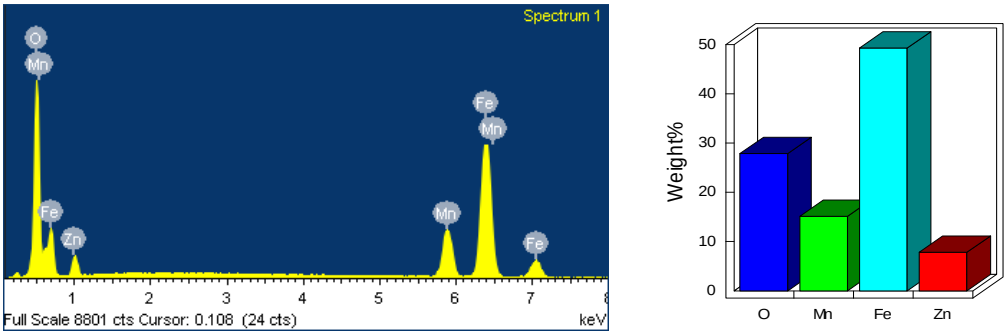

Figure 4.10. Elemental analysis of MnZn samples [71]

Since the abrasives of cutting may contaminate the ferrite, from different spots of it the elemental composition (it was assessed by energy dispersive X-ray spectrometry: ESD, Oxford Instruments 7378, Fig. 4.9 and Fig. 4.10) and RAMAN spectra (recorded on "Nanofinder – S" using the 532 nm excitation line; Fig. 4.6, Fig. 4.7).

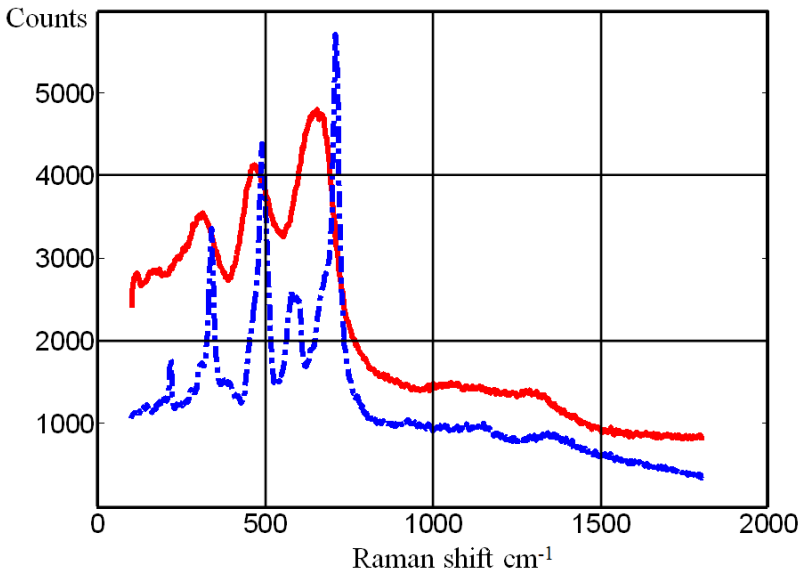

Fig. 4.11 RAMAN spectra of NiZn ferrite [71] (red-polycrystal and blue – single crystal for reference)

In reality the elements analysis didn't reveal any appreciable contamination, rather – the cut surface of ferrite cores were clean. Thus, the cutting technique was chosen properly.

The RAMAN spectroscopy is the powerful tool for revealing the structural properties of materials [154] (including oxides [4]). The properties of RAMAN spectrum can reveal the quality of material. For instance – the spectrum of NiZn single crystal (Fig. 4.11) has sharp peaks (i. e. good quality of the material); but broader width and slight frequency shift of RAMAN peaks for NiZn as polycrystal (Fig. 4.11) signals about sufficient level of defects in the MST.

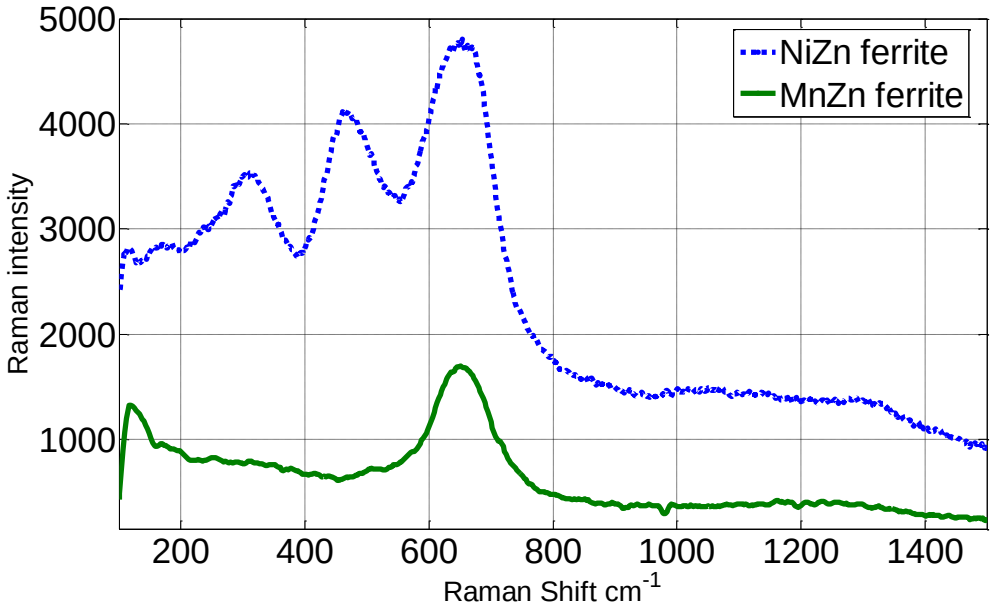

Fig. 4.12 RAMAN spectra of MnZn and NiZn PF

The study of Zn ferrites in [150] revealed that observation of broad maximum at around 680 cm^{-1} can be the result of coexistence of FeO_4 and ZnO_4 groups (as it is also seen on the RAMAN spectra of NiZn and MnZn ferrites (Fig. 4.12)). The peaks at around 450 cm^{-1} and 330 cm^{-1} (Fig. 4.7, NiZn ferrite) correspond to that of $NiFe_2O_4$ bulk ferrite [4]. The identical picture lies with the MnZn ferrite (Fig. 4.12): the peak at around 680 cm^{-1} corresponds to that of FeO_4 and ZnO_4 groups [150]; the ill-defined maximum at around 350 cm^{-1} provides information about identical Zn and Mn concentration (or slightly higher Mn concentration) in MnZn compound [154]. Nevertheless broad width of peaks signals about some defects in the microstructure.

Therefore we can assume that Raman spectra of NiZn and MnZn ferrites are taken properly, yet the material itself is not of rather good quality; still there are no traces of contamination of these materials.

4.3 Role of microstructure in magnetic power loss of SMPS

From the very outset acceptance of SMPS in electronics (at 70s and 80s of the past century) efforts are underway to find the magnetic materials that are best suited for them – first of all with the lowest power loss since low magnetic loss is the most important item for improving power supply overall efficiency [85]. It turns out that the most appropriate material at frequencies (0.5...1...) MHz are MnZn ferrites, the power loss of which has been possible to decrease continuously (Fig. 4.13, [85]) as a consequence of lot of performed studies (mainly empirical). The studies led to different conclusions, e. g., about needed quality of raw materials, typical compositions, additives, processing technologies, and microstructure.

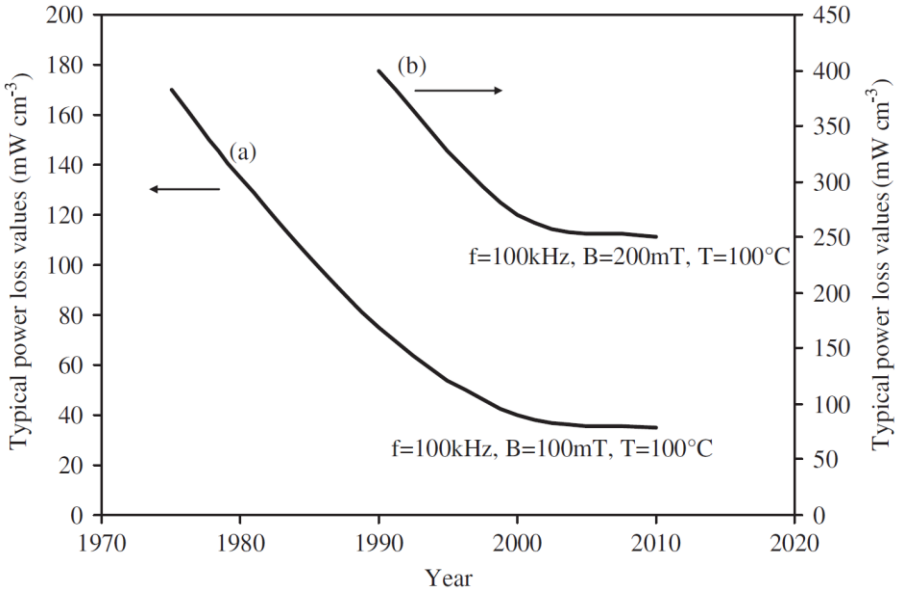

Fig. 4.13 Progress made in MnZn ferrite power loss at (a) 100 kHz, 100 mT, 100 °C and (b) 100 kHz, 200 mT, 100 °C from their development untill today [85].

As for microstructure, generally it is pointed out on its important role (especially on significance of average grain size D_a; sometimes on distribution of grain sizes as well [133]), but on the whole the guidelines nevertheless are obscure. Thus, in [122] it is stated that eddy current loss P_e and total one P_{tot} decreases while hysteresis loss P_h increases with a decrease of D_a (at frequencies $f > 500\ kHz$ and $D_a > 5\ \mu m$); in [49] is noted that optimal D_a at $f = 100\ kHz$ is near $6\ \mu m$ (when there is only intergrain porosity, contrary to the case of greater ones, e. g., $D_a \approx 9\ \mu m$, when intragrain defects clearly appear, Fig. 2.16); in [20] it is shown, that Steinmetz coefficients for smaller D_a ferrites are greater than for higher ones; the results for newly developed ferrite 6H40 of FDK company [101] gives the loss minimum near $D_a \approx 16\ \mu m$ (although the experimental data are highly scattered, Fig. 4.14). As the general

agreement to this broad spectrum of experimental observations is that the hysteresis loss is dominating at lower frequencies (typically up to *200 kHz* [85])but at higher ones both eddy current and residual ones, because of forced need for considerable lowering of flux density B_m (to maintain P_{tot} at acceptable level).

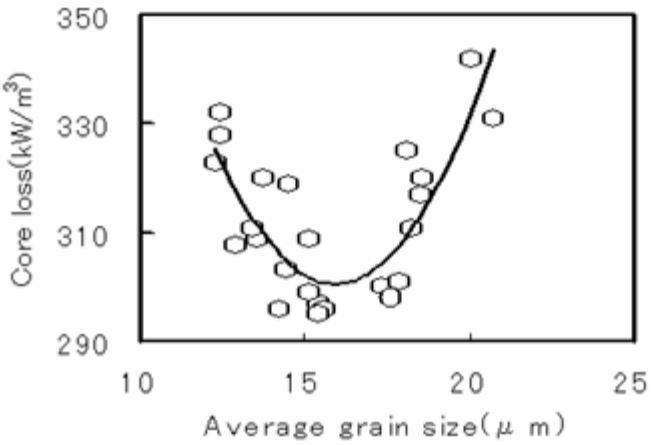

Fig. 4.14 Relationship between core loss and grain size of MnZn ferrites (100 kHz, 200 mT, 100 °C) [101]

In view of the fact that outcomes in relation to the role of microstructure on loss are rather indefinite, an effort can be performed to use Eq. 2.17 for theoretical estimation of loss. Consequently, in the case of high frequencies and low fields Eq. 2.17 is presented as:

$$p = \left[\left(\mu''(f)/\mu'(f)\right)/\mu''(f)/\mu_0\mu'(f)\right]\pi f B_m^2 \qquad (4.6)$$

If the frequency dependence of $\dot{\mu}(f)$ in rough approximation is presented by simple relaxation dependence (Eq. 2.25), then $\mu''(f)/\mu'(f) = f/f_u$ and $\mu'(f) = \mu(0)/[1 + (f/f_u)^2]$, where $f_u = 1/\tau$ is the relaxation frequency and $\mu(0) = const \cdot D_a$. Substitution of these dependencies into Eq. 4.6 gives:

$$p = \frac{(f/f_u)[1+(f/f_u)^2]}{\mu_0 \cdot const \cdot D_a}\pi f B_m^2. \qquad (4.7)$$

Taking into account that usually $f \ll f_u$, that for f_u there principally may be at least two possibilities (subsection 2.1.8.3): $f_u \propto 1/D_a^2$ or $f_u \propto 1/D_a$, from Eq. 4.7 follows (with a precision to constant multiplier):

$$p \propto D_a f^2 B_m^2 \text{ or } p \propto f^2 B_m^2. \qquad (4.8)$$

At least the first of these relations is in agreement with aforementioned experimental data. On the whole, the relations show that principally there is the way leading from complex permeability spectra to Steinmetz type relations.

5 MEASUREMENTS OF FERRITE MAGNETIC AND DIELECTRIC PROPERTIES

All items about CIP experimental data are of primary importance for this investigation, since they are forming the basis for accomplishing the main task – practical evaluation of suitability of model "accounting for grain size distribution effects" for presentation of CIP. The data used are of two kinds: firstly, the ones following from our measurement on our samples, and, secondly, the data published (from different laboratories all over the world). Such broad experimental basis (the quality of which is verified) provides strong evidence for making our conclusions.

5.1 Measurement of CIP

For the correct implementation of power supply HF components we need to know their real characteristics. Often we need to compare component actual parameters to the datasheets. The analysis involves accurate measurements of different currents and voltages, ratios of incident and reflected signals etc. For a complete component description (analysis) and, also, for the best metering device calibration (to perform vector error correction), we need the data of both magnitude and phase of a signal. To completely characterize an unknown component we must make measurements under desired conditions and then calculate needed parameters, thus, the parameters must be universal. For low frequency signals H, Y and Z parameters are used; all of them require short or open circuit to be applied for measurements. Open or short circuit application to high frequencies is rather difficult task; also the device can malfunction if it is not applied correctly. There were developed a parameters that do not have the drawbacks of low frequency parameters – the scattering or S-parameters [1, 2]. The S-parameters are defined in terms of travelling waves, and there is no need of open or short circuit to be applied during measurements as it was with H, Y or Z parameters. Also S-parameters can be converted to any of other needed parameters.

We are dealing with magnetic components in this work. So, according to [151] the material permeability is the best parameter in describing the magnetic material's physical properties (as it directly connects B and H, Eq. (2.18)). The CIP measurements are performed for a long time period already. So there are a bunch of classical methods (e. g. phase meters, LRC bridges measurements, etc. [1, 97, 193]) and developed some new ones (like vector network analyzer (VNA) measurements [1, 2, 58, 59]). All of the developed measuring methods have their cons and pros in measuring and calculations. For the medium and high testing frequency range it is suggested to use a toroidal sample (despite the harsh winding

procedure) [151]. The reasons are several: toroid forms a closed loop, so the losses are minimal and it represents the standard core shape for inductors and transformers working in this frequency range [151]. For the medium frequency range the use of impedance analyzers and phase-shift detectors (phase meters) is suggested [151]. For the higher frequencies it is suggested to use the shortened coaxial line. Both methods are successfully used in this work.

5.2 Parameters of two port network

To analyze the sample with *mostly* unknown parameters it is suggested [2, 3, 58, 59] to use a *N*-pole model which is described by square matrix of complex numbers. In this work we are mainly using 2-pole network model, so parameters will be described to 2-pole network model. The 2-pole network is an electrical network (often a "black box") with two pairs of terminals for connection. Two terminals form a port when the electric current entering one terminal is equal to the current emerging from the other. Usually, the input port is called port1 and output port is called port 2 (Fig. 5.1).

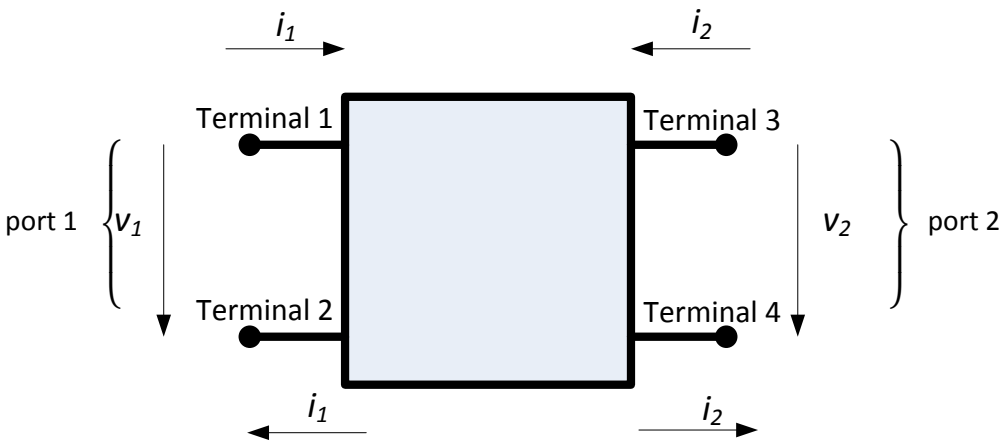

Figure 5.1. Two port network

In the Fig. 5.1, i_1, v_1 and i_2, v_2 are input and output currents and voltages, respectively. It is assumed that the linear 2-pole network contains no independent sources of energy and that the circuit is initially at rest (no stored energy). Furthermore, any controlled sources within the linear 2-pole network cannot depend on variables that are outside the circuit. Describing the 2-pole network with a matrix of numbers gives us a way to describe a "black box" without calculating all inner voltages and currents in the network.

There are described ***z-parameters***, ***y-parameters***, ***h-parameters***, ***g-parameters***, ***ABCD-parameters*** and ***s-parameters*** matrix. The *z, y, h, g,* and *ABCD parameters* are defined by voltages and currents at 2-pole network ports, as V_1 – voltage across port 1, I_1 – currents into

port 1, V_2 – voltage across port 2, I_2 – current into port 2. The s-parameters are described by travelling waves that are scattered or reflected when a network is inserted into transmission line with characteristic impedance *Z*. The application of these parameters is defined by the need of the model used. All the parameters have their advantages and disadvantages for example: advantage of *z* parameters is that they are intuitive, easy to calculate, but requires difficult open circuit measurements, which add noise and high open-circuit capacitance at high frequencies; advantage of *y* parameters is that they are intuitive too, but requires difficult short circuit measurements, which add noise and high short-circuit inductance at high frequencies; advantage of ABCD parameters is that they are intuitive, allows easy cascading of networks, can be easily related to common circuit topologies, disadvantage – that it is difficult to measure the ABCD parameters directly, and it must be converted from another parameters.

In the RF measurements the wave quantities are commonly used [58]. Differ incident (*a*) and reflected (*b*) waves at test ports. In 1-pole network the ratio between incident and reflected wave is described by reflection coefficient Γ.

$$\Gamma = \frac{b}{a} = \frac{z-1}{z+1} \tag{5.1}$$

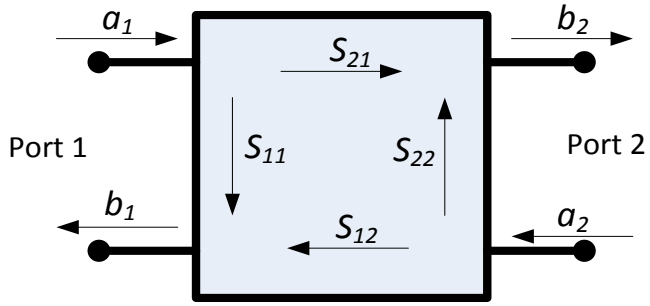

Figure 5.2. S-parameters of two port network

Reflection coefficient can be calculated by use of normalized impedance $z = {}^{Z}/_{Z_0}$, where *Z* – complex impedance of the device under test (DUT), Z_0 – the characteristic impedance (in this work it is 50 Ω). In a 2-pole network besides the reflection at two ports there are 2 additional parameters for transmission from one port to another [2, 59]. These parameters are called scatter (or scattering, s-parameters) parameters (Fig. 5.2) and for 2-pole network model in the matrix form are described as follows:

$$\begin{pmatrix} b_1 \\ b_2 \end{pmatrix} = \begin{pmatrix} S_{11} & S_{12} \\ S_{21} & S_{22} \end{pmatrix} \begin{pmatrix} a_1 \\ a_2 \end{pmatrix} \tag{5.2}$$

where $a_{1,2}$ and $b_{1,2}$ are incident and reflected waves from ports 1 and 2 respectively, S11 – input port voltage reflection coefficient (or input return loss i. e. how good the matching is in

relation to Z_0), S12 – reverse voltage gain (or isolation i. e. how much power you are getting on port 1, driving port 2), S21 – forward voltage gain (or insertion gain i. e. how much power you are getting on port 2, driving port 1), S22 – output port voltage reflection coefficient (or output return loss).

The measuring of S coefficients is performed by forward measurements (when the reflection coefficient Γ at port 2 = 0), and reverse measurements (when the reflection coefficient Γ at port 1 = 0):

$$S_{11} = \frac{b_1}{a_1}\Big|_{a_2=0};\ S_{21} = \frac{b_2}{a_1}\Big|_{a_2=0};S_{12} = \frac{b_1}{a_2}\Big|_{a_1=0};\ S_{22} = \frac{b_2}{a_2}\Big|_{a_1=0} \quad (5.3)$$

The applied termination of ports greatly influence the accuracy of S parameters. If the termination is not perfect it will result in a_1 or a_2 not being zero. For this reason we need to care about source and load match, if the source and load match is imperfect we need to use two port error correction.

Measuring at very low frequencies the wavelengths are much larger than the line, so the transmission line can be transformed to a simple wire. This approach can be used for DC or very low power measurements. In this case the wire resistance is relatively low and has no influence on low-frequency signals. The measurements do not depend of where the probe is connected to the transmission line.

Measuring at higher frequencies, wavelengths become comparable to or smaller than the length of the transmission line, and here the traveling waves or the wave quantities can be used. In comparison to other RF measurement parameters (Y parameters for example) we do not need to make the whole line short or open to perform measurements using the *s*-parameters [2]. Therefore transmission line can be terminated by different loads (matched, short-circuit and open circuit loads).

With the matched load (if the line is terminated by characteristic impedance Z_0), there will be maximum signal absorption at the load, because there will not be a reflected signal. In fact the impedances of source and of load must be complex conjugate (i. e. their resistances must be equal, and their reactances must be equal in magnitude but of opposite signs). In low-frequency or DC networks (or networks with purely resistive sources and loads) the reactances are zero, or small enough to be ignored. So, when the transmission line is terminated with its characteristic impedance, maximum power is transferred to the load. When the termination is not equal to the characteristic impedance, that part of the signal that is not absorbed by the load is reflected back to the source.

The short-circuit load reflects incident voltage wave back to source with 180 degree phase difference of an incident voltage wave. The reflected and incident waves have equal magnitudes but opposite phases.

The open-circuit load reflects incident current wave back to source with 180 degree phase difference of an incident current wave, and incident voltage wave back to source with no phase difference of an incident voltage wave, so the current at the load will be zero. The reflected and incident waves have equal magnitudes but opposite phases.

Advantage of *s*-parameters are that they can be easily measured by vector network analyzer, without open/short circuits at high frequencies. Disadvantage – the understanding of parameters is not that simple as of *z* or *y* parameters, and interpretation is difficult.

Z parameters (also known as open circuit impedance parameters since they are obtained by open-circuiting the input or output ports) are easier to understand, they are measured in ohms, Ω, (since they are obtained as voltage and current ratio), and 2-pole network can be described with *z* parameters as follows:

$$v_1 = Z_{11}i_1 + Z_{12}i_2;$$
$$v_2 = Z_{21}i_1 + Z_{22}i_2; \quad (5.4)$$

and in the matrix form:

$$\begin{bmatrix} v_1 \\ v_2 \end{bmatrix} \begin{bmatrix} Z_{11}\ Z_{12} \\ Z_{21}\ Z_{22} \end{bmatrix} \begin{bmatrix} i_1 \\ i_2 \end{bmatrix}; \quad (5.5)$$

all *Z* parameters can be found as:

$$Z_{11} = \frac{v_1}{i_1}\Big|_{i_2=0};\ Z_{21} = \frac{v_2}{i_1}\Big|_{i_2=0};\ Z_{12} = \frac{v_1}{i_2}\Big|_{i_1=0};\ Z_{22} = \frac{v_2}{i_2}\Big|_{i_1=0} \quad (5.6)$$

where Z_{11} – open circuit input impedance, Z_{12} – open circuit transfer impedance from port 1 to port 2, Z_{21} – open circuit transfer impedance from port 2 to port 1, Z_{22} – open circuit output impedance.

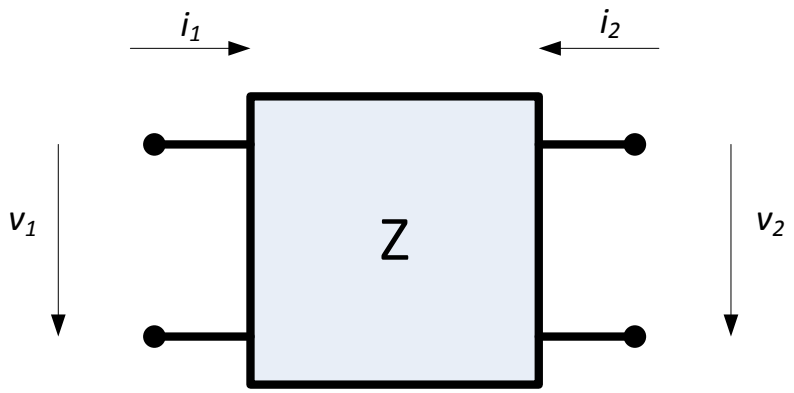

Figure 5.3. Z parameters of the network

For two port network input and output impedance is defined as:

$$Z_{in} = Z_{11} - \frac{Z_{12}Z_{21}}{Z_{22}+Z_l} \tag{5.7}$$

where Z_l is impedance of the load of the two port network;

$$Z_{out} = Z_{22} - \frac{Z_{12}Z_{21}}{Z_{11}+Z_s} \tag{5.8}$$

where Z_s is impedance of a two port network source.

The relations between the *Z* parameters and the *S* parameters of the same two port network are expressed as follows [2, 58]:

$$\begin{aligned} Z_{11} &= \frac{\left((1+S_{11})(1-S_{22})+S_{12}S_{21}\right)}{(1-S_{11})(1-S_{22})-S_{12}S_{21}}Z_0; \\ Z_{12} &= \frac{2S_{12}}{(1-S_{11})(1-S_{22})-S_{12}S_{21}}Z_0; \\ Z_{21} &= \frac{2S_{21}}{(1-S_{11})(1-S_{22})-S_{12}S_{21}}Z_0; \\ Z_{11} &= \frac{\left((1-S_{11})(1+S_{22})+S_{12}S_{21}\right)}{(1-S_{11})(1-S_{22})-S_{12}S_{21}}Z_0; \end{aligned} \tag{5.9}$$

and relations to S parameters are expressed as follows:

$$\begin{aligned} S_{11} &= \frac{(Z_{11}-Z_0)(Z_{22}+Z_0)-Z_{12}Z_{21}}{(Z_{11}+Z_0)(Z_{22}+Z_0)-Z_{12}Z_{21}}; \\ S_{12} &= \frac{2Z_{12}Z_0}{(Z_{11}+Z_0)(Z_{22}+Z_0)-Z_{12}Z_{21}}; \\ S_{21} &= \frac{2Z_{21}Z_0}{(Z_{11}+Z_0)(Z_{22}+Z_0)-Z_{12}Z_{21}}; \\ S_{11} &= \frac{(Z_{11}+Z_0)(Z_{22}-Z_0)-Z_{12}Z_{21}}{(Z_{11}+Z_0)(Z_{22}+Z_0)-Z_{12}Z_{21}}; \end{aligned} \tag{5.10}$$

5.3 Measurement methods and equipment.

There are presented many different ways of measuring CIP: waveguide techniques, coaxial line techniques, bridge techniques, etc.

In our CIP measurements we use toroidal ferrite samples with one layered evenly placed windings. We use different approaches and methods to obtain CIP data. For lower frequencies (up to 2 MHz) we use classical methods in coup with VNA (ZVR-E) help, for higher frequencies we use ZVR-E with shortened coaxial line support [193].

5.3.1 Classical measurement methods

5.3.1.1 CIP measurements using phase measurer

The phase measurer working principle uses the property of harmonic signals to determine the phase shift angle. According to which:

$$U_{\Sigma}^2 = \left(U_{in} + U_{out}\right)^2 = U_{in}^2 + U_{out}^2 + 2U_{in}U_{out}\cos\varphi \tag{5.11}$$

where U_{in} and U_{out} are input and output voltages; then phase shift angle φ :

$$\varphi = \arccos\left(\frac{U_{\Sigma}^2 - U_{in}^2 - U_{out}^2}{2U_{in}U_{out}}\right) \tag{5.12}$$

Not only harmonic signals can be summarized or subtracted, but specially shaped rectangular signals too. The essence of the method is to convert the two sinusoidal voltages into the periodic sequence of short pulses corresponding to the transition moments of these voltages through the zero with the derivatives of the same sign. The time intervals between the nearest pulses are proportional to the determined phase difference.

After the convertion the relative value of the time interval is measured (in relation to the period). Using that we can write a relation for the phase shift:

$$\varphi^\circ = 360^\circ \frac{t}{T} \tag{5.13}$$

where t is impulse width, T – period. This transformation of the phase shift in the time interval is accompanied by a random error due to the influence of noise.

5.3.1.2 Other classical measurement techniques

The main methods, that we are using for measuring CIP spectra are VNA and phase measurer methods, but for verification of results (or some experimentally gained points) the measurements are performed with Q-meters and LRC bridges. The resonant method imperfection is in uncontrolled voltage growth at the resonance, which is influencing magnetic state of the sample, increasing error value. Also Q-meters have narrow working frequency range in which CIP can be measured. The low frequency LRC bridges are mainly used for determination of initial permeability of the sample (at frequencies around some kHz), more advanced LRC bridges can measure CIP up to 250 MHz [127]. Let's look more closely to these measurement techniques.

The bridge method (Fig. 5.4, a): the value of the unknown impedance Z_x can be obtained by the relationship of the other bridge elements as

$$Z_x = Z_3 Z_1 / Z_2 \tag{5.14}$$

when there is no current indicating in the measuring element (ME).

The resonant method (Fig. 5.4, b): the value of unknown impedance L_x and R_x values can be obtained by tuning system to resonance by adjusting a tuning capacitor *C*, and measuring resonant frequency, *Q* and *C* values.

There is also so called **voltage-current method** of measurement (Fig. 5.5, a), or V-I method. An unknown impedance Z_x can be obtained by measuring current and voltage as:

$$Z_x = U_1 / I = UR / U_2. \tag{5.15}$$

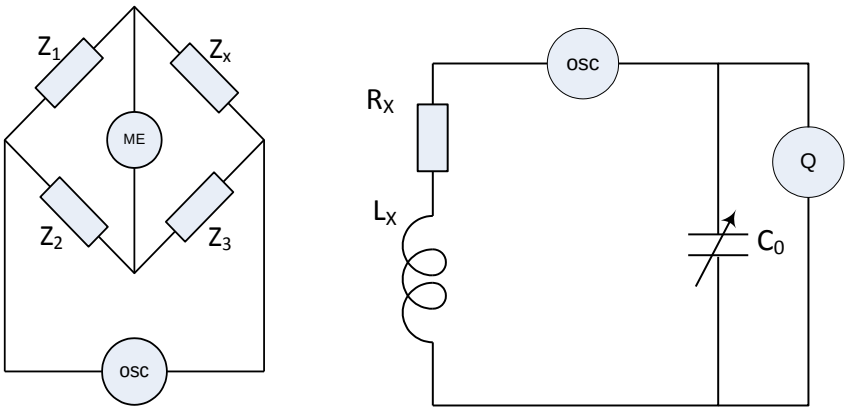

Figure 5.4. Block schemes a) for bridge method [1], b) for resonant method [1]

The RF V-I method is based on the same principle [1], with some changes in configuration of the circuit, so the measuring frequency range can be expanded to RF frequencies (with help of coaxial line).

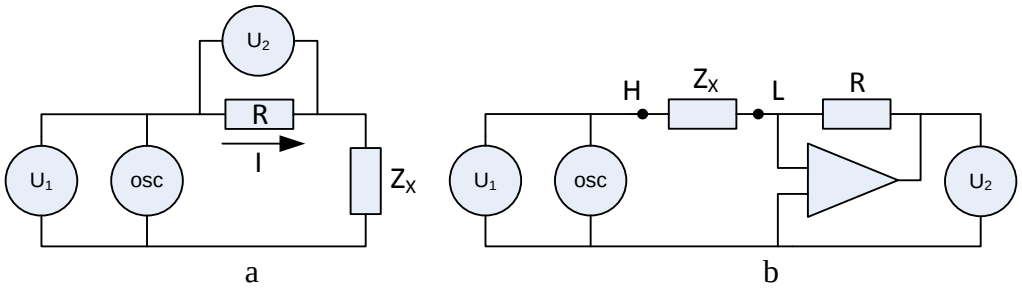

Figure 5.5. Block schemes a) for V-I method [1], b) for auto balancing bridge method [1]

Auto balancing bridge method (Fig. 5.5, b). The auto balancing bridge usually have the 4 terminals: *Hc* – High-current, *Hp* – High potential, *Lp* – low potential and *Lc* – low current terminals. The value of unknown impedance Z_x is obtained by relation of voltage at High terminal and voltage at *R*. The V-I converter-amplifier balances the current through the Z_x and *R*, so the *L* terminal has zero potential. There are several connection configurations to choose, with their own advantages and disadvantages [1].

5.3.2 CIP measurements with VNA

The basic measurement technique is measuring CIP with vector network analyzer (VNA, Fig. 5.6). The VNA are used for components, circuits, devices measurements, and it is a stimulus-response system, i. e. the generated signal is well known. With vector-error correction VNA provides much higher measurement accuracy then classical methods.

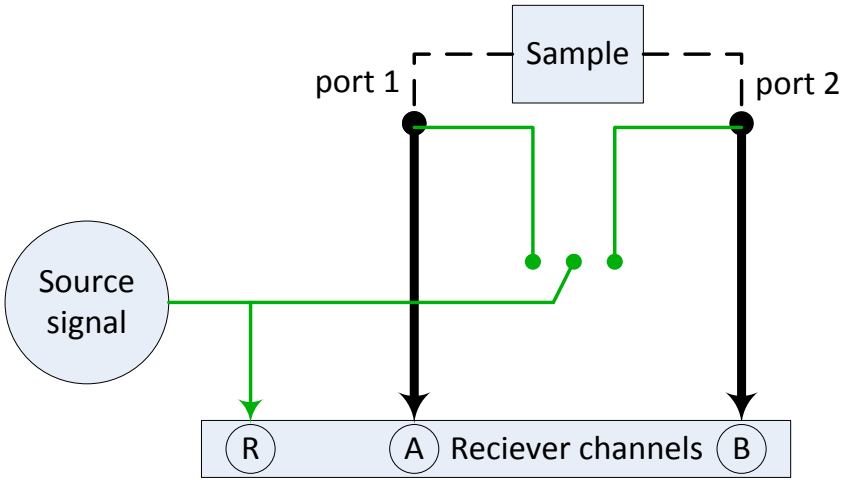

Figure 5.6. VNA block diagram

The Source supplies VNA with incident swept signal. It can be the frequency sweep or a signal power sweep. The source can be based on open-loop voltage-controlled oscillators (VCO), or more expensive synthesized sweepers. The phase noise of VCOs influenced on measurement accuracy, so modern VNA uses synthesized sweepers, with excellent frequency resolution and stability.

The sent and received signal separation in VNA is done for measuring incident and reflected signals [2]. There are two ways of completing this task: splitters and/or directional couplers [2]. Splitters are usually resistive and provide 6 dB or more loss, with no directivity. Directional couplers instead have very low insertion loss, good isolation and directivity but suffer from frequency range (unusable below 40 MHz). However the finite directivity causes error to measured results.

The measurement blocks provides detection of a signal. Detection can be provided via diode, which converts the RF signal to a proportional DC signal. But diode provide only magnitude part of a signal, the phase information is lost, the detection is broadband, which involves excess harmonics and higher noise. Another way of detecting a signal is the tuned receiver with local oscillator, which mixes the RF down to lower "intermediate" frequency (IF), with band pass filtering. This results in excess harmonics removal, also the harmonics

associated with the source become at frequencies outside of IF band and are removed by filtering. VNA generates a sinusoidal test signal and measures the response of a sample. These two signals have different amplitudes and phases [2, 58]. The *S* – parameters are formed from this signal ratios. They are expressed as pairs of real and imaginary parts or magnitude and phase parts. The displaying of data we can decide by our need – we can view only magnitude (real) part of measurements, or the phase (imaginary) part. The scale can be linear or logarithmic, the most common format is a log-magnitude format, as it let us see wider dynamic range than a linear format [2, 58].

5.4 VNA error sources and calibration

Like in measurements with all other methods, there are measurement errors in measurements with VNA. Which can be classified as systematic, random and drift errors (Fig. 5.7).

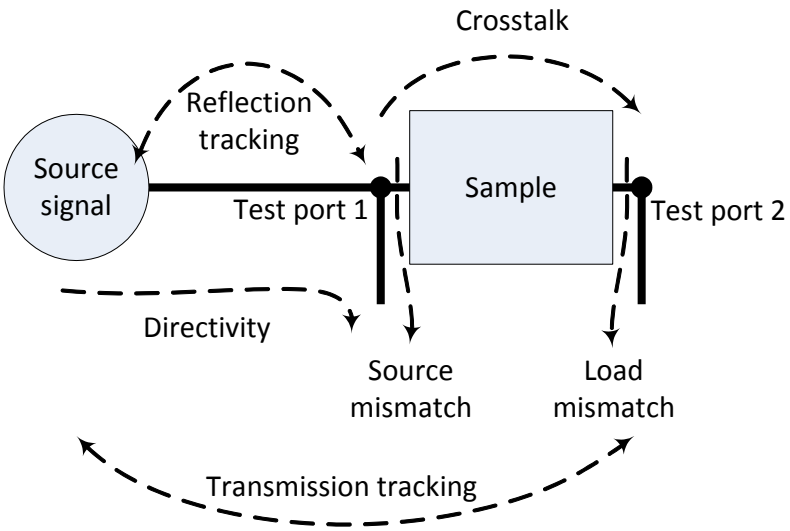

Figure 5.7. VNA error sources [2, 58, 59]

Systematic errors are known errors linked to a specific device. They are repeatable and can be removed with calibration and/or mathematically. The systematic errors can be divided into signal leakage (directivity and crosstalk), signal reflections (source and load match) and frequency response (reflection and transmission tracking) errors. So, there are defined twelve errors for a two-port model (six for the forward direction and six for the reverse direction) (Fig. 5.9) [2, 58].

Random errors come from an unknown source, and cannot be removed by calibration or with mathematical solutions. The reason for this kind of errors can be noise source, poor signal processing through sample, etc. The random errors can be divided into: instrument

noise errors (due to electrical fluctuations inside the measurement equipment), switch repeatability errors (if there are used mechanical RF switches) and connector repeatability errors (if the connectors are worn out).

Drift errors are because of the change of state of measuring equipment. Drift errors appear after the calibration. They can be removed by maintaining constant environment in place, where the measurements are done. If VNA was not used for a long time period it should take about half an hour for it to obtain an operating mode, while it's 'warming up' state is done.

To characterize and compensate the systematic errors, the vector error correction method is used for VNA calibration. There are different loads with known parameters, stored in the calibrating kits and definition files in the VNA for different calibration kits. For accurate measurements parameters of calibration kit must match the definitions stored in the VNA file. The calibration [2, 58] can be performed by one of the methods: one-port calibration and two-port calibration. The one-port calibration provides defense against three of the systematic errors: directivity, source match and reflection tracking; and requires only three measurements (open load, short load and match load measurements). With the two-port calibration all twelve systematic errors are corrected; but requires minimum of seven measurements with four loads (open load, short load, match load and through measurements).

In this work we are using only one-port and two-port connection models, so the error correction models are the same: *a* – for the one-port and *b*- for the two-port measurements.

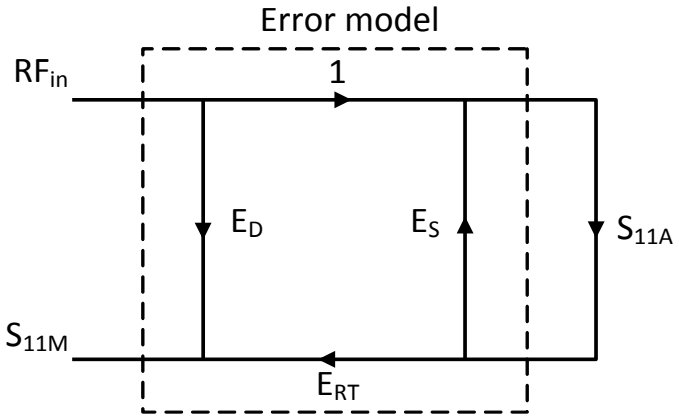

Figure 5.8 One port error model [2, 58]

a. In the one-port error model there are three systematic errors: directivity (E_D), reflection tracking (E_{RT}), and source match (E_S). Taking measurements with short, open and matched loads we can extract needed errors, and then [2, 58]

$$S_{11_M} = E_D + E_{RT}\left(\frac{S_{11_A}}{1 - E_S S_{11_A}}\right) \tag{5.16}$$

where S_{11_M} and S_{11_A} are measured and actual values of S_{11}.

b. In the two-port error model all 12 systematic errors are taken into account. Thus it is the most accurate. There are defined [2, 58]:

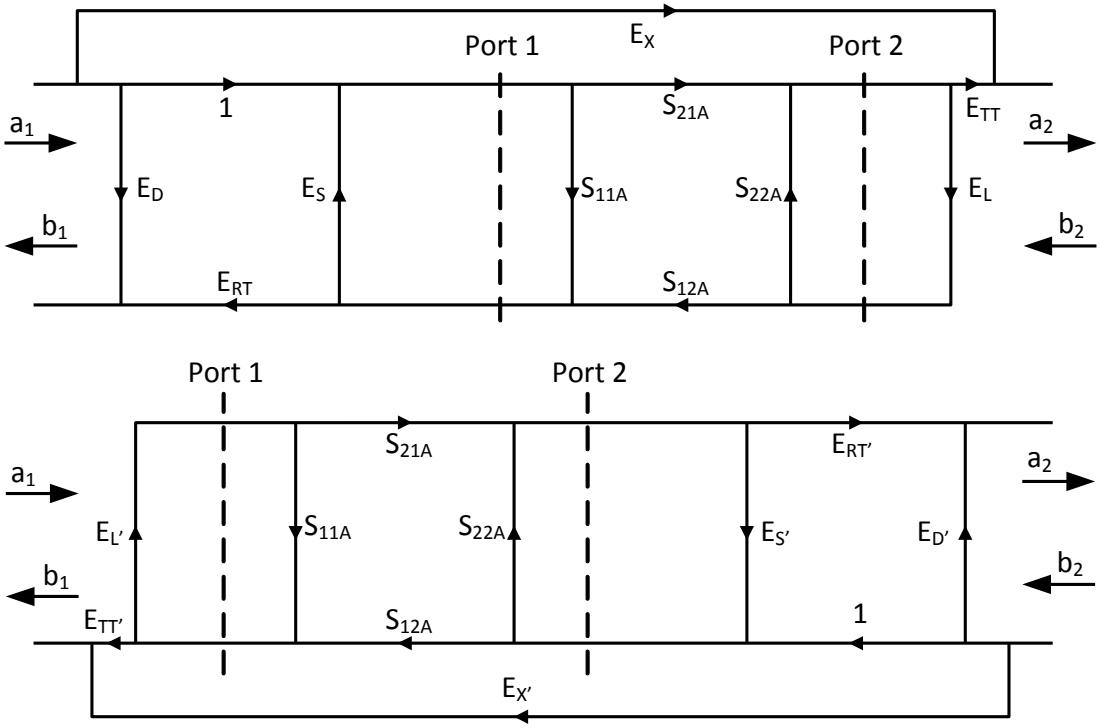

Figure 5.9. Two port error model [1, 57]

E_D – forward directivity;

E_S – forward source match;

E_{RT} – forward reflection tracking;

E_L – forward load match;

E_{TT} – forward transmission tracking;

E_X – forward isolation;

$E_{D'}$ – reverse directivity;

$E_{S'}$ – reverse source match;

$E_{RT'}$ – reverse reflection tracking;

$E_{L'}$ – reverse load match;

$E_{TT'}$ – reverse transmission tracking;

$E_{X'}$ – reverse isolation;

As can be seen – VNA need to make forward and reverse measurements, using open, short, match loads and through connection to obtain all of parameters (as is seen on Fig. 5.9).

The equations for two-port error correction model are:

$$S_{11_A} = \frac{\left(\frac{S_{11_M} - E_D}{E_{RT}}\right)\left(1 + \frac{S_{22M} - E_{D'}}{E_{RT'}} E_{S'}\right) - E_L\left(\frac{S_{21_M} - E_X}{E_{TT}}\right)\left(\frac{S_{12_M} - E_{X'}}{E_{TT'}}\right)}{\left(1 + \frac{S_{11_M} - E_D}{E_{RT}} E_S\right)\left(1 + \frac{S_{22M} - E_{D'}}{E_{RT'}} E_{S'}\right) - E_{L'} E_L\left(\frac{S_{12_M} - E_X}{E_{TT}}\right)\left(\frac{S_{12_M} - E_{X'}}{E_{TT'}}\right)}; \quad (5.17)$$

$$S_{21_A} = \frac{\left(\frac{S_{21_M} - E_X}{E_{TT}}\right)\left(1 + \frac{S_{22_M} - E_{D'}}{E_{RT'}}\left[E_{S'} - E_L\right]\right)}{\left(1 + \frac{S_{11_M} - E_D}{E_{RT}} E_S\right)\left(1 + \frac{S_{22M} - E_{D'}}{E_{RT'}} E_{S'}\right) - E_{L'} E_L\left(\frac{S_{12_M} - E_X}{E_{TT}}\right)\left(\frac{S_{12_M} - E_{X'}}{E_{TT'}}\right)}; \quad (5.18)$$

$$S_{12_A} = \frac{\left(\frac{S_{12_M} - E_{X'}}{E_{TT'}}\right)\left(1 + \frac{S_{11_M} - E_D}{E_{RT}}\left[E_S - E_{L'}\right]\right)}{\left(1 + \frac{S_{11_M} - E_D}{E_{RT}} E_S\right)\left(1 + \frac{S_{22M} - E_{D'}}{E_{RT'}} E_{S'}\right) - E_{L'} E_L\left(\frac{S_{12_M} - E_X}{E_{TT}}\right)\left(\frac{S_{12_M} - E_{X'}}{E_{TT'}}\right)}; \quad (5.19)$$

$$S_{22_A} = \frac{\left(\frac{S_{22_M} - E_{D'}}{E_{RT'}}\right)\left(1 + \frac{S_{11M} - E_D}{E_{RT}} E_S\right) - E_{L'}\left(\frac{S_{21_M} - E_X}{E_{TT}}\right)\left(\frac{S_{12_M} - E_{X'}}{E_{TT'}}\right)}{\left(1 + \frac{S_{11_M} - E_D}{E_{RT}} E_S\right)\left(1 + \frac{S_{22M} - E_{D'}}{E_{RT'}} E_{S'}\right) - E_{L'} E_L\left(\frac{S_{12_M} - E_X}{E_{TT}}\right)\left(\frac{S_{12_M} - E_{X'}}{E_{TT'}}\right)}; \quad (5.20)$$

The main benefit here is, that calculation of error correction is done by VNA, when the calibration is performed [2, 58].

Overall we get over 1000 points of data with each measurement in short period of time, which is far better than the classical approach. After the data is collected we can easily process this data with a MATLAB® program and construct CIP specter. But measurements at lower frequencies still ought to be done with classical approach.

5.5 Main measurement methods used for experiments

The **phase measurer** used for our experiments – Φ2-16 can afford frequency range from 20 Hz to 2 MHz, with error of 0.2°. The measurements can be taken from 0…360°.

For the measurements (Fig. 5.10) we need a ferrite core (sample, with a known amount of windings) and an etalon element with apriori known parameters (in our case it's resistor $R = 160\ \Omega$) in series. The frequency generator is connected to the sample (with frequency *f*

and input voltage U_{in}). We can easily measure input and output voltage (U_{in} and U_{out}) of the circuit and phase shift (φ) between voltage and current.

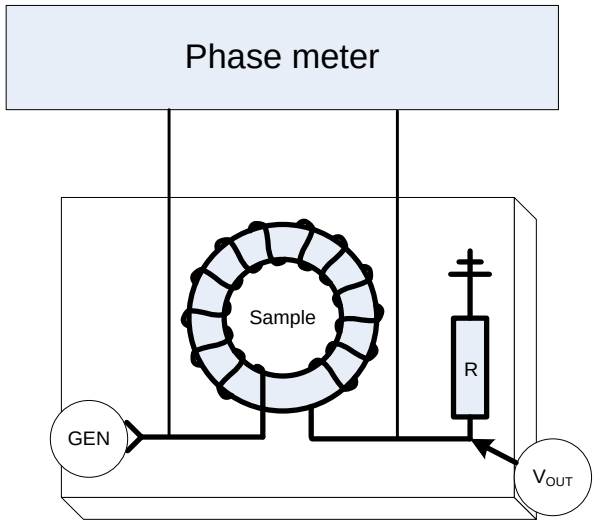

Figure 5.10. Phase meter measurement setup

The main principle of measurement is that we need to hold same output voltage level within all measurement frequency range (in our case U_{out} *=15 mV*). Then we can construct CIP spectrum knowing voltage before sample (U_{in}, source voltage), voltage on load (U_{out}, voltage on known output load R) and phase shift between these two voltages [193]:

$$\mu' = {L}/{L_0} = \frac{U_{in}Rsin(\varphi)}{U_{out}\omega L_0}; \quad \mu'' = {R_m}/{\omega L_0} = \frac{U_{in}Rcos(\varphi)-U_{out}R}{U_{out}\omega L_0} \ . \tag{5.21}$$

Our **VNA ZVR-E** has the frequency range from 9 kHz up to 4 GHz. Thus, there are many bugs accruing if the whole frequency range is measured at once, so to do more precise measurements we need to couple the results with narrower frequency ranges (data coupling errors occur frequently, it can be related to recalibration processes of the unit). There are several ways of measuring CIP with this unit. Firstly we can connect sample to ZVR-E's 1-port (Fig. 5.11, a) and measure S11 parameter (Z11 can be measured as well, but initial parameter is S11). From many experimental data measured and proofed with classical methods it was stated, that there is agreement between the results obtained. To deal with slight noise there was done a shielded ferrite connection to ZVR-E, with possibility to connect ferrite both to one or two ports (Fig. 5.11, b). It increased accuracy in comparison with one port connection and, thus, lasts as our prime measurement technique. CIP can be constructed by measuring complex value of S11, S12, S21, S22 parameters for two ports and then moving to Z parameters to obtain complex impedance value $\dot{Z}_{in}$ from them.

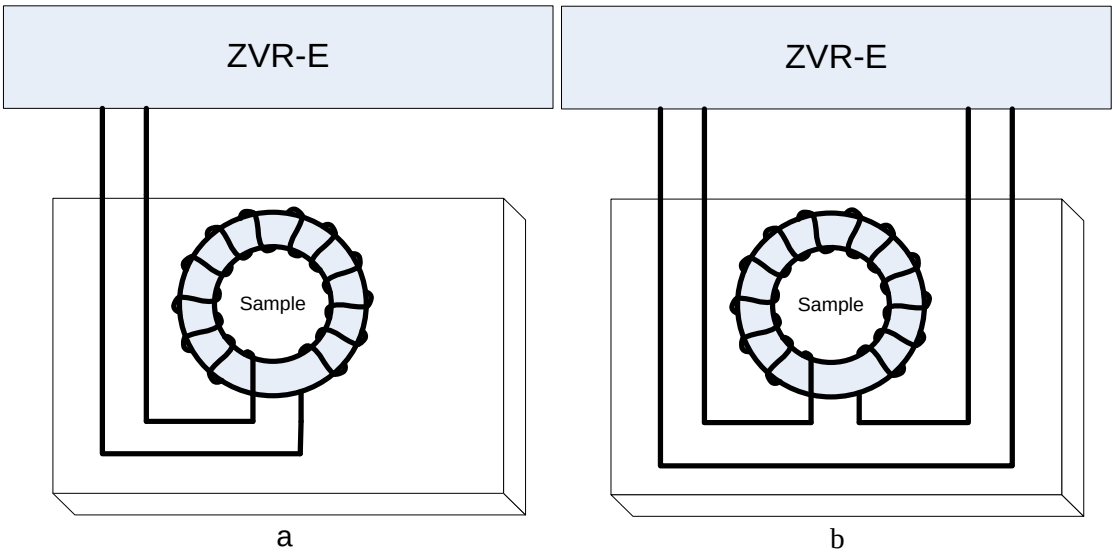

Figure 5.11. VNA sample connection methods a) one pole, b) two pole

$$\dot{Z}_{in} = \dot{Z}_{11} - \frac{\dot{Z}_{12}\dot{Z}_{21}}{\dot{Z}_{22}+Z_0} \tag{5.22}$$

where $Z_0 = 50\Omega$ is characteristic impedance of test port. Then CIP of a sample

$$\dot{\mu}(f) = 1 + \frac{\dot{Z}_{in}}{j2\pi f L_0} \tag{5.23}$$

where L_0 – inductance without magnetic sample.

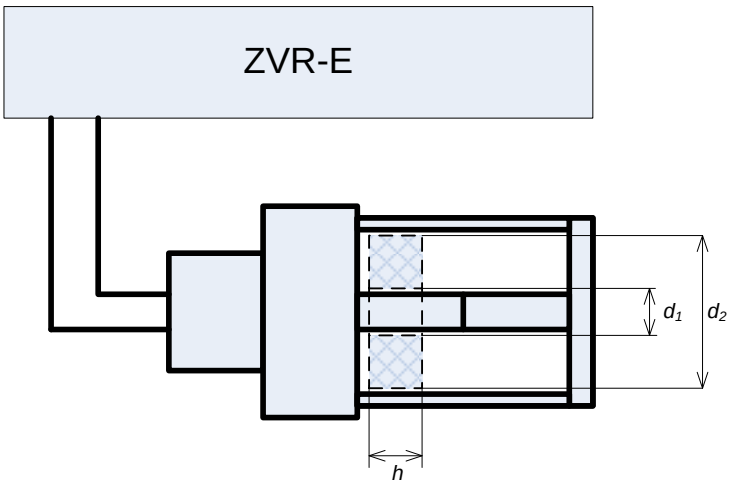

Figure 5.12. Shortened coaxial line connection to VNA

Also it was stated [26, 130, 137, 193] that ferrite ring core measurements can be done with shortened coaxial line (SCL) (Fig. 5.12). We made our own SCL with help of R&S radiofrequency waveguide parts. Main benefit for coaxial line is that magnetic field is distributed evenly in the whole sample, and we do not suffer from parasitic capacitance that occurs between windings of a sample. The measuring parameter for SCL is S11. In [130] the relation for CIP is presented as:

$$\dot{\mu}(f) = 1 + \frac{\dot{Z} - \dot{Z}_{air}}{jh\mu_0 f \ln\left(\frac{d_2}{d_1}\right)} \tag{5.24}$$

where $\dot{Z}$ and $\dot{Z}_{air}$ are complex values of impedances measured with and without sample, d_1 and d_2 is inner and outer diameter of a toroid sample respectively, h – height of a sample. So, the SCL method gave us another trustworthy results even with one port connection.

5.6 CIP measurement results

The CIP was measured for all studied ferrites in three groups (A, B, C). The results are representing CIP dependence of frequency. The quality of experimental results was tested for measured CIP accordance to KKR, as well as for accordance of experimental data taken with different measurement methods (phase meter, vector network analyzer, LRC bridge and with shortened coaxial line, when it was possible) for the same sample. VNA was chosen as the main measurement equipment (as it provides fast and reliable measurement results), and subsequent CIP spectra are plotted basing on the data taken with VNA (until it is mentioned otherwise).

First measured ferrite group – A (NiZn ferrite, 4S60) results are presented in Fig. 5.13 (m1, m2 correspondingly stands for $\mu'(f)$ and $\mu''(f)$).

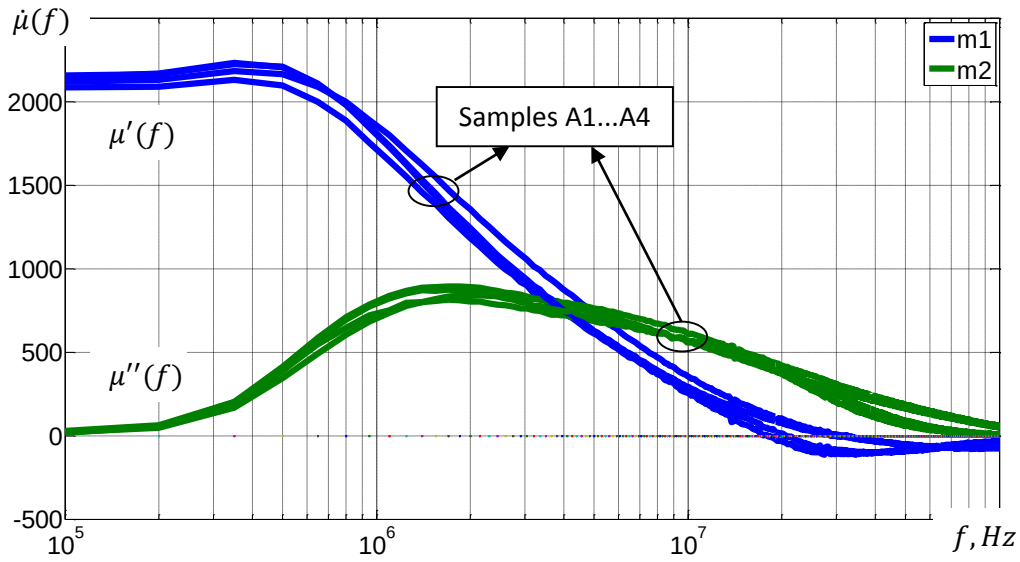

Figure 5.13. Measured CIP of samples A1..A4

As it is seen – for samples A1...A4 there is no real difference in CIP dependence on size of the cores (the results varies within measurement error boundaries). The separate curves for each measured sample of group A are presented in Appendix 2, Figures A2.1–A2.4.

The next measured ferrite groups are – B (MnZn ferrite, 6000HM-1 results are shown on Fig. 5.14), and C – (MnZn ferrite, T37) results are shown on Fig. 5.15.

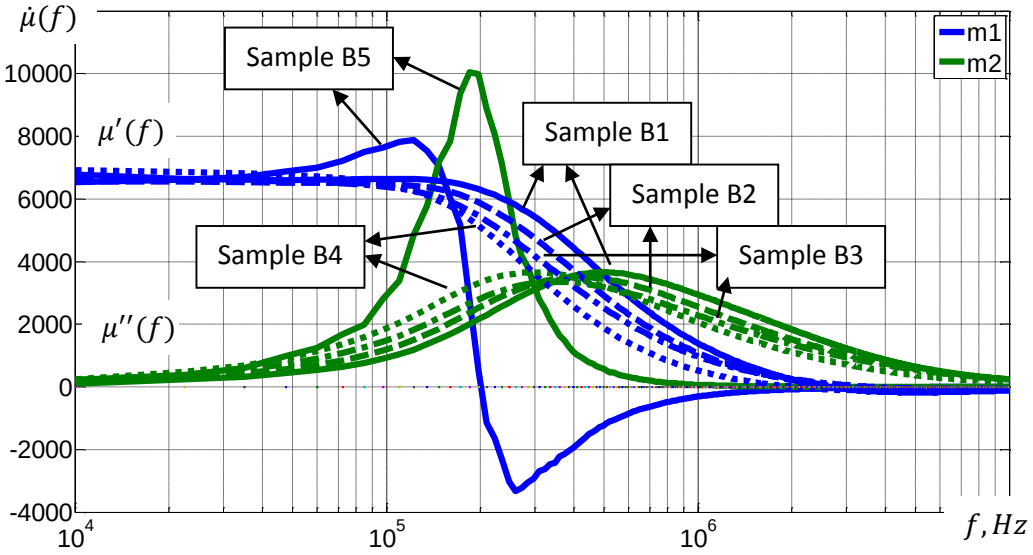

Figure 5.14. Measured CIP of sample B1..B5

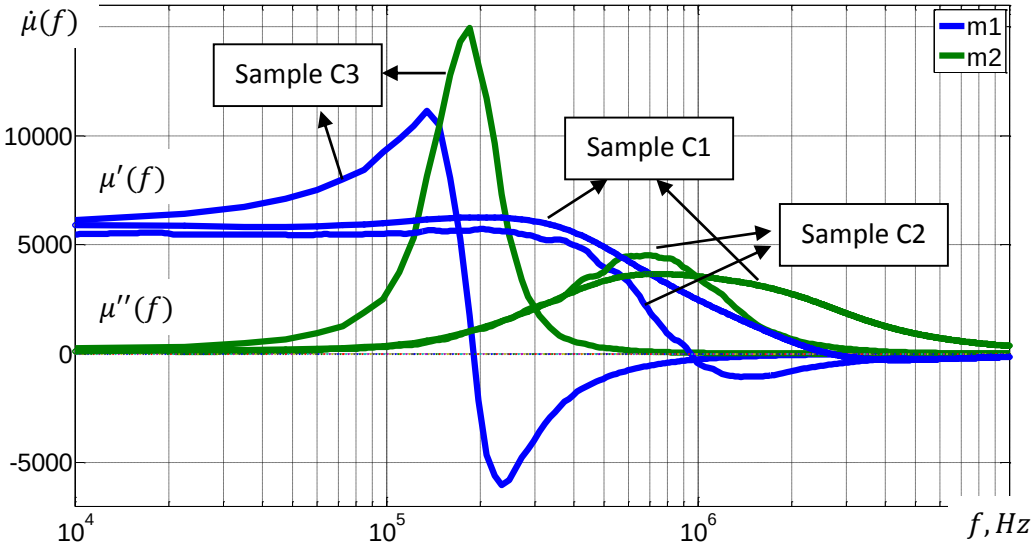

Figure 5.15. Measured CIP of samples C1..C3

From the measurement results of B1...B5 samples (Fig. 5.14) it is seen that, ACp maximum of CIP became dependent on frequency (samples B1...B4, the bigger the core size – the lower the ACp maximum frequency), and, in case of pronounced resonant character of sample B5 – dimensional resonance conditions obviously were met. Nevertheless, the DR phenomena do not manifest itself appreciably (as it does within sample C3, Fig. 5.15). The separate curves for each measured sample of group B are presented in Appendix 2.

The results for C1...C3 (MnZn ferrite, T37) proves, that dimensional resonance highly influence the CIP of MnZn T37 ferrite core, making it more resonant and decrease the ACp maximum frequency for almost a decade (Fig. 5.15). The separate curves for each measured sample of group C are presented in Appendix 2, Figures A2.10–A2.13.

As was stated above – experimental measurements in wide frequency range is rather difficult task. There are many different errors involved – reading measurement inaccuracy in classical methods, calibration errors, different measurements coupling errors, many parasitic factors involvement, etc. So, as a final step in measuring CIP – all measurements should be verified. The verification of experimental data is performed by their agreement to Kramers-Kronig relations (subsection 5.9) and by comparing the results with phase meter and Q-meter results (subsection 5.7).

5.7 VNA measurement results comparison with other measurement methods results

For verification of throughtfulnes of VNA measurements – the classical phase meter and Q-meter measurements were performed within all of the samples. For the demonstration of these approaches there are chosen C1 (Fig. 5.16) and C2 (Fig. 5.17) samples.

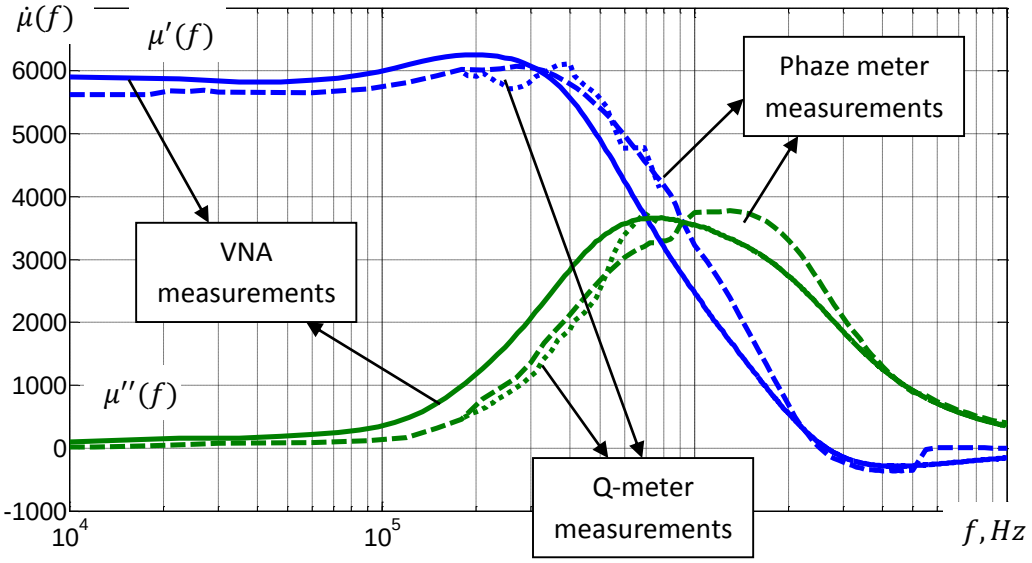

Figure 5.16 Verification of measured with VNA CIP of sample C1 by classical measurement methods.

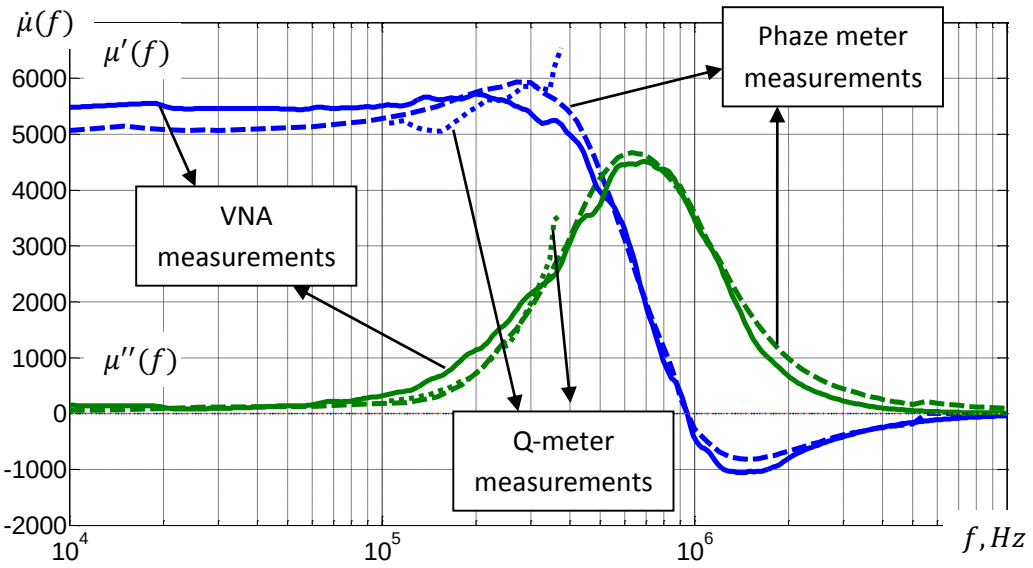

Figure 5.17 Verification of measured with VNA CIP of sample C2 by classical measurement methods.

As it is seen from Fig. 5.16 and Fig. 5.17 data obtained from VNA and phaze meter measurements are in good correlation. The data obtained with Q-meter has good correlation only within lower frequencies (the AF data is not precise due to parasitic parameters).

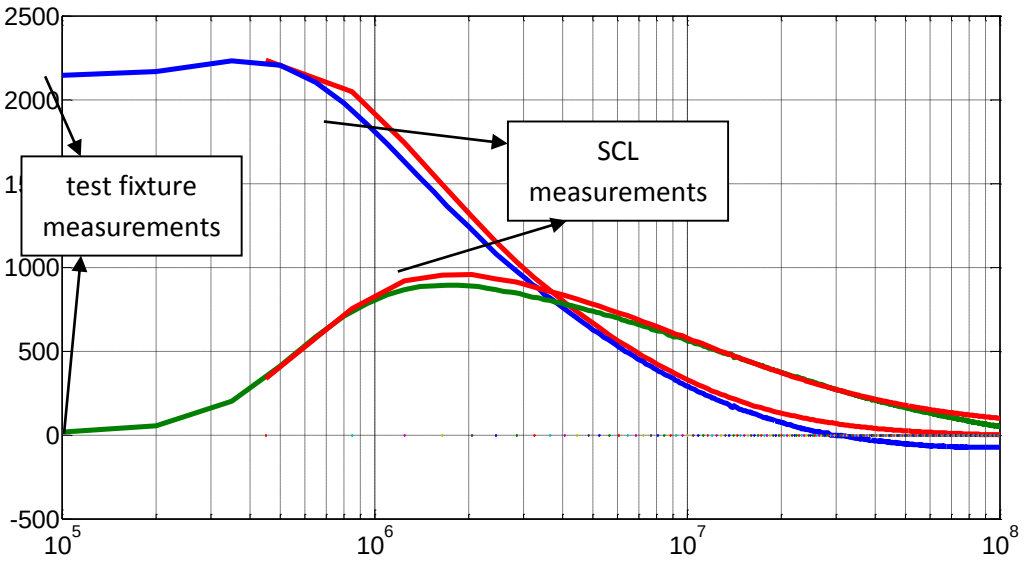

Figure 5.18 Comparison of measured with VNA CIP of sample A3 (with SCL and test fixture).

For the SCL measurements there are needed samples within very narrow band of geometrical dimensions (that can fit inside of the SCL). Therefore this method cannot be used as a prime one, but it is good enough for the proofing of the results. As it is seen from the

Fig. 5.18 - the CIP of sample A3 have good correlation, which once again points to correct measurement method and results reliability.

5.8 Measurements of complex permittivity

Complex permittivity ($\dot{\varepsilon} = \varepsilon' - j\varepsilon''$) can be obtained by equations of parallel plate capacitor [140]. The values for real and imaginary parts of complex permittivity for such a case then are equal:

$$\varepsilon' = \frac{C}{C_0} = \frac{Cd}{\varepsilon_0 A} \tag{5.25}$$

$$\varepsilon'' = \frac{G}{\omega C_0} = \frac{Gd}{\omega \varepsilon_0 A} \tag{5.26}$$

where $C = \frac{\varepsilon S}{d}$ stands for capacitance of such capacitor; $G = \frac{\sigma S}{d}$, where d - is thickness of a sample; S stands for sample cross section area; σ stands for material characteristic impedance C_0 is the geometric capacitance; A stands for sample cross section area; $\varepsilon_0 = 8.85 \ldots 10^{-12}$ $(\frac{F}{m})$ is vacuum permittivity.

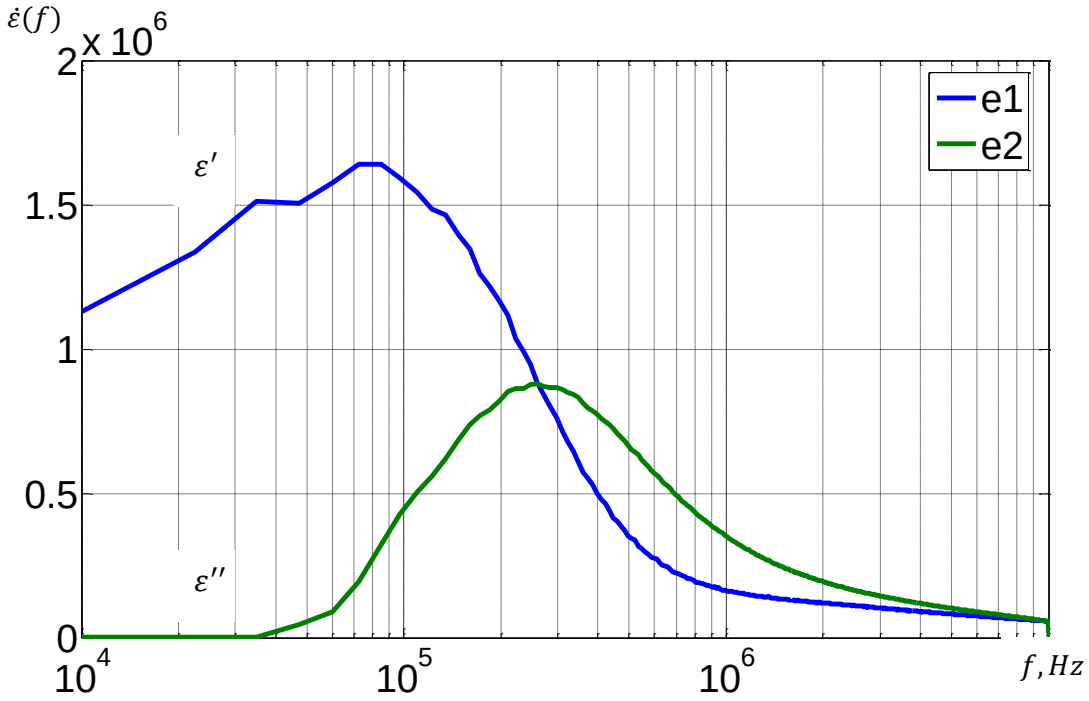

Figure 5.19 Measured complex permittivity of MnZn ferrite 6000HM-1 sample.

The complex admittance of this capacitor is then:

$$\dot{Y} = j\omega C + G = j\omega C_0(\varepsilon' - j\varepsilon'') \tag{5.27}$$

Table 5.1. Sample parameters for complex permittivity measurements

Material	Sample size, mm	Metallization area, mm	$\varepsilon_r(0)$
6000HM-1	11x11x2	8.5x9	1.6×10^6
T-37 *a*	16x8x1.1	4x9.6	13.3×10^6
T-37 *b*	16x8x0.9	3.5x9.5	13.5×10^6
T-37 *c*	16x8x0.8	4x7	13.1×10^6

The experimental measurements of complex permittivity were performed on ferrite samples cut from studied MnZn ferrite ring cores (Table 5.1). On the polished surface of these samples were sputtered (in Laboratory of Microelectronics, J. Barloti) thin copper electrodes (about 50 μm).

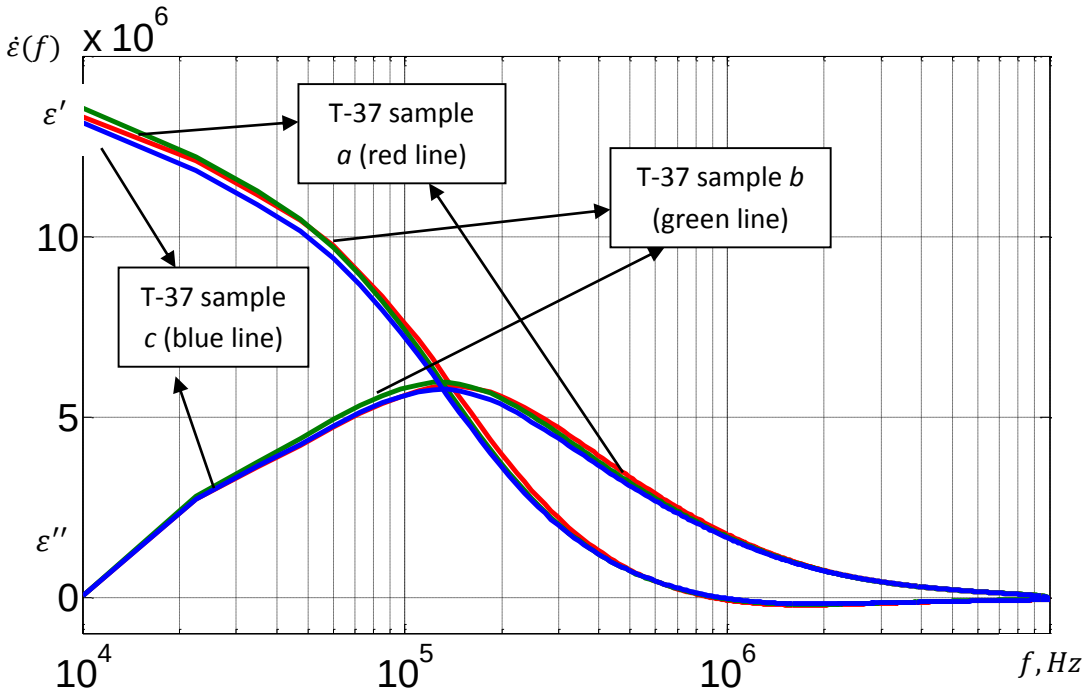

Figure 5.20 Measured complex permittivity of MnZn ferrite T-37 samples.

The results showed that real part of permittivity of MnZn ferrites has at lower part of frequencies high values (Table 5.1). Therefore, together with high value of permeability, conditions for dimensional resonance can be achieved.

5.9 Verification of CIP experimental data by KKR

For verification of overall quality of measured data the KKR are used. If ACp or DCp of the measured CIP spectra does not correlate with the calculated ACp or DCp, then we can conclude, that the measurements were performed inaccurately. On the following figures m1, m2 stands for $\mu'(f)$ and $\mu''(f)$; $m1_{kk}$ and $m2_{kk}$ stands for KKR evaluation of $\mu'(f)$ and

$\mu''(f)$. The application of Kramers-Kronig relations to experimental magnetic spectra of studied A1 ferrite core can be seen on: Fig. 5.21 (A2..A4 samples CIP spectra are shown in Appendix 4 due to their close correlation).

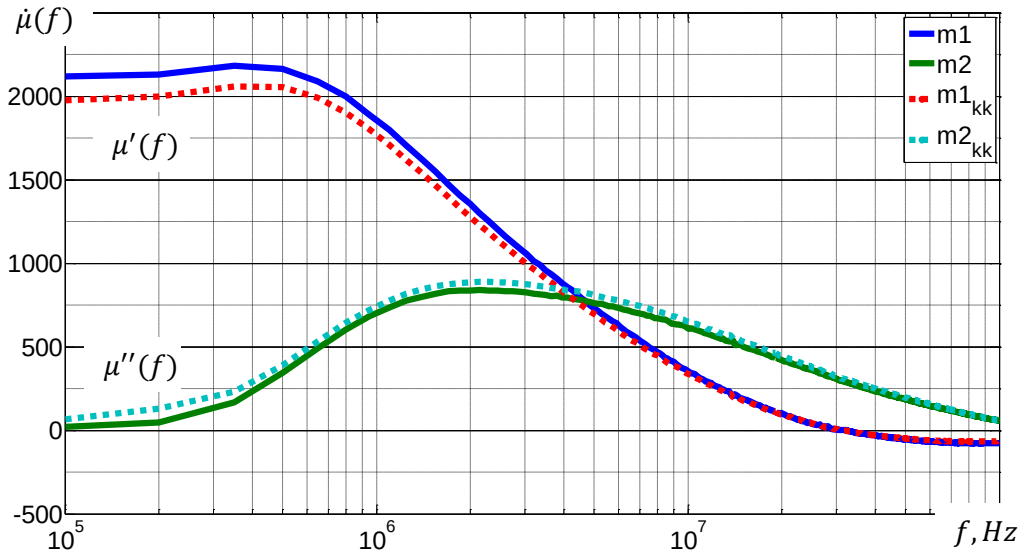

Figure 5.21 KKR application to A1 sample.

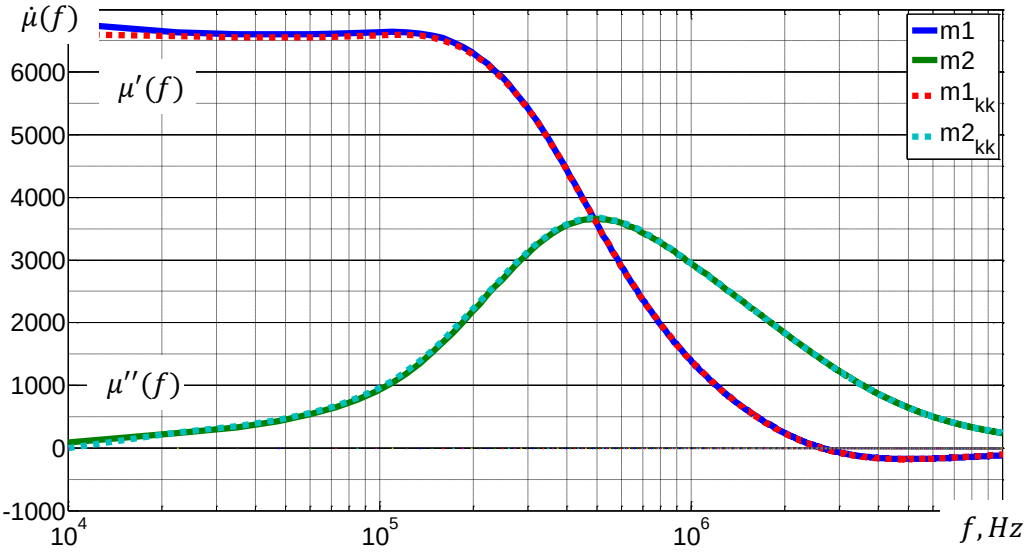

Figure 5.22 KKR application to B1 sample.

The CIP spectra on Fig. 5.22 and Fig. 5.23 stands for B1 and B5 samples (KKR for B2...B4 samples are presented in Appendix 4, as the CIP spectra of these samples is similar to the CIP of the B1 sample). The KKR evaluation of CIP spectra of B1–B4 samples showed good correlation with experimental data. Thus we can conclude that the measurements of CIP were performed correctly. The CIP of B5 sample is influenced by the DR (e. g., is influenced

by extrinsic factors), nevertheless – the KKR evaluation showed good correlation with experimental data, thus we can conclude too, that this CIP spectrum is of good quality (Fig. 5.23).

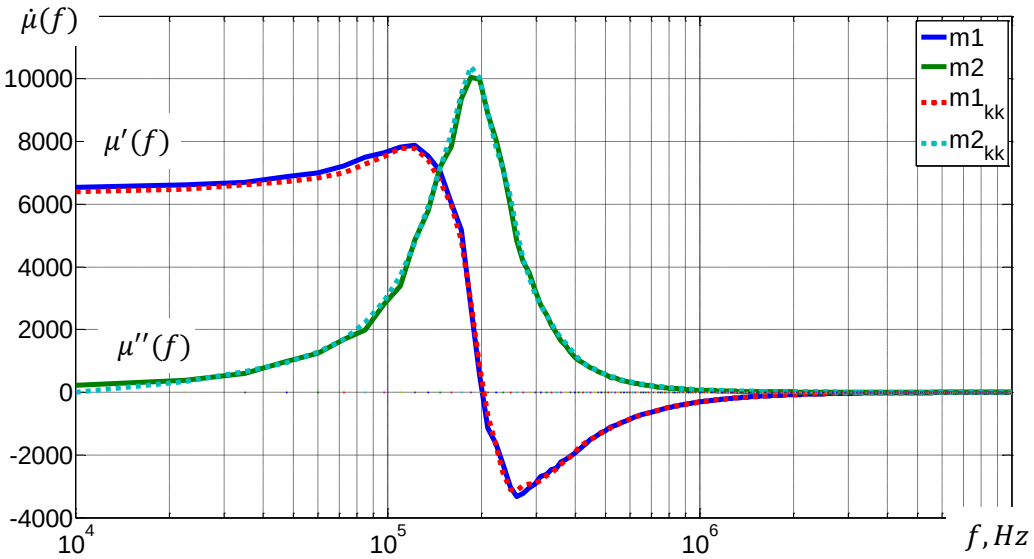

Figure 5.23 KKR application to B5 sample.

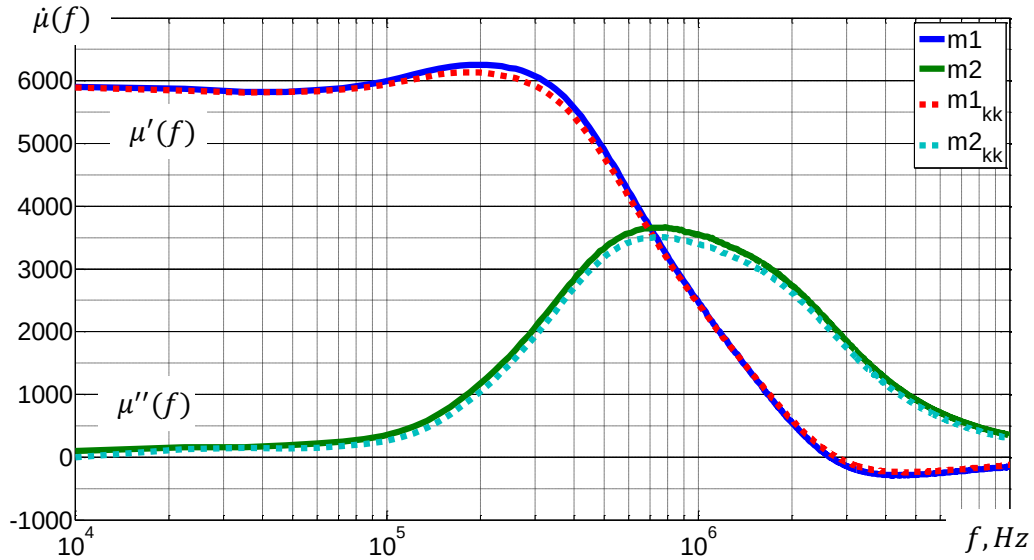

Figure 5.24 KKR application to C1 sample.

The CIP spectra of the C group are presented on Fig. 5.24–5.26. The study of these samples revealed, that there is C1 sample, that represents CIP as InP and C2, C3 samples represents CIP as ExP. The influencing factors are different for these samples and moreover – the influence of DR differs within C2 and C3 samples. Nevertheless the KKR evaluation of spectra quality of all of these samples showed good correlation, which signals about good spectra quality within CIP measurements both as InP and ExP.

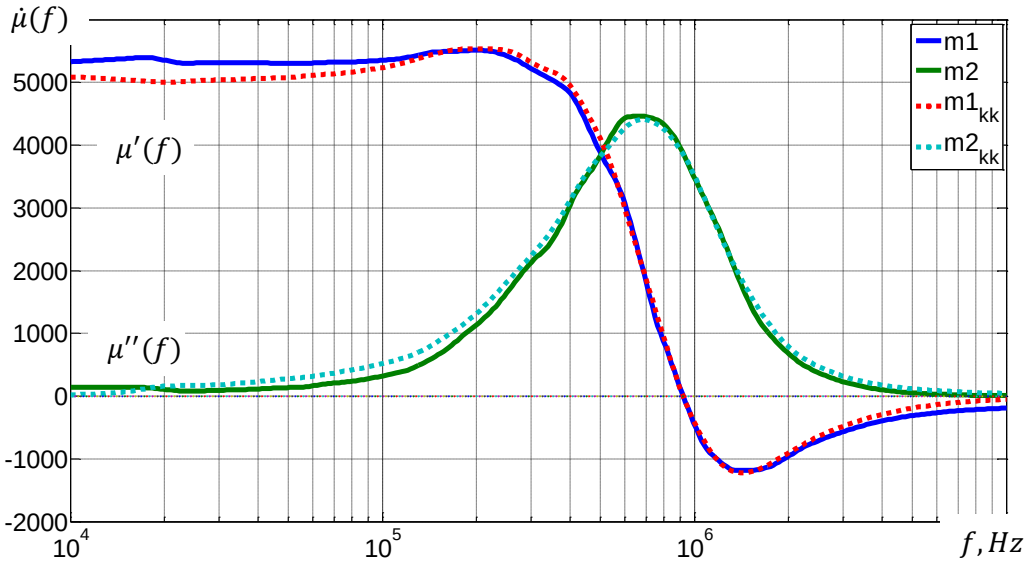

Figure 5.25 KKR application to C2 sample.

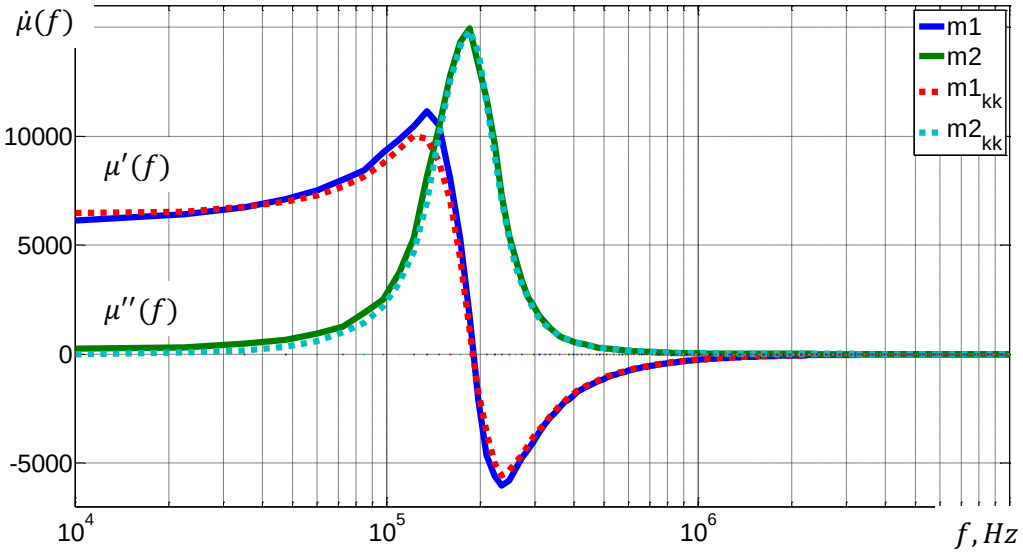

Figure 5.26 KKR application to C3 sample.

As is seen from figures, all of the obtained experimental data correlates well with Kramers-Kronig relation evaluations. This proves that measurement methods are performed correctly and obtained experimental data is correct (in case of DR too, Fig. 5.23, 5.26).

5.10 CIP measurements methods summary

The verification of measurement results with KKR proved correctness and quality of obtained data. Comparing the VNA measurement results with other performed measurement methods (i. e. Q-meter and phase meter measured data) results revealed the good match of them, which proves the correctness of obtained data as well. The most common [1] measurement methods cons and pros are combined in the Table 5.2.

Table 5.2. CIP measurement methods summary

Method	Advantages	Disadvantages	Frequency range
Bridge method	• High accuracy • Wide frequency coverage with different types of bridges • Low cost	• Manual balancing • One bridge provides narrow frequency range.	DC – 300 MHz
Resonant method	• Best in measuring Q	• Resonance measurements • Low impedance measurement accuracy.	10 kHz – 70 MHz
V-I method	• Grounded device measurements • Probe type measurements	• Operating frequency is limited by transformer used in probe	10 kHz – 100 MHz
RF V-I method	• High accuracy • Wide impedance range at RF	• Operating frequency is limited by transformer used in test head	1 MHz – 3 GHz
Network analysis method	• High frequency range • Good accuracy at matched load	• Recalibration with frequency change • Narrow impedance measurement range	9 kHz and above
Auto balancing bridge method	• Wide frequency range • High accuracy • Wide impedance measurement range • Grounded measurements	• Higher frequencies not available	20 Hz – 110 MHz

The performed measurements of CIP prove that DR can appear if there are met conditions of high permeability and permittivity within sufficiently large ferrite core dimension. Such phenomena was observed in MnZn ferrite cores (B and C studied ferrite groups), especially with C3 ferrite sample. The study of this phenomena revealed, that there is DR dependence not only from known factors, but from number of turns as well.

6 STUDY OF CORRELATION BETWEEN THE MODELING AND EXPERIMENTAL MS

For the proof of the practical validity of Eq. 2.44 for definite MS it should be recalled that the modeling basically was developed for samples from IQG, and later on modified for TQG ferrites as well at frequencies corresponding to the large amplitude (domain wall) dispersion region. The quality of approximation of $\dot{\mu}_{DW}(f)$, with the numerical values of σ (or σ_a and σ_b) consistent with the data of microstructure of PF under study, will be taken as the modelling figure of merit.

6.1 The data and the samples used in the study

For the detailed analysis of the correctness of the model there are used a great number of various CIP spectra both from international scientific publications, and ones measured by us on our samples (Tab. 6.1). In the former case the great body of known experimental CIP spectra allow wider choice of spectra of different types (including, e. g., symmetrical ones, not found in collection of spectra from our samples). From this large general collection of PF with different compositions we first use two types of internationally widely studied ferrites (often viewed as reference ones): yttrium-iron garnet (YIG, $Y_3Fe_5O_{12}$) [39, 148] and nickel ($NiFe_2O_4$) [129] ferrites. Despite the quantity of CIP data the full set of data needed for the ferrite microstructure of interest are, as a rule, not available. Thus sending us in the research of several similar examples as well.

In the second case, the experimental data for a number of samples from NiZn and MnZn ferrites available to us and are used; these samples are covered adequately both from CIP and MST viewpoints.

Table 6.1. The groups and the dimensions of samples studied.

Group	№	Dimensions, mm	Group	№	Dimensions, mm	Group	№	Dimensions, mm
NiZn, 4S60 [33]	A1	R12 × 8 × 6	MnZn, 6000HM1 [97]	B1	R10 × 4.3 × 10	MnZn, T37 [31]	C1	R12.5 × 7.5 × 5
	A2	R20 × 10 × 6		B2	R20 × 9.1 × 10		C2	R20 × 10 × 7
	A3	R31.5 × 20.5 × 6		B3	R25 × 12 × 10		C3	R40 × 24 × 16
	A4	R40 × 23.5 × 6		B4	R30 × 14.3 × 10			
				B5	R33 × 10 × 10			

6.2 Investigation of symmetrical spectra of CIP

Among the numerous published MS in scientific literature, symmetrical ones are rare (although it is possible to find such spectra in ordinary reference books, nevertheless these are in the class of MnZn-ferrites [38], measured on rather large toroidal cores, when DR may be a factor (§ 6.4)).

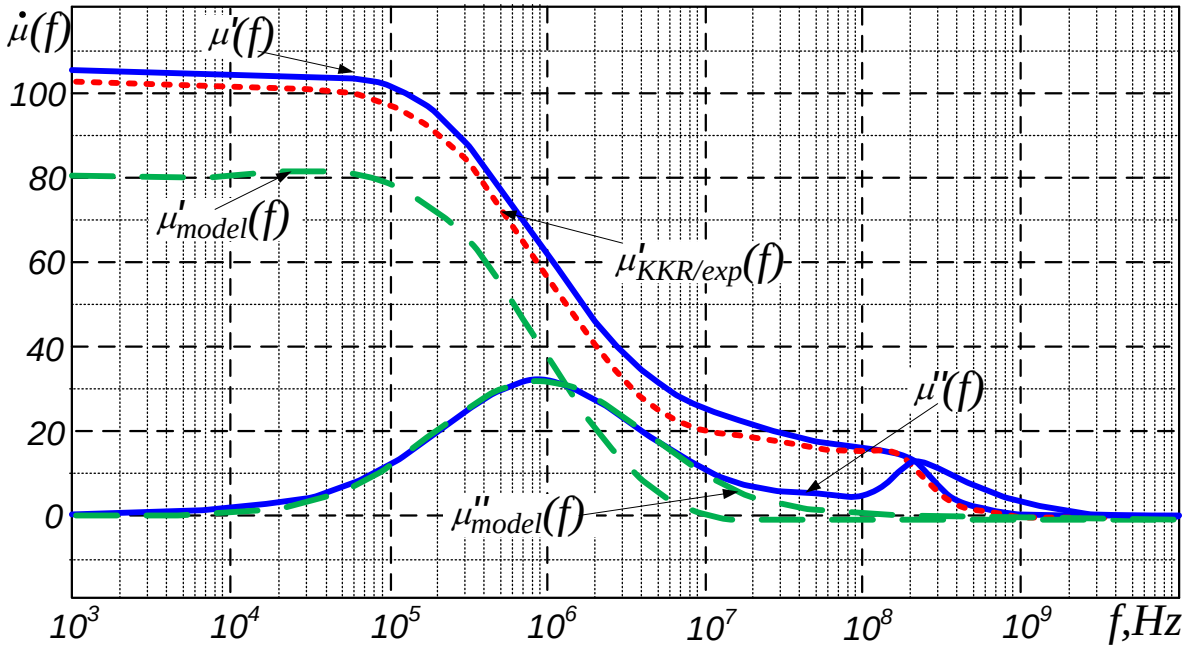

Figure 6.1 Broad frequency band experimental MS of YIG and its approximations for large-amplitude dispersion range DW process (experimental data from [39, 148])

One clear example of a symmetrical spectrum (from YIG group), measured in the broad frequency band at room temperature and having clear two dispersion regions (bimodal spectrum), is found [39, 148] (Fig. 6.1). This spectrum is well-known, and much-reproduced, not only as being the prototype of the class, but because of the rather high general quality as well (quality according to KKR as curve $\mu'_{KKR/exp}(f)$ is shown in the Fig. 6.1). Even so, no physical analysis of its DW absorption region is known. In the following such an analysis is performed on the basis of the model.

Close approximation of DW absorption by curve $\mu''_{DW}(f)$ follows from Eq. 2.44 with $\sigma = 0.7$. This value exceeds the typical ones ($\sigma \approx 0.45$, § 2.1.9) (for ferrites produced in the process of normal grain growth and no intragranular defects that are supposed for symmetrical spectrum). Similar results were obtained in the case of decomposition of iron-deficient YIG (§ 3.3, Fig. 3.9 and 3.10) when spectra were practically symmetrical as well, but with $\sigma \approx 0.6$.

Since these values are not possible to analyze within the context of the corresponding ferrites' MST data for lack of them, we should look at possible ones from similar ferrites. Unfortunately, only limited data are available: particular for YIG samples of T- and D-type materials from [43, b] being correspondingly of special, low temperature technology (Fig. 6.2; MST practically without intragranular defects) and common technology (Fig. 6.3; MST with considerable amount of intragranular defects). Experimental spectra data of these ferrites are rather limited (*f* varying basically within decade) but they nevertheless allow us to say that D-sample have asymmetrical absorption corresponding to its MST. The case of T-sample suffers from a limited frequency range as well but there are possibilities for further analysis.

In this analysis we assume that the ascending part of ACp is experimentally correctly presented (Fig. 6.2: solid blue, continued as dashed curve at lower frequencies for ability to use KKR). Symmetrical approximation by the model with $\sigma = \sigma_a = 0.34$ flawlessly reproduces the ascending part of the experimental ACp; the use of KKR for all symmetrical curve traces DCp appropriately (Fig. 6.2, blue dotted curve) with a *const* shift from experimental curve (due to neglecting NSR dispersion). The value of σ used allows us to determine from this spectrum (Eq. 2.39) that $\sigma_{lnD} \approx 0.4$, which matches the value $\sigma_{lnD} \approx 0.49$ relating to the fragment of MST depicted in Fig. 6.2 (our calculation). The only drawback of this approximation is considerable difference between the descending part of the experimental ACp and the approximation (within narrow, experimentally poorly presented frequency band).

To determine the validity of the previously mentioned descending part of the experimental ACp, it is smoothly extrapolated to higher frequencies (Fig. 6.2, blue dashed curve) and then KKR is applied to calculate DCp (red dashed curve). It practically coincides with the experimental DCp curve at lower frequencies accordingly not allowing the place for contribution from inevitable NSR. Thus the analysis on a whole allows us to conclude that the spectrum of YIG sample without intragranular defects really tends to a symmetrical one in accordance with the assumptions of the model.

On the basis of the preceding estimations, it is possible to return to the previously mentioned symmetrical spectrum of YIG (Fig. 6.1). It is pertinent to note that the ferrite is sintered at high temperature (1450 °C for 16 hours), has a density of 95 % of the theoretical value, and MST with average grain size of 12 μm [39]. Undoubtedly this ferrite is of common ceramic technology and contains a great amount of intragrain defects. For this reason the

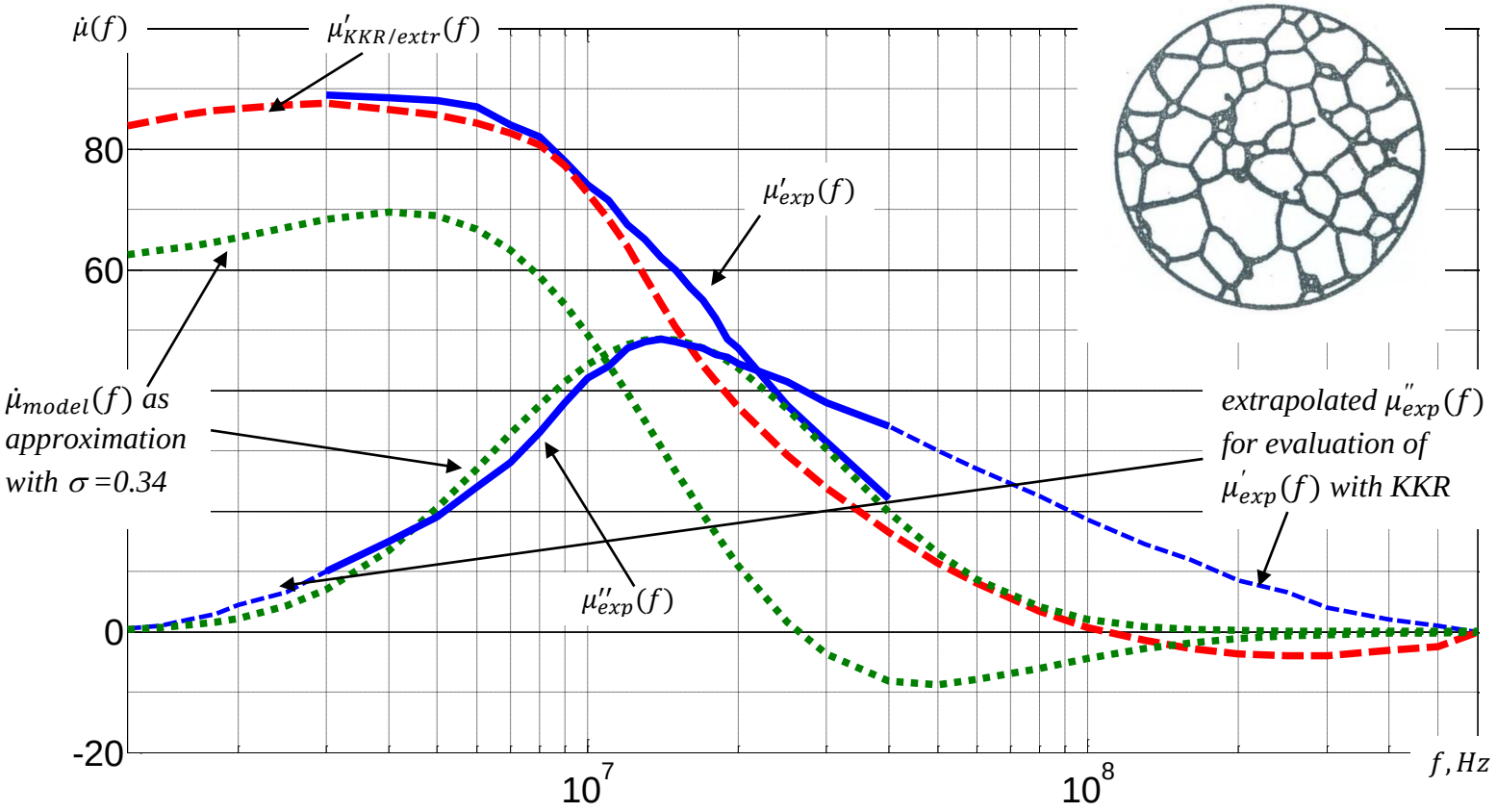

Figure 6.2 Analysis of experimental CIP of YIG sample of T-type material [data from Fig. 2 in 43 b] and its microstructure

sample's effective grain size D_{eff} (§ 2.1.8.3) is much lower than D_a (based on a value of $\mu(0) \approx 100$ and Fig. 2.19c it is near only 4 μm). As a consequence, for this coarse grained ferrite its MST may be thought of as an aggregate of several log-normal distributions generated by the populations of grains containing, e. g., one, two, three, ..., intragrain defects pinning DWs. In the frequency domain the composition of these log-normal components (similar to the case of asymmetrical MS, § 2.1.9 and § 6.3) causes considerable symmetrical broadening of the ACp of spectrum. Correlation of the spectrum data with highly defected MST of this ferrite is only qualitative.

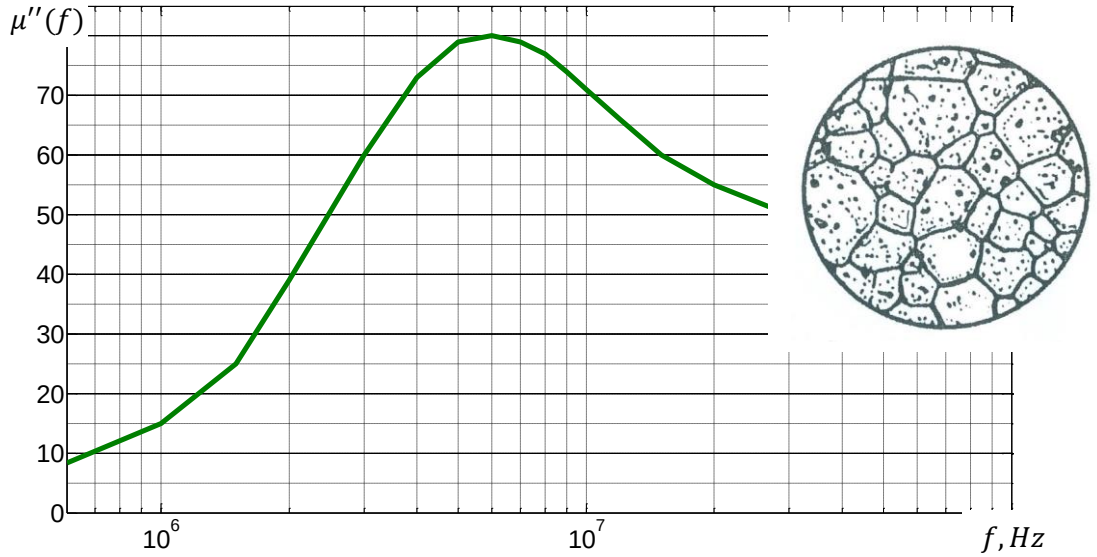

Figure 6.3 ACp of YIG sample of D-material [data from Fig. 3 in 43 b] and its microstructure

Since there are practically no symmetrical MS within the group of mentioned nickel ferrites we are searching for the one most close to symmetrical. To find such samples, with which to check Eq. 2.44, we should search among those PF sintered at relatively low temperatures (in order to avoid defects in the grains [43] (that is one of starting prerequisites of the model). A large body of such samples were produced by A. Globus' branch [43, 45–47]; nevertheless some asymmetry occurs in their ACp of CIP spectra as well (evidence of the existence of at least a few defects in grains). Even so, at this moment these are the best available representatives. In the following, the most broadband ACp with relative small asymmetry (Fig. 6.4) is taken as the experimental prototype of $\mu''_{exp}(f)$: this corresponds to $NiFe_2O_4$ ferrite from [43 a] (sintered at relatively low temperature; having $D_a = 1.8\,\mu m$ and ACp measured within 0.01...1 GHz). For verification of the quality of this spectrum by KKR, the full spectrum is needed. Hence, it is extended beyond 1 GHz by adding next typical –

natural spin resonance region (NSR) dispersion component to experimental $\mu''_{exp}(f)$ one (being studied as DW component which as a such at HF is further extrapolated (Fig. 6.1)). NSR components are extracted from two recent publication data [143, Fig. 2] and [30, Fig. 3.1]) by decomposition of corresponding spectra. Such a composite spectrum gives, using KKR and either of two mentioned $\mu''_{NSR}(f)$, almost the same value of $\mu(0) - 1$ and $\mu'(f)$ (differing from experimental values only near NSR region). So it is possible to assume that $\mu''(f)$ as DW component is measured (for $f \leq 1\ GHz$) and continued properly (for $f \geq 1\ GHz$) and can be used to verify practicability of Eq. 2.44.

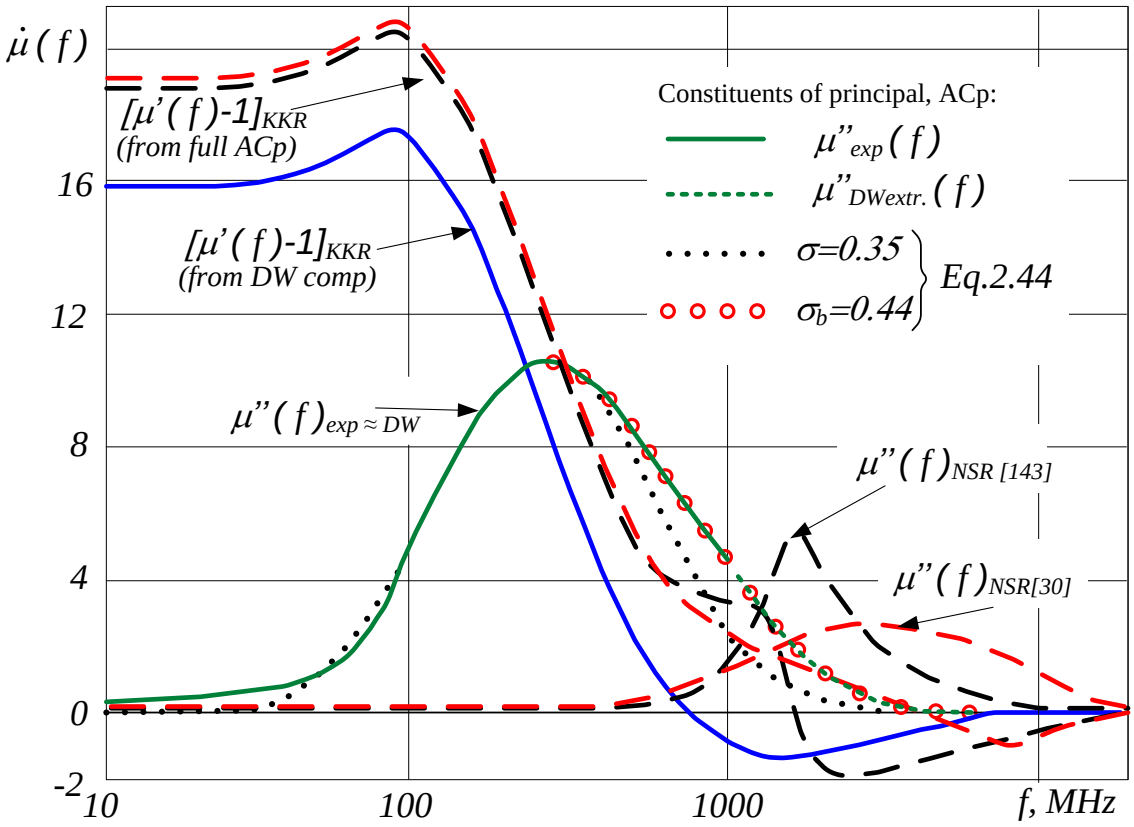

Fig.6.4. Analysis of experimental $\mu''_{exp}(f)$ [43] based on Eq. 2.44 ($[\mu'(f) - 1]_{KKR}$is calculated by KKR) [70]

Estimation based on (2.44) for the ascending part of $\mu''_{DW}(f)$ gives $\sigma = 0.35$; this allows for symmetrical spectrum (Fig. 6.4, dotted) that noticeably differs from $\mu''_{DW}(f)$ only at HF. If values $\sigma_a = \sigma$ and $\sigma_b = 0.44$ are used (for descending part of $\mu''_{DW}(f)$) then approximation correlates well along the whole $\mu''_{DW}(f)$ curve. Thus in this case of rather small asymmetry of the spectrum the values of σ differ slightly: $\sigma_a = 0.35$ and $\sigma_b = 0.44$; the use of them now allows us to cover the whole ACp (with very close approximation both for the ascending and descending parts of ACp, Fig. 6.4). The values of σ_a and σ_b regardless of

publication authors' claim that this PF is of PFI type, nevertheless show that obviously there are few defects in coarser grains. This means that value of σ_a is slightly lower, but σ_b– higher than that of true PFI. Because the asymmetry of this spectrum is small, presumably the true picture may be characterized by the average dispersion $\sigma_{av} = (\sigma_a + \sigma_b)/2 = 0.4$; the use of (2.29) in this case gives the value for grain's distribution $\sigma_{lnD} = 0.46$ and this value thus tells us that MST of PF under study is really close to the normal one (since the criterion: $\sigma_{lnD} \approx 0.5$ was developed in [89], for normal MST, i. e., one formed in the process of normal grain growth (§ 2.1.8.1)).

6.3 Application of the model for presentation of asymmetrical spectra

As it was mentioned before, real experimental CIP spectra almost without exceptions are asymmetrical. Analysis of possibilities of their presentation are based on the modified model (§ 2.1.9), firstly, on the basis of experimental data for nickel ferrite from different international publications (§ 6.3.1); later on there are added data following from our samples.

6.3.1 Presentation of CIP spectra of nickel ferrites.

If another nickel PF sample of the same composition as before [143] (Fig. 6.5), but apparently tending to TQG because of rather pronounced asymmetric character of CIP, is

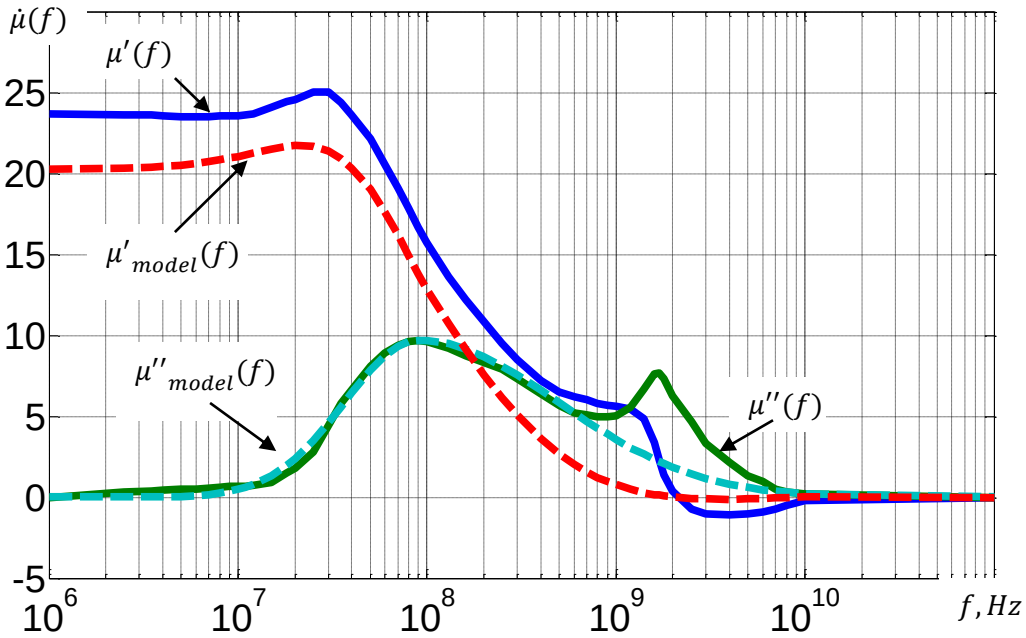

Figure 6.5 Application of the model to broadband $NiFe_2O_4$-ferrite spectrum (experimental data from [143])

subjected to similar analysis (as it was with symmetrical spectra) then it is possible to get the following data: $\sigma_a = 0.35$ $\sigma_b = 0.79$, $\sigma_{av} = 0.57$ (Fig. 6.5).

The character of DCp as DW one (Fig 6.5; $\mu'_{model}(f)$ obtained by the use of KKR to $\mu''_{model}(f)$) replicates correctly the measured data (up to ~300 MHz) until the influence of NSR component becomes significant; thus the application of the model to DW component is successful. The value of σ_{av}points to lower quality of MST of this PF as it was for a ferrite with a symmetrical spectrum.

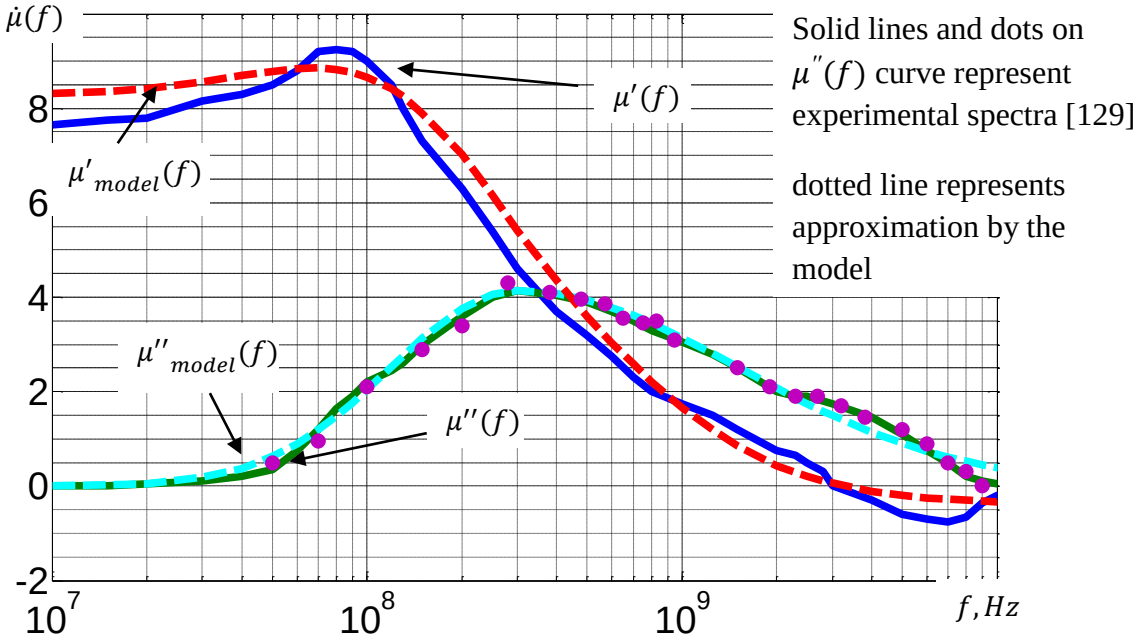

Figure 6.6 Application of the model to magnetic spectrum of $NiFe_2O_4$ ferrite (experimental data from [129])

In the case of another $NiFe_2O_4$ ferrite [129] (Fig. 6.6) the approximation by the model gives good correlation with the measured data on the whole measured CIP range with the parameters: $\sigma_a = 0.42$ $\sigma_b = 0.68$, $\sigma_{av} = 0.55$. Obviously this ferrite is fine-grained as compared with previously analyzed samples (because of low value of $\mu(0)$ and high value of f_u). Nevertheless its MST characteristics, obtained through the use of the model, are typical for common ceramic technology samples.

6.3.2 Presentation of CIP of samples with identical microstructure

Analysis of CIP of the above mentioned ferrites show that their spectra are in close correlation with MST of the specific sample. In the case of industrial grade samples their MST may vary considerably and so their spectra. In the event of similar MST the spectra as well should be similar. To prove this hypothesis we analyze the samples with similar MST.

In order to obtain the identical MST within the group of samples, we cut such samples of different inner/outer diameters (Tab. 6.1) from corresponding ferrite tiles (more details in § 4.2). In Fig. 6.7 is shown MS of one representative from group (ring sample A1 of NiZn-ferrite Ferroxcube 4S60 measured by us). The application of the model firstly is used as a symmetrical approximation with one $\sigma = \sigma_a = 0.51$ value (Fig. 6.7, dotted curve), which shows, that the spectrum is asymmetrical: there is good correlation only within $f < f_u$ region. The use of $\sigma_b = 0.81$ for the frequencies within $f > f_u$ provides good approximation for this region as well (Fig. 6.7, teal dotted line). Thus, ACp parameters: $\sigma_a = 0.51$ and $\sigma_b = 0.81$ allow for a very close approximation of the entire curve but $\sigma_{av} = 0.66$ is rather high (micrograph in Chapter 4, Fig. 4.2 b, indeed shows a considerable amount of defects in grains, having $D_a \approx 7.5\ \mu m$).

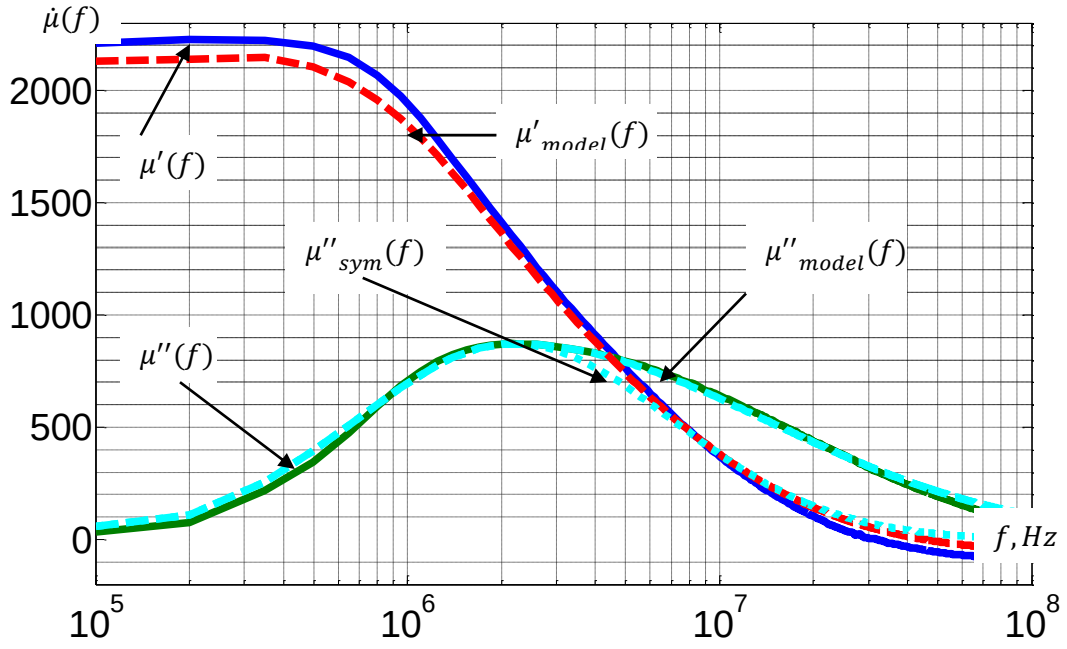

Figure 6.7. Spectrum of sample A1and its approximations.

Identical asymmetrical spectra are measured within this group of NiZn ferrite for the other 3 samples with identical MST (Tab. 6.2, group A; the CIP of samples A2…A4 are presented in Appendix 3), and the values of the model are similar (Tab. 6.2). The σ_{av} value being greater than 0.5 for this entire group allows us to conclude that MST of these samples are the normal one but with defects, which is in agreement with micrographs (Chapter 4, Fig. 4.2) – there are clearly seen a great amount of defects. A summary depiction of the CIP spectra of samples studied is shown in Fig. 6.8 (slight differences in CIP of measured samples (A1...A4) are represented by scatter marks). The dashed curve in Fig 6.8 represents data from

the Ferroxcube databook [40] and shows a slight difference with our measured CIP spectra. This difference can arise due to different microstructure of test sample material. All this demonstrates that the hypothesis about similar spectra in the case of similar MST is true, at least in case of NiZn-ferrites.

Table 6.2. Model parameters for studied ferrite cores.

Group	№	σ_{lnD}	σ_a	σ_b	σ_{av}	*The making of samples*
NiZn, 4S60	A1	0.55	0.51	0.81	0.66	*Cut from ferrite tile*
	A2	0.55	0.50	0.80	0.65	
	A3	0.55	0.52	0.81	0.66	
	A4	0.55	0.52	0.84	0.68	
MnZn, 6000HM1	B1	0.53	0.41	0.53	0.47	*Cut from ferrite tile*
	B2	0.53	0.43	0.55	0.49	
	B3	0.53	0.44	0.54	0.49	
	B4	0.53	0.44	0.57	0.50	
	B5	0.53	←	DR	→	
MnZn, TDK T37	C1	0.53	0.39	0.50	0.44	*Commercial products*
	C2	0.52	←	DR	→	
	C3	0.53	←	DR	→	

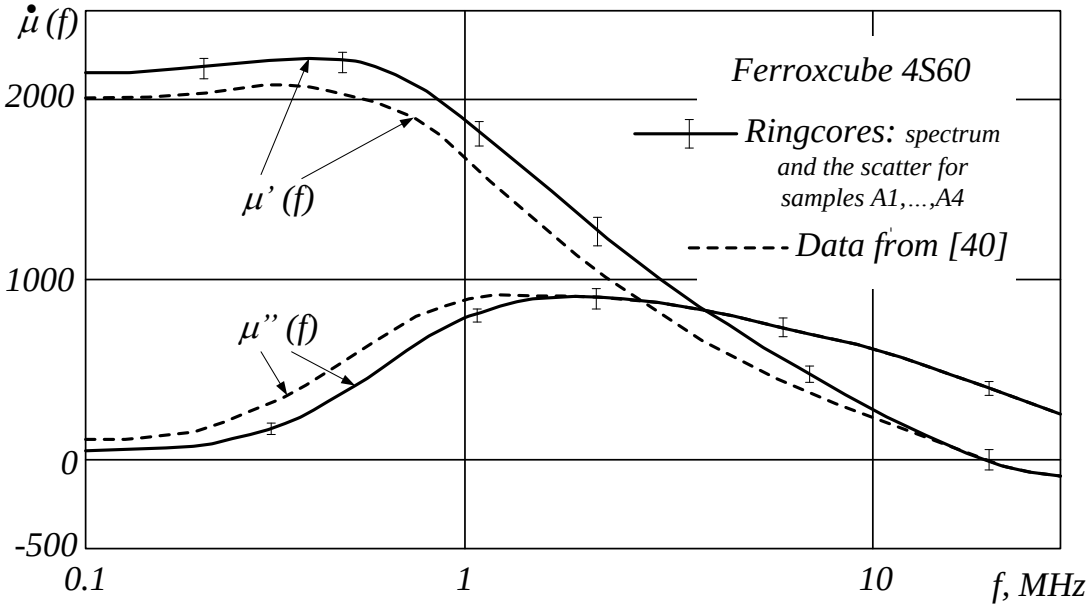

Figure 6.8 Collection of CIP spectra of 4S60 NiZn-ferrite [71].

To prove this hypothesis for MnZn-ferrites another group of samples (dimensions in Tab. 6.1) are cutted from corresponding tile, thus having similar MST are forming group B –

MnZn 6000HM-1ferrite toroidal cores (Tab. 6.2). The application of the model to the smallest sample – B1 is presented in Fig. 6.9. The model parameters for B1 sample are $\sigma_a = 0.41$ $\sigma_b = 0.53$, $\sigma_{av} = 0.47$. The approximation showed good correlation with experimental data. Directly carried microstructure analysis provided a value of $\sigma_{lnD} = 0.53$, which is in good correlation with the σ_{av} value. In principle it points to a more or less normal microstructure, with only a few intragrain defects. The micrograph provided by SEM (Chapter 4, Fig. 4.4, a) indeed show that there is minimal amount of defects, but the porosity level is still is considerable. Nevertheless the close correlation between the model parameters and of the microstructure indicates that the assumption that a large amplitude absorption region is determined by DW processes is correct.

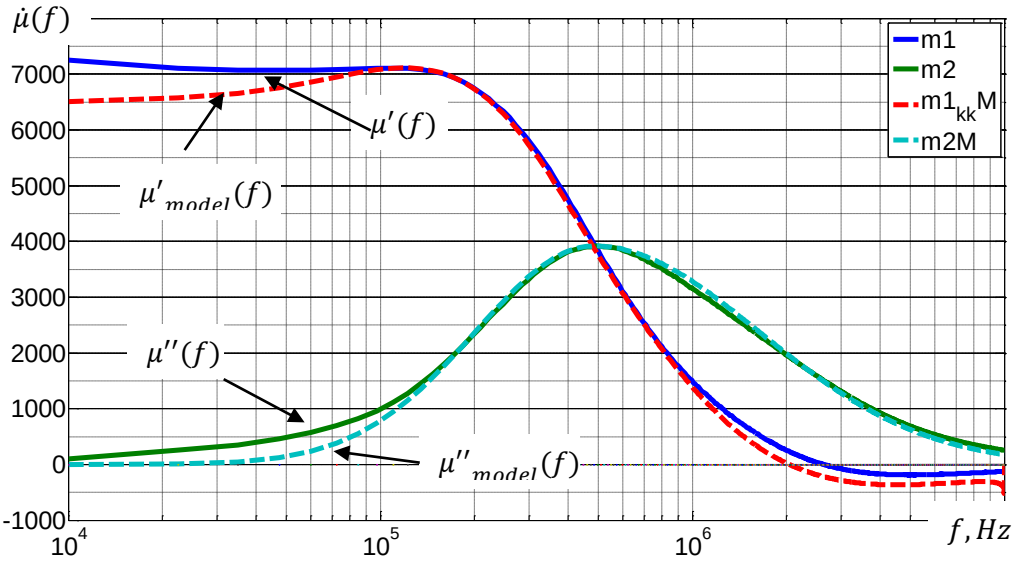

Figure 6.9. Spectrum of sample B1 and its approximations.

If we look at the spectra of other samples of this group with the succeedingly growing dimension (Fig. 6.10 and 6.11) then it is noticeable that the maximum of absorption f_u gradually shifts to lower frequencies with the growth of dimensions of the samples (Tab. 6.1). However the general view of spectra B1...B4 are similar and they can be approximated by nearly the same parameters of the model: these parameters obviously still represent the MST and its similarity. Contrary to this the spectrum of sample B5 (Fig. 6.11) is something else compared to previously mentioned CIPs – it is pronouncedly resonant, near-symmetrical and narrow band – evidently the dimension resonance (DR, § 6.4) becomes significant and the spectrum is no longer directly connected with MST. It is likely that a small component of DR is there in samples B1...B4 as well, and is the chief cause of shift of f_u.

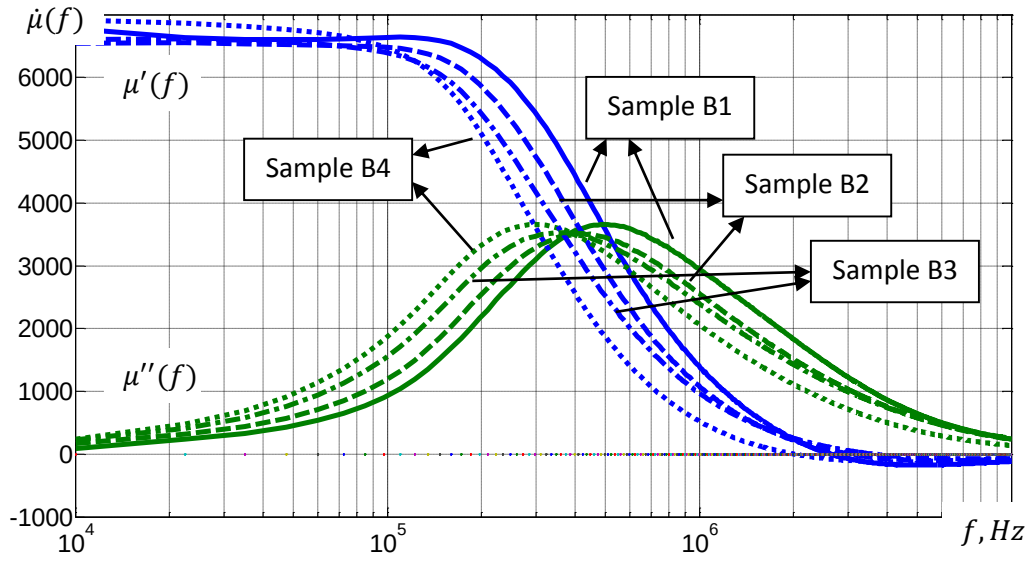

Figure 6.10. CIP of samples B1...B4

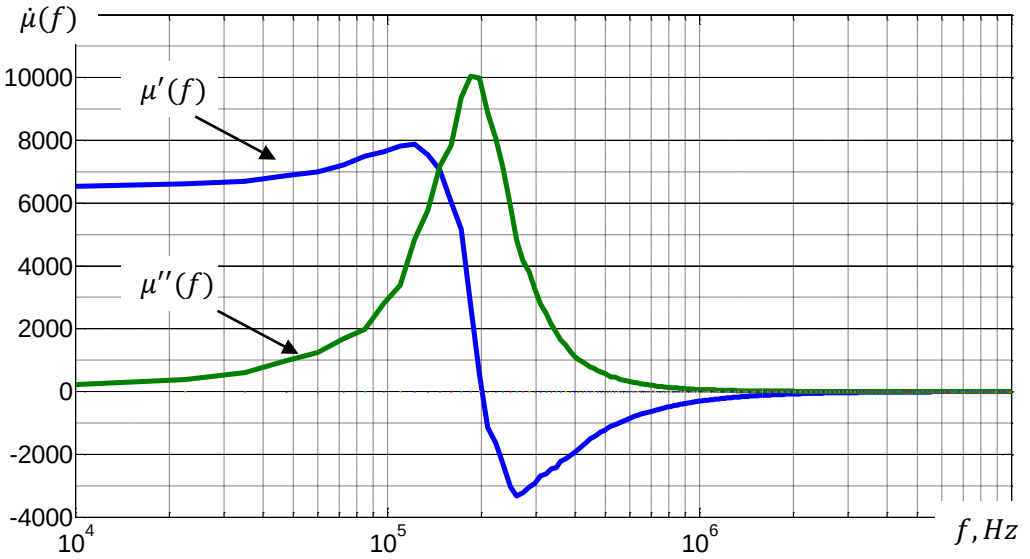

Figure 6.11. CIP of sample B5

The CIP of samples with identical MST for both the NiZn and MnZn ferrite materials showed good correlation between CIP and MST of different sized samples in each group, except the sample B5, where the conditions for the DR are realized. With this exception, evaluation of model parameters for both the ferrite materials studied are in agreement with the parameters obtained from their microstructure.

6.4 Presentation of CIP of samples exhibiting dimensional resonance

The dimensional resonance (DR) phenomena still is not well studied. However understanding of DR is essential – the effects related to this phenomena should be avoided in designing SMPS magnetic components [140–142]. These effects often need to be obviated since they convert not only the spectrum of CP (i. e., $\dot{\mu}_{int}(f)$ to $\dot{\mu}_{ext}(f)$) but can destroy devices by cracking or shattering magnetic core if excited at DR frequencies f_{DR}. Due to the work of Brockman, et. al., [26], Snelling [146] and Skutt [140], a simplified theory behind this phenomena has been developed. This theory is based on calculations for infinite slab; therefore it addresses the problem only in principle. Thus, the cause of this phenomenon is based on forming the standing electromagnetic waves that in actual dimensions of devices can appear due to high values of permeability μ' and permittivity $\varepsilon'$of material simultaneously, from it there are possible to define several conditions for the dimensional resonance in ferrites to occur:

- high permeability value;
- high permittivity value;
- one of the core cross-sectional dimensions must be comparable to half of the wavelength.

So, the wavelength in the material with relative permittivity ε_r and permeability μ_r can be written as [146]:

$$\lambda = \frac{c}{f\sqrt{\varepsilon_r \mu_r}} \tag{6.1}$$

For a material with losses the Eq. (6.1) can be reworked as [146]:

$$\lambda/2 = \sqrt{(c_0^2/2f^2)/\left[|\mu||\varepsilon| + \mu'\varepsilon'(1 - tan\delta_m tan\delta_d)\right]} \tag{6.2}$$

where $c_0 = 1/\sqrt{\mu_0 \varepsilon_0}$ – velocity of electromagnetic waves in vacuum.

This means, that for MnZn-ferrite cores having high permittivity the wavelength is shortened, therefore the third criteria can, in practice, be readily achieved.

Based on Eq. (6.2) and three defined conditions, taking a typical value for MnZn ferrites [146] $\varepsilon_r \approx 10^5$, and three different μ_r values (2000, 5000, 10000) – it is

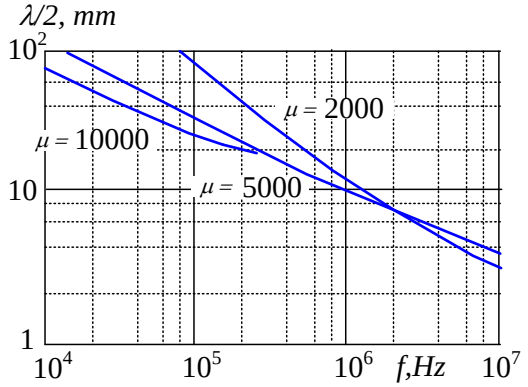

Figure 6.12 Dimensional resonance relation to $\frac{\lambda}{2}$, μ and f [146].

possible to construct DR appearance dependency from wavelength and frequency (Fig. 6.12). As can be seen – the DR resonant frequency becomes smaller for higher permeability ferrites. So for a ferrite with $\mu = 5000$ and $L = 10\ mm$ the DR can occur at a frequency of 1 MHz. This means that large MnZn cores cannot be used for HF applications [140, 146]. Avoidance of DR means to ensure, that that cross-sectional dimensions are much smaller than the half-wavelength obtained by (6.2).

For the experimental study of DR, firstly the industrially made toroidal high permeability (~ 6000) MnZn cores of TDK ferrite T37, with dimensions (in mm) R12.5 × 7.5 × 5, R20 × 10 × 7, R40 × 24 × 16 (Fig. 6.13, Tab. 6.3) were selected. The permittivity of this material was measured on plates cutted from C3 core (largest) with sputtered copper electrodes (§ 5.6). In the similar way was obtained the permittivity for the other studied MnZn material 6000HM-1. Measured values of permittivity for both studied ferrite materials are very high (with values of $\varepsilon(0)_{exp} = 1.5 \times 10^6$ for 6000HM-1 and $\varepsilon(0)_{exp} = 13.5 \times 10^6$ for T37 materials (Tab. 6.3)). Obviously, with these high values of $\varepsilon(0)_{exp}$ the conditions for DR can be realized already within samples with only moderately large dimensions.

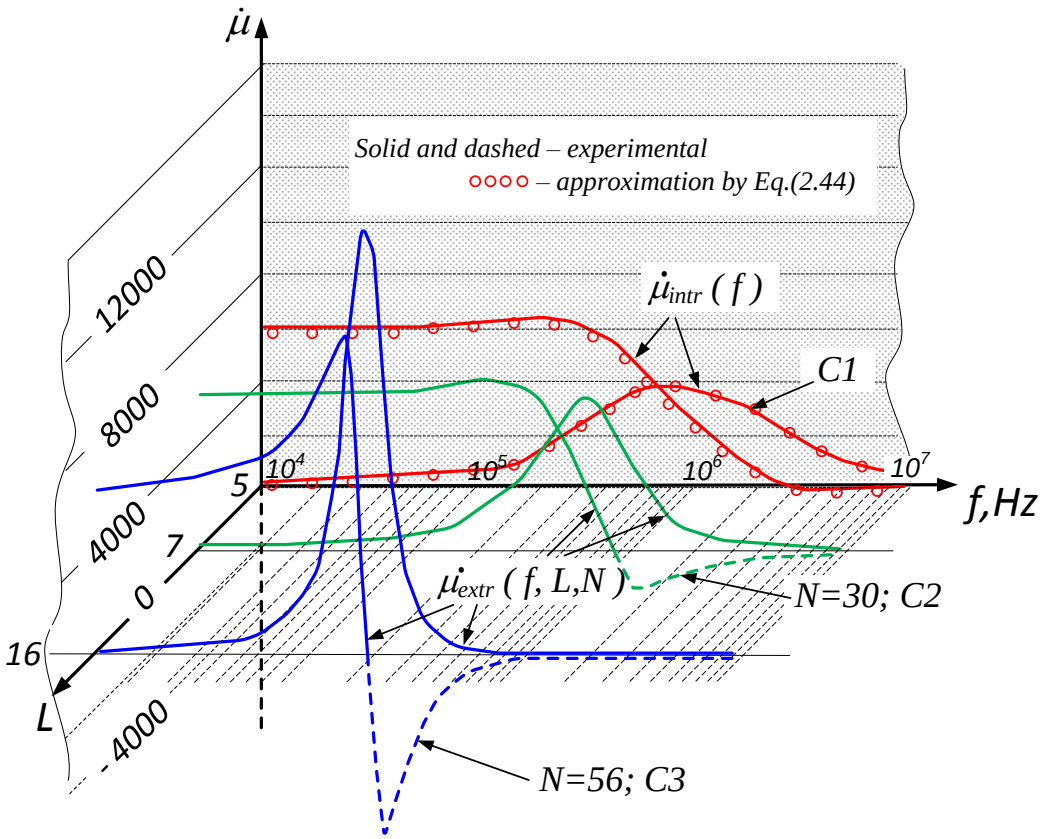

Figure 6.13 The advancement of DR in samples C1…C3 (Tab. 6.2.) in relation *L* and *N* [70]

For experiments the ferrite samples were provided with the windings covering most of the ferrite core surface. The dimensional resonance was observed in ferrite cores with relatively large cross sectional area (C2 and C3 cores), within MHz frequency range (Fig. 6.13), while the smallest C1 core did not show this resonance response. In such a medium, the deciding factor in setting up DR is L: Fig. 6.13 shows that no DR arises (sample C1) if L is small enough but with its growth DR appears and enhances (samples C2, C3) – f_{DR} shifts to lower frequencies and $\dot{\mu}(f) = \dot{\mu}_{ext}(f)$ as extrinsic characteristic gets more and more resonant. It is particular remarkable that in these processes $\mu(0) \approx const$, that $\dot{\mu}_{ext}(f)$ continues keeping with KKR.

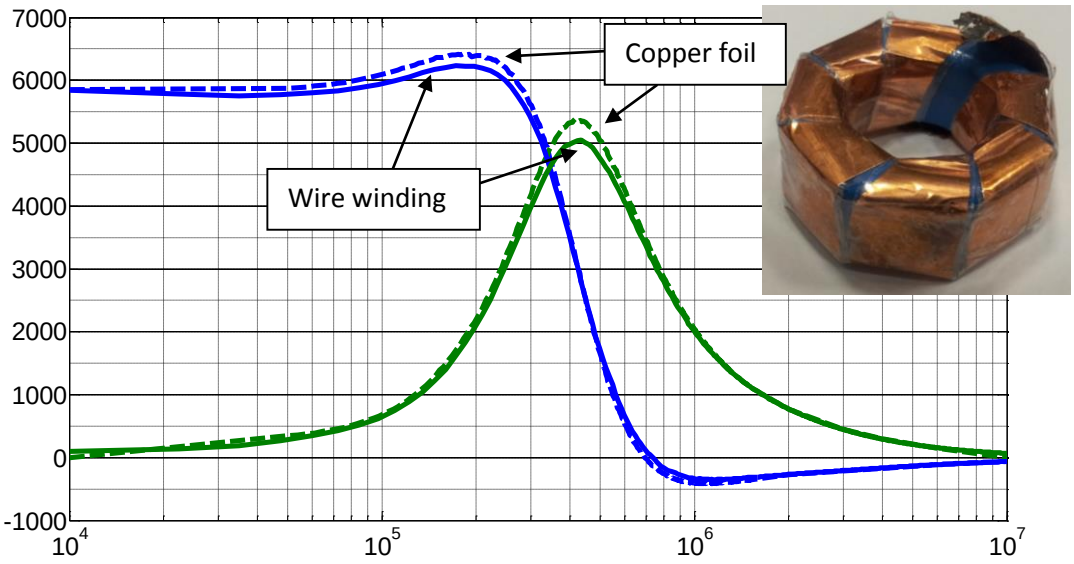

Fig. 6.14. CIP measured with copper foil winding (N = 7) and wire winding (N = 10)

Besides these our investigations show that a great influence on DR comes from number of turns N of winding (Fig. 6.15), that has not been mentioned in other known publications on DR. It was verified, that influence from N does not come from stray inductance and self-capacitance of winding, but is fundamental. There were made special windings from copper foil in order to cover most of the ferrite core surface . The measured CIP spectra with copper foil windings (N = 7) and wire windings (N = 10) showed practically identical values over whole measured frequency range (Fig. 6.14).

This DR dependence on N is not fully understood; formally it can be explained on the basis of Eq. 6.2. If an inductive PF device is powered by *const.* voltage, then for higher N the impedance of coil increases (as N^2), which results in decreased magnetic field and decreased magnetic losses, therefore from (6.2) λ grows and f_{DR} is shifted to lower frequencies.

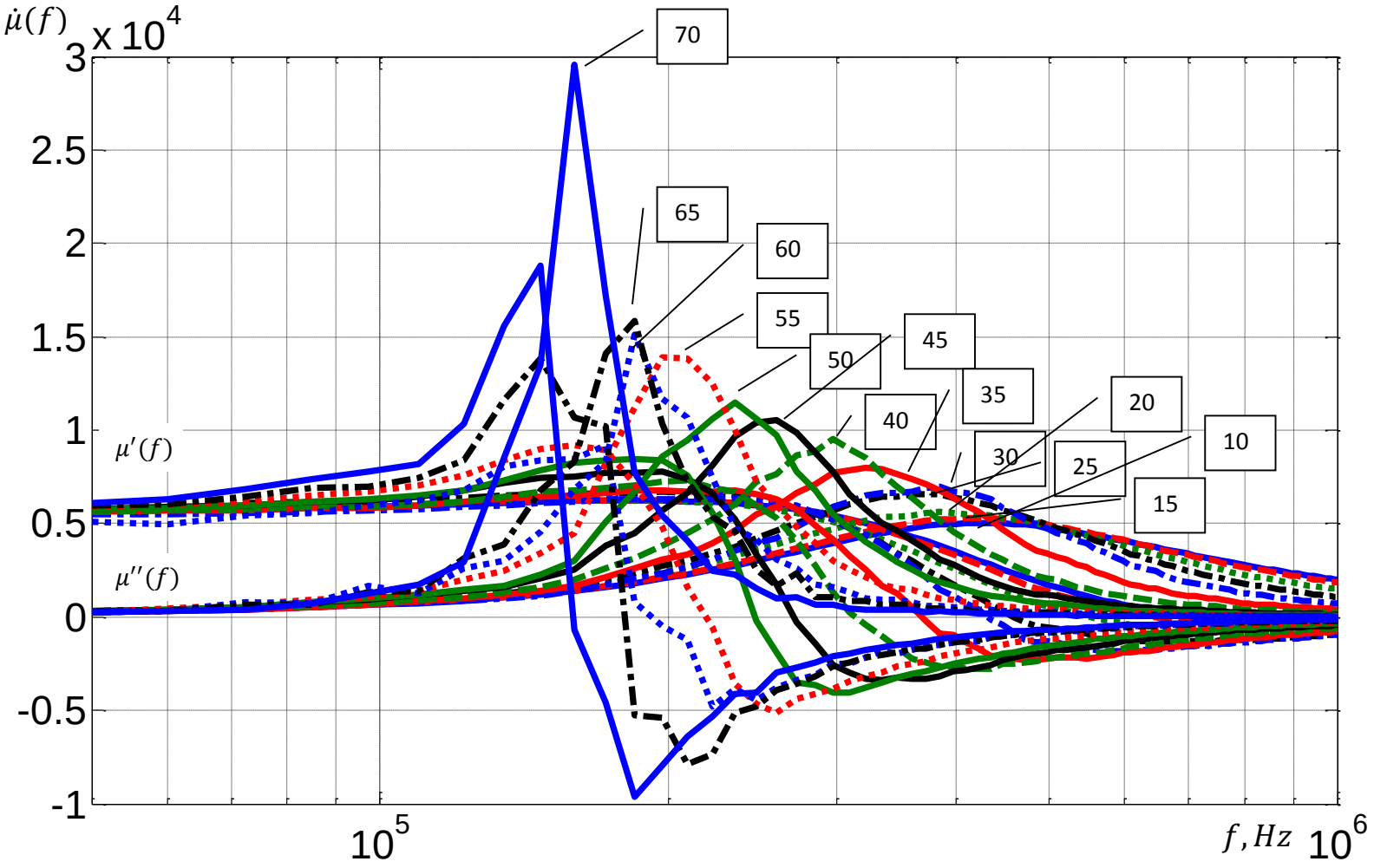

Figure 6.15. Dimensional resonance dependence from the number of turns *N* for sample C3.

Table 6.3. Characteristics of MnZn ferrite cores used in the study.

Group	№	Dimensions, mm	A, mm^2	$\varepsilon(0)_{exp}$	$\mu(0)$	$\mu(0)_{exp}$	D_a, μm	σ_{lnD}
MnZn 6000HM-1	B1	R10 × 4.3 × 10	28.5	1.5×10^6	6000	6750	12.9	0.53
	B2	R20 × 9.1 × 10	54.5	1.5×10^6	6000	6530	12.9	0.53
	B3	R25 × 12 × 10	65	1.5×10^6	6000	6650	12.9	0.53
	B4	R30 × 14.3 × 10	78.5	1.5×10^6	6000	6850	12.9	0.53
	B5	R33 × 10 × 10	115	1.5×10^6	6000	6523	12.9	0.53
MnZn, T37	C1	R12.5 × 7.5 × 5	12.5	13.5×10^6	6500	5800	10.7	0.53
	C2	R20 × 10 × 7	35	13.5×10^6	6500	5900	12.7	0.52
	C3	R40 × 24 × 16	128	13.5×10^6	6000	6000	13.4	0.53

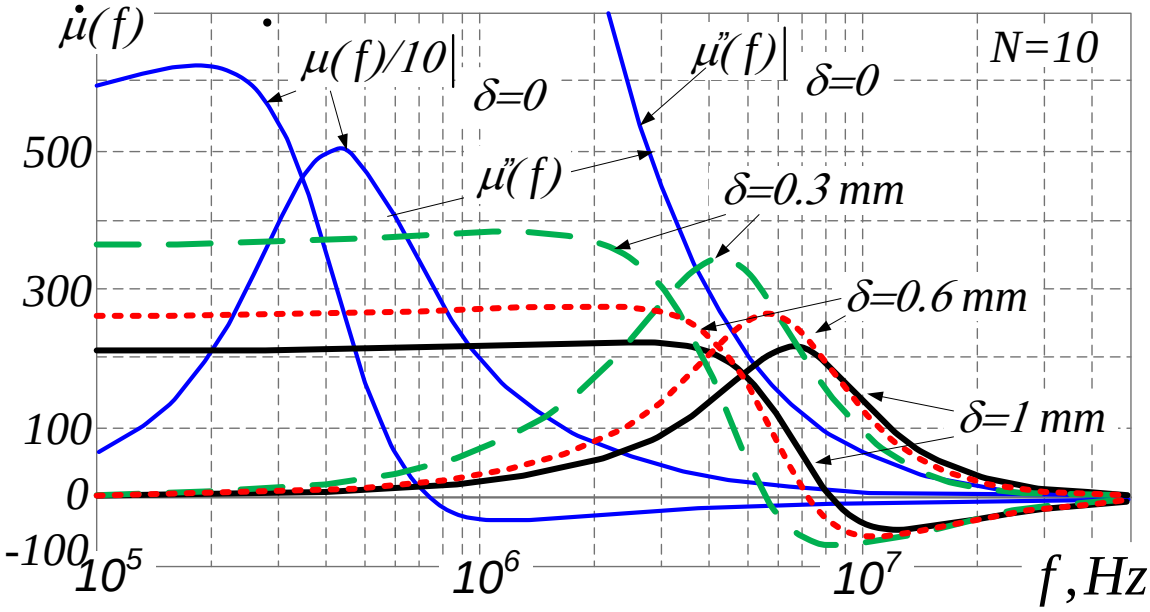

Figure 6.16. Dependence of DR from nonmagnetic gap size δ in C3 core [70].

We continued experimental investigations and obtained curves for different numbers of winding turns (Fig 6.15). It is seen that the number of winding turns *N* dramatically affects the $\dot{\mu}_{extr}(f, L)$ – for smaller number of turns the DR effect becomes weaker, and the maximal frequency of DR shifts to higher frequencies. Thus, by changing the number of winding turns, we can shift the DR, and with lower number of turns DR effect becomes less pronounced (the μ''_{max} changes from 15000 at N=70 to 5000 with N = 10; Fig. 6.17, *b*; Fig. 6.15).

It is well known that non-magnetic gap δ for non-DR ferrites translates characteristics of spectrum to higher frequencies. To appreciate the significance of δ for ferrites with DR,

corresponding experiments are carried out, because it is not known [140; 146] which permeability assures DR – intrinsic permeability of ferrite sample (measured on toroids without nonmagnetic gap δ) or effective one of circuit (measured on gapped toroids: calculated by Eq. 6.13), when the high value of intrinsic permeability is lost.

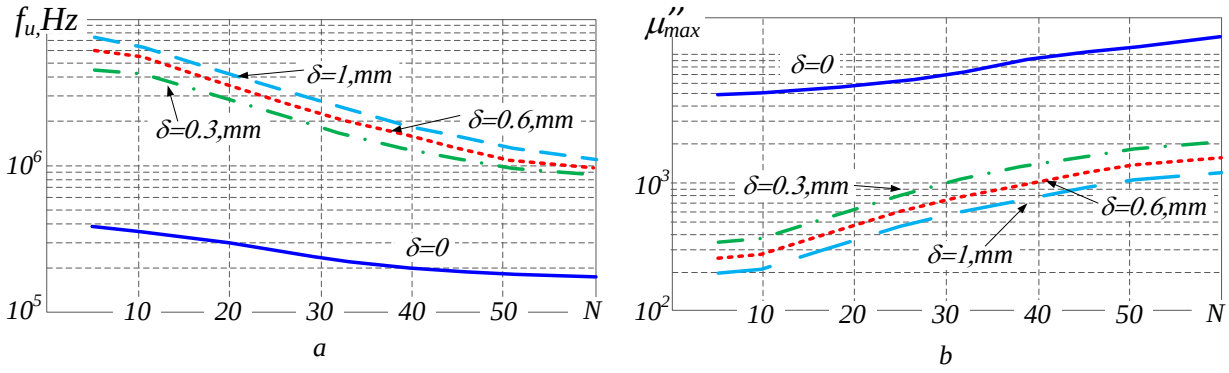

Figure 6.17. DR characteristic f_u and μ''_{max} dependence from N in sample C3.

Our experiments show that introduction of the nonmagnetic air gap in the C3 core, as it usually is, shifts CP spectrum to higher frequencies with dimensional resonant processes presence in the core (Fig. 6.16, 6.17, 6.18, Appendix 5). The amplitude is getting smaller and f_u increases with larger gap size. The ACp maximal frequency f_u dependence on air gap size (for different *N*) is presented in Fig. 6.18, *a*; in Fig. 6.18, b is presented ACp maximum value μ''_{max} dependence on air gap size (for different *N*).

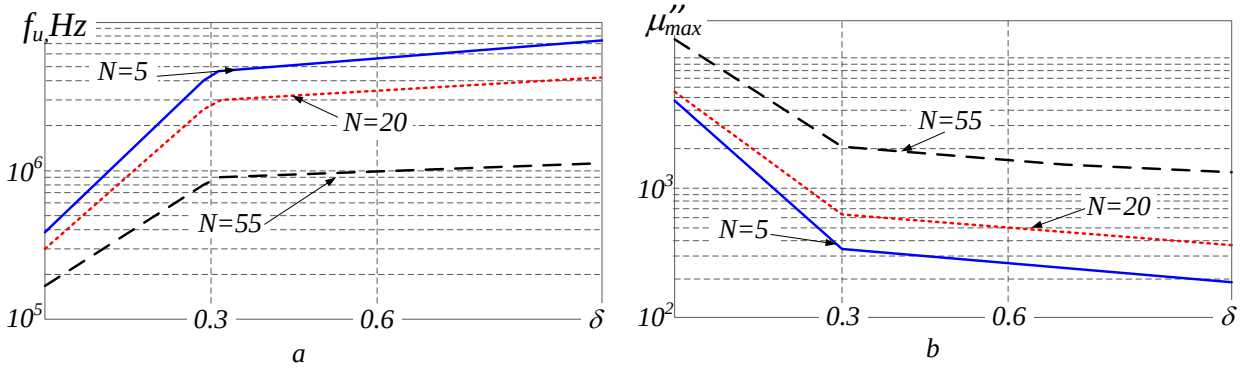

Figure 6.18. DR characteristic f_u and μ''_{max} dependence from gap in sample C3.

Yet it can be seen (Fig. 6.16) that the shifting is more pronounced for the ascending part of $\mu''_{ext}(f)$ (controlled by coarser grains) than for the descending part (ensured by finer grains). This once again (similarly as in modelling of $\dot{\mu}_{int}(f)$) shows that coarser grains with their higher permeability and lower coercivity are more sensitive to excitations, this time to demagnetizing fields.

The ACp maximal frequency f_u dependence on N (for different core gap sizes) is presented in Fig. 6.17, *a*; in Fig. 6.17, b is presented ACp maximal value μ''_{max} dependence on N (for different core gap sizes). In both cases this dependence for gapped ferrite cores and for ones without an air gap are similar.

The DR phenomena analysis was also performed on lower permeability MnZn toroidal sample (sample–DR, with geometrical dimensions of R32 × 16 × 8; 2000HM-A material with permeability μ = 2000, CIP spectrum with δ = 0 in Fig. 6.19); the experimental measurements were performed with a constant number of turns $N = 25$ (for reference, for confirmation of DR appearance in our sample-DR the another sample of the same material, presented in [193] obviously for smaller dimension sample is added). As it is seen (Fig. 6.19) – the CIP spectrum is shifted to lower frequencies and is showing clear resonance attributes for this permeability and dimension values of sample as well.

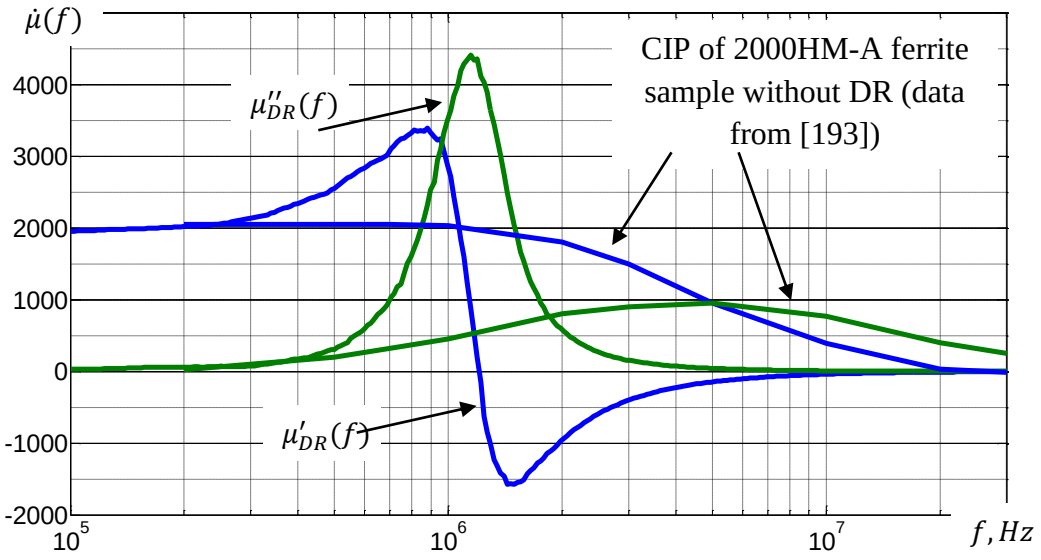

Figure 6.19 CIP of 2000HM-A ferrite samples ($\delta = 0$)

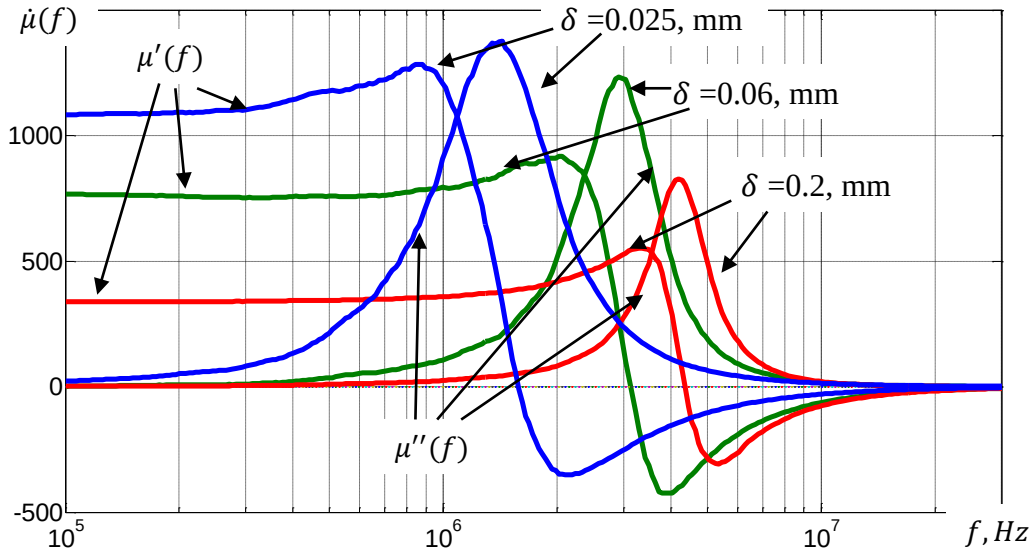

Figure 6.20 CIP of 2000HM-A ferrite sample-DR, measured with three different gap δ sizes

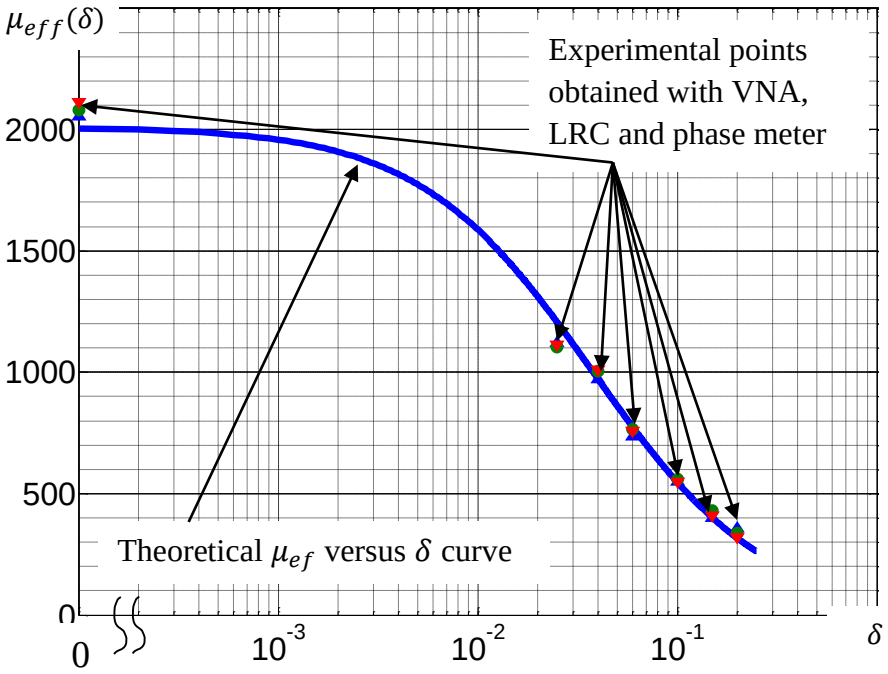

Figure 6.21. Effective permeability μ_{eff} versus δ according to Eq. 6.3 (with parameters: $\mu = 2000$; $0 < \delta < 0.5\ mm$; l = 75.4 mm), and measured experimental results from CIP

The DR dependence on air gap for sample-DR, similarly as with C3 core, once again showed that the amplitude is lowered and f_u increases with increased gap size (the measurement results for three air gap values are presented on Fig. 6.20). In order to verify the validity of the experimental results, they should be compared with the theoretical effective permeability values:

$$\mu_{eff} = {\mu}\Big/{1 + \left(\frac{\delta}{l}[\mu - 1]\right)} \tag{6.3}$$

where μ_{eff} is the effective permeability, δ – the gap size, $l = 2\pi\left(\frac{R+r}{2}\right)$ – the magnetic line length in the toroidal core of outer radius *R* and inner radius *r*.

The close match of theoretical and experimental μ_{eff} (Fig. 6.21, experimental points were measured with VNA, LRC bridge and phase meter for different gap sizes: $\delta = 0.2; 0.15; 0.1; 0.06;\ 0.04; 0.025$, mm) confirms the validity of the obtained experimental data. From the above assumptions and experiments we can conclude, that DR cannot be removed by introducing a nonmagnetic air gap in the core (the gap only shifts the DR to HF together with lowered μ''_{max} (Fig. 6.16, Fig. 6.20)).

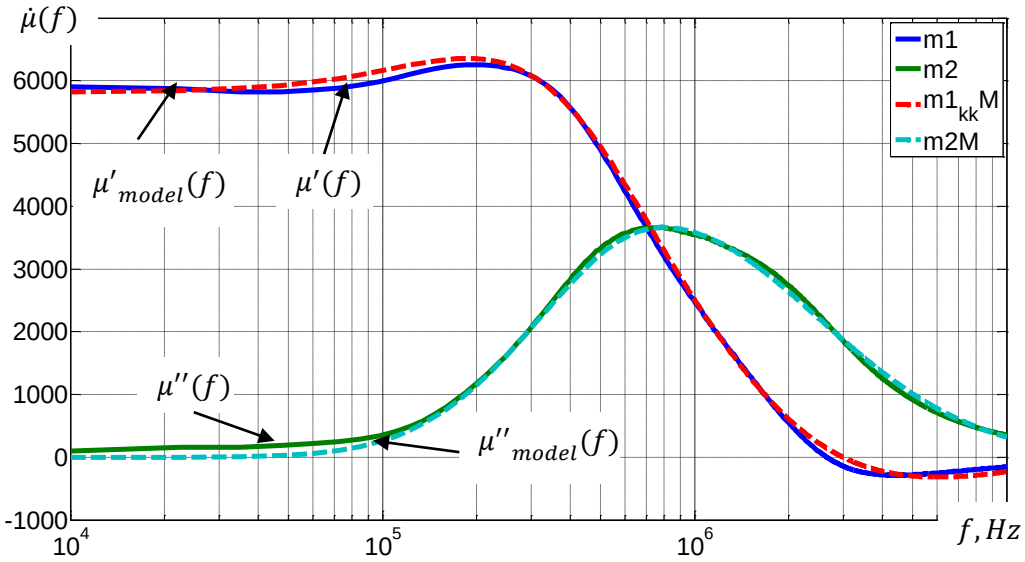

Figure 6.22. Model application to C1 sample.

The collection of CIP data for set of T37 ferrite cores is correlated with the standard Snoek's relation (Eq. 2.37; zone in Fig. 6.23). There C1 sample data is used as a reference (without the influence of DR and turns number *N* of winding, representing the material properties; Fig. 6.22) The model parameters of C1 sample are: $\sigma_a = 0.39$ $\sigma_b = 0.50$, $\sigma_{av} = 0.44$, and this points to good MST quality. The data obtained from micrographs $\sigma_{lnD} = 0.53$ for this sample indeed correlates with the obtained σ_{av} (see Tab. 6.1 and Tab. 6.2). Yet, – the more evident asymmetric character of CIP spectrum and bigger difference between the σ_{av} and σ_{lnD} shows, that there are still some defects.

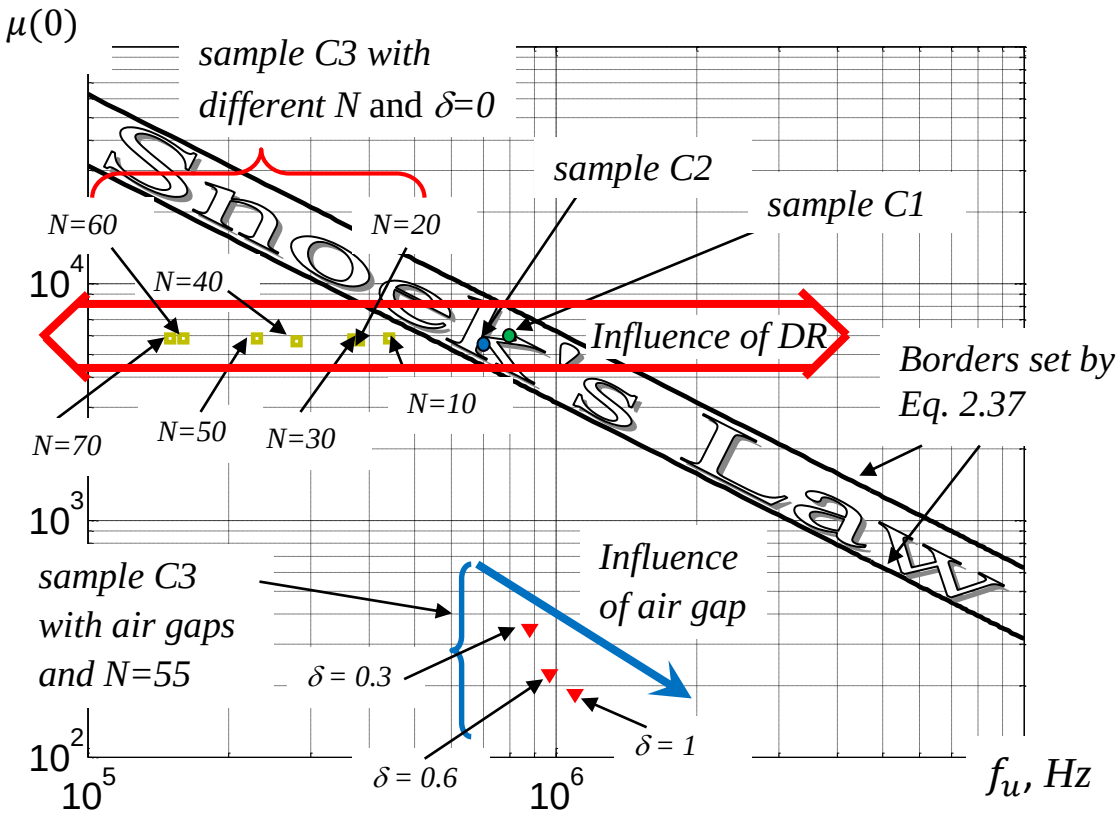

Figure 6.23 Analysis of CIP data of T37 ferrite samples (group C) with of DR on non magnetic gap δ and different winding turn N count for C3 sample.

In Fig. 6.23 sample C1 appears (as blue dot) in zone of Snoek's Law. For greater dimension samples (e. g., C3) there is seen clear deviation from Snoek's Law type relations on change of N (Fig. 6.23). This once again demonstrates that DR first of all represents the ferrite as the electromagnetic resonator rather than intrinsic material of ferrite. In its turn the dependence only on δ seems to follow Snoek's Law type relations (Fig. 6.23, sample C3, *N=const*).

6.5 Complex initial permeability as intrinsic and extrinsic property

As a whole the application of the model to experimental CIP spectra of ferrites as intrinsic property showed good correlation with CIP measurement results and microstructure (additional graphs of the studied ferrites CIP spectra and data of applied model are presented in Appendix 3). The data obtained by applying the model to our studied samples is combined in Table 6.2. The outcomes of modelling – successful quantitative estimations of σ_{lnD} from CIP spectrum is of principal importance showing that there exists a fundamental connection between the characteristics of CIP and that of MST. The analysis of CIP spectra measured by

other scientists revealed that big amount of these spectra belongs to TQG (i. e. [53, 129, 143], a. o.), but still there can be found some samples that are close to IQG (with near-symmetrical CIP spectra and the value of $\sigma \approx 0.5$ [39, 43, 148]).

At the same time the study of CIP as extrinsic properties $\dot{\mu}_{ext}(f)$ reveals that there is a significant distinction from intrinsic properties $\dot{\mu}_{int}(f)$ in response to influential parameters. This results in indirect dependence of $\dot{\mu}_{ext}(f)$ from the intrinsic influence factors, e. g., the microstructure of the samples studied. But in opposition to this for extrinsic CIP there is a definite influence from the core dimensions and number of measurement winding turns (i. e., the extrinsic factors). The analysis of influence of a non-magnetic air gap on the DR revealed that regardless of the gap size – the DR remains within the core. Thus, the only possible solution found in decreasing the influence of DR to CIP – is to decrease the number of measurement winding turns. Even so – we cannot completely remove this phenomenon (as can be seen from Fig. 6.23 – there still remains a difference between C1 sample data and that of C3 with 5 measurement winding turns). Therefore samples B5, C2 and C3 exhibiting dimensional resonance, means that CIP is controlled by extrinsic factors (see Ch. 6.4). This makes it impossible to use the model in present form for the spectra influenced by extrinsic factors.

Thus, the conclusions on the practical use of the model are:

(1) the modelling of $\dot{\mu}_{intr}(f)$ based on effects coming from grain sizes distribution and defects (shorter: MBDD – modelling based on distributions and defects) works well in practice;

(2) the use of the model MBDD gives grounds for the statement that CIP spectra can be applied as qualitative nondistructive method for evaluation of MST: ACp typically have the width (in units of σ): $\sigma_{av} = 0.4 \cdots 0.5$ for high quality laboratory samples, and greater values for industrial ones;

(3) DCp have pronounced negative values ($f > f_u$) for IQG and small or moderate values for TQG (if they are not masked with NSR dispersion);

(4) DW processes indeed are related with the large amplitude dispersion region of CIP spectrum;

(5) in the case of magnetic spectrum with single absorption and dispersion region (when dispersions from DW and NSR processes overlap), parameters σ_a and σ_b of (2.14) are with limited exactness (especially σ_b) and so there is need for further investigations (aimed for more clear separation of DW and NSR contributions).

7 CONCLUSIONS AND FUTURE INVESTIGATIONS

7.1 Conclusions

In the promotion work the applied aspects of analytic presentation of the CIP both for the intrinsic and extrinsic properties of ferrite materials are investigated. A significant part of this work is based on experimental measurements of the complex initial permeability of MnZn and NiZn ferrites (toroidal samples with different dimensions both – factory made-cores and those cut from ferrite tiles). As the result of this work there are proved all of the promoted thesis. Briefly summarizing, the main results of this work can be formulated as follows:

1. All of the experiments were performed in weak excitation fields. So, the measured data correspond to CIP. CIP spectra of the nickel-zinc (NiZn, 4S60) and manganese-zinc (MnZn, 6000HM-1 and T37) ferrites were measured in wide frequency range (from 10^3–10^4 to 10^7–10^8 Hz), thus covering the large amplitude absorption region of CIP in full measure for correct evaluation of DW component contribution. The obtained results can be used not only for the low-power elements of SMPS (such as common-mode chokes ferrite beads a. o.), but for magnetic components for high frequencies as well.

2. For the CIP measurement both the classical and less labor-saving approaches were used. The CIP spectra obtained with the VNA was compared with the classical measurement methods, such as phase meter and Q-meter measurements, and showed a good correlation between them. All of the obtained CIP spectra was verified by the correspondence to the Kramers-Kronig relations. The correlation turned out to be quite good for all of the studied samples CIP spectra, which proves that the measurement methods used are valid and with a high degree of accuracy. Thus we can conclude that experimental CIP data is correct and the analysis based on the use of this data is valid.

3. The use of Water-jet technology to cut the samples from ferrite tiles was the most appropriate choice of cutting method. As the SEM element analysis of cut samples does not reveal any contamination nor change (e. g., additives, melting) of microstructure (even on the cutting edge).

4. The microstructure of the ferrite samples was examined and analyzed experimentally. The characteristic feature of their MST is that standard deviation of grain size diameter logarithm (σ_{lnD}) has the value close to 0.5. This approximate equality also holds for many other ferrites of different compositions (also studied by other authors). Thus this value of

$\sigma_{lnD} \approx 0.5$ is a characteristic value for ferrites with normal MST and may point to homogeneity of MST.

5. The study of NiZn and MnZn ferrites with similar MST revealed, that:

- the MST of NiZn 4S60 ferrite material is with moderate amount of defects in grains and high porosity level (according to micrographs). And the application of the model to these ferrite CIP spectra although proved that there are defects in microstructure (with $\sigma_{av} > 0.5$). The CIP spectra of NiZn ferrite samples remains the same (regardless of the dimensions of the tested sample) if their MST is similar;

- the MST and model parameters of MnZn ferrites (small dimension samples) showed better microstructure quality (with σ_{av} close to 0.5). In its turn the CIP for relatively small and medium MnZn ferrite cores are similar, but f_u shifts to lower frequencies with incrementally increasing dimensions of the sample. That shift of f_u probably is caused by the weak influence of DR. And, the CIP of the largest of tested samples showed clear resonance attributes , which points to appearance of DR.

6. The Kramers-Kronig relations optimization for large amounts of data was successfully developed within the MATLAB® programming language. This proved, that:

- by using the Kramers-Kronig relations, we can evaluate CIP spectra quality (i.e. evaluate the correspondence of ACp and DCp parts), made more clear the noisy measurement data and together with CIP spectra model allow for the spectra reconstruction, which is essential if the measurement equipment does not support all the desired frequency range (or in case, when there is need in combining of various CIP data from different publications).

- KKR also can be used for CIP spectra decomposition to DW and NSR parts, which allows evaluating the spectral components and their contribution to whole CIP spectra.

7. The experimental investigations of CIP as extrinsic properties $\dot{\mu}_{ext}(f)$ (mainly on MnZn T37 material large toroidal cores) reveals its essential difference from $\dot{\mu}_{int}(f)$, its response to influential parameters. The results include that:

- that dimensional resonance in fact is dependent from wound coil turns and from non magnetic air gap.

- the application of the nonmagnetic gap does not remove the DR, the whole CIP is shifted to higher frequencies with the DR remaining;

- the CIP influenced from DR does not follow Snoek's Law type relations;

- the analytical model is applicable within ferrites with normal microstructure till the appearance of the dimensional resonance, when the CIP dependence on MST fades.

The above findings can be used in:

- calculation of ferrite beads active component for EMI suppression (imaginary part with KKR)

- designing of a new type of common mode noise filters for better electromagnetic compatibility;

- for model-based optimization of calculations of common mode chokes for current SMPS;

- for preventing the damage of magnetic components due to dimensional resonance.

Performed analysis reveals PF CIP physical significance. Besides, the analytical model in coup with KKR makes it possible to quantitatively analyze the spectra (which, judging from publications, cannot do other researchers).

7.2 Future investigations

The complex permeability was studied as CIP, so as the next step, there could be performed experiments within stronger magnetic fields in order to obtain dependencies for high power elements of SMPS within high frequencies. Besides there is used a number of empirical parameters for modeling the CIP spectra. Particularly, as such is static permeability $\mu(0)$, for which there still is not known a clear theory (of real processes that determine its value). Thus, the research in this field would be actual as well.

Contrary to the CIP spectra, that were broadly studied and described in this work, a dimensional resonance phenomena was mainly studied experimentally. On possible future study of the dimensional resonance phenomena may come from the electrodynamics point of view. There could be significant practical application for such investigation in the future (for example for regulated AF resonators).

LIST OF LITERATURE

1. Agilent: The impedance measurement handbook, 2003.
2. Agilent: Vector analyzer basics, 2004
3. Agilent: Анализаторы цепей: полная характеристика линейных цепей.
4. Ahlawat A., Sathe V.G. Raman study of NiFe2O4 nanoparticles, bulk and films: effect of laser power. // J. Raman Spectroscopy, No. 42, 2011, p. 1087–1094.
5. Akhter S., Paul D. P., Hakim M. A., Akhter S., Saha D. K., Anjuman B., Islam F. Microstructure and complex permeability spectra of polycrystalline Cu-Zn ferrites. // J. SCI. Res. 4(3), 551–560 (2012)
6. Albach M., Durbaum T., Brockmeyer A. Calculating core losses in transformers for arbitary magnetizing currents – a comparison of different approaches. // IEEE Power electronics Specialists Conference, 1996, pp. 1463–1468.
7. Al-Haj M. Structural and magnetic properties of $Mg_{0.8-x}M_{0.2}Ni_xFe_2O_4$ (M = Zn, Mn) ferrite powders // Turk. J. Phys.– 2009.–Vol. 33.– 185–192 p.
8. Alley R. E. A review of new magnetic phenomena // The bell system technical journal.– 1953.– 1155–1172 p.
9. Amarald A. M. R., Cardoso A. J. M., An economic offline technique for estimating the equivalent circuit of aluminum electrolytic capacitors // IEEE Trans. Instrum. Meas., vol. 57, no. 12, pp. 2697– 2710, 2008.
10. AMCCAPS. Switch-Mode Ceramic Capacitors // www.kluvoelectronics.de/pdf/AMC_Switch-Mode_2005-11.pdf
11. Amorese G. LCR/Impedance measurement basics. // Hewlett Packard 1997
12. ASTM Standards, Part 11: Metallography; Nondestructive Testing // Philadelphia, Pa. 19103, 1979, p. 205–237
13. Baez-Pimiento S., Betancourt I., Hernandez-Rojas M. E., Badini-Confalonieri G. A., Jacas A., Vazquez M. Low-field magnetization process and complex permeabiltiy of FeCoBSiTa wires coated with hard magnetic CoNi layer. // Bull. Mater. Sci., Vol. 36, No. 4, 2013, pp. 559–562.
14. Barbara A., Clausell C., Feliu C., Monzo M. Study of NiZn ferrite complex permeability effect of relative density and microstructure. // J. Am. Ceram. Soc., **87** [7] 1314–1318 (2004)
15. Beljers H. G., Polder D. Magnetization in ferrites // Nature publishing group.– 1950.– Vol. 165.– 798.–800. p.
16. Bertotti G. Hysteresis in magnetism. // Accd. Press, San Diego, CA, 1998.
17. Bertotti G. General properties of power losses in soft ferromagnetic materials // IEEE Trans. Magn., 1988, v. 24, No. 1, 621–630.
18. Bishop J. E. L. Enchanted Eddy Current Loss due to Domain Displacement. // J. Magn. Mag. Mat. No. 49, 1985, pp. 241–249.
19. Blaž N., Marič A., Radosavljevič G., et al. Modeling and characterization of frequency and temperature variation of complex permeability of ferrite LTCC material // Progress in electromagnetics research B.– 2010.– Vol. 23.– 131–146 p.
20. Boerekamp J. G., Visser E. G. grain size dependency of the Steinmetz coefficient of soft ferrite power losses // J. PHYS. IV France.– 1997.– Vol. 7. p.– C1-125–C1-126.
21. Borah S., Bhattacharyya N. S. Broadband measurement of complex permittivity of composite at microwave frequencies using scalar scattering parameters // Progress in electromagnetics research M.– 2010.– Vol. 13.– 53–68 p.
22. Bossche A., Valchev V., Georgiev G. Measurement and loss model of ferrites in non-sinusoidal waves. // IEEE Power electronics Specialists Conference, 2004.

23. Brabers V. A. M. Ferrimagnetic Insulations. // In: Handbook of Magnetism and Advanced Materials. Eds. H. Kronmüller, S. Parkin; vol. 4: Novel Materials, 2007. J. Wiley&Sons, 2079 – 2097.
24. Brander T., Gefer A., Rall B. Trilogy of magnetics. // 4thEd., Würth Elektronik, 2009. – 704 p.
25. Brockman F. D., Dowling P. H., Steneck W. G. Dimensional effects from a high dielectric constant found in a ferromagnetic ferrite // Physical review.– 1950.– Vol. 77., No. 1.– 85–93 p.
26. Brockmeyer A., Experimental Evaluation of the Influence of DC-Premagnetization on the Properties of Power Electronic ferrites. // APEC'96 Conf. Proc., Vol. 1, 1996, 454–460 pp.
27. Brockmeyer A., Paulus-Neues J. Frequency Dependence of the Ferrite-Loss Increase Caused by Premagnetization. // APEC, 1997 Vol. 1., pp. 375–380.
28. Cagan V., Guyot M. Fast and convenient technique for broadband measurements of complex initial permeability of ferrimagnets // IEEE Transactions on Magnetics,– 1984.– Vol. MAG–20, No. 5.– 1732.–1734. p.
29. Chubykalo O., Lengsfield B., Jones B. Longitudinal Recording Media Performance as a Function of Exchange, Linear Recording Density and Media Texture // IEEE Trans. Mang, Vol. 37, No 4, 2004.
30. Cruickshank D. B., Microwave materials for wireless applications, // Artech House, 2011;– 221 p.
31. Dehmelt F. Pulse-skipping – Minimum on-time: reasons, effects and relevance for automotive applications – Part 2. // EE Times europe, 2013.
32. Dehmelt F. Pulse-skipping: reasons, effects and relevance for automotive applications – Part 1. // EE Times europe, 2013.
33. Diniz V. C. S., Vieira D. A., Kiminami R. H. G. A., Cornejo D., Costa A. C. F. M., Microstructural and magnetic analysis Ni-Zn ferrite sinterized in the conventional and microwave oven. // Materials Science Forum Vols. 727–728 (2012) pp 971–976
34. Drofenik M., Znidarsic A., Makovec D. Use of the retarded solution – reprecipitation process to attain a higher initial permeability of MnZn ferrites // J. Anc. Ceram. Soc., 2003, v. 86, pp. 1601–1604
35. Drofenik U., Kolar J. W., Biela J., Heldwein M. L., Ertal H., Friedli T., Round S. D. PWM converter power density barriers // Power Convertion Conference (PCC'07), Nagoya (Japan), April 2007, pp. 9–29.
36. Dunlop C. J. Modeling Magnetic Core Loss for Sinusoidal Waveforms. // Naval Engineer and Master Thesis. Massachusetts, 2008.
37. Eichhorn T. Estimate Inductor Losses Easily in Power Supply Designs. // J. Power Electronics Technology, 2005, pp. 14–24.
38. Epcos Databook, 2008
39. Epstein D. J., Franckiewicz B. Temperature-Dependent lag in polycrystalline Yittrium-Iron Garnet // J. Appl. Phys, 1959, Suppl. to v. 30, No. 4, 295S–296S
40. Ferroxcube, "3F45 Material specification" – Data, pp. 188–190, 2008
41. Fiorillo F., Beatrice C., Bottaucio O., Mauzin A. Approach to magnetic losses and their frequency dependence in Mn-Zn ferrites // Applied Physics Letters, v. 89, 2006
42. Friedel J. Dislocations. // Pergamon Press, 1964
43. a) Gieraltowski J., Globus A., Domain wall size and magnetic losses in frequency spectra of ferrites and garnets, // IEEE Trans. Magn., vol. MAG-13, no. 5, pp. 1359, 1977.

b) Gieraltovski J., Le Floc'h M., Loaec J. Relaxation frequency as a function of domain wall topography in soft polycrystalline ferrites // J. Magn. Magn. Mat., 1985, v. 49, 357–360 p.
c) Gieraltovski J. Initial susceptibility frequency spectra and distribution of the grain sizes in Ni-Zn and YIG polycrystalline ferrites // J. Magn. Magn. Mat., 1989, v. 81, 103–106 p.
44. Ginley R. A. Confidence in VNA Measurements // IEEE microwave magazine.– 2007.– 54–58. p.
45. Globus A. Some physical considerations about the domain wall size theory of magnetization mehanisms // Journal de Physique, 1977, v. 38, No. 4, 1–15.
46. Globus A., Duplex P., Initial susceptibility of ferromagnetic materials and topography of DW// Phys. stat. sol. Vol. 31, no. 2, pp. 765–774, 1969.
47. Globus A., Guyot M., Control of the susceptibility spectrum in polycrystalline ferrite materials and frequency threshold of the losses, // IEEE Trans. Magn. Vol. 6, no 3, pp. 614–617, 1970.
48. Gorter E. W. Saturation magnetization of some ferrimagnetic oxides with hexagonal crystal structures // Convention of ferrites.– 1957.– No. 2355R.– 255–260 p.
49. Gotoh S., Otake T., Fukuda Y., Togawa J. High Performance MnZn Ferrites for Transformer Core Used in Forward Mode Switching Power Supply. // JFE Techn. Rep. No. 16, 2011.
50. Gottstein G. Physical Foundations of Materials Science // Springer-Verlag Berlin Heidelberg, 2004, pp. 303–307.
51. Gradzki P. M., Lee F. C. Domain Wall Resonance and Its Effect on Losses in Ferrites. // IEEE PESC'91 Record, 1991, pp. 627–632.
52. Greifer A. P. Ferrite Memory Materials // IEEE transactions on magnetics.– 1969. Vol. MAG-5, No. 4.– 774–811 p
53. Guyot M., Merceron T., Cagan V., Messeker A., Mobility and/or damping of the DW, // Phys. stat. sol. (a), vol. 106, no. 2, pp. 595–612, 1988.
54. Haijun Z., Zhicao L., Chengliang M., et al., Complex permittivity, permeability, and microwave absorption of Zn- and Ti- substituted barium ferrite by citrate sol-gel process // Materials science and engineering.– 2002.– Vol. B96.– 289–295 p.
55. Hamilton N. The small-signal frequency response of ferrites // High frequency electronics.– 2011 – June.– 36.–52. p.
56. Healy G., Selecting a power inductor to Your SMPS design. // Hearst Electronic products. Herrenberg, Germany, 08/01/2006
57. Herbert E. User-Friendly data for Magnetic Core Loss Calculations. // FMTT, Inc., November 10, 2008.
58. Hiebel M. Fundamentals of network analysis // Rohde&Schwarz – 2007.– 419. p.
59. Hiebel M. Vector Network Analyzer (VNA) Calibration: The basics. // R&S whitepaper, 2008.
60. Hongo K., Miyazaki Y. Calculation Method of Pulse Characteristics of Ferrite Cores for Pulse Transformers. // Ferrites, Proc. Int. Conf, Japan, July, 1970.
61. Huang R., Zhang D., Tseng K.-J. Determination of dimension – independent magnetic and dielectric properties for Mn-Zn ferrite cores and its EMI applications // IEEE transactions on electromagnetic compitability.– 2008. vol. 50, No. 3.– 597–602 p.
62. Huang Y. D., Froyen L., Quantitative analysis of microstructure in metals with computer assistance. // NDT.net – May 2001, Vol. 6 No. 5.
63. Islam R., Rahman Md O., Hakim M. A., Saha D. K., Saiduzzaman, Noor S., Al-Mamun M. Effect of Sintering temperature on Structural and Magnetic Properties of $Ni_{0.55}Zn_{0.45}Fe_2O_4$ Ferrites. // Materials Sciences and Applications, 2012, 3, 326–331

64. Jankovskis J. Complex permeability of ferrites correlated with their microstructure // Advances in Sc. & Techn., 2006, v. 45, 2560–2565.
65. Jankovskis J. Empirical Relations. Analogous to Snoek's Law, for Account of Polycrystalline Ferrites Grain Size Effects. // RTU Proc. Series 7., Telecom. and Electr., 2002, pp. 68–76.
66. Jankovskis J. Modelling of Frequency Dependence of Complex Permeability Based on Statistics from Polycrystalline Ferrites Microstructure. // Ferrites: Proc. 8th Int. Conf. (ICF8), pp. 319–321, 2000.
67. Jankovskis J. Presentation of complex permeability spectra of polycrystalline ferrites based on grain size distribution, // J. Magn. Magn. Mat., vol. 272–276, pp. e1847-1849, 2006.
68. Jankovskis J. Relations analogous to Snoek's one, for domain wall processes, // J. Magn Magn. Mat., vol. 304, pp. e492-e494, 2006.
69. Jankovskis J. Research into problems of radiofrequency losses in polycrystalline ferrites and small signal inductors. // Riga, RTU, 1998, (manuscript).– 49 p.
70. Jankovskis J., Ponomarenko N. Complex permeability of ferrites as intrinsic and extrinsic properties. // J. Chem. Chem. Eng. Vol. 8, 2014, p. 85–91.
71. Jankovskis J., Ponomarenko N., Mironova-Ulmane N., Jakovlevs D. Dimensional effects of sample geometry and microstructure of MnZn and NiZn ferrites. // 2012 IOP Conf. Ser.: Mater. Sci. Eng. 38 012018.
72. Jankovskis J., Ponomarenko N., Mironova-Ulmane N., Jakovlevs D. The study of correlation between microstructure of ferrites and their complex permeability spectra. // 2013 IOP Conf. Ser.: Mater. Sci. Eng. 49 012045.
73. Jankovskis J., Ponomarenko N., Narica P. An Investigation on High Frequency Permeability of Polycrystalline Ferrites. // Proceedings of the 8th International Scientific and Practical Conference, Latvia, Rezekne, 20.–22. June, 2011.– pp 194–201.
74. Jankovskis J., Ponomarenko N., Stepins D. Frequency Dependence of Complex Permeability of Polycrystalline Ferrites Based on the Realities of Microstructure. // 2013, Key Engineering Materials, 543, 507.
75. Jankovskis J., Stepins D., Pikulins D. Efficiency of PFC operating in spread spectrum mode for EMI reduction // Elektronika ir Elektrotechnika (Electronics and Electrical Engineering), no. 7, pp. 13–16, 2010.
76. Jankovskis J., Stepins D., Ponomarenko N. Effects of Spread Spectrum on Output Filter of Buck Converter. // Electronics and Electrical Engineering, 2013, Vol. 19, No. 5, pp. 45–48. e-ISSN 2029-5731. ISSN 1392-1215.
77. Jet Edge waterjet systems. How a Water Jet Machine Works, / http://www.jetedge.com/content.cfm?fuseaction=dsp_applications_101
78. Jin Z., Bertram H. N. Simulation of effect of Medium Noise on Servo Position Error Signal Detection in Longitudinal Recording // IEEE Trans. Magn. Vol. 36, No. 6, 2000
79. Joong-Hee Nam, Sang Jin Park, and Won Ki Kim. Microstructure and Magnetic Properties of Nanostructured NiZnCu Ferrite Powders Synthesized by Sol-Gel Process. // IEEE TRANSACTIONS ON MAGNETICS, VOL. 39, NO. 5, SEPTEMBER 2003, pp 3139–3141
80. Jordan D., Choosing a capacitor for use as a SMPS filter. // NASA Tech Briefs., 01.12.2011.
81. Kazimierczuk. High-Frequency Magnetic Components. Wiley, 2009.
82. Keeping S. design Trade-offs in Integrating an inductor into a Power Module. // Journal of Power solutions, 2011.

83. Kim S. S. Microwave Absorbing Properties of Magnetic Composite Sheets for Oblique Incidence Angles. // IEEE Trans. Magn., Vol. 47, No. 10, 2011.
84. Koblischka-Veneva A., Koblischka M. R., Mucklich F., Advanced microstructural analysis of ferrite materials by means of electron backscatter diffraction (EBSD). // Journal of Magnetism and Magnetic Materials 322 (2010), 1178–1181
85. Kogias G., Tsakaloudi V., Van der Valk P., Zaspolis V. Improvements on the microstructure of the compacts. // J. Magn. Magn. Mat., 2012, v. 324, pp. 235–241
86. Komma T., Gueldner H. The effect of different air-gap positions on the winding losses of modern planar ferrite cores in switch mode power supplies // International Symposium on power electronics, electrical drives, automation and motion SPEEDAM 2008.
87. Kozakova Z., Kuritka I., Babayan V., et al. Magnetic iron oxide nanoparticles for high frequency applications // IEEE transactions on magnetics.– 2013. Vol. 49, No 3.– 995–998 p.
88. Krupka J., Derzakowski K., Harnett J. G. Measurements of the complex permittivity and the complex permeability of low and medium loss isotropic and uniaxially annisotropic metamaterials at microwave frequencies. // IOP Publishing, Meas. Sci. Tecnol. 20 (2009) 105702 (5pp).
89. Kurtz S. K., Carpay F. M. A. Microstructure and normal grain growth in metals and ceramics. Pt. 1. // J. Appl. Phys., 1980, v. 51, No. 11, 5725–5744.
90. Laflin M. High frequency implications for switch-mode DC/DC converter design. // Empirion Design Article, 11 pp., 2007.
91. Lebourgeois R. J.-P. G., Lloret B. High Frequency Mn-Zn Power Ferrites // J. Phys. IV, France 1997, pp. C1-105–C1-108
92. Lebourgeois R., Ganne J.-P., Lloret B. High frequency Mn-Zn power ferrites // Journal de Physique IV, 1997, Coll. C1, C1-105–C1-106.
93. Lee D. W., Wang S. X., Tang Y. J., Hong J. I., Berkowitz A. E. Permeability of Fine Magnetic Particles: Measurements, Calibration, and Pitfalls. // IEEE Trans. Magn., Vol. 42, No. 10, 2006.
94. Lee J.-G., Kim J. H., Chae K. P., Lee Y. B. Crystallographic and magnetic properties of Zn-Mn ferrite // Journal of Korean Physical Society – 2011.– Vol. 49.– No. 2.– 604–607 p.
95. Li J., Abdallah T., Sullivan C. R. Improved Calculation of Core Loss with Nonsinusoidal Waveforms. // IEEE Industry Applications Society Annual Meeting, Oct. 2001, pp. 2203–2210.
96. Lin D., Zhou P., Fu W. N., Badics A., Cendes Z. J. A dynamic core loss model for soft ferromagnetic and power ferrite materials in transient finite element analysis // IEEE Trans. Magn., 2004, v. 40, No. 2, 1318–1321.
97. Lomovs. S. Increasing of accuracy for experimental magnetic spectra of high-permeability ferrites // RTU.– 2003. 71 p.
98. Loyau V., Wang G.-Y., M. Bue Lo, and Mazaleyrat F. An analysis of Mn-Zn ferrite microstructure by impedance spectroscopy, scanning transmission electron microscopy and energy dispersion spectrometry characterizations. // J. Appl. Phys. 111, 053928 (2012)
99. Lu H. M., Zheng W. T., Jiang Q. Saturation magnetization of ferromagnetic and ferrimagnetic nanocrystals at room temperature // Journal of Physics D.– 2007.– Vol. 40.– 320–325 p.
100. Lu J., Jia H., Wang X., Padmanabhan K., Hurley G. W., Shen J. Z. Modeling, design, and Characterization of multiturn bondwire inductors with ferrite epoxy glob cores for

power supply system on chip or system in package applications // IEEE Trans. Power Electronics, Vol. 25, No. 8, August 2010
101. Matsuo Y., Otobe S., Nakao F., Sakamoto H. Development of a ferrite material for inductive chargers// FDK technical information http://www.fdk.com/cyber-e/technical/pi_technical06.html
102. McCutcheon J. FFDMs Promise Optimized Wireless Power Charging // Electronic Design, 2011, http://electronicdesign.com/power/ffdms-promise-optimized-wireless-power-charging
103. Meuche H., Esguerra M. Correlation between losses, complex permeability and electron diffusion in power ferrites // J. PHYS. IV France.– 1997.– Vol. 7.– C1-95–C1-98. p
104. Microchip. Switch mode power supply (SMPS) topologies Part 1 AN1114
105. Mitchell D. M., Book Review: Introduction to Power Electronics by Daniel W. Hart, Prentice-Hall Inc., 1997. // IEEE Power Electronics Society Newsletter, July 2000.
106. Mochizuki T., Hirohashi T., Tsumura T., Sasaki I. A multiple-output 400 kHz switching power supply using a new ferrite material H63A // IEEE Trans. Mangetics, Vol. MAG-23, No. 5, September 1987
107. Mori N., Ukai T., Otsuka S. Calculation of anisotropy constants // Journal of magnetism and magnetic materials.– 1983.–V. 31-34.–43-44 p.
108. Moses A. J. Advanced soft magnetic materials for power applications. // In: Handbook of Magnetic and Advanced Magnetic Materials, Eds. H.Kronmüller, S. Parkin; vol. 4: Novel Materials, 2007. J. Wiley&Sons, 1926–1942.
109. Mossman P., Deakin I. R., High quality, high stability Manganese-Zinc ferrites. // Ferrites: Proc. Int. Conf., 1970, Japan, pp. 199–202.
110. Mpenou X. 20th Soft Magnetic Materials SMM20 Abstract Book.
111. Naito Y. Inverse Cole-Cole plot as applied to the ferromagnetic spectrum in VHF through the UHF region. // In: Ferrites: Proc. of Intern. Conf., July 1970 (Japan), 558 – 560.
112. Neva ferrite, "6000HM-1 material specification".
113. Nien H. H., Liang T. J., Huang K. C., Changcien S. K., Shieh H. W. Implementation of low loss Mn-Zn ferrite cores for power electronics applications // IEEE Power India conference 2006.
114. Nigam M., Sullivan C. R. Multi-layer folded high frequency toroidal inductor windings // IEEE applied power electronics.– 2008.– 682–688 p.
115. Nowarowski R., King B. Challanges of designing high-frequency, high-input-voltage DC/DC converters. // Texas Instruments, Analog Applications Journal, vol. 20, pp. 28–31, 2Q 2011.
116. Nowosielski R., Babilas R., Wrona J. Microstructure and magnetic properties of commercial barium ferrite powders. // Journal of achievements in materials and manufactufing engineering, Vol. 20. 2007
117. Nuno L., Barbara A., Balbastre J. V., Clausell C., Vines A. Study of NiZn Ferrite Absorption: Effect of Relative Density and Microstructure. // IEEE Int. Symp. EMC Europe, 2009, pp. 1–4.
118. Oliver C.. A new core loss model // Switching Power Magazine, Spring 2002, 28–30.
119. ON Semiconductor. Effects of High Switching frequency on buck regulators. // TND338-D
120. ON Semiconductor. Switchmode power supplies, Reference manual and design guide. // SCILLC, 2007
121. Otsuki E., Yamada S. Analysis of power loss in Mn-Zn ferrites// J. PHYS. IV France.– 1997.– Vol. 7.– C1-113–C1-114. p

122. Otsuki E., Yamada S., Otsuka T., Shoji K., Sato T. Microstructure and physical properties of Mn-Zn ferrites for high-frequency power supplies. // J. Appl. Phys. 69 (8), 15 April 1991.
123. Parvatheeswara Rao B., Subba Rao P. S. V., Rao K. H. Unusual dielectric behaviour of Ni-Zn ferrites in the lower megahertz region (1–10 MHz) due to dimensional resonance // Journal of materials science letters.– 1996.– Vol. 15.– 781–783 p.
124. Postupolski T. Topological-and-geometrical approach to the determination of spatial features of granular structure // Prace ITR, 1987, z.107/87, 2–49.
125. Power Perspective Journal. Resonant Converter IC. EPN issue No. 11, 2011, p. 46.
126. Price E. Magnetic dipoles, hysteresis and core losses // Enviromental potentials white paper.– 2006. 1–9. p.
127. QuadTech LCR measurement Primer. 2005.
128. Queffelec P., Automatic Measurements of Complex Tensorial Permeability of Magnetized Materials in a Wide Microwave Frequency Range. // IEEE Trans. Microwave Theory and Techniques, vol. 50, No. 9, 2002.
129. Rado G. T. Magnetic spectra of ferrites // Rev. Mod. Phys., 1953, v. 25, No. 1, 81–89.
130. Radonič V., Blaž N., Živanov Lj. Measurement of complex permeability using short coaxial line reflection method // ACTA PHYSICA POLONICA A,– 2010.– Vol. 117 No. 5.– 820.–824. p.
131. Reinert J., Brockmeyer A., R. W. A. A. De Donker. Calculation of losses in ferro- and ferromagnetic materials based on the modified Steinmetz equation // IEEE Trans. Industry Appl., 2001, v. 37, No. 4, 1055–1061.
132. Roess E., Magnetic properties and microstructure of high permeability Mn-Zn ferrites. // Ferrites: Proc. Int. Conf. (Japan), 1970, pp. 203–209
133. Rosales M. I., Plata A. M., Nichno M. E., Ponce M. A., Castano V. M. Effect of sintering conditions on microstructure and magnetic properties of Mn-Zn ferrites// J. Mat. Scien., Vol. 30, 1995, pp. 4446–4450
134. Roshen W. Ferrite Core Loss for Power Magnetic Components Design. // IEEE Trans. Magn. Vol. 27, No 6, 1991, pp. 4407–4415.
135. Sarjeant W. J., Clelland J. W., Price R. A., Capacitive components for power electronics // Proc. of the IEEE, 2001, vol. 89, no. 6, pp. 846–855.
136. Schlõmann E. Behavior of ferrites in the microwave frequency range // Journal de physique.– 1971.– Tome 32.– C1-443–C1-451 p.
137. Shenhui J., Quanxing J. An alternative method to determine the initial permeability of ferrite core using network analyzer // IEEE Transactions on Electromagnetic Compitability,– 2005.– Vol. 43, No. 3.– 651–657. p.
138. Sibille R. Ferrite materials for switched mode power supplies // IEEE Trans. On Magnetcs, Vol. MAG-17, No. 6, November 1981
139. Singh P. K. Effect of dimensional resonance and damping constant on various parameters used in magneto-microwave Kerr effect in ferrites // Phys. sts. sol.– 1985.– Vol. 91.– 583–596 p.
140. Skutt G. R., High-frequency dimensional effects in ferrite-core magnetic devices. // Ph. D. Dissertation. Blacksburg, Virginia, 1996.
141. Skutt G. R., Lee F. C. Characterization of dimensional effects in ferrite-core magnetic devices // IEEE 0-7803-3500-7/96.– 49–54 p.
142. Skutt G. R., Lee F. C., Breslin J. G. Measurement issues in the characterization of ferrite magnetic material // VPEC seminar series.– 1996.– 1–9 p.
143. Slama J., Shiroky P., Shoka M., et. al., Frequency analysis of nickel based magnetic dielectrics // J.Electr. Eng., vol. 60, no1, pp. 39–42, 2009.

144. Slama J., Shiroky P., Shoka M., et. al., Magnetic spectra analysis of dielectrics // Journal of Electrical Engineering, Vol 59. No 7/s, 2008
145. Smith J., Wijn H. P. J. "Ferrites" // Philip's Tehn. library, Eindhoven, 1959.– 313 p.
146. Snelling. E. C., Soft Ferrites: properties and applications. Second edition. // Batterworth &Co. Ltd. 1988
147. Snoek J. L. Dispersion and absorption in magnetic ferrites at frequencies above one Mc/s // Physica, 1948, v. 14, 207–217.
148. Standley K., J. Oxide Magnetic Materials // Oxford, At the Clarendon Press, 1962
149. Texas instruments. Introduction to power supplies. AN-556, May 2004.
150. Tian Q., Wang Q., Xie Q., Li J. Aqueous solution preparation, structure, and magnetic properties of nano-granular $Zn_xFe_{3-x}O_4$ ferrite films. // Nanoscale Res. Lett. No. 5, 2010, p. 1518–1523.[1]
151. Tumanski S. Handbook of Magnetic Measurements. CRC Press, 382 p.
152. Tung M. J., Tseng T. Y., Tsay M. J., Chang W. C. The effect of grain boundary impedance on the power loss of Mn-Zn ferrites over 1 MHz // J. PHYS. IV France.– 1997.– Vol. 7.– C1-129–C1-130. p
153. Van der Bosshe A., Valchev V. C., Inductors and Transformers for Power Electronics. // Taylor and Francis, 2005.
154. Varshney D., Verma K., Kumar A. Structural and vibrational properties of $Zn_xMn_{1-x}Fe_2O_4$ (x = 0.0, 0.25, 0.50, 0.75, 1.0) mixed ferrites. // Mat. Chem. Phys. No. 131, 2011, p. 413–419.
155. Venkatachalam K., Sullivan C. R., Abdallah T., Tacca H., Accurate Prediction of Ferrite Core Loss with Nonsinusoidal Waveforms Using Only Steinmetz Parameters. // IEEE Proceedings. Workshop on Computers and Power electronics, 2002
156. Venugopal. B. N. More effective EMI reduction techniques for high-demand consumer applications. // Interference Technology: EMC Directory & Design Guide, pp. 96–100, 2009
157. Visser E. G., Johnson M. T., P. J. van der Zaag. A new interpretation of the permeability of ferrite polycrystals // In: Ferrites. Proc. 6th Int. Conf. Ferrites, Tokyo, 1992, 807–811.
158. WARDjet waterjet univercity / http://www.wardjet.com/waterjet-university.html
159. Waseem R. A Practical, Accurate and Very General Core Loss Model for Nonsinusoidal Waveforms. // IEEE Trans. on Power Electronics, Vol. 22, No. 1, 2007
160. Waseem R. Ferrite Core Loss for Power Magnetic Components Design. // IEEE Trans. Magn. Vol. 27, No. 6, 1991
161. WaterJets.org, / http://waterjets.org/index.php?option=com_frontpage&Itemid=1
162. Watson J. K. Applications of magnetism. // J.Wiley&Sons,1980.– 468 p.
163. Watson J. K., Amoni S. Using Parallel Complex Permeability for ferrite Characterization. // IEEE Trans. Magn. Vol. 25, No. 5, 1989, pp. 4224–4226.
164. Wilson P. R., Modeling Frequency – Dependent Losses in Ferrite Cores. // IEEE Trans. Magn., Vol. 40, No. 3., 1537–1541 pp., 2004.
165. Wu J., Wray P. J., Garcia C. I., Hua M., Derado A. J., Image quality analysis: a new method of characterizing microstructures. // ISIJ International, Vol. 45 (2005), No. 2, pp. 254–262
166. Yamada S., Otsuki E. Analysis of eddy current loss in Mn-Zn ferrites for power supplies // IEEE Trans. Magnetics, Vol. 31, No. 6, November 1995
167. Yamada S., Otsuki E. Analysis of eddy current loss in MnZn ferrites for power supply // J. Applied Phys., 1997, vol. 81, No. 8, pp. 4791–4793.
168. Yamamoto Y., Makino A., Nikaido T. Low loss of fine grained Mn-Zn ferrite // J. PHYS. IV France.– 1997.– Vol. 7.– C1-123–C1-124. p

169. Yanagisawa K., Zhang F., Sato T., Yamasawa K., Miura Y. A wideband Common-mode noise filter with a Mn-Zn ferrite and Cu/Polymide Tape Wound Coil For Switching power supplies used in electronic measuring instruments // IEEE Magnetics Conference, 2005. INTERMAG Asia.
170. Yoon S. Determination of the dependence of the magnetic anisotropy constant in magnetite nanoparticles//Journal of Korean Physical Society – 2011.– Vol. 59.– No. 5.– 3069–3073 p.
171. Yoon S., Krishnan K. M. Temperature dependence of magnetic anisotropy constant in manganese ferrite nanoparticles at low temperature// Journal of applied physics.– 2011.– V. 109, 07B534.
172. Yoshida S., Kondo K., Kubodera T. Suppression of GHz Noise Emitted From a Four-Layered PWB With Ferrite-Plated Inner Ground Layer // IEEE Trans. Magn. Vol. 44, No. 11, 2008
173. Zahi S., Synthesis, permeability and microstructure of the optimal Nickel-Zinc ferrites by Sol-Gel route. //J. Electromagnetic Analysis& Applications, 2010, 2: 56–62
174. Zhang S. Y. Resonance model of ferrite assembly for window frame magnet kicker impedance // Collider – Accelerator department C-A/AP/20.– 2000.– 1–12 p.
175. Zirka S. E., Moroz Y. I., Marketos P., Moses A. J. Loss separation in nonoriented electrical steels // IEEE Trans. Magn., 2010, v. 46, No. 2, 286–289.
176. Znidarsic A., Drofenik M. Soft Magnetic Ferrite Materials. // Materiali in Tehnologije, 37, 2003, pp. 87–90.
177. Znidarsic A., Limpel M., Drofenik M. Effect of dopants on the magnetic properties of MnZn ferrites for high frequency power supplies // IEEE Trans. Magnetics Vol. 31, No. 2, March 1995
178. Абельс В. Р. Внутренний размагничивающий фактор и коэффициент прямоугольности нетекстурированных магнитомягких материалов// Физика металлов и металловедение.– 1970.– Том 30, в. 2.– 303–308 с.
179. Бронштейн И. Н., Семендяев К. А. // Справочник по математике, Москва, 1957
180. Костиков В. Г. Функциональные устройства систем электропитания наземной РЭА// Радио и связь.– 1990. 193 с.
181. Куневич А., Максимов А. Современные магнитомягкие материалы для силовой электроники // Современная электроники – 2006. № 5.– 34–35 с.
182. Ландау Л. Д., Лифшиц Е. М. Теоретическая физика. Том 8: Электродинамика сплошных сред. // Москва, Наука, 1982.
183. Мартинсон А. К., Морозов А. Н., Физика в техническом университете, том 6, // МГТУ им. Н. Э. Баумана, 2002.
184. Муслаков В. П., Кунина Г. П., Павлович В. М., и др. Исследование возможности применения магнитомягких ферритов для широкополосных трансформаторов передающих и приемных устройств // Электронная техника.– 1979.– Серия 6 в. 8.– 42–46 с.
185. Пальчун Ю. А. Обеспечение единства измерений параметров передачи в коаксиальных трактах в диапазоне СВЧ // Сборник научных трудов НГТУ.– 2008.– № 4 (54) – 95–98 с.
186. Петрова Г. Н. Внутренний размагничивающий фактор // Известия академии наук СССР.– 1949. № 4. 363–368 с.
187. Салтыков С. А. Стереометрическая металлография. Москва, Металлургия 1976
188. Смит Я., Вейн Х. Ферриты // Издательство иностранной литературы.– 1962.– 504 с.

189. Смолин Р. П., Дрокин А. И, Терехова С. Л. О размагничивающем факторе поликристаллических магниймарганцевых ферритов // Известия высших учебных заведений.– 1964. № 5.– 168–170 с.
190. Фоменко Л. А. Магнитные спектры ферритов // Успехи физических наук 1958, 669–731.
191. Фоменко Л. А. Радиочастотные магнитные и электрические спектры проницаемостей тела и вещества MnZn-ферритов // Журнал технической физики.– 1958.– Том XXVIII № 3.– 506–510 с.
192. Шиликов А. Г., Мукимов К. М. Внутренний размагничивающий фактор никельцинковых ферритов, содержащий кобальт // ФММ.– 1966. Т.22.– 154–157 с.
193. Юршевич В. В. Температурные измерения в магнитных спектрах Ni-Zn и Mn-Zn ферритов для Индуктивных элементов // РТУ.– 1987. 185 с.
194. Юршевич В. В., Ранкис Г. Ж. Магнитные спектры марганец – цинковых ферритов с разными типами температурной зависимости магнитной проницаемости // Известия академии наук ЛССР.– 1987.– № 1.– 63–68 с.

APPENDIX 1. MATLAB® PROGRAM FOR KRAMERS-KRONIG RELATIONS.

for evaluation of imaginary part from real part:

```
function im=kkim(omega,re)
if size(omega,1)>size(omega,2);
omega=omega'; end;
if size(re,1)>size(re,2);
re=re'; end;
g=length(omega);
im=zeros(size(re));
for j=1:g-1
    omega(1)=0;%for the evaluation to be made from 0
    f=omega(j)+0.0001;% so not to get 0 at f-omega(i)
    b=0;
for i=1:g-1;
m=(re(i+1)-re(i))/(omega(i+1)-omega(i));
c=(re(i)*omega(i+1)-re(i+1)*(omega(i)))/(omega(i+1)-omega(i));
imTemp =-m*f/2*...
    log(abs(omega(i+1)^2-(f)^2)/abs((f)^2-omega(i)^2))+...
    c/2*(log((abs((f)-omega(i))*(omega(i+1)+(f)))/...
    (((omega(i)+(f))*abs(omega(i+1)-(f))))));
b = b + imTemp; end;
im(j) = 2/pi()*b; end;
```

and for evaluation of real part from imaginary part:

```
function re=kkre(omega,im)
if size(omega,1)>size(omega,2);
omega=omega'; end;
if size(im,1)>size(im,2);
im=im'; end;
g=length(omega);
re=zeros(size(im));
for j=1:g-1
    omega(1)=0;%for the evaluation to be made from 0
    f=omega(j)+0.0001;% so not to get 0 at f-omega(i)
    b=0;
for i=1:g-1;
    im(1)=0.0001;%the imitation of 0 point
m=(im(i+1)-imjan(i))/(omega(i+1)-omega(i));
c=(im(i)*omega(i+1)-im(i+1)*omega(i))/(omega(i+1)-omega(i));
reTemp = m*(omega(i+1)-omega(i))-((m*(f))/2)*...
    log((abs((f)-omega(i))*(omega(i+1)+(f)))/...
    ((abs(omega(i+1)-(f))*(omega(i)+(f))))+(c/2)*...
    log((abs(omega(i+1)^2-(f)^2))/(abs((f)^2-omega(i)^2)));
b = b + reTemp;end;
re(j) = 2/pi()*b;end;
```

APPENDIX 2. EXPERIMENTAL MEASUREMENTS OF STUDIED FERRITE CIP SPECTRA

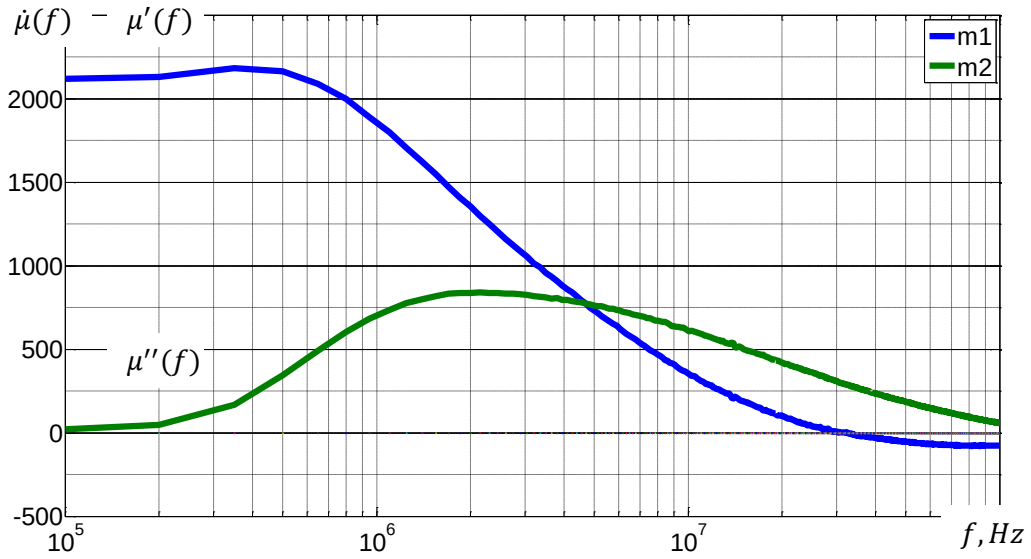

Figure A2.1. Measured CIP of sample A1 (m1 stands for $\mu'(f)$ and m2 for $\mu''(f)$)

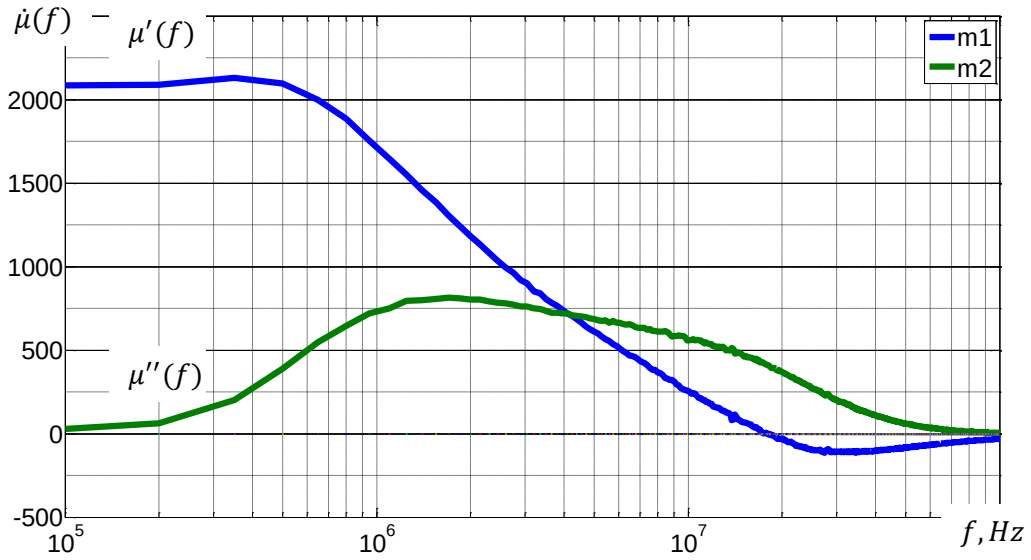

Figure A2.2. Measured CIP of sample A2 (m1 stands for $\mu'(f)$ and m2 for $\mu''(f)$)

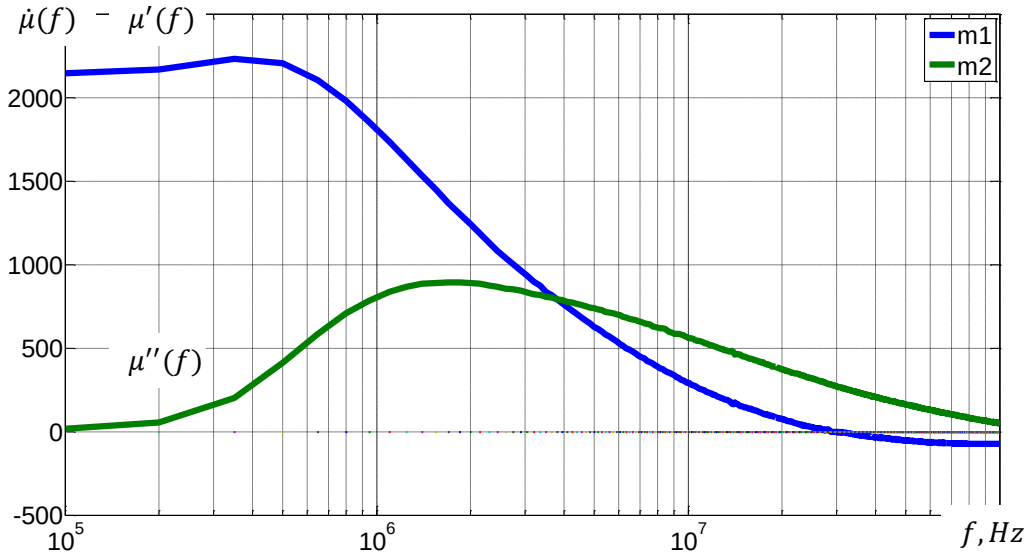

Figure A2.3. Measured CIP of sample A3 (m1 stands for $\mu'(f)$ and m2 for $\mu''(f)$)

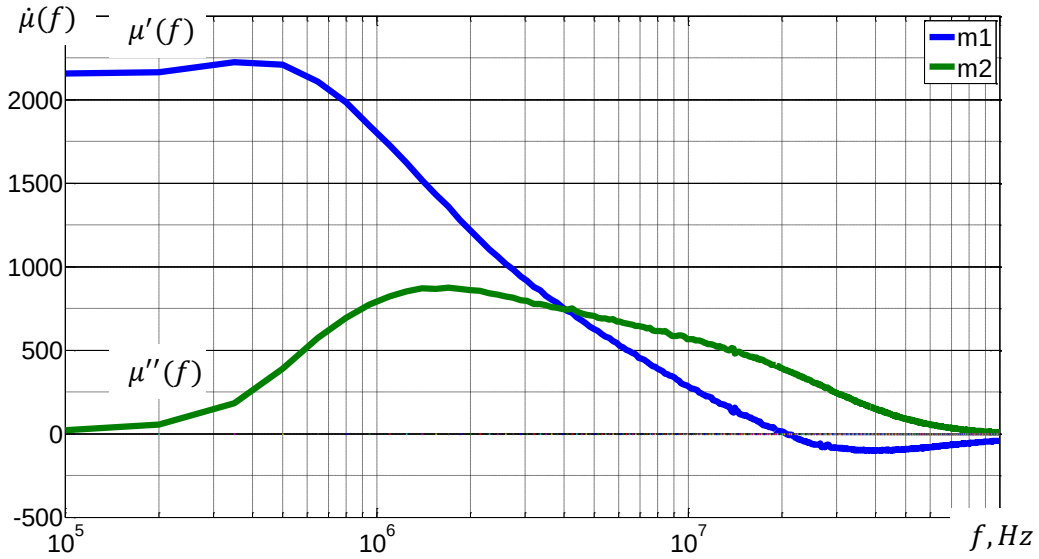

Figure A2.4. Measured CIP of sample A4 (m1 stands for $\mu'(f)$ and m2 for $\mu''(f)$)

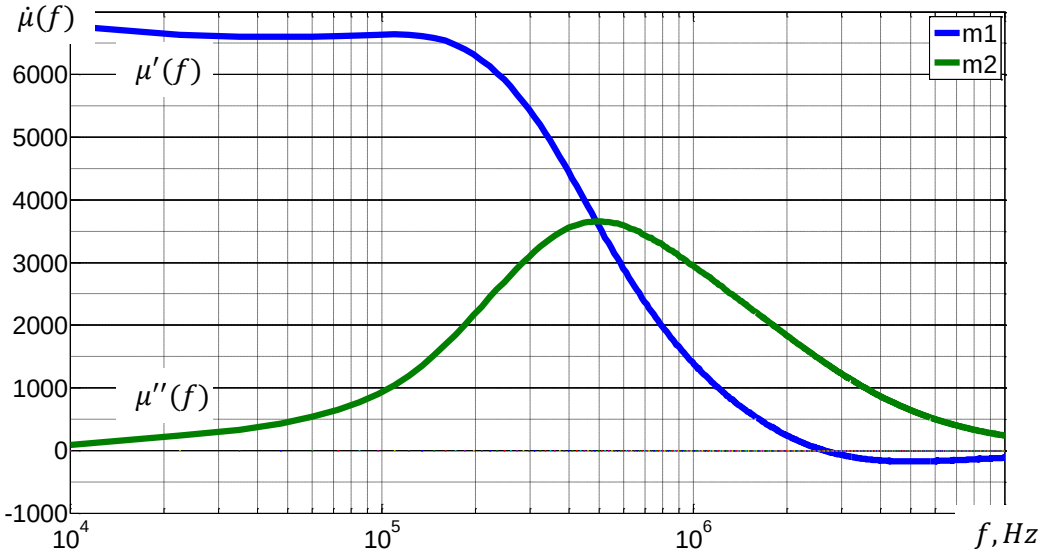

Figure A2.5. Measured CIP of sample B1 (m1 stands for $\mu'(f)$ and m2 for $\mu''(f)$)

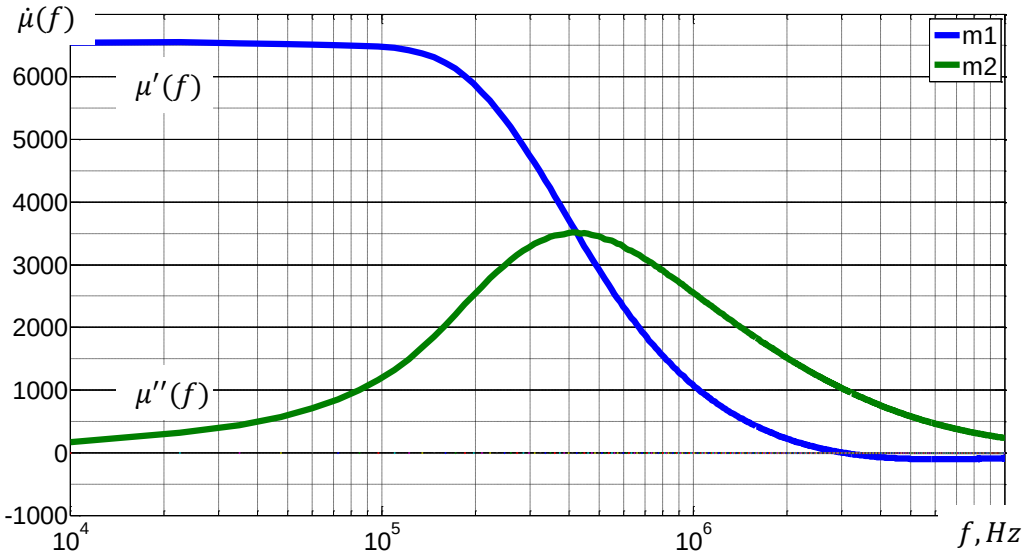

Figure A2.6. Measured CIP of sample B2 (m1 stands for $\mu'(f)$ and m2 for $\mu''(f)$)

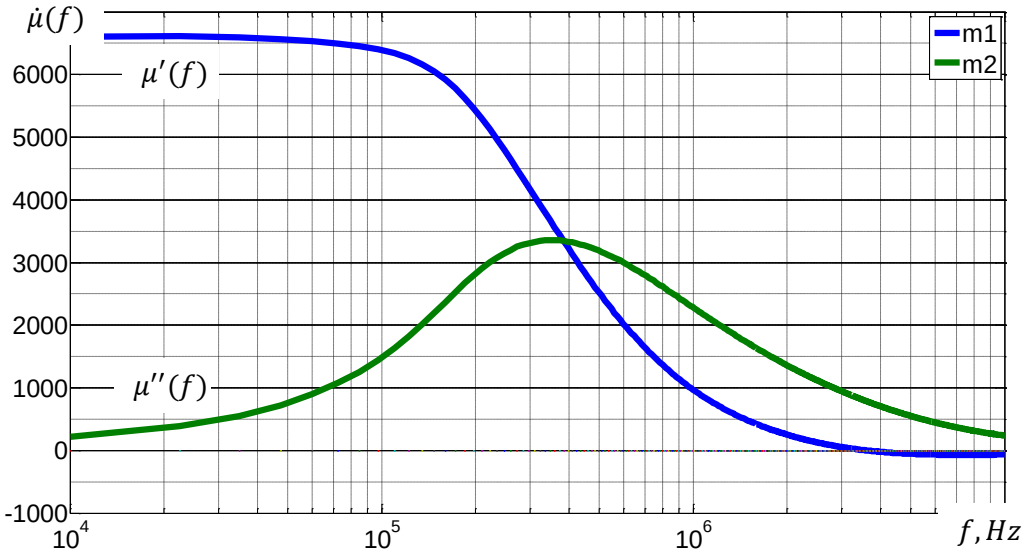

Figure A2.7. Measured CIP of sample B3 (m1 stands for $\mu'(f)$ and m2 for $\mu''(f)$)

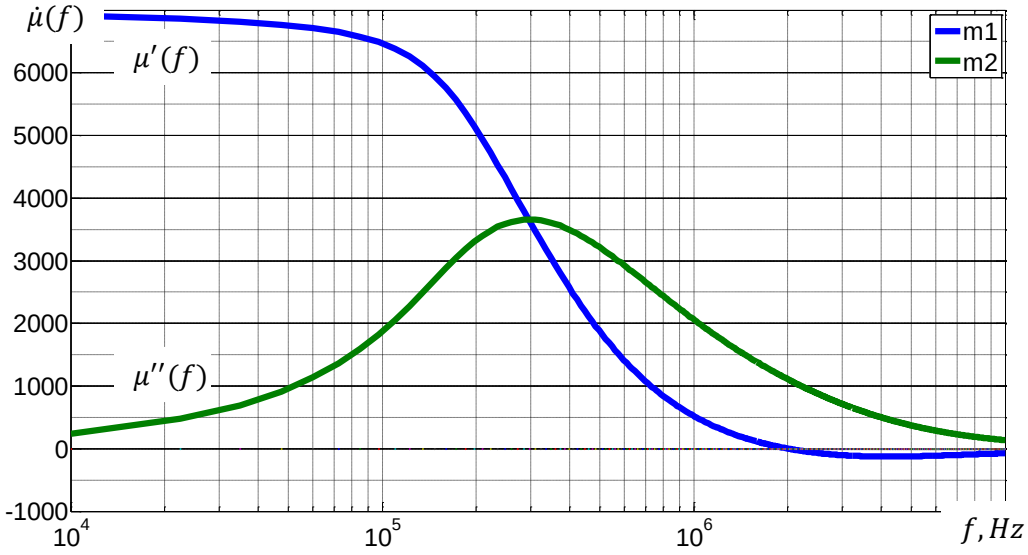

Figure A2.8. Measured CIP of sample B4 (m1 stands for $\mu'(f)$ and m2 for $\mu''(f)$)

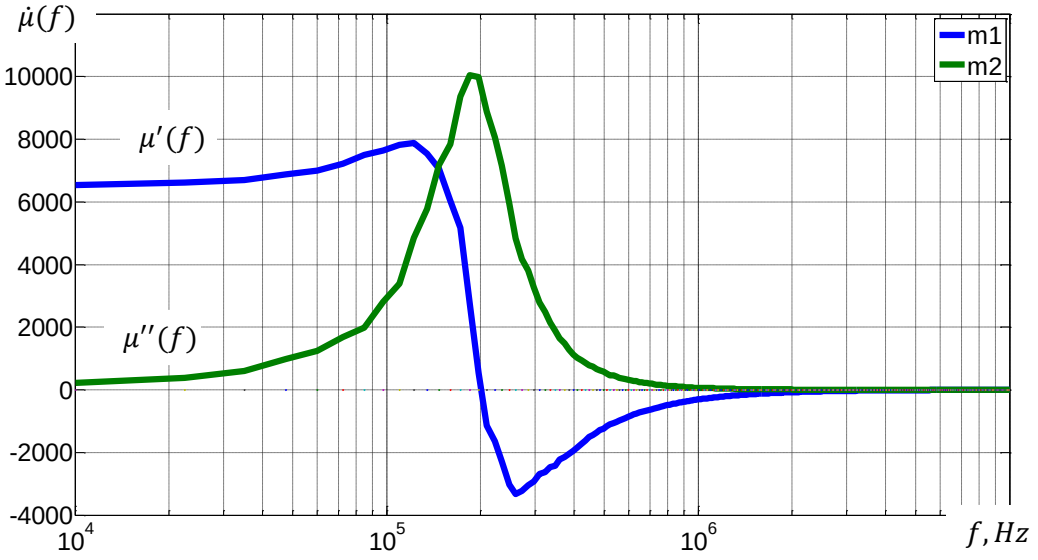

Figure A2.9. Measured CIP of sample B5 (m1 stands for $\mu'(f)$ and m2 for $\mu''(f)$)

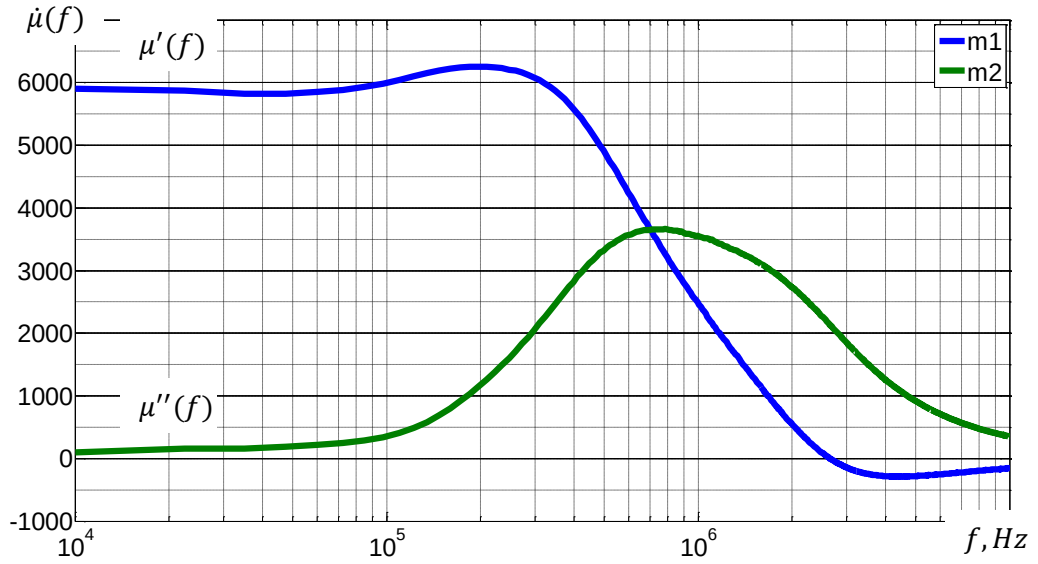

Figure A2.10. Measured CIP of sample C1 (m1 stands for $\mu'(f)$ and m2 for $\mu''(f)$)

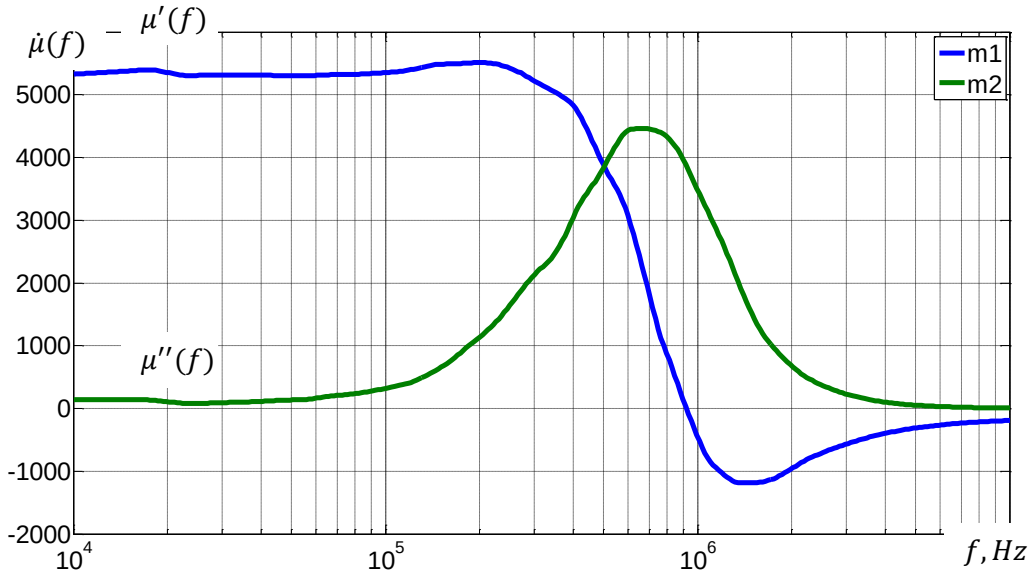

Figure A2.11. Measured CIP of sample C2 (m1 stands for $\mu'(f)$ and m2 for $\mu''(f)$)

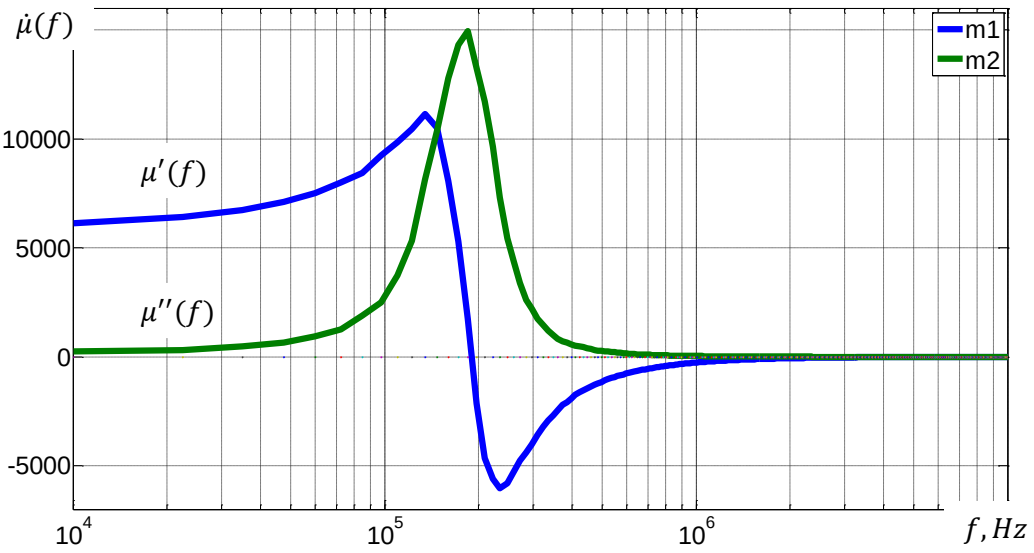

Figure A2.12. measured CIP of sample C3 (m1 stands for $\mu'(f)$ and m2 for $\mu''(f)$)

APPENDIX 3. MODEL APPLICATION TO STUDIED FERRITE CIP SPECTRA

On the following figures m1, m2 stands for $\mu'(f)$ and $\mu''(f)$ respectively; m2M – stands for model application on spectra; $m1_{kk}M$ stands for KKR evaluation of model $\mu'(f)$:

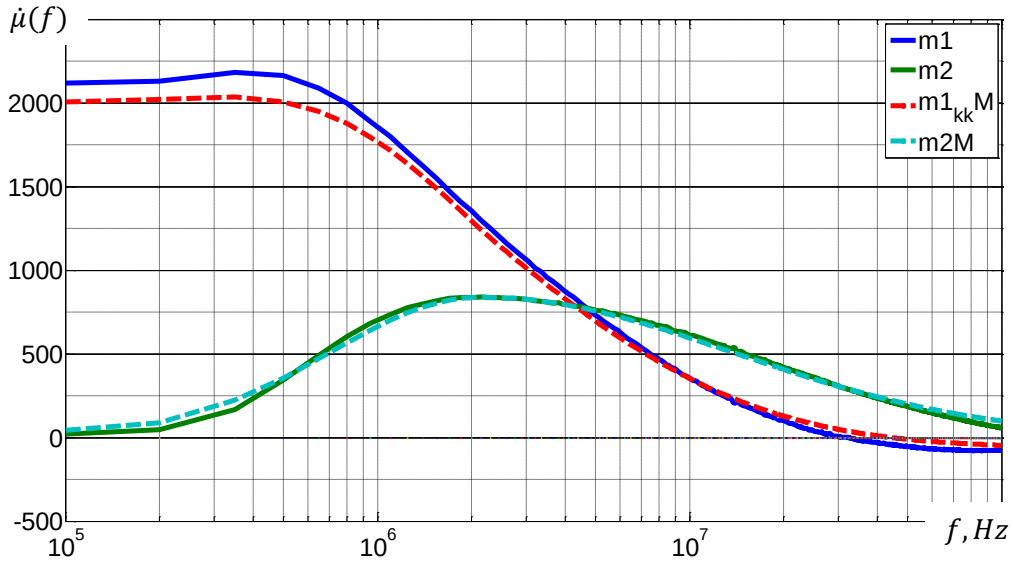

Figure A3.1. Model application to A1 sample.

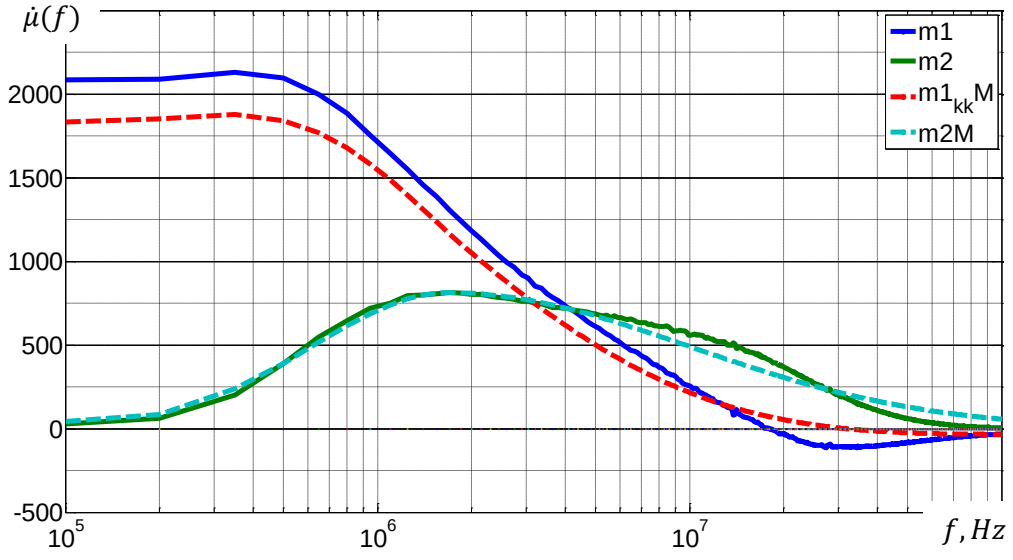

Figure A3.2. Model application to A2 sample.

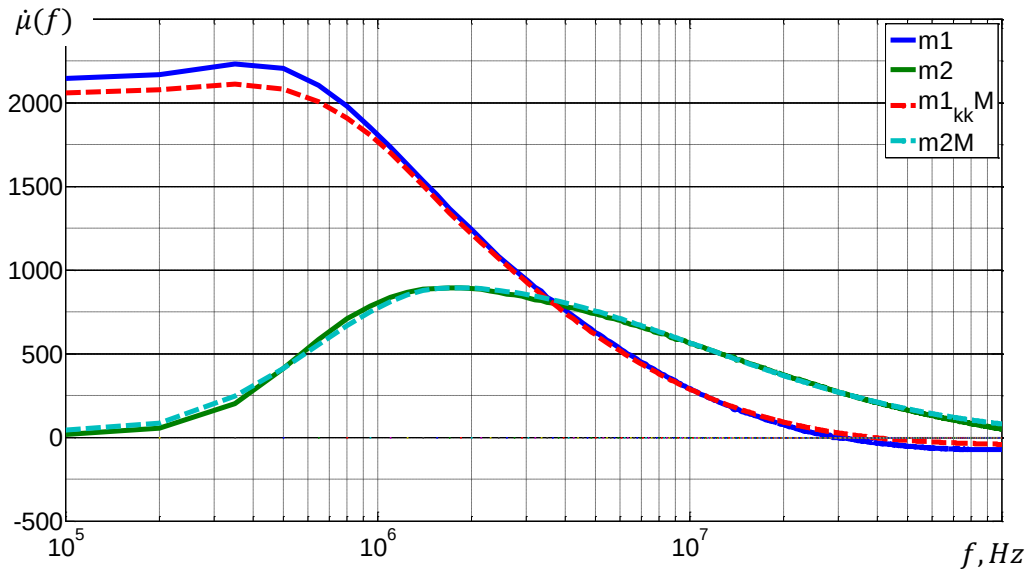

Figure A3.4. Model application to A3 sample.

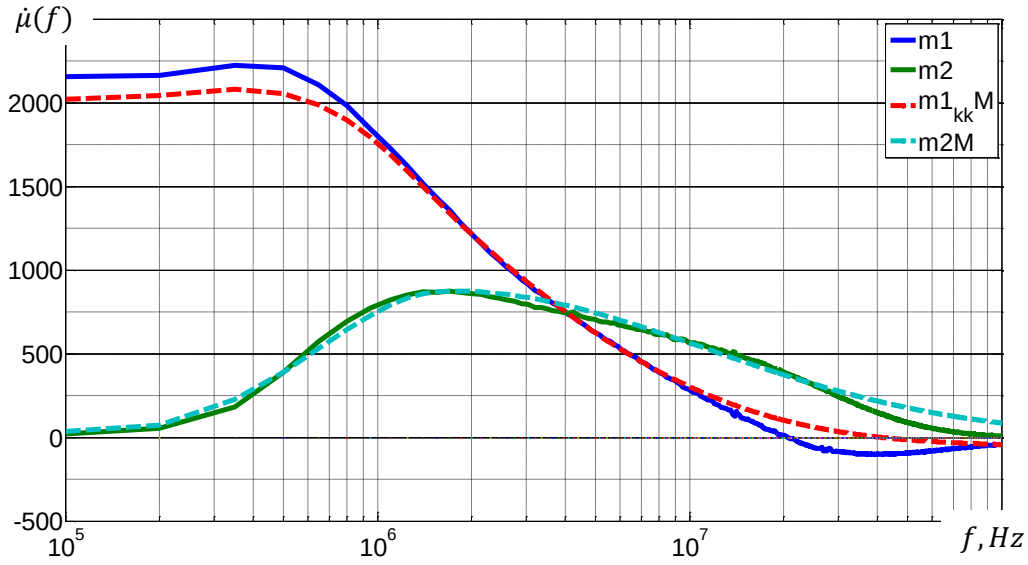

Figure A3.5. Model application to A4 sample.

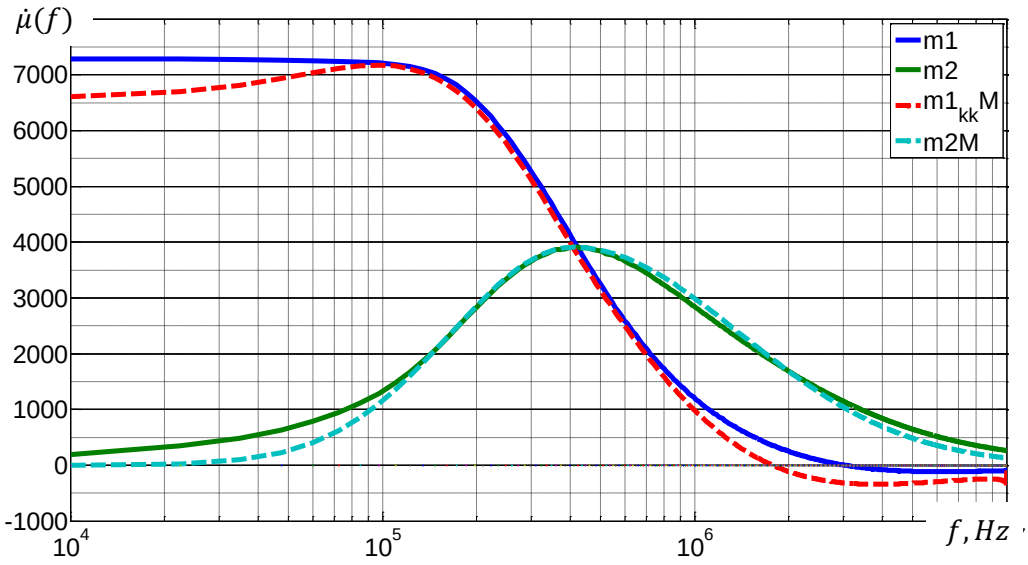

Figure A3.7. Model application to B2 sample.

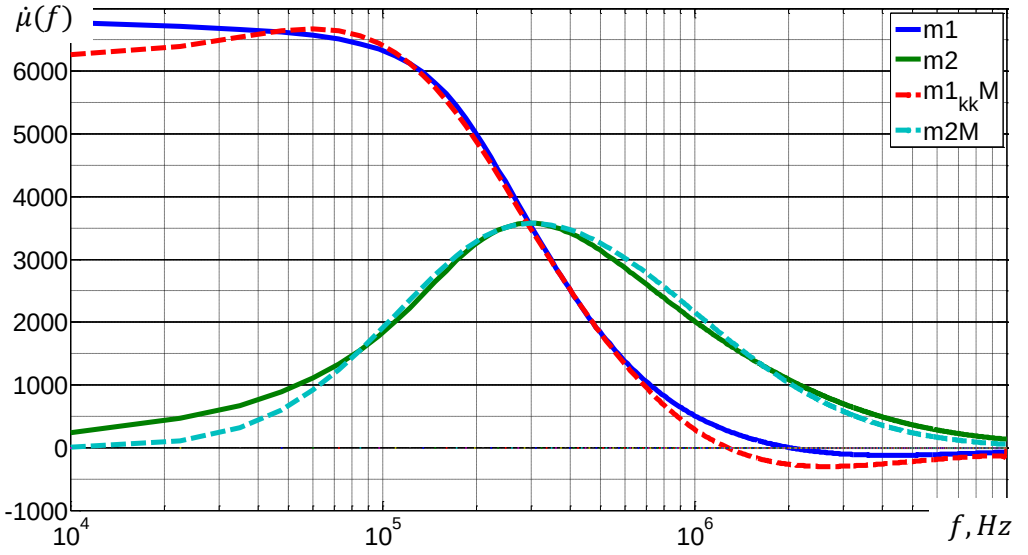

Figure A3.8. Model application to B3 sample.

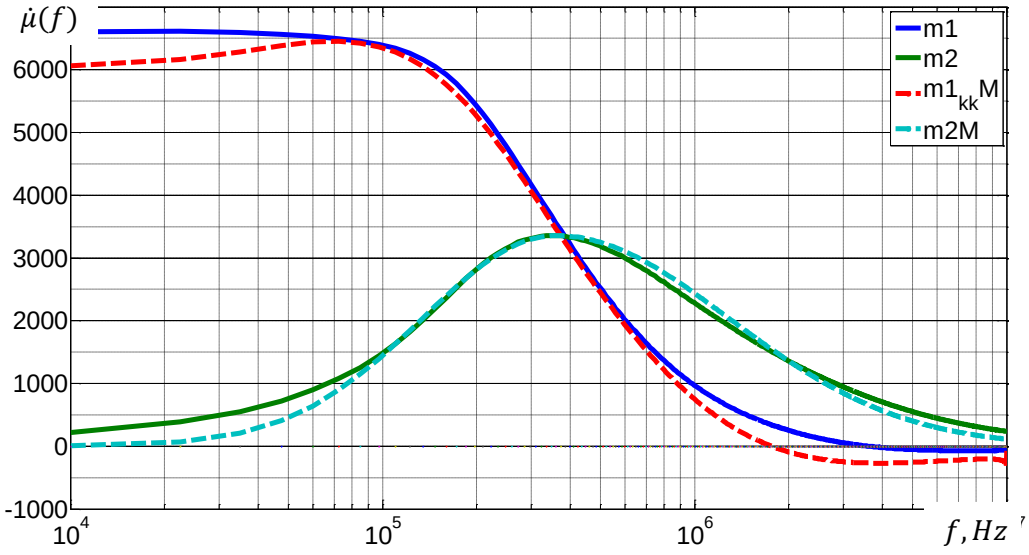

Figure A3.9. Model application to B4 sample.

APPENDIX 4. KRAMERS KRONIG RELATIONS APPLICATION TO EXPERIMENTAL DATA

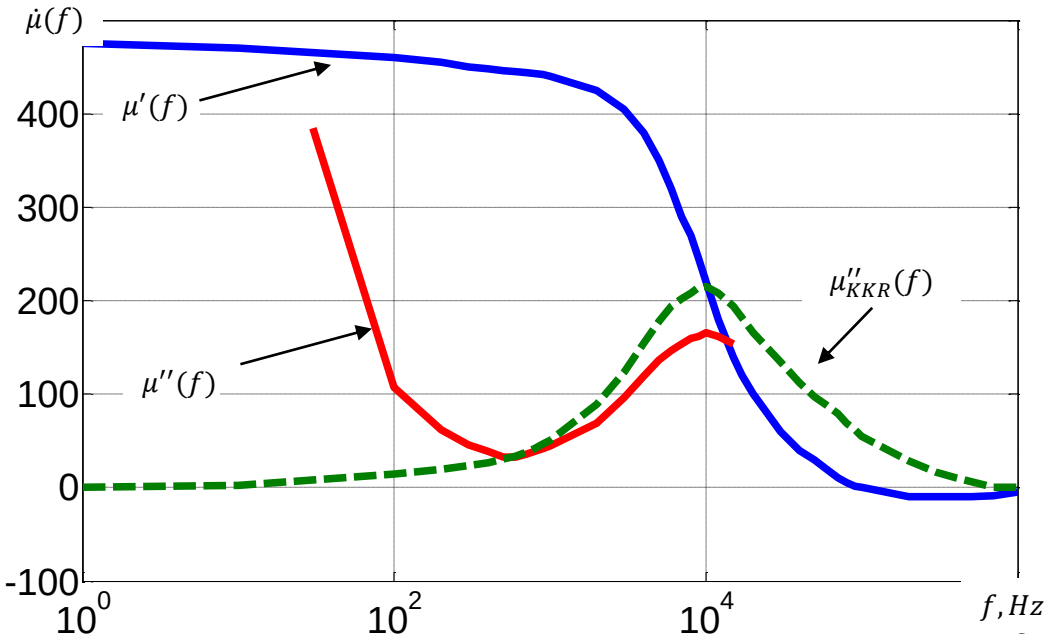

Figure A4.1. Permeability of spectra of $Ni_{0.55}Zn_{0.45}Fe_2O_4$ ferrite, adopted from [62, Fig. 3, Fig. 4, T = 1300 °C]

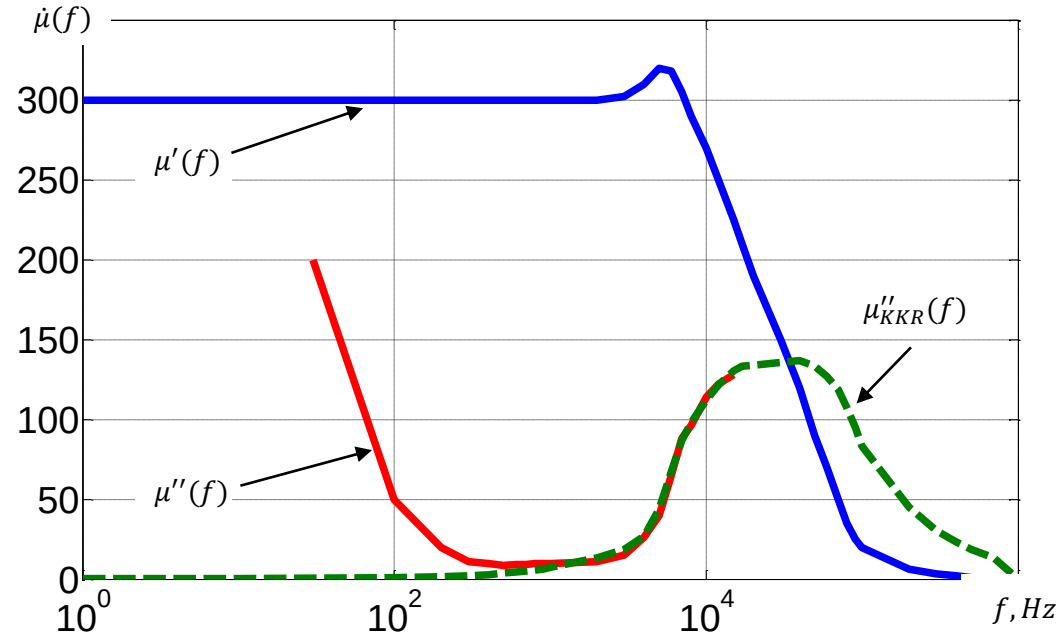

Figure A4.2. Permeability of spectra of $Ni_{0.55}Zn_{0.45}Fe_2O_4$ ferrite, adopted from [62, Fig. 3, Fig. 4, T = 1200 °C]

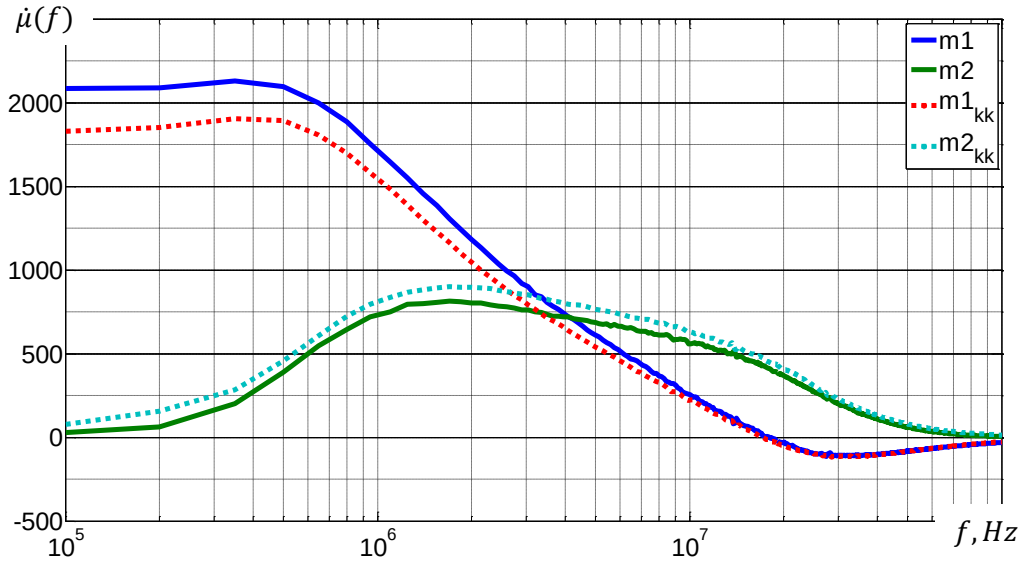

Figure A4.3. KKR application to A2 sample.

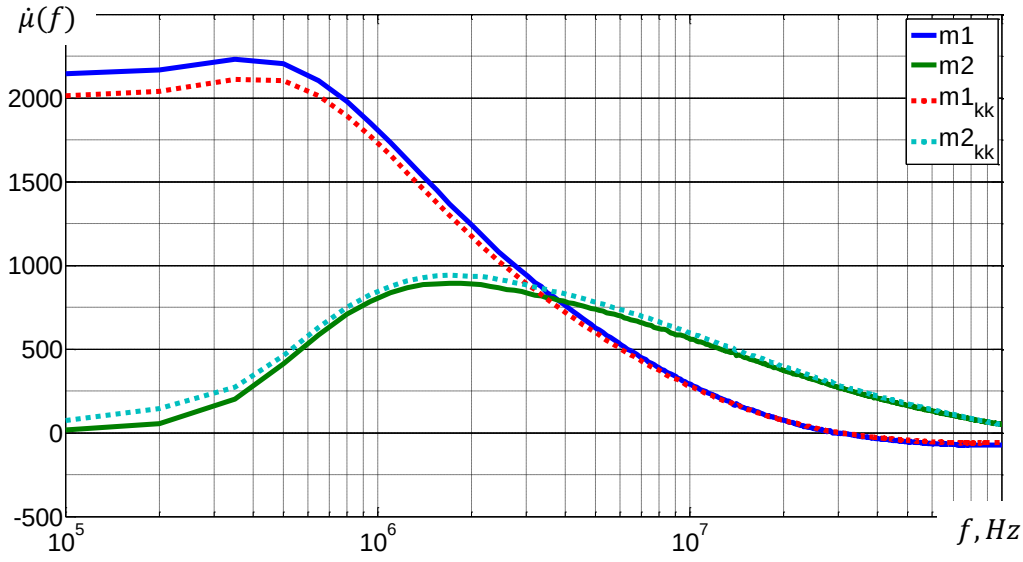

Figure A4.4. KKR application to A3 sample.

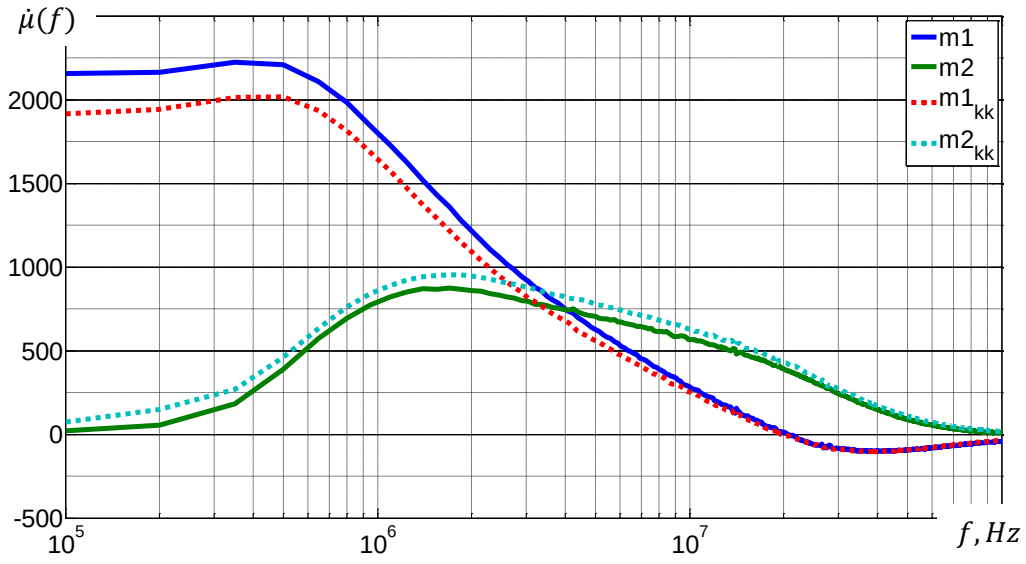

Figure A4.5. KKR application to A4 sample.

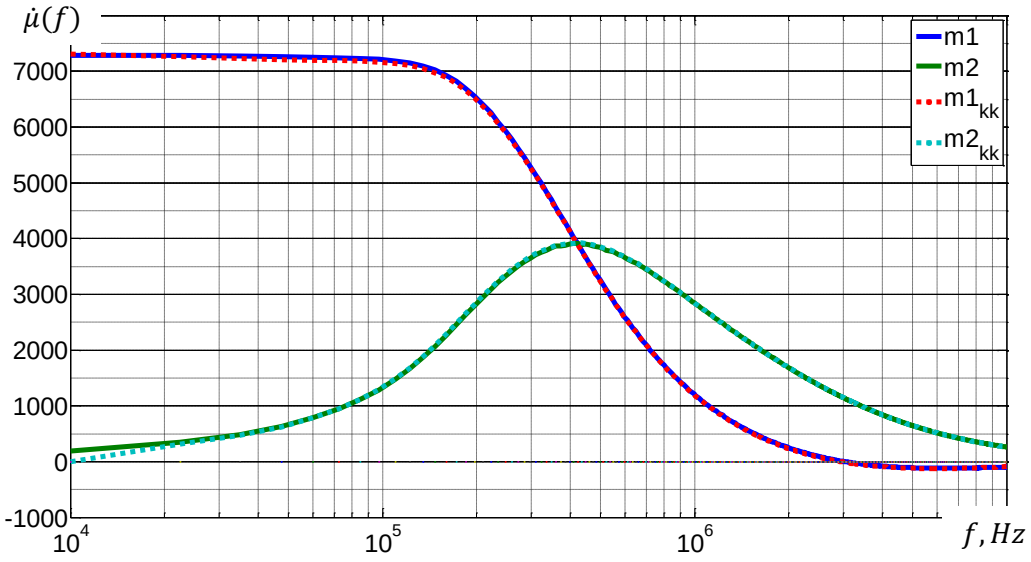

Figure A4.6. KKR application to B2 sample.

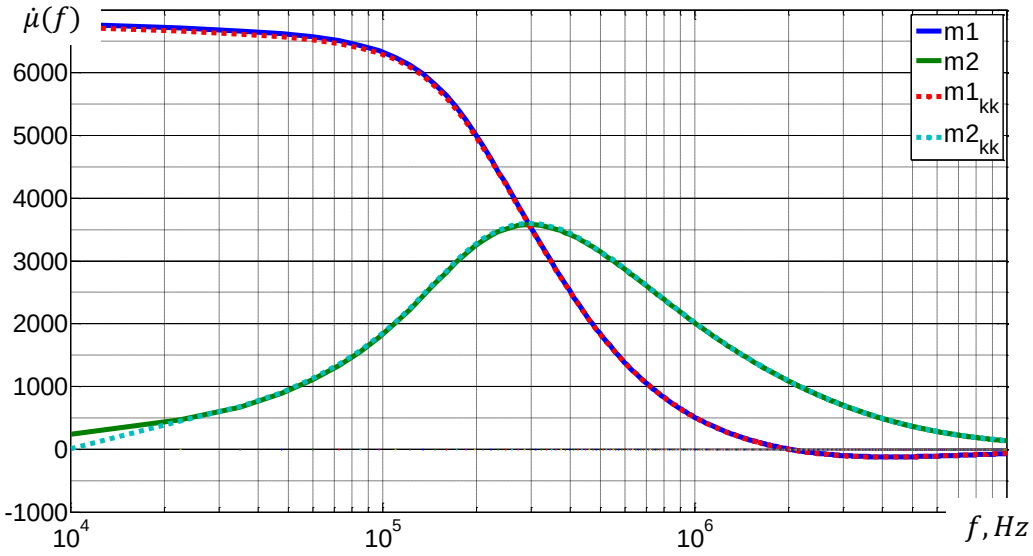

Figure A4.9. KKR application to B3 sample.

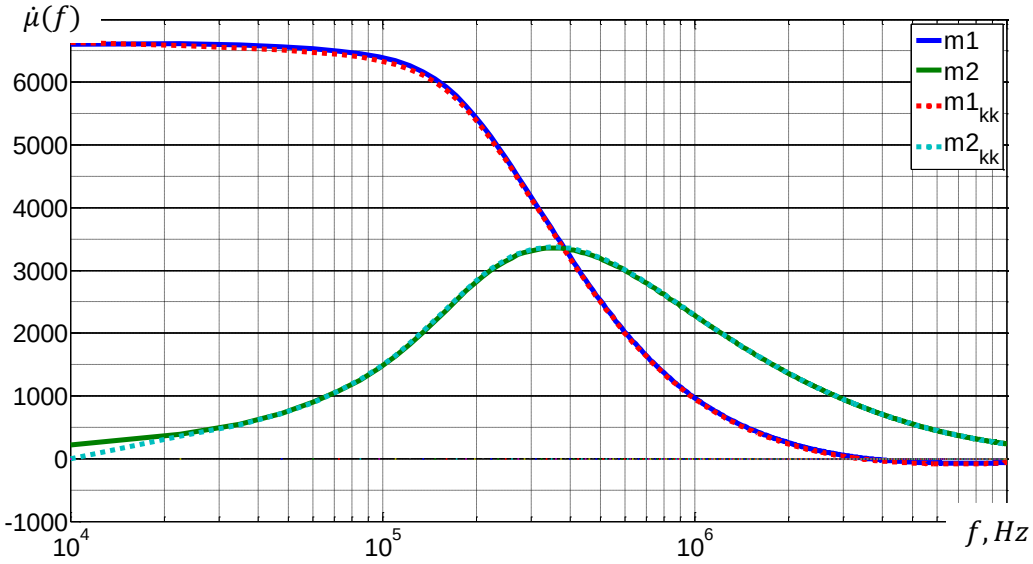

Figure A4.10. KKR application to B4 sample.

APPENDIX 5. DIMENSIONAL RESONANCE IN GAPPED C3 SAMPLE

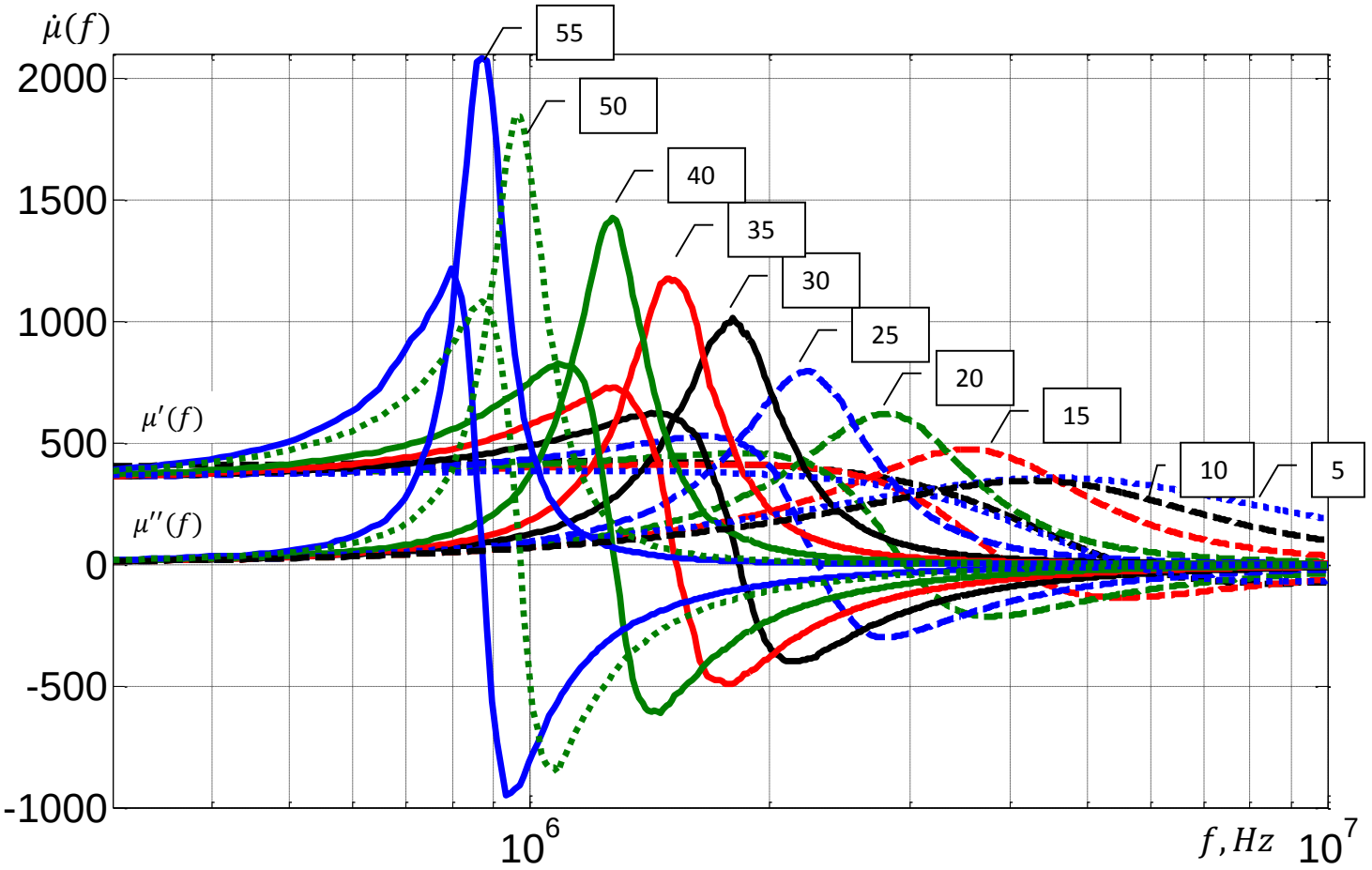

Figure A5.1 Dimensional resonance dependence from turn count N for the C3 core with nonmagnetic air gap = 0.3 mm.

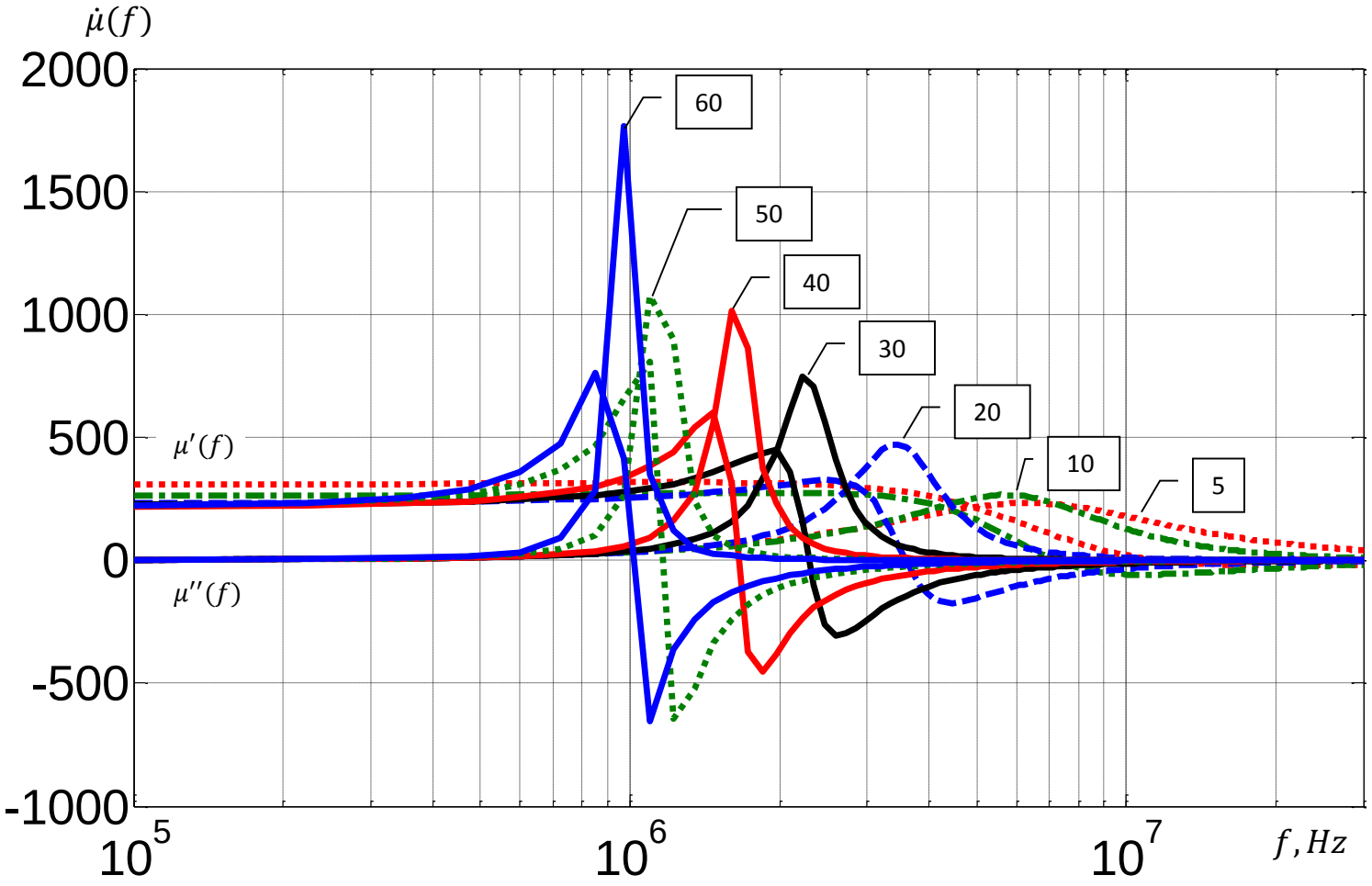

Figure A5.2 Dimensional resonance dependence from turn count N for the C3 core with nonmagnetic air gap = 0.6 mm.

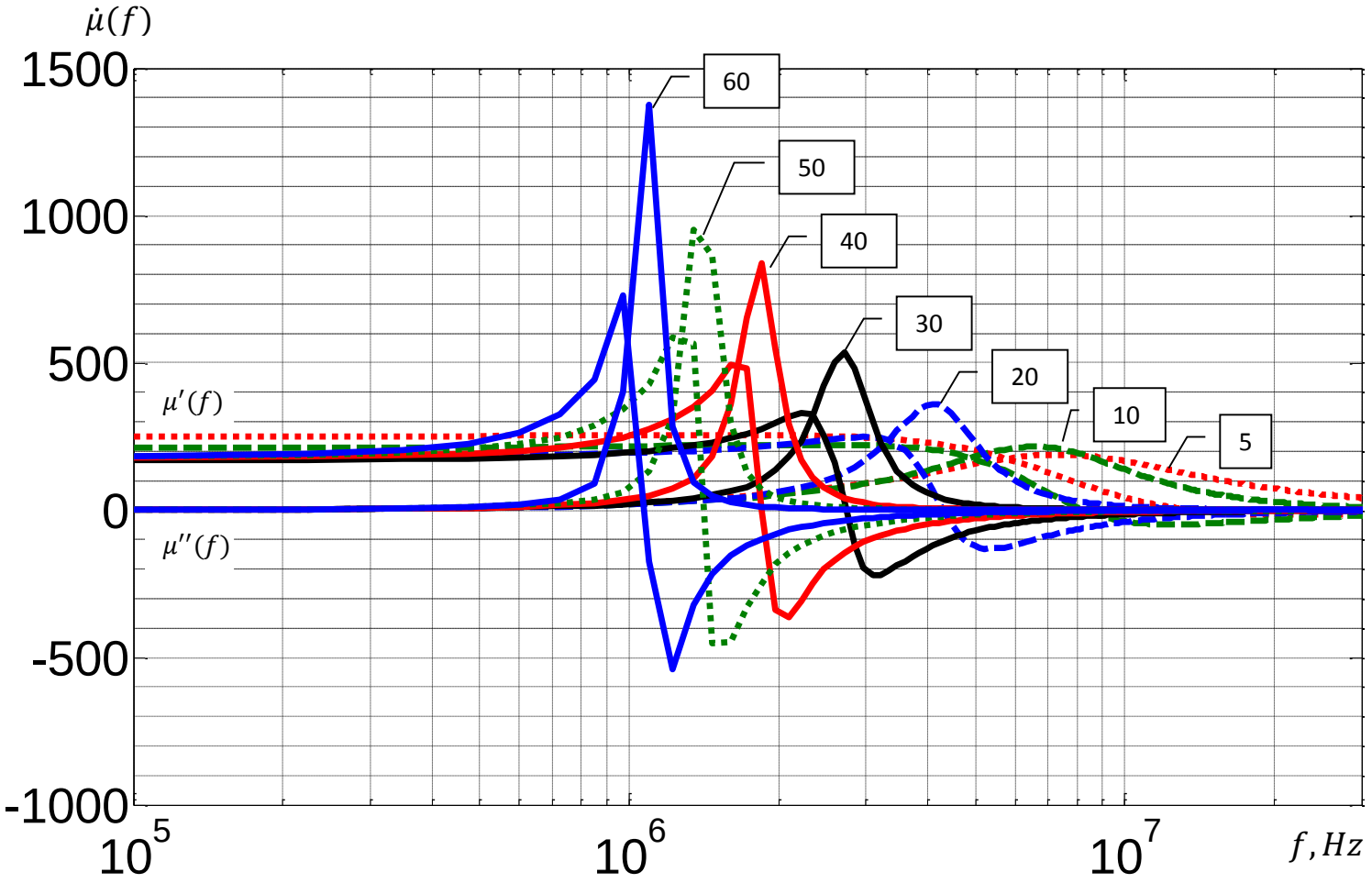

Figure A5.3 Dimensional resonance dependence from turn count N for the C3 core with nonmagnetic air gap = 1 mm.